THE ROLE OF MAFIC HETEROGENEITY IN THE GENERATION OF LAVAS ON MAURITIUS

A Dissertation

Presented to the Faculty of the Graduate School

of Cornell University

In Partial Fulfillment of the Requirements for the Degree of

Doctor of Philosophy

by

Jacob C. Moore

August 2009

THE ROLE OF MAFIC HETEROGENEITY IN THE GENERATION OF LAVAS ON MAURITIUS

Jacob C. Moore, Ph. D.

Cornell University 2009

Mauritius Island (20°20' S, 57°30' E) is the penultimate volcanic island of the Réunion mantle plume. Mauritius has a unique history of episodic volcanism characterized by three temporally distinct eruptive phases: 1) the shield-building Older Series lavas (8.4-5.5 Ma), 2) the Intermediate Series (3.5-1.9 Ma), and 3) the Younger Series (1.0-0.00 Ma). The study of newly available drill cores has facilitated an advanced subsurface investigation into the evolution of the island. Radiometric dating of deep lava units has identified the earliest known samples (8.4 Ma) and demonstrated the existence of deep post-erosional lavas (>200 m). The Intermediate and Younger Series remain chemically indistinguishable, apart from curious differences in $^{206}Pb/^{204}Pb$ and $^{208}Pb/^{204}Pb$. Contrary to other worldwide observances of post-erosional volcanism (*e.g.*, Hawaii, Tahaa, Madeira), the Older Series lavas are enriched in incompatible trace elements relative to the post-erosional lavas. However, isotope systematics remain consistent with other islands, with shield building lavas having more enriched isotopic signatures. Calculated volumes for the combined post-erosional lavas exceed 35 km^3, closely resembling Hawaiian analogues (20-60 km^3), and form decreasing linear trends with increasing shield volume. The chemically distinct shield and post-erosional lavas cannot be explained solely by variations in the extent of partial melting and require distinct sources for each class. Two scenarios for magma generation from a lithologically heterogeneous plume composed of enriched

(eclogitic) and depleted (peridotitic) components are modeled using Adiabat_1ph: 1) mixing of melts from the enriched and depleted components, and 2) generation and melting of a hybrid pyroxenite component. P-T conditions for the system are modeled as a weighted composite of the two components, producing enhanced eclogite and depressed peridotite productivity. Iterative forward modeling of trace element data to the shield lavas allows for the calculation of post-erosional and source component compositions. The post-erosional lavas are plausibly reproduced in each model with a T_P = 1525 °C and maximum post-erosional ascent pressure of 2.5 GPa. Light REE enriched source components are required by both models. A lithologically heterogeneous plume consisting of stretched heterogeneous filaments can plausibly account for the required generation of the Intermediate and Younger Series from a single packet of plume material.

BIOGRAPHICAL SKETCH

Jacob Cecil Moore was born in Tulsa, Oklahoma but grew up in La Verne, California. He spent his youth immersed in sports and Boy Scouts, each of which contributed to his love of the outdoors. After graduating from Bonita High School in June 1999, Jacob matriculated to the University of California, Davis. At Davis he fell in love with geology, in part because it allowed him to continue exploring the great outdoors. Jacob graduated with a Bachelor of Science in Geology with High Honors in 2003 before beginning his graduate study in geochemistry at Cornell University.

To Mom and Dad, for always seeing the best in me.

And to my wonderful wife Holly: my love, my life, and my best friend.

ACKNOWLEDGMENTS

The author would like to acknowledge those that helped make this work possible. The guidance of my committee allowed me to develop scientifically, yet continually prodded me in the right direction: Drs. William White, Jason Phipps Morgan, Robert Kay, and Frank DiSalvo. Numerous conversations with Dr. Debajyoti Paul greatly clarified many of the difficulties encountered in the work. The Mauritius Water Resources Unit provided invaluable support and assistance in the field and secured access to otherwise unavailable sampling locations. Facilities for analytical work and assistance were kindly provided by Drs. Steve Galer and Wafa Abouchami at the Max-Planck-Institut für Chemie in Mainz, Germany and by Drs. Yongjun Gao and Jon Snow at Department of Earth and Atmospheric Sciences at the University of Houston. Paula Smith provided priceless guidance with Adiabat_1pH that facilitated the thermodynamic modeling in this work. To the faculty and graduate students of EAS, my colleagues and friends, who were always willing to discuss seeming insignificant details over a pitcher of beer, especially Adam, Jack, Greg, Brian, and Peter. Lastly, to my parents and family and wife Holly, whose love and patience were never ending. This work was funded in part by National Science Foundation Grant EAR-0635865 to William White and Debajyoti Paul.

TABLE OF CONTENTS

LIST OF FIGURES

LIST OF TABLES

LIST OF ABBREVIATIONS

CIR – Central Indian Ridge

HFSE – High field strength elements

HREE – Heavy rare earth elements

IS – Intermediate Series

LLOD – Liquid line of descent

LREE – Light rare earth elements

Ma – *Mega annum*; millions of years ago, i.e., a specific point in time

MCFZ – Marie Celeste fracture zone

MORB – Mid ocean ridge basalt

Myr – Million years, i.e., a period of time

OIB – Ocean island basalt

OS – Older Series

REE – Rare earth elements

YS – Younger Series

CHAPTER 1 – INTRODUCTION AND GEOLOGIC SETTING

"You gather the idea that Mauritius was made first, and then heaven; and that heaven was copied after Mauritius."

–Mark Twain, "Following the Equator", 1897

Geological Setting of Mauritius

Mauritius Island is located in the Mascarene Basin of the western Indian Ocean (21° 20' S, 57° 30' E; Figure 1), approximately 1000 km east of Madagascar, 1100 km west of the Central Indian Ridge, and 215 km northeast of Réunion Island. The island is the penultimate island of the Réunion hotspot track (*e.g.*, Morgan, 1981), inferred to have erupted from magmas of the deep-seated Réunion mantle plume (Courtillot et al., 2003; Montelli et al., 2004) as the Indian plate moved northeastward over the stable plume. NUVEL 1A calculations of the modern African plate vector indicate Mauritius is drifting northeastward at 050.6° at a rate of approximately 24.3 mm/a (DeMets et al., 1994), consistent with the northeast-southwest trace of the Mascarene Plateau. In addition to Mauritius, the Réunion hotspot is believed to be responsible for producing the Deccan Traps of western India, the Chagos – Maldives – Laccadive Ridge system, the Mascarene Plateau, and Réunion Island. Mafic rocks from the South Tethyan suture zone of Pakistan dating to ~ 73 Ma show geochemical signatures similar to other Réunion plume products, suggestive of a pre-Deccan origin (Mahoney et al., 2002).

Rodrigues Island and the Rodrigues Ridge, nearly normal to the Mascarene Plateau, have been suggested as the products of channelized asthenosperic flow from the Réunion hotspot toward the Central Indian Ridge (CIR) (Morgan, 1978; 1987; Mahoney et al., 1989; Murton et al., 2005), and as a post-erosional phase

Figure 1. Simplified geologic map of Mauritius modified from Paul et al. (2005) depicting the Older Series (green), Intermediate Series (purple), and Younger Series (orange). Locations of drill core (square) and surficial samples (circle) are shown. Inset shows regional geology of the western Indian Ocean.

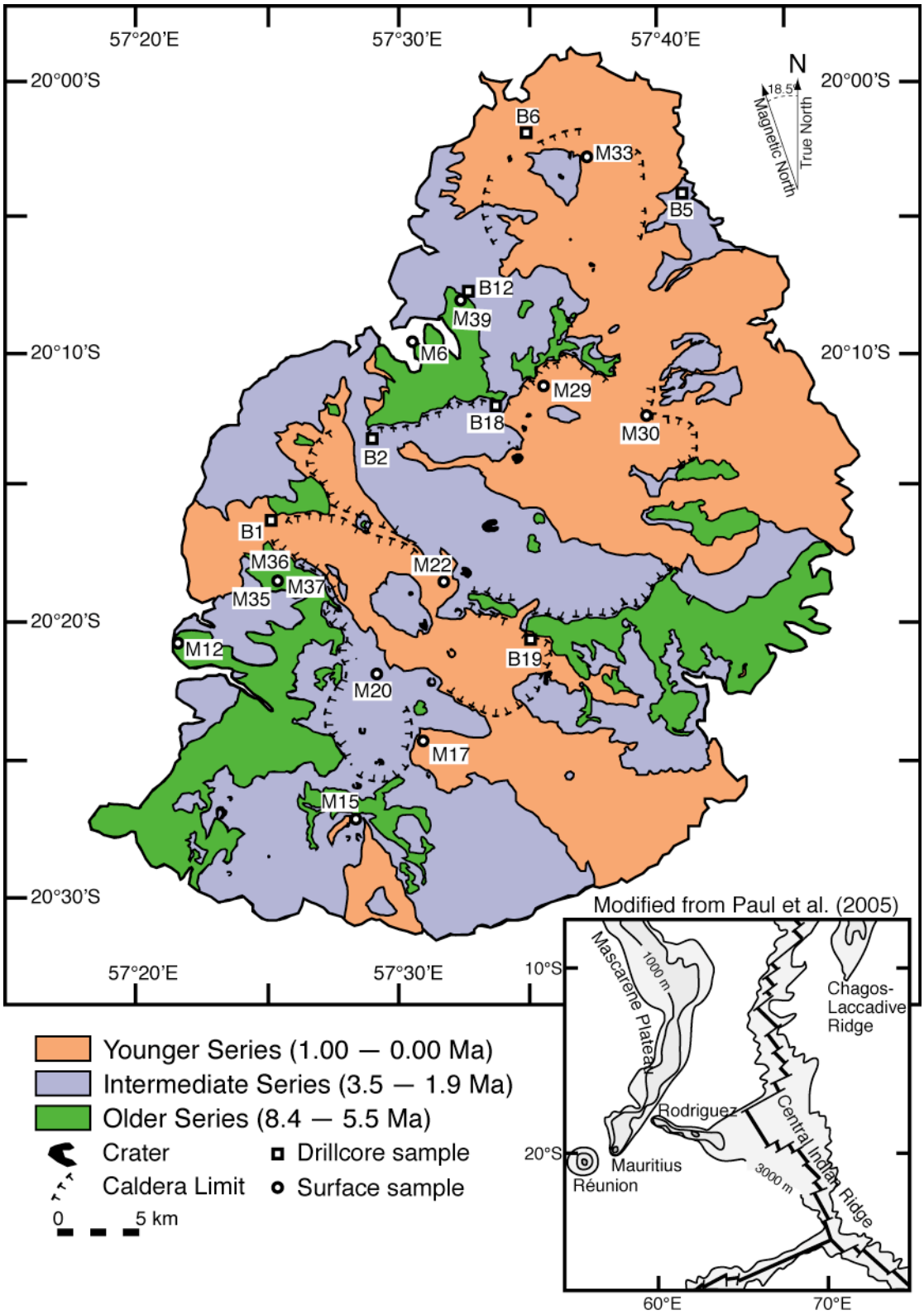
57°20'E
57°30'E
57°40'E
20°00'S
20°10'S
20°20'S
20°30'S
N
18.5
Magnetic North
True North
B6
M33
B5
B12
M39
M6
M29
B18
M30
B2
B1
M36
M37
M35
M22
M12
B19
M20
M17
M15
Younger Series (1.00 — 0.00 Ma)
Intermediate Series (3.5 — 1.9 Ma)
Older Series (8.4 — 5.5 Ma)
Crater
Caldera Limit
Drillcore sample
Surface sample
0
5 km
Modified from Paul et al. (2005)
10°S
20°S
60°E
70°E
Mascarene Plateau
1000 m
Chagos-
Laccadive
Ridge
Rodriguez
Central Indian Ridge
3000 m
Mauritius
Réunion

(Duncan, 1990). This lineament extends almost all the way to the CIR via the Three Magi, a series of *en echelon* ridges, and Gasitao Ridge. The Three Magi have a maximum age of 6.5 Ma (age of underlying ocean crust), though relatively fresh-looking samples were collected in 1998 (Dyment et al., 1999). The easternmost portion of the Gasitao Ridge dates between 0.4 and 1.8 Ma (Dyment et al., 2000). Dredge samples from the Rodrigues Ridge range between 8 – 10 Ma in age (Duncan, 1990), but no westward progression with age is apparent. Thus, the Rodrigues Ridge formed almost immediately before the onset of shield building volcanism on Mauritius. Volcanic activity from Rodrigues Island dates to 1.32 – 1.54 Ma (McDougall et al., 1965; Upton et al., 1967), *i.e.*, during the volcanic hiatus on Mauritius between the Intermediate and Younger Series.

While imprecisely known, the current location of the Réunion hotspot has been proposed as ~ 300 km southwest of Réunion Island (Bonneville et al., 1988; Sleep, 1990), although a young seamount 160 km west of Réunion has been proposed as the youngest volcanic edifice along the hotspot trace (Duncan, 1990). Plate reconstructions of the Mascarene basin indicate Mauritius would have erupted through oceanic crust created at the CIR at about 50 – 60 Ma (Royer et al., 1992), whereas Fretzdorff et al. (1998) depict Mauritius as built on magnetic anomaly A32 (their Figure 2b), corresponding to eruption through ~ 65 Ma oceanic crust (Berggren et al., 1985). The thickness of oceanic lithosphere of this age is approximately 75 km. These reconstructions indicate the Réunion plume has experienced progressively thickening crust since it crossed the CIR, resulting in a steady decrease in melt production rate for the last ~ 35 Myr (White, 1993).

The southern section of the Mascarene Plateau (including Mauritius) lies between the Wilshaw Fracture Zone to the west, and the Mauritius Fracture Zone (MFZ), which closely bounds the plateau to the east. These fracture zones strike

approximately 048°, and date to the formation of the oceanic crust at the CIR during the late Paleozoic and early Cenozoic. Volcanism along nearly the entire length of the Mascarene Plateau (> 700 km and ~ 45 Myr) appears to be strongly controlled by the MFZ to the east. Despite this strong, apparent, structural control on volcanism, Réunion Island is offset approximately 130 km westward. This offset projects itself as a kink in the trace of the Réunion hotspot. Fretzdorff et al. (1998) suggested that the staggered position of Réunion may be a consequence of lava erupting preferentially through a preexisting weakness within the ocean lithosphere from a fossil ridge segment, though Deplus et al. (2007) argue the geophysical data are more consistent with a small 035° fracture zone. Geochemical similarities between Réunion lavas and samples from the Rodrigues Ridge, the *en echelon* Three Magi, the Gasitao Ridge, and the CIR south of the Marie Celeste Fracture Zone (MCFZ) are suggestive of progressive mixing between Réunion plume material and oceanic lithosphere over a 1000 km course (Murton et al., 2005; Nauret et al., 2006). Moreover, the trace from Réunion, through Mauritius and the Rodrigues Ridge to the CIR at the MCFZ is along a very similar vector to the direction of modern CIR spreading. The modern CIR near the MCFZ at 20° S is spreading at a full rate of 43 mm/a at 063.9° (Müller et al., 1993; DeMets et al., 1994; Royer et al., 1997).

Geophysical analysis of paleomagnetic anomalies and fracture zones traces from areas adjacent to the modern CIR and Carlsberg ridge suggest a small change in the regional tectonics preceding the period of eruptive activity at Mauritius (Figure 2). The pole of rotation for the Africa – India pair migrated toward the plate boundary from 11 – 9 Ma, shifting the opening direction and somewhat increasing the angular opening rate between the two plates (DeMets et al., 2005; Merkouriev and DeMets, 2006). This deviation in pole position is consistent with the timing of several regional geotectonic events between 11 – 8 Ma, including deformation within the equatorial

Figure 2. Cartoon depicting the proposed history of plume material from geodynamic and tectonic evolution of the western Indian Ocean for since 20 Ma (see text for references). (a) > 12 Ma. The Reunion hotspot is forming the southeastern part of the Mascarene Plateau. The CIR is spreading roughly perpendicular to the MFZ and WFZ. Réunion hotspot indicated by white circle. (b) 8 – 11 Ma. Changes in regional tectonics result in a more northerly spreading direction. Flow of plume material shifts to follow plate motion. The Rodrigues Ridge erupts rapidly between 8 - 10 Ma, possibly from regional trans-tensive forces and the onset of plume material flowing at the base of the lithosphere toward the ridge. Mauritius begins erupting *c*. 8 Ma. (c) < 2 Ma. Northeastly flow of plume material toward the ridge continues. Three Magi are as old as 6.5 Ma, though likely younger. The Gasitao Ridge (not depicted, east of TM) dates between 0.4 - 1.8 Ma. Plume-contaminated E-MORB occurs south of the MCFZ. Réunion begins erupting *c*. 2.0 Ma. CIR-Central Indian Ridge, M-Mauritius, MCFZ-Marie Celeste Fracture Zone, MFZ-Mauritius Fracture Zone, MP-Mascarene Plateau, Reu-Réunion, Rod-Rodrigues Island, RR-Rodrigues Ridge, TM-Three Magi, WFZ-Wilshaw Fracture Zone. After Murton et al. (2005) and Nauret et al. (2006) and references therein.

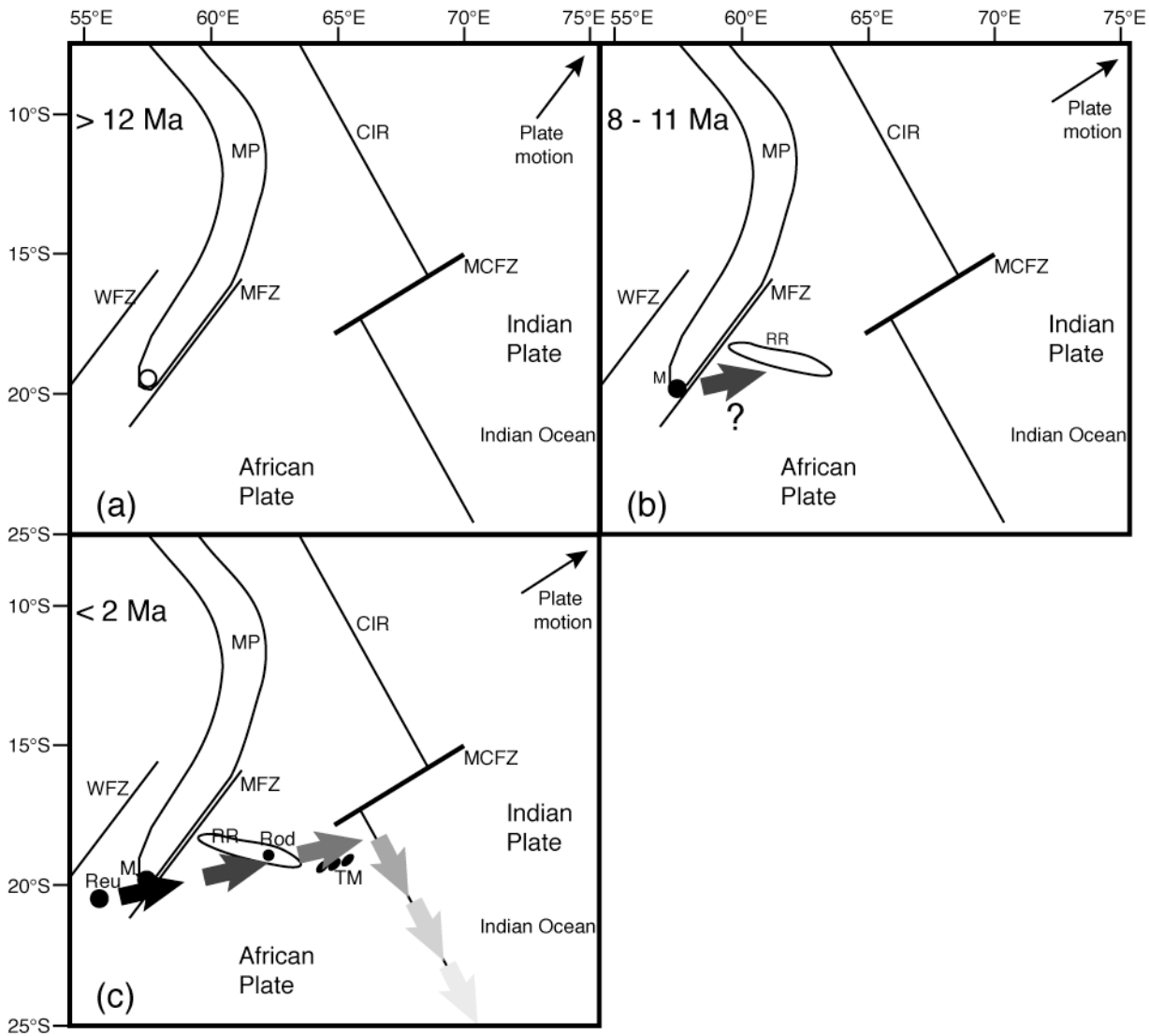
55°E
60°E
65°E
70°E
75°E
10°S
15°S
20°S
25°S
> 12 Ma
MP
CIR
Plate motion
WFZ
MFZ
MCFZ
Indian Plate
Indian Ocean
African Plate
(a)
8 - 11 Ma
RR
M
?
(b)
< 2 Ma
Rod
TM
Reu
(c)

Central Indian basin (Moore et al., 1974; Weissel et al., 1980; Cochran, 1990) and the possible maximal elevation and subsequent onset of collapse of the Tibetan Plateau (Harrison et al., 1992; Molnar et al., 1993). Using similar techniques, Royer et al. (1997) established the continuity of the modern CIR plate motion for the past 11 Ma. These authors identified the similarity between the poles of rotation at chron 2A (3 Ma) and chron 5 (11 Ma) for the Indian, African, and Australian plates. These calculated poles show minimal difference for the Africa – India pair and only a small increase in the easterly component for the Africa – Australia pair between chron 2A a chron 5. These results indicate that plate motions of the overlying African plate above the Réunion plume have been relatively regular since the onset of eruptive activity on Mauritius (at least 8 Ma), and are thus broadly consistent with the proposed flow of Réunion plume material toward the Rodrigues Ridge and the MCFZ at the CIR.

Alternatively, Dyment et al. (2001) argue that the Rodrigues, Three Magi, and Gasitao Ridges are the product of volcanism associated with regional scale intra-plate deformation. The geochemical signatures at these ridges associated with the Réunion plume would thus indicate sampling of an upper mantle metasomatized by plume material.

Volcanic History and Evolution of Mauritius

A volcanic origin for Mauritius has long been recognized (Darwin, 1844). In the first systematic study of the geology and mineral resources of the island, Simpson (1950) mapped the surficial volcanics, classifying the lavas into three periods of eruptive activity: the Older Volcanic Series, the early Younger Volcanic Series, and the late Younger Volcanic Series. Simpson (1950) concluded the Older Volcanic Series and early Younger Volcanic Series were separated by an interval of "considerable duration", whereas the early and late Younger Volcanic Series were

separated by an interval of "no great duration." Walker and Nicolaysen (1954) completed a complementary petrologic study. These stages were later renamed the Older Series, Intermediate Series, and Younger Series, and the classification scheme confirmed by the extensive K-Ar geochronology and paleomagnetic study of McDougall and Chamalaun (1969). Combined, these works identified the three volcanic series as temporally and petrologically distinct, each separated by extensive periods of volcanic hiatus, erosion, and soil formation. The study of Simpson (1950) has defined the traditional history and interpretation of Mauritius, and remains the basis for all subsequent work.

The Older Series volcanics form the erosional remnants of a massive shield volcano built from the ocean floor in (at least) two stages (Figures 1 and 3). The earlier lavas are believed to comprise the bulk of the voluminous shield-building stage, consisting of transitional basalts in alternating lava-agglomerate sequences (Baxter, 1975a). Lavas from this stage are either nepheline or hypersthene normative, though the latter are dominant, and demonstrate evidence for moderate degrees of low-pressure fractionation of olivine and clinopyroxene (Baxter, 1975a). Suites of basic and ultrabasic nodules are associated with some of the porphyritic lavas of this stage and likely represent cumulate xenoliths (Baxter 1975a; 1978). The later lavas of the Older Series form a late-shield sequence that are more differentiated and show greater compositional variation than early lavas (Baxter, 1975a). These lavas are composed of feldspar-phyric basalts and trachybasalts, with associated high-level trachyte intrusions (Baxter, 1975a). Exposures of these lavas indicate they are volumetrically minor relative to the shield-building lavas, though they may have been removed by erosion or merely covered by subsequent eruptions (Baxter, 1975a). The exposed lavas of the Older Series have been dated from 7.9 to 5.5 Ma, late Miocene in age,

Figure 3. Cartoon illustrating the eruptive history of Mauritius. The Older Series consists of a basal breccia unit dated to at least 8.0 Ma, the main shield sequence, and a rare evolved post-shield stage. An eruptive hiatus exists from 5.5 to 3.5 Ma and predates the Intermediate Series, the first post-erosional stage. A second eruptive hiatus exists from 1.9 to 1.0 Ma, predating the Younger Series, the second post-erosional stage. Geologic units are as in Figure 1. Hawaiian analogues are given for each series.

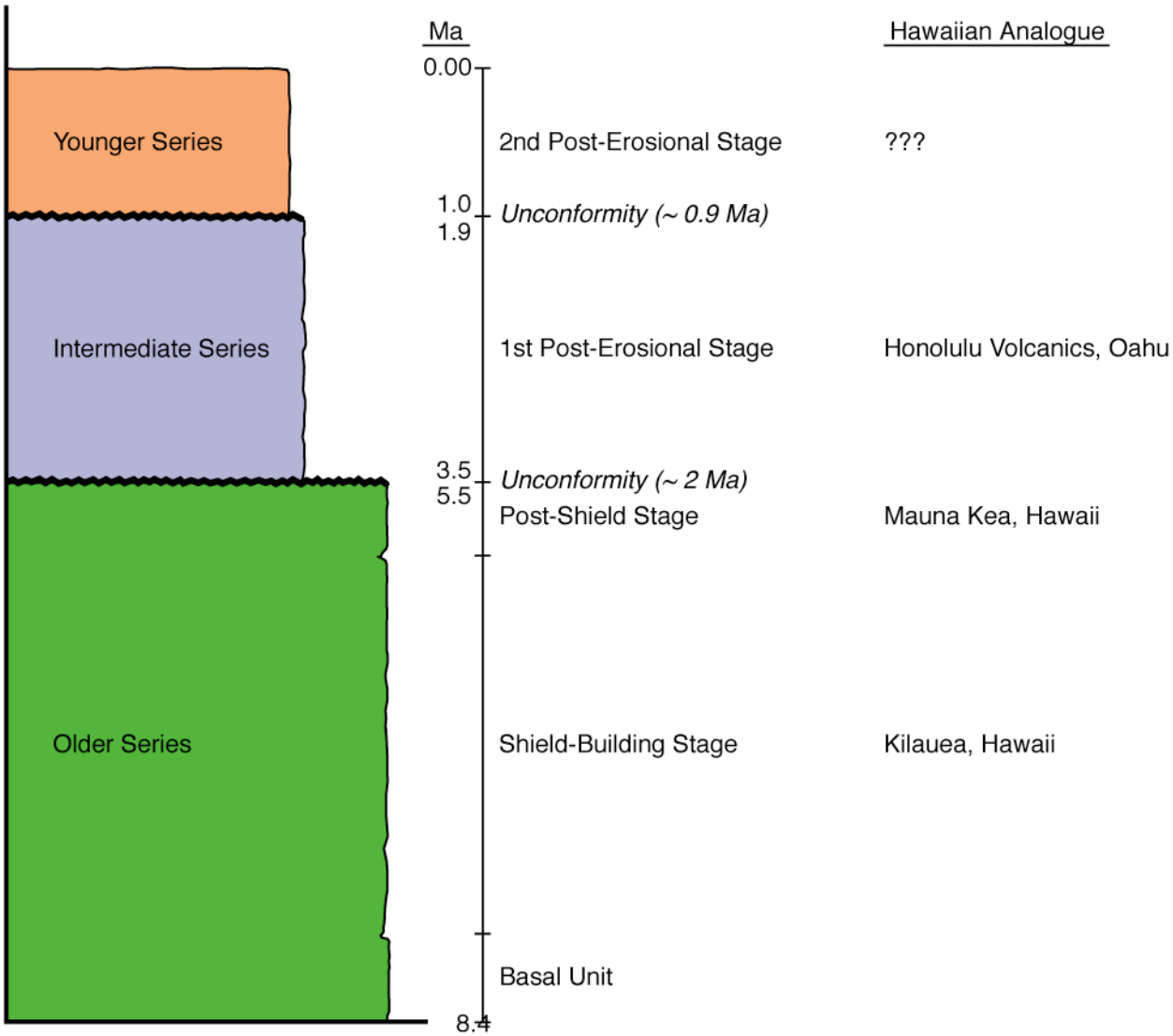
Younger Series
Intermediate Series
Older Series
Ma
0.00
1.0
1.9
3.5
5.5
8.4
2nd Post-Erosional Stage
Unconformity (~ 0.9 Ma)
1st Post-Erosional Stage
Unconformity (~ 2 Ma)
Post-Shield Stage
Shield-Building Stage
Basal Unit
Hawaiian Analogue
???
Honolulu Volcanics, Oahu
Mauna Kea, Hawaii
Kilauea, Hawaii

with the more differentiated lavas erupting more recently (McDougall and Chamalaun, 1969; Nohda et al., 2005).

The eruption of Intermediate Series lavas is predated by a volcanic interlude and extensive erosion of the Older Series massif, lasting approximately 2.0 Myr. Intermediate Series lavas are primitive in composition, showing pronounced silica-undersaturation trends and a general lack of evidence for extensive low-pressure crystal fractionation, suggestive of erupting unmodified from deeper levels (Baxter, 1976). Once thought to be restricted to outcrops along the southwestern corner of the island, recent mapping has demonstrated a more expansive coverage for the series and increased unit thickness (Perroud, 1982; Giorgi et al., 1999; Paul et al., 2005). Exposed lavas from the Intermediate Series have been dated from 3.5 to 1.9 Ma, late Pliocene to Pleistocene in age (McDougall and Chamalaun, 1969; Nohda et al., 2005).

A second period of volcanic hiatus and erosion, of approximately 0.9 Myr preceded the appearance of the earliest Younger Series lavas. These lavas are classified predominantly as alkali basalt, though subordinate basanite lavas have been identified, and are less alkaline than the Intermediate Series (Baxter, 1976). Lavas from this stage show strong evidence for low-pressure fractionation of olivine (Baxter, 1976), similar to the lavas of the Older Series. Exposed lavas of the Younger Series have been dated as less than 1 Ma, Pleistocene in age (McDougall and Chamalaun, 1969; Nohda et al., 2005; Duncan, unpublished data).

Older Series exposures are predominantly restricted to topographic highs and the outer flanks of the island. Eruptive in-filling of the large central caldera complex has covered low-lying outcrops, though Older Series lavas are known to exist within the caldera at depth from drill core sampling (Figure 4). The central caldera complex can be further subdivided into a trilobic southern section, and a more complicated northern section. The study of Perroud (1982) identified the central caldera as a

Figure 4. Structural map of Mauritius illustrating the orientation and position of the fault systems on the island. Bold lines outline the caldera complexes of the island. Two main caldera units form the central caldera complex, and a third caldera is shown in the north. The ranges of the Intermediate and Younger Series post-erosional craters are shown, with the size of the circle proportional to the size of the crater. Colors after Figure 1. Map after Giorgi et al. (1999).

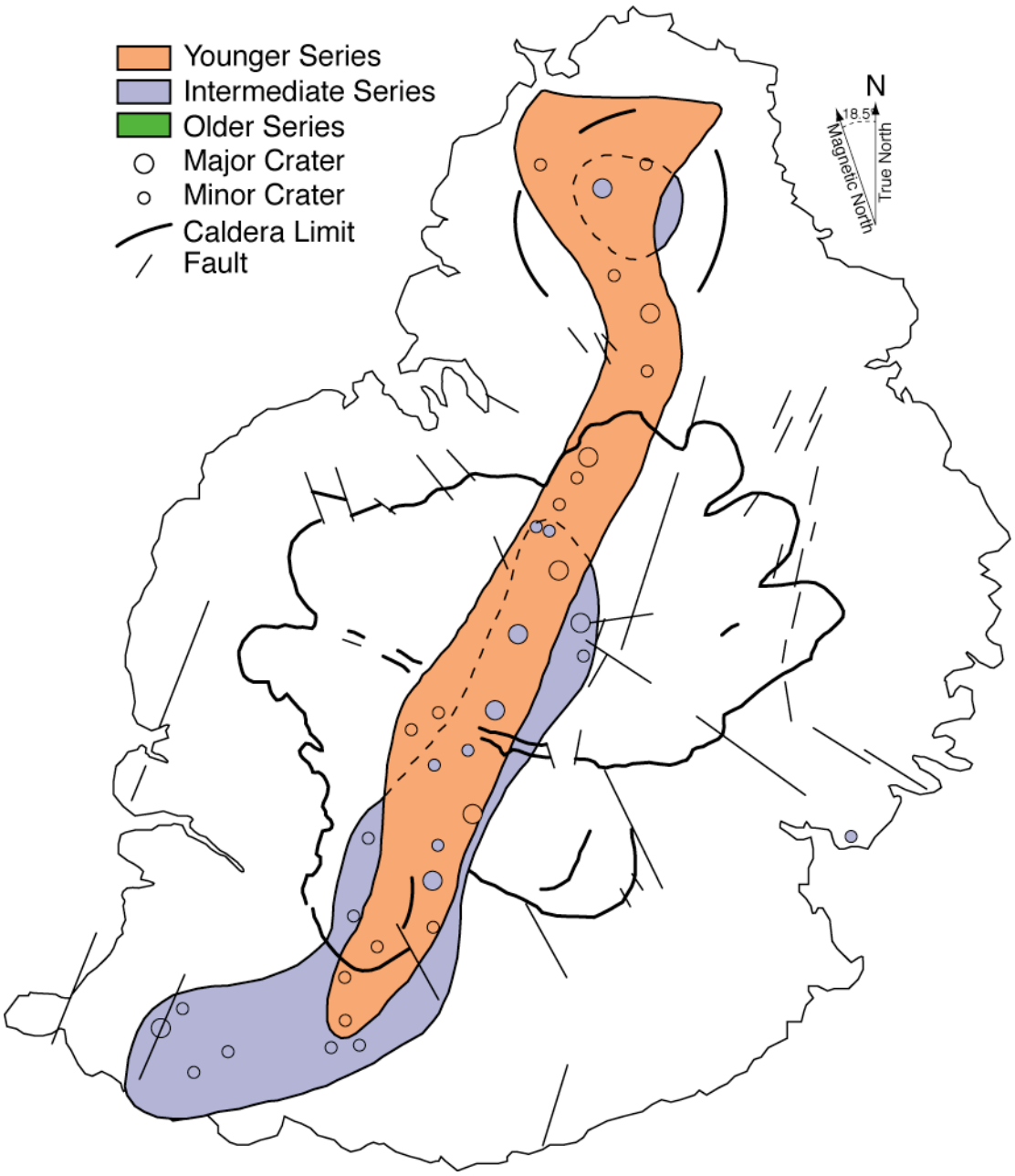
Younger Series
Intermediate Series
Older Series
Major Crater
Minor Crater
Caldera Limit
Fault
N
18.5
Magnetic North
True North

relatively complex system, likely formed through multiple stages of collapse. Additionally, a second caldera has been identified at the northern extent of the island (Giorgi et al., 1999). Further structural analysis by Perroud (1982) also identified fault systems striking 100° and 020°, likely related to the initial growth and construction of the island and caldera formation, respectively. In contrast to the Older Series, the lavas of the Intermediate and Younger Series are caldera- and valley-filling flows, and are found in the topographic lows. Thirty cones and craters have currently been identified on Mauritius, belonging to both the Intermediate Series and Younger Series. Excluding a single outlying Intermediate Series crater to the east, these vents are *en echelon* and trend roughly 020°, coincident with the principle structural fabric of the island. Intermediate Series activity is predominantly found in the south, whereas Younger Series activity is dispersed throughout the entire length of the island. Together, the lavas of the Intermediate and Younger Series cover 90% or more of the surface of the island, but have always been thought of as volumetrically minor regardless.

While there has been little revision to the volcanic history of Mauritius since Simpson (1950), several authors have since provided differing petrogenetic interpretations over the evolutionary history of the island. Baxter (1975a) hypothesized an Older Series derived from low-pressure fractionation with a strong phenocrystic control on composition (olivine + clinopyroxene ± plagioclase feldspar). Baxter (1976) interpreted the Intermediate Series as demonstrating no effects of low-pressure fractionation, and erupting as primitive mafic liquids from upper mantle depths with primary geochemical signatures. Similar to the Older Series, the Younger Series also experienced low-pressure fractionation, though limited to olivine control. No direct suggestions were presented for sources of any of the lavas, apart from peridotite at upper mantle depths. More recent work by Sheth et al. (2003) suggested

all three lavas series were the product of variable melting of an EM-source metasomatized by small degree (0.1 %) melts of a MORB-source. Trace element and isotope systematics for the Older Series and Réunion could be reproduced by 2 – 6 % partial melts of a 0.25 – 1% metasomatized EM-source. Likewise, the Intermediate and Younger Series can be produced, respectively, from approximately 2.5 % melts of a 1 – 1.5 % metasomatized EM-source, and 6 – 8 % melts of a similar source. However, Sheth et al. (2003) specified that using this method to generate the observed variations in Pb isotope compositions for the three series was untenable at best, and was better fit by a heterogeneous source. Nohda et al. (2005) proposed a relatively simplistic origin for the Older Series, wherein the lavas are large volume melts of the Réunion plume source. The Intermediate Series, however, is the product of the interaction between the plume source and a drifting EM domain. The Younger Series is a binary mixing product of MORB-source melts and plume source produced from the downstream melting tail of the plume. Paul et al. (2005) proposed a heterogeneous mantle plume that is itself responsible for producing each of the three lavas suites. Simply put, the Older Series is the product of melt-melt mixing between enriched mafic lithologies and depleted peridotite. Further melting of the depleted peridotite component, with lesser melting of the mafic lithology, in the downstream plume tail produces the Intermediate and Younger Series lavas.

Whereas these models did not deviate from the classical interpretation of Mauritian evolution (Baxter, 1975a; 1975b; 1976; 1978), Paul et al. (2007) have suggested the presence of two diverse, and distinct, trends within the primitive lavas of the Older Series. They show that Older Series lavas sampled from drill cores at depths below ~ 30 meters have depleted trace element signatures relative to surficial Older Series lavas and closely resemble lavas of the Intermediate and Younger Series. From these results Paul et al. (2007) argue that surficial Older Series lavas record a period of

magma generation from a chemically distinct domain within the Réunion plume, while the deep Older Series lavas share a common source with the Intermediate and Younger Series. The compatibility of this model with new results and applicability to Mauritius lavas will be evaluated below.

Post-Erosional Volcanism and the Hawaiian Model

The Hawaii-Emperor island chain is the most comprehensively studied example of a mantle plume derived oceanic island chain, and have long been established to evolve through a series of volcanic stages, culminating in a "post-erosional" phase of activity (*e.g.*, Macdonald and Katsura, 1964). Post-erosional volcanism characteristically occurs after a hiatus of eruptive activity lasting anywhere from a few hundred thousand to several million years. This phase is also commonly known as rejuvenescent or secondary volcanism. The eruptive products of these post-erosional eruptions are distinct from those of the shield building stages and characterized by small erupted volumes (« 1 vol. % of island) of silica-undersaturated alkaline melts with unradiogenic (depleted) Sr and Nd isotopic compositions (*e.g.* Chen and Frey, 1985). Due in large part to the extensive study and the activity of the volcanoes, the Hawaiian Islands represent the "type locality" for an intraplate ocean island chain. As such, much of what has been learned from Hawaii has been widely applied elsewhere, including the four-stage evolutionary process for oceanic islands (*e.g.*, Clague, 1987). This idealized progression is as follows:

1) *Pre-shield stage* – The initial stage of volcanism was first observed at Loihi seamount, Hawaii (Moore et al., 1982) and is characterized by relatively alkaline lavas. This stage builds the island from the seafloor, forming a seamount some several thousand meters above the seafloor. Presumably, the eruptive products of the stage decrease in alkalinity with time (initially basanites and alkali basalts), transitioning

into more shield-like lavas (alkali basalts to tholeiities). Like subsequent alkalic stages, the pre-shield stage has relatively depleted Sr and Nd isotopic signatures. Apart from Loihi, the presence of the pre-shield stage lavas have not been documented and must be assumed to be covered by ensuing shield lavas.

2) *Shield stage* – The shield stage is characterized by the relatively rapid eruption of large volumes of relatively silica-saturated homogeneous tholeiitic lavas. These lavas build directly upon the submarine pre-shield seamount, constructing the sub-aerial volcanic edifice. Shield lavas tend to have the most isotopically enriched Sr and Nd lavas erupted throughout an island's history. Erupted lavas tend to become more alkalic and differentiated as eruption rates slow toward the end of this stage. Kilauea is a modern and active example of this stage, while Mauna Loa is near the end of the stage. All Hawaii-Emperor seamount volcanoes "downstream" of the island of Hawaii have progressed beyond the shield stage.

3) *Post-shield stage* – The waning production of the shield stage lavas marks the beginning of the transition towards the increasingly alkalic lavas of the post-shield stage. This stage is often referred to as a "capping" stage, and commonly produces small volumes of differentiated lavas that erupt in infrequent, if numerous, small alkalic cones (typically < 1 vol. %). Post-shield lavas have more depleted isotopic compositions than their shield stage counterparts, but are still generally more enriched than the pre-shield and post-erosional stages. Mauna Kea represents the youngest example of the post-shield stage.

These three stages together are collectively referred to as the "main stage" lavas.

4) *Post-erosional stage* – Whereas the first three stages proceed through a mostly gradual transition, the post-erosional stage is characterized by a volcanic hiatus in which the shield volcano undergoes considerable erosion lasting from several hundred

thousand years to several million years. Only after this period of inactivity does volcanism resume, with infrequent eruptions of strongly silica-undersaturated alkalic lavas (basinitic to nephelinitic). Erupted volumes of post-erosional lavas are volumetrically minor when compared to the shield building main stage lavas, contributing insignificantly to the total volume of the island (« 1 vol. %). These lavas have depleted Sr and Nd isotopic signatures that are commonly, though not always, distinct from those of the shield stage. The Honolulu Series of Oahu, Hawaii represents, perhaps, the best known example of post-erosional volcanism. It has also been observed that post-erosional lavas tend to form within a window at characteristic distances (200 – 400 km) from active shield volcanoes (Clague and Dalrymple, 1987; Bianco et al., 2005). In this work the terms rejuvenescent and post-erosional can be used interchangeably, but secondary volcanism will be restricted to certain types of off-axis volcanism, *i.e.*, those that occur away from the axis of a plume source.

The occurrence of post-erosional volcanism has been observed worldwide on oceanic island chains, including Samoa, the Society Islands, Madeira, the Canaries, Pitcairn, Mauritius, the Carolines, the Louisville Seamount chain, and the Magellan seamounts (*e.g.*, Baxter, 1976; Keating et al., 1984; Natland and Turner, 1985; Cheng et al., 1987; Woodhead and McCulloch, 1989; Hoernle and Schminke, 1993; Duncan et al., 1994; Koppers et al., 1998; Geldmacher and Hoernle, 2000). These oceanic island chains are all seemingly derived from deep-seated mantle plumes and, to varying degrees, follow the general evolutionary trend outlined for Hawaii. As an example, Tahaa, one of the older Society Islands, was inferred to have three phases of older activity which together compose the mildly alkalic main shield stage (a pre-caldera collapse, a post-caldera collapse, and a caldera filling stage), and a post-erosional stage following a hiatus of 1.2 Myr (Brousse, 1986). This final stage erupted small volumes of highly undersaturated alkaline lavas with dramatically depleted

isotopic compositions (Brousse, 1986; White and Duncan, 1996). Volcanism is known to reactivate after a period of inactivity in the Australs (Chauvel et al., 1997), though the situation is more complicated as certain islands may have experienced activity associated with more than one mantle plume throughout their history. Despite an abundance of examples of post-erosional volcanism, it seems clear that this final eruptive stage is not ubiquitous. The Marquesas, Cape Verde, Ascension, St. Helena, the Azores, and the Galapagos are all examples of plume-derived oceanic islands that lack the post-erosional stage, for one reason or another.

Apart from those lavas associated with the downstream migration of the oceanic crust and volcanic edifice away from the stationary plume source, several classes of late-stage lava have been identified with similar characteristics to the more traditional post-erosional series. The young Hawaiian North Arch (0.75-2.7 Ma; Clague et al., 1990) and South Arch (1-10 ka; Lipman et al., 1989) volcanics are found on the outer limb of the flexural arch surrounding the Hawaiian moat, the depression created by the loading of the Hawaiian Islands on the elastic oceanic lithosphere. The Hawaiian Arch lavas are found within the same characteristic range of distances (200 – 400 km from an active shield source) as the on-shore post-erosional lavas and are geochemically similar to the onshore post-erosional lavas (Bianco et al., 2005). These lavas have strongly alkalic compositions and depleted isotopic compositions relative to the shield stage (Lipman et al., 1989; Clague et al., 1990), with erupted volumes orders of magnitude less (Clague et al., 2002). A second class of off-axis volcanism has been identified on the outer rise of the flexural bulge of the Japan Trench, a series of small volume (0.005 – 1 km^3 each) volcanic edifices (Hirano et al., 2006). These lavas are alkalic and believed to be derived from small-degree melts, though no isotopic composition measurements have been collected. Although the tectonic settings differ between these off-axis secondary volcanic groups, the relative position

of the lavas on a flexural arch suggests a similar mechanistic derivation, though the melt sources are likely quite different.

The combined theories of seafloor spreading (*e.g.*, Hess, 1962) and mantle plumes (*e.g.*, Morgan, 1971) seemingly do a thorough job of explaining many of the large-scale (*i.e.*, the bend in the Hawaiian-Emperor seamount chain; Wilson, 1963) and the small-scale (*i.e.*, evolution of a single oceanic island; Macdonald and Katsura, 1964) observations related to oceanic intraplate volcanism. However, these theories make no direct predictions about the occurrence or origin of post-erosional volcanism on oceanic islands. In this sense, the occurrence of post-erosional volcanism represents a test of the integrated plate tectonic-mantle plume theory. A successful model that incorporates post-erosional volcanism associated with a mantle plume should directly account for the following: (1) the classical evolution of an oceanic island from the pre-shield through post-shield stages, (2) a mechanistic principle behind the temporal (and spatial) hiatus in volcanic activity (or lack of post-erosional activity), (3) the relatively small volumes of infrequently erupted post-erosional lavas, (4) the (often) strongly alkalic major element compositions of erupted post-erosional lavas, (5) and the distinctively depleted isotopic compositions of post-erosional lavas relative to the shield stage. A complete model should also be readily able to account for the absence of specific features, including the complete lack of post-erosional volcanism, as observed on some island chains. Current models do not fully satisfy all of these geophysical and geochemical observations, and are thus not satisfactory. Here I present new data for Mauritius and test an internally consistent model for post-erosional volcanism that will attempt to address all observations and the underlying causes behind post-erosional volcanism, representing the further development of the work of Paul et al. (2005) and ideas presented by Sobolev et al. (2005; 2007).

Comparison to Réunion and the Hawaiian Model

Réunion Island is the modern subaerial expression of the Réunion mantle plume, at present composed of two volcanic edifices, Piton des Neiges and Piton de la Fournaise. Eruptive activity at Réunion has been continuous since *c*. 2 Ma (McDougall and Chamalaun, 1969), with activity at Piton de la Fournaise continuing today. Piton des Neiges comprises the northwestern portion of the island and was constructed in two stages. The first stage was a shield-building stage called the Oceanite Series, composed of transitional olivine basalts (Upton and Wadsworth, 1965), lasting from at least 2.0 to 0.43 Ma (McDougall and Chamalaun, 1969). The second stage at Piton des Neiges was a capping post-shield stage called the Differentiated Series, consisting of olivine basalt to trachytic compositions (Upton and Wadsworth, 1965), extending from 0.35 Ma to 12 ka, Pliocene to Pleistocene in age (McDougall and Chamalaun, 1969; Deniel et al., 1992). The shield-building growth of Piton des Neiges is contemporaneous with the closing stages of Intermediate Series activity and the onset of Younger Series activity.

Piton de la Fournaise, among the world's most active volcanoes, comprises the southeastern portion of Réunion Island, having grown from the flank of Piton des Neiges. The volcano is currently in its shield-building phase, erupting transitional olivine basalts similar to those of the Oceanite Series (*e.g.*, Gillot and Nativel, 1989), though the lavas have evolved toward more (mildly) tholeiitic compositions with time (Albarède et al., 1997). Eruptions at Piton de la Fournaise have been active since at least 0.53 Ma ago, Pleistocene in age (Gillot and Nativel, 1989), remaining active through historical times. Like Piton des Neiges, eruptions at Piton de la Fournaise are contemporaneous with Younger Series activity. While a detailed geochemical and petrologic comparison between the two volcanoes is not available, Bosch et al (2008) identified inter-volcano variability between Piton de la Fournaise and Piton des

Neiges. Amongst these two sister shield volcanoes, the Older Series is more closely similar to the lavas of Piton de la Fournaise.

Volcanism observed along the track of the Réunion plume appears to generally follow the classical Hawaiian evolution, albeit with some minor differences. As of yet, exposures of Loihi-type volcanism has not been identified at either Mauritius or Réunion, but are likely buried by subsequent activity. The young seamount identified by Duncan (1990) to the west of Réunion provides a potential locality for such pre-shield lavas, deserving of future attention. The Older Series of Mauritius, the Oceanite Series of Piton des Neiges, and the active lavas of Piton de la Fournaise, Réunion, all are analogous to the shield-building stage, though have more transitional basaltic compositions rather than tholeiitic. Similarly, the differentiated, more alkalic late-stage Older Series lavas of Mauritius and the Differentiated Series of Piton des Neiges, Reunion are broadly analogous to Hawaiian post-shield lavas, though the differentiated lavas on Mauritius are very rare. While no post-erosional activity has been documented at Réunion, and is unlikely to have occurred to date, the Intermediate Series of Mauritius would appear to be analogous to the post-erosional lavas of the Honolulu Volcanics. In both instances, these post-erosional lava series appear after extended volcanic hiatus and each illustrate a shift toward more depleted isotopic compositions and trace element patterns (*e.g.*, Baxter, 1976; Chen and Frey, 1985). The Younger Series represents a second pulse of post-erosional volcanism and has no known direct analogue, at Hawaii or elsewhere.

The cones and craters of Mauritian post-erosional stages are distinctive from those of Hawaii. Hawaiian post-erosional centers tend to form small, steep-sided explosive centers that pockmark the landscape. Detailed volume calculations for the Honolulu Series of Oahu have estimated the volumes of eruptive lavas from these vents as approximately 20 km^3 (Garcia, personal communication), with somewhat

Figure 5. Cross sections of Mauritius lava units, modified from Giorgi et al. (1999). The combined thicknesses of the two post-erosional units (Intermediate and Younger Series) exceed 50 m almost everywhere, and commonly exceed 100 m. Locations of each cross section and given on the small inset map of Mauritius, with geographic locations for reference. Geologic units after Figure 1. Vertical exaggeration approximately 5:1 for each section

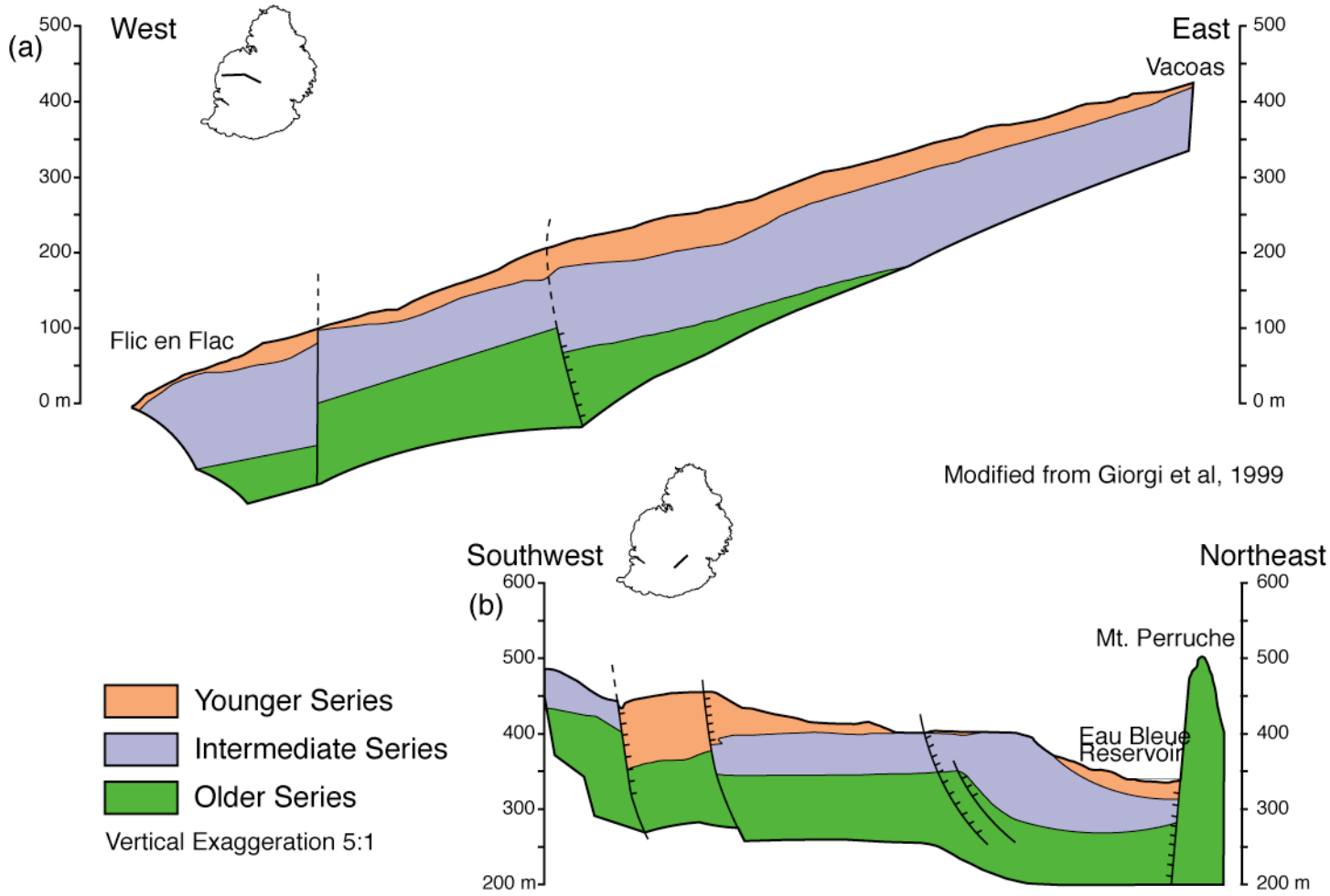
(a)
West
East
Vacoas
Flic en Flac
500
400
300
200
100
0 m
Modified from Giorgi et al, 1999
Southwest
Northeast
(b)
Mt. Perruche
Eau Bleue
Reservoir
600
500
400
300
200 m
Younger Series
Intermediate Series
Older Series
Vertical Exaggeration 5:1

Figure 5 (*continued*)

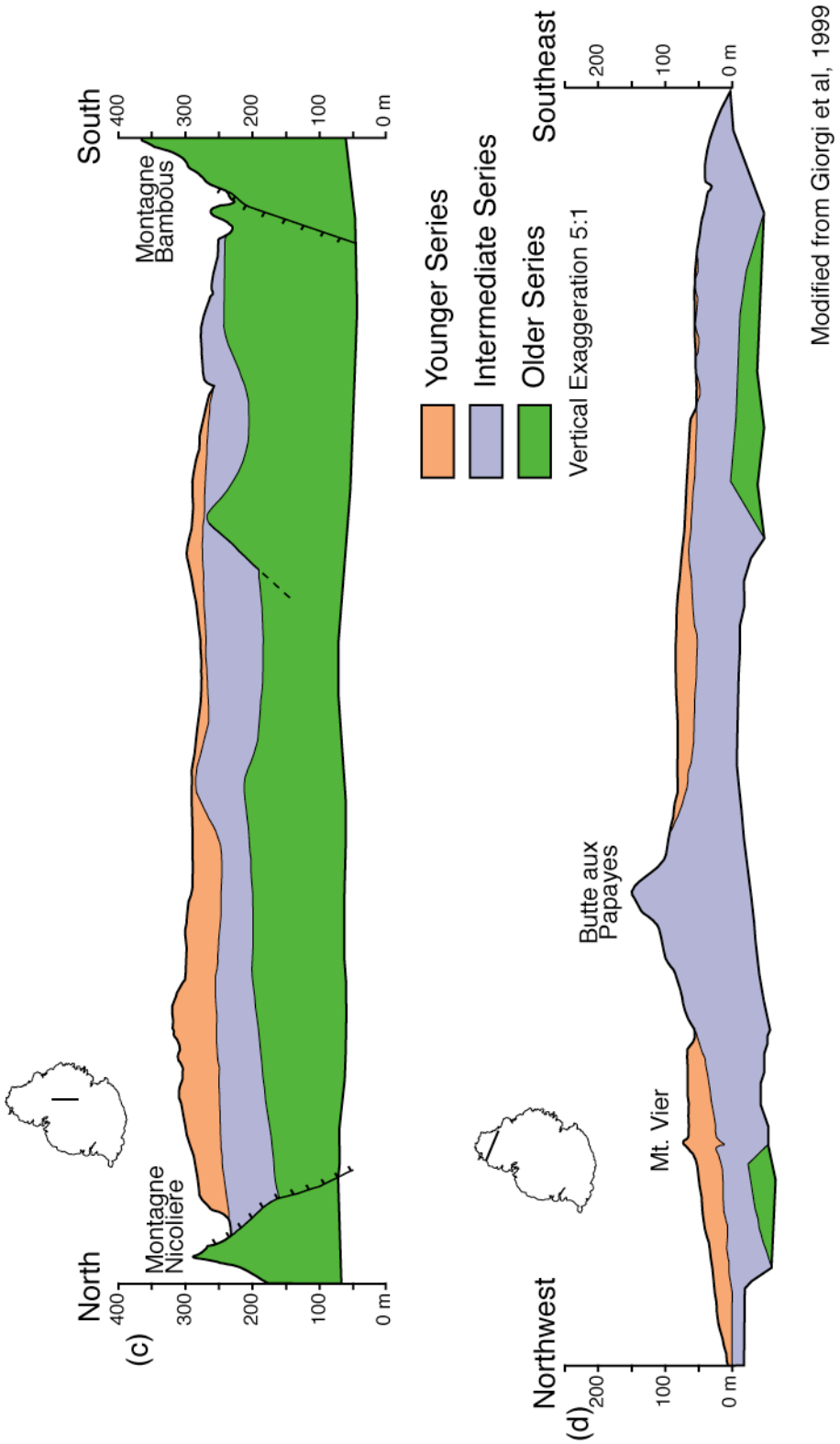

larger eruptive volumes from the Koloa volcanics of Kauai, approximately 60 km^3 (Gandy et al., 2005; submitted 2008). In contrast, the relatively shallow sloped flanks that produce lateral flows capable of extending kilometers from steep-sided apical cones are reminiscent of small shield volcanoes (see geologic map of Giorgi et al., 1999). Where these flow units have built up from the caldera floor they form a topographic backbone all along the central axis of the island, and are morphologically distinct from the sharp ridges and sheer cliffs of the remnant Older Series massifs. Cross-sections constructed from drill core data (Figure 5) indicate the Intermediate and Younger Series units represent caldera filling flows, with combined post-erosional sections commonly approaching or exceeding 100 meters in collective thickness (Giorgi et al., 1999). Eruptive volumes calculated for the Mauritian post-erosional lavas from these graphical sections estimate approximately 35 km^3 of erupted lavas from the two phases during their nearly 3 Myr of activity.

CHAPTER 2 – METHODOLOGY

Sampling

All new samples were collected from Mauritius Island during the Austral winter of 2007 by the author. Samples include sections of drill core as well as surficial outcrops. Thirty-nine surficial samples were collected, with thirteen analyzed and presented here. Older Series samples were collected from exposed remnants of an eroded shield volcano. Breccia samples were collected from basal units of Older Series exposures at Trois Mamelle and Long Mountain. Samples from cross-cutting dikes and altered country rock were taken from a quarry near Montagne D'hauvillard, though these samples were not analyzed. Intermediate and Younger Series samples presented here are exclusively from the north-northeast trending dome suite, although flow units both interior and exterior to the caldera complex were also sampled, though not analyzed.

Ninety-five samples were collected from twenty-one drill cores, with twenty-six samples from eight cores analyzed here. The analyzed cores range in length from 61 to 223 meters, extending to 105 meters below sea level, and were chosen on the basis of length and location in an effort to maximize penetration into the Older Series at depth. The cores consist of interlayered lava flow units and discontinuous horizons of highly altered lava to lateritic soil. Samples in the cores were collected both above and below major discontinuities (greater than several meters), and intraflow where suites of uninterrupted lava flows extend beyond several tens of meters. The Mauritius Water Resources Unit graciously provided assistance and access to the core storehouses. Location and sampling details and notes on each the analyzed cores can be found in Table A.1.

Two additional suites of Mauritius samples and data were generously made available for this work. R. Duncan provided a subset of seven Younger Series samples, complete with K-Ar dates (unpublished), from the collection of A. N. Baxter. D. Paul provided a subset of nine samples from Paul et al. (2007; two surficial, seven drill core) and a suite of Hf, Sr, Nd and Pb isotopic compositions for samples from the same work (Paul and Abouchami, unpublished).

Analytical Methods

Major Elements

Sample powders were prepared for major element analysis at Cornell University and the University of Texas at San Antonio by ceramic disc mill. Major element concentrations were measured at the GeoAnalytical Lab at Washington State University by X-ray fluorescence (XRF) following the methods of Johnson et al. (1999). Spec pure dilithium tetraborate ($Li_2B_4O_7$) was thoroughly mixed with sample powder in a 2:1 ratio and loaded into graphite crucibles. Samples were fired in a muffle furnace for five minutes at 1000 °C. Fused glass beads are reground, replaced in their graphite crucible and re-fired for an additional five minutes at the same temperature, re-fusing the sample. Samples are inscribed, ground flat along one side, washed, ultrasonicated and rinsed before being allowed to dry at room temperature. Measurements were conducted on a Rigaku 3370 XRF Spectrometer. Concentrations for ten major element oxides (SiO_2, TiO_2, Al_2O_3, FeO, MnO, MgO, CaO, Na_2O, K_2O) were determined by comparing the X-ray intensities of each element against the intensity of two beads each of nine USGS standard samples (PCC-1, BCR-1, BIR-1, DNC-1, W-2, AGV-1, GSP-1, G-2, and STM-1, using the recommended values of Govindaraju, 1994) and two beads of pure vein quartz run as blanks for all elements except Si. Total Fe is expressed as FeO, represented by FeO_T.

Trace Elements

Sample preparation for trace element analysis follows the methods outlined in Cheatham et al. (1993). Approximately 50 mg of standard sample powder and external calibration standard powders (BHVO-2, BEN, BIR-1, BCR-2, and the Cornell in-house standard PAL-889) were dissolved via hot plate digestion for 24 hours using a mixture of 4B HF and concentrated perchloric acid ($HClO_4$) in closed Savillex containers. Digestions were dried down after dissolution and twice re-dissolved in *6 N* QD HCl to remove remaining fluorides. Samples were converted to nitride-form by re-dissolution in 2 mL of *15 N* HNO_3 and dried down. Samples were re-dissolved in 4 mL of *8 N* HNO_3 and diluted to 100 g (approximately 0.025% total dissolved solids). Approximately one gram of trace element spike consisting of 1 ppm each Rh, In, Bi, Re, Tm, and enriched isotopes ^{6}Li, ^{61}Ni, ^{84}Sr, and ^{145}Nd was included in each dilution for use as an internal calibration standard at 1 ppb (Gao et al., submitted to G^3). The masses of the internal standard span the mass spectrum of the analytes, allowing monitoring and correcting for mass-dependent fractionation within the ICP-MS. Trace element concentrations were measured at the University of Houston using a Varian quadrupole-ion inductively coupled plasma mass spectrometer (ICP-MS) with a Varian SPS3 Auto-sampler operating in normal resolution mode for 37 trace elements (Li, Be, B, Sc, Ti, V, Cr, Co, Ni, Cu, Zn, Ga, Rb, Sr, Y, Zr, Nb, Cs, Ba, La, Ce, Pr, Nd, Sm, Eu, Gd, Tb, Dy, Ho, Er, Yb, Lu Hf, Ta, Pb, Th, U). Typical analytical runs consisted of one blank measurement, a 5 ppb Nd solution, a Nd blank, the five external calibration standards, and 22 sample unknowns. During a single run seven replicate analyses of BHVO-2 and BCR-2 were conducted for calibration and to monitor the analytical precision and accuracy of each run, respectively, with the remaining three external standards run as unknowns. Data reported herein include the

means of each sample (up to four replicate analyses) measured over different days. Replicate analyses were completed over a period of two week and show no systematic variation with time. Raw ICP-MS data was reduced by the methods of Gao et al. (submitted to G^3) to yield the final trace element concentrations, and includes an oxide interference correction for Ba, the REEs, Hf, and Ta as determined from the analysis of the 5 ppb Nd solution (Hollocher, 2008).

Isotopic Compositions

Sample preparation and analytical methodology for Sr and Nd isotopic compositions is similar to White and Duncan (1996). An ~ 50 mg aliquot of sample powder was leached in *2.5 N* QD HCl for fifteen minutes and washed with QD H_2O, with the leachate retained for subsequent analysis. Samples were dissolved via hot plate digestion for 24 hours in a mixture of 4B HF and concentrated perchloric acid ($HClO_4$) in closed Savillex containers. Samples from the Older Series breccias suspected of seawater alteration were leached in hot *2.5 N* QD HCl for 30 minutes, washed with QD H_2O and dissolved in a similar manner to the "cold" dissolution procedure. Digestions were dried down and twice re-dissolved in *6 N* QD HCl. Samples were dissolved in *2.5 N* QD HCl and centrifuged for 5 minutes at 5000 rpm prior to column chemistry. Sr and rare earth elements (REE) were sequentially separated by elution with *2.5 N* and *6 N* QD HCl, respectively, through AG50W-x8 (200-400 mesh) resin cation exchange columns. Nd elution was conducted using LN Resin and 0*.25 N* QD HCl, following a modified version of Pin and Zalduegui (1997). Purified Sr was loaded onto single W filaments with TaF activator and Nd loaded onto single Re filaments with Biorad AG resin beads (which serve as a reductant) and phosphoric acid. Strontium and Nd isotopic ratios were measured at the Keck Isotope Laboratory at Cornell University using a VG Sector 54 thermal ionization mass

spectrometer (TIMS) operating in dynamic mode. Isotopic ratios were normalized to $^{88}Sr/^{86}Sr = 0.11940$ and $^{146}Nd/^{144}Nd = 0.71290$, respectively, using an exponential correction. During the period of analysis the NBS-987 Sr standard yielded $^{87}Sr/^{86}Sr = 0.71025 \pm 0.00001$ (2σ) ($n = 47$) and the Ames Nd standard yielded $^{143}Nd/^{144}Nd = 0.512131 \pm 0.000006$ (2σ) ($n = 13$).

Analysis for Pb isotopic composition utilized rock chips (~ 150 mg), with all samples subjected to the cleaning and leaching procedure of Abouchami et al (2000). Sample chips were washed and ultrasonicated in ultrapure (18.2Ω) H_2O, then ultrasonicated in *6 N* HCl for 15 minutes, and finally leached in hot *6 N* HCl for 1 hour. The leachate was retained from several of the samples for additional analysis, and residues were washed repeatedly with ultrapure H_2O to remove any remaining leachate. Following leaching, the samples were dissolved via hot plate digestion in a mixture of HF and HNO_3 in closed Savillex containers. The triple spiking techniques of Galer and Abouchami (1998) and Galer (1999) was used for determination of Pb isotopic compositions. The Pb was separated by anion exchange through AG1x8 (100-200 mesh) resin using two HBr-HNO_3 mixtures as eluents (Galer, 1986; Abouchami et al., 1999). Following elution, a small aliquot of the sample Pb (~ 10%) was taken, to which a triple spike amount estimated as optimal was added. The spiked aliquot was homogenized by drying down. The spiked and unspiked aliquots were loaded separately onto single zone refined Re filaments using the colloidal silica gel-H_3PO_4 emitter of Gerstenberger and Haase (1997) at ~ 2x concentration. Lead isotopic ratios were measured at the Max-Planck-Institut für Chemie (MPI) in Mainz, Germany using a Thermo Scientific Triton TIMS operating in static mode. The data reduction procedures of Galer (1997, 1999) and Galer and Abouchami (1998) were followed to yield the bias-corrected Pb isotopic compositions from the combined results of the spiked and unspiked analyses. Repeat analysis ($n = 25$) of the NBS-981 Pb standard

yielded $^{206}Pb/^{204}Pb$ = 16.9436 ± 0.0026 (2σ) (152 ppm), $^{207}Pb/^{204}Pb$ = 15.5016 ± 0.0030 (2σ) (195 ppm) and $^{208}Pb/^{204}Pb$ = 36.7316 ± 0.0085 (2σ) (231 ppm). Results from $^{206}Pb/^{204}Pb$ and $^{208}Pb/^{204}Pb$ are consistent within error with the ratios reported by Galer and Abouchami (1998), but $^{207}Pb/^{204}Pb$ slightly exceeds these values. Lead blanks (n = 4) were between 15 and 40 pg, and are considered negligible.

Radiometric Dating

Crystallization ages for eight whole rock samples were measured using ^{40}Ar-^{39}Ar methods at Oregon State University (Duncan and Keller, 2004). Approximately 200 mg sized minicores were drilled from fresh surfaces of centimeter-sized cubes of fresh sample. Samples were irradiated for 10 hours at 1 MW power in the Oregon State University TRIGA research reactor. Neutron fluence was monitored via the Fish Canyon Tuff biotite standard (28.03 ± 0.16 Ma; Renne et al, 1998). Following irradiation and decay of short-lived radionuclides, samples were loaded into two ultra-high vacuum gas extraction lines. The first is a Heine low-blank, double vacuum resistance furnace and the second a computer controlled Merchantek integrated 10 W CO_2 continuous fire laser with infrared pyrometer gas extraction system. Low volume Zr-Al getters were used for gas cleanup. Isotopic composition of Ar released at each heating step with a MAP 215/50 mass spectrometer. Samples were heated in 100 – 200 °C increments, from 400 °C to fusion in seven to ten steps.

Additionally, seven Younger Series samples from the collection of A. N. Baxter (Duncan, unpublished data) were dated at Oregon State University by similar techniques.

CHAPTER 3 – ANALYTICAL RESULTS

In addition to their usual classification by age, I have grouped lava samples from Mauritius by sample locality and/or stratigraphic level, and fall into the following groups: drill core (26), cone (6), massif (3) and breccia (4) samples (Table 1). The term 'surficial' is used to distinguish the latter three groups from the sub-surface drill core samples. Results will be discussed in terms of both age and sampling locality. Here we present whole rock major and trace element and isotopic composition data for surficial and drill core samples from Mauritius collected by the authors in 2007.

Major Elements

Analytical evidence for distinctions between the Older, Intermediate and Younger Series of Mauritius began with major element chemistry, first presented by Walker and Nicolaysen (1954) in an effort to confirm the volcanic stratigraphy developed by Simpson (1950), and later furthered by Baxter (1975a, 1976) in the first systematic geochemical study of the island. These works identified the somewhat alkalic nature of the lavas, the well-defined inter-oxide trends for each series, and the close relationship between bulk chemical variation and mineralogy.

Major element variations for Mauritius bulk rock compositions lie along common fractionation trends and show similar results to the published literature data, with no significant outliers from these established fields (Figure 6; Tables 2, B.1, and B.2). Data for all analyzed points are plotted on the total alkali-silica diagram of Le Bas et al. (1986) with the majority of samples straddling the alkalic-subalkalic divide of MacDonald and Katsura (1964) in Figure 7. Samples are predominantly basaltic in composition, with minor picrobasalts and trachybasalts. The basanites described in

Table 1. Locations of sampled Mauritius lavas and drill cores

Sample	Locality	Elev (m)	Depth (m)	Core #	Lat (DD)	Lon (DD)	Location
Older Series							
B18-1	Drill core	222	219.8	89	20.2072	57.5641	Beau Bois
M6	Massif	78	--		20.1633	57.5097	The Citadel
M12	Massif	72	--		20.3415	57.3711	Tamarin Mountain
M30	Massif	283	--		20.2074	57.6654	Motte A Therese
M35	Breccia	225	--		20.3107	57.4402	Trois Mammelle
M36	Breccia	225	--		20.3107	57.4402	Trois Mammelle
M37	Breccia	225	--		20.3109	57.4406	Trois Mammelle
M39	Breccia	149	--		20.1435	57.5488	Long Mountain
Intermediate Series							
B2-1	Drill core	85	219.8	110	20.2384	57.4804	Trianon
B5-1	Drill core	-51	63.1	448	20.0630	57.6786	Poudre d'Or
B6-1	Drill core	-105	144.8	746	20.0380	57.5764	Fond du Sac
B6-2	Drill core	-50	89.9	746	20.0380	57.5764	Fond du Sac
B12-1	Drill core	65	70.1	480	20.1435	57.5543	Notre Dame
B18-2	Drill core	264	177.7	89	20.2072	57.5641	Beau Bois
B18-3	Drill core	287	154.5	89	20.2072	57.5641	Beau Bois
B18-4	Drill core	303	139.0	89	20.2072	57.5641	Beau Bois
B18-5	Drill core	343	99.1	89	20.2072	57.5641	Beau Bois
B18-6	Drill core	371	71.0	89	20.2072	57.5641	Beau Bois
B18-7	Drill core	378	64.3	89	20.2072	57.5641	Beau Bois
B18-8	Drill core	400	41.8	89	20.2072	57.5641	Beau Bois
B19-1	Drill core	305	89.9	3	20.3438	57.5844	Eau Bleu
B19-2	Drill core	323	71.6	3	20.3438	57.5844	Eau Bleu
B19-3	Drill core	360	35.1	3	20.3438	57.5844	Eau Bleu
M15	Cone	502	--		20.4517	57.4773	Bassin Blanc
M20	Cone	581	--		20.3667	57.4884	Trou de Madame Bouchet
Younger Series							
B1-1	Drill core	234	1.2	B1	20.2736	57.4236	Pierrefonds
B1-2	Drill core	221	14.3	B1	20.2736	57.4236	Pierrefonds
B1-3	Drill core	206	29.6	B1	20.2736	57.4236	Pierrefonds
B1-4	Drill core	147	88.4	B1	20.2736	57.4236	Pierrefonds
B1-5	Drill core	83	152.7	B1	20.2736	57.4236	Pierrefonds
B6-3	Drill core	23	16.8	746	20.0380	57.5764	Fond du Sac
B6-4	Drill core	37	3.4	746	20.0380	57.5764	Fond du Sac
B18-9	Drill core	421	20.7	89	20.2072	57.5641	Beau Bois
B19-4	Drill core	376	18.9	3	20.3438	57.5844	Eau Bleu
B19-5	Drill core	386	8.5	3	20.3438	57.5844	Eau Bleu
M17	Cone	560	--		20.4057	57.5201	Kanaka Crater
M22	Cone	585	--		20.3123	57.5321	Malherbes
M29	Cone	504	--		20.1961	57.5951	Nouvelle Decouverte
M33	Cone	84	--		20.0484	57.6279	Forbach Hill Crater

Elevation of sample in meters above sea level (masl). Depth in meters below surface (mbs). Core numbers from Mauritius Water Resources Unit. Elevation for drillcore samples is calculated from depth and elevation of drill site.

Figure 6. Major element oxides plotted as a function of wt. % MgO. Solid colored samples represent new Mauritius data presented here. Open colored symbols represent previously published data for Mauritius (see text for references). Data for Central Indian Ridge (CIR) MORB, Réunion, and Rodrigues taken from PetDB and GeoROC databases. Solid lines depict liquid lines of descent (LLOD) calculations from MELTS (Ghiorso and Sack, 1995) for hypothesized Mauritian parental magmas. LLOD were calculated at 0.8 GPa with an oxygen fugacity of QFM+2 (Albarède et al., 1997; Horn et al., 1994). LLOD are as follows: Green – sample A171 of Baxter (1975); Purple – from Sobolev and Nikogosian (1994); Black – sample 15 of Lacroix (1936). Compositions of selected parental compositions can be found in Table 14, with discussion in Chapter 5. Regardless of the choice of parental composition, the Mauritius samples follow similar trends with decreasing MgO content.

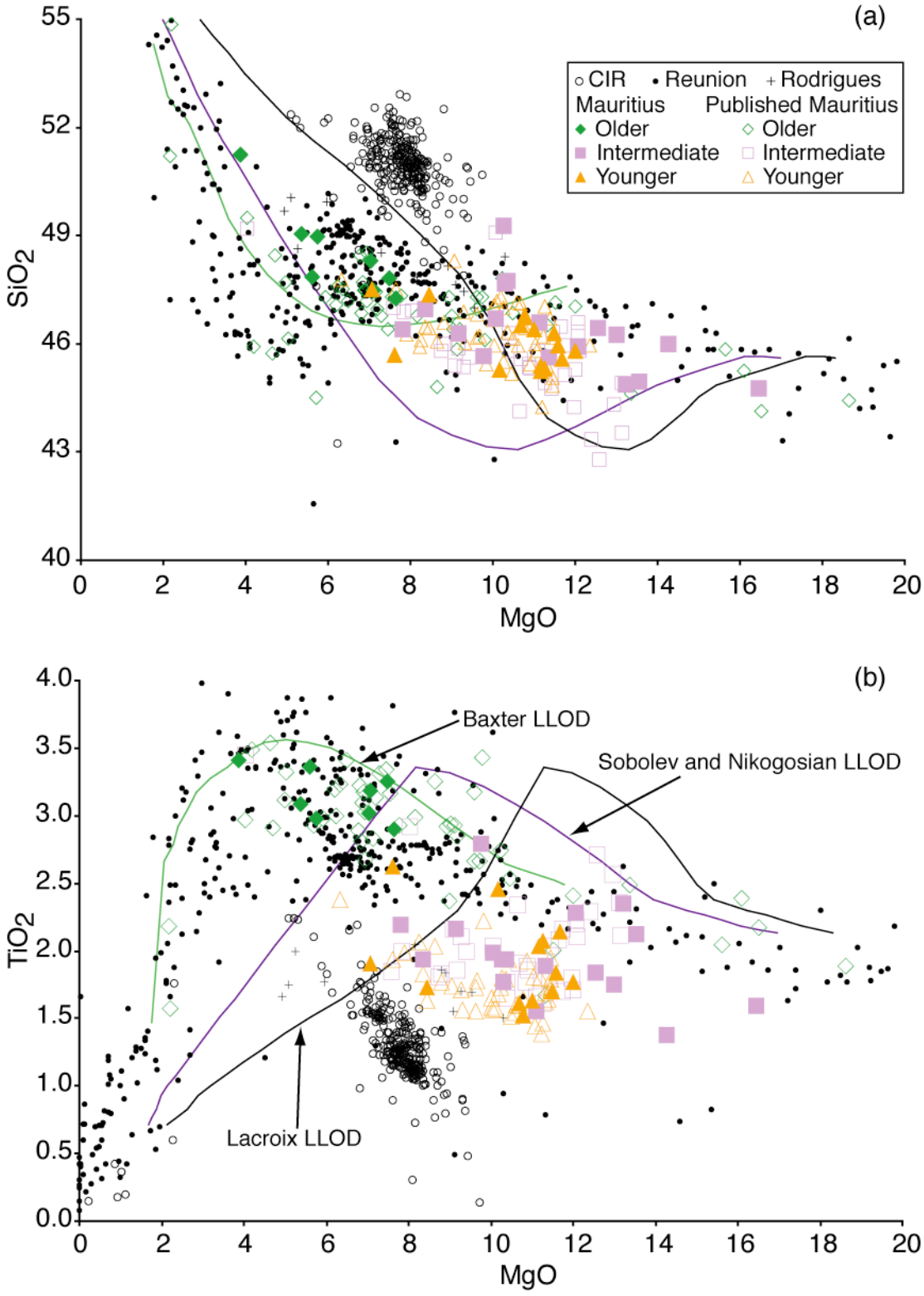
(a)
CIR
Reunion
Rodrigues
Mauritius
Published Mauritius
Older
Older
Intermediate
Intermediate
Younger
Younger
SiO2
MgO
55
52
49
46
43
40
0
2
4
6
8
10
12
14
16
18
20
(b)
Baxter LLOD
Sobolev and Nikogosian LLOD
Lacroix LLOD
TiO2
MgO
4.0
3.5
3.0
2.5
2.0
1.5
1.0
0.5
0.0

Figure 6 (*continued*)

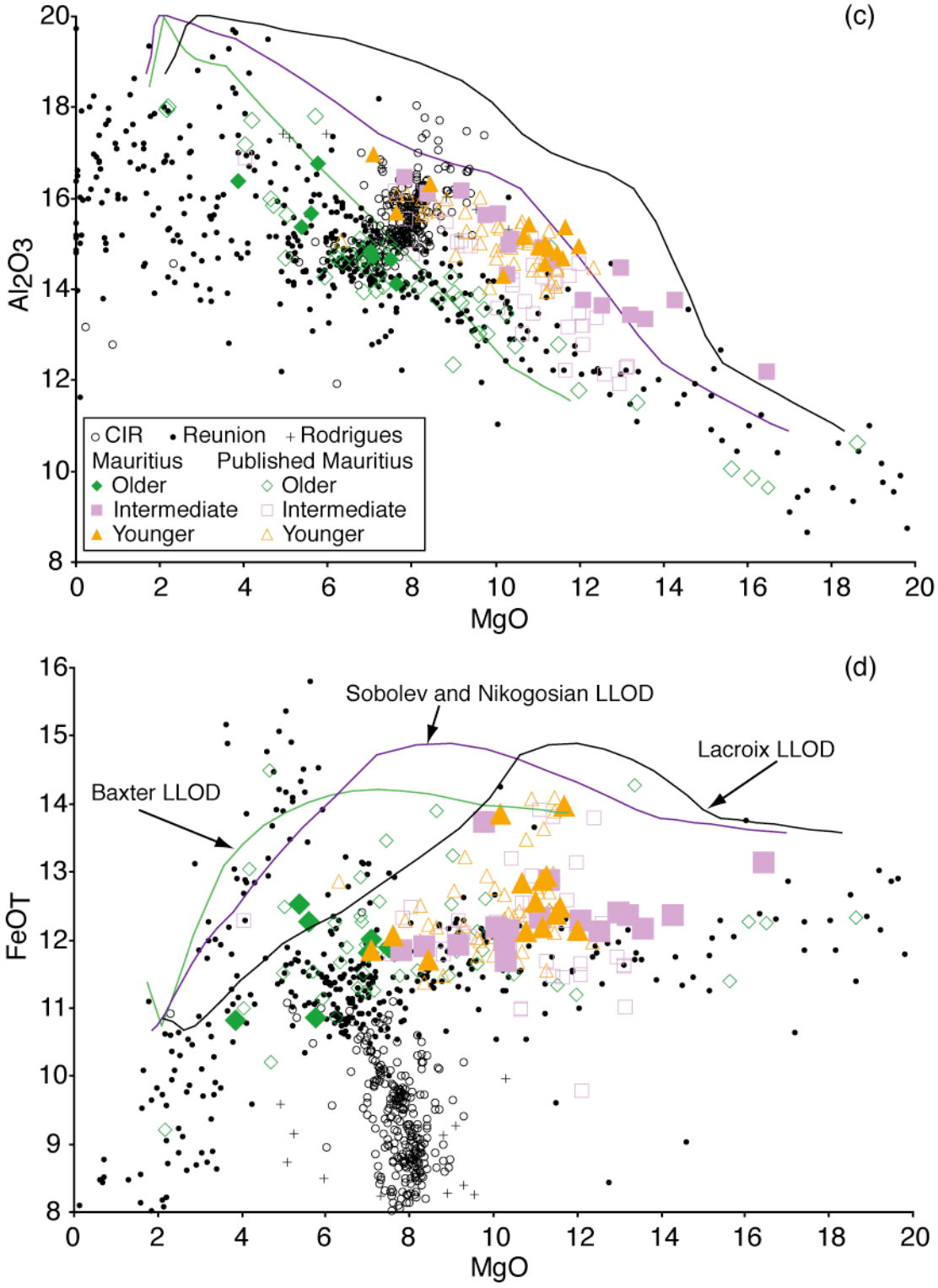

Figure 6 (*continued*)

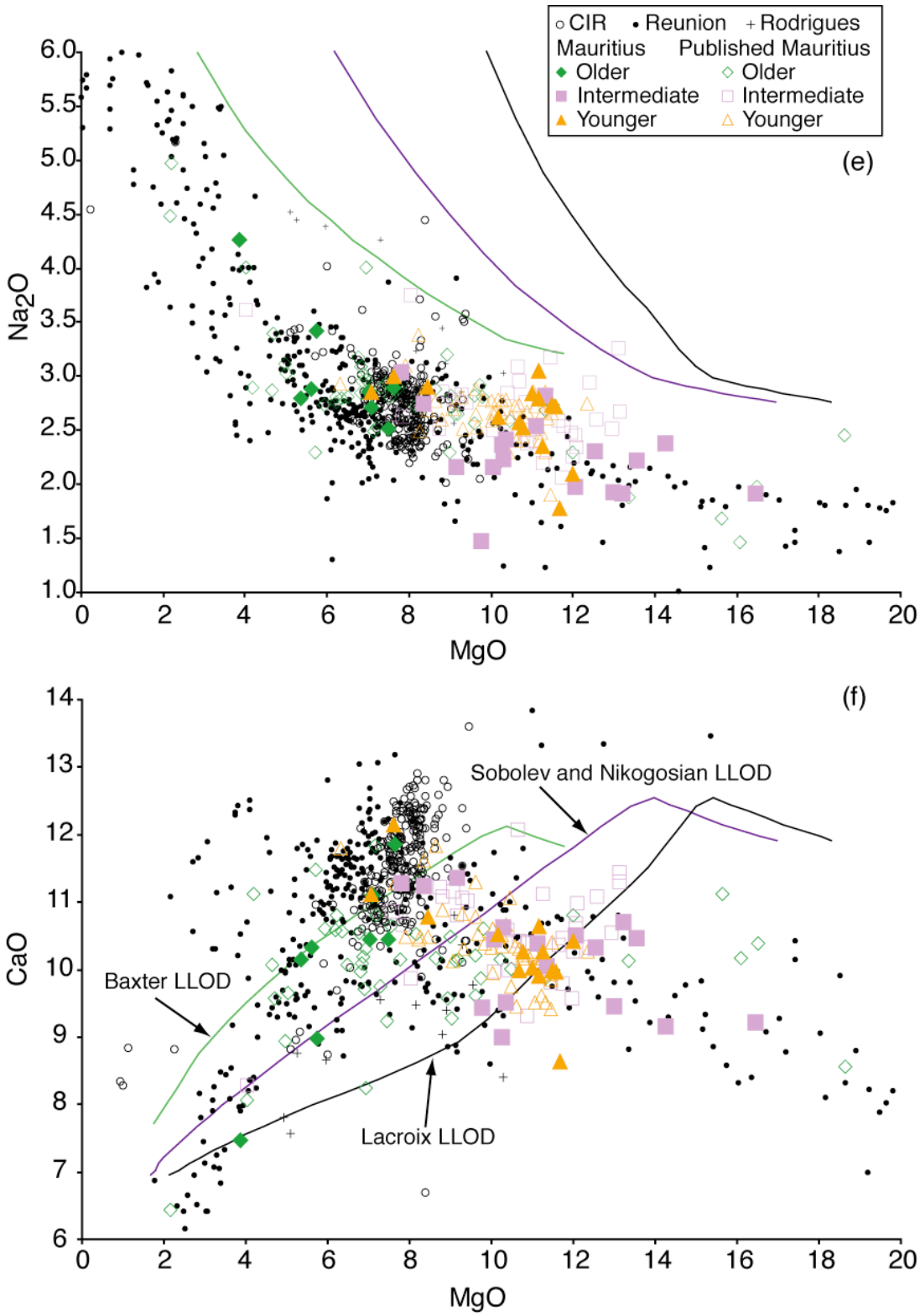

Figure 6 (*continued*)

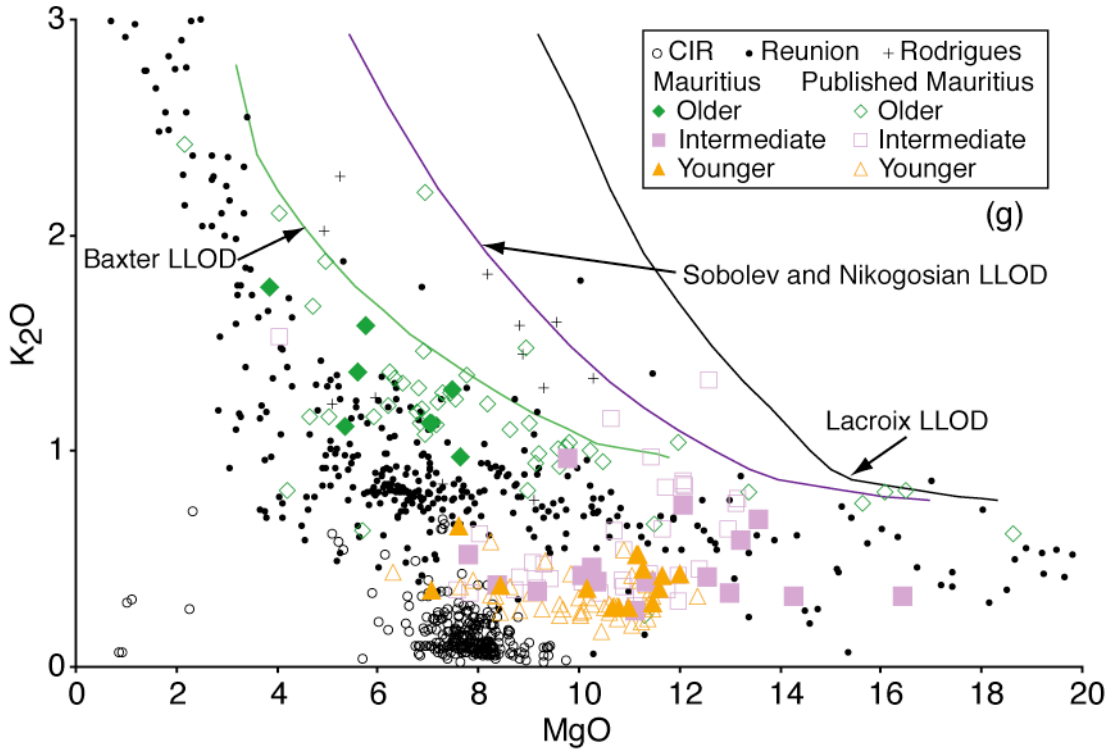

Table 2. Unnormalized major element XRF data for Mauritius lavas. Total Fe reported as Fe^{2+}. Rock names and normative mineralogy from MAGMA program of Wohletz (1999). Rock names after IUGS classification of Le Bas and Streckeisen (1991). AOB – Alkaline olivine basalt; B – Basanite; OB – Olivine basalt; TB – Trachybasalt. Normative mineralogy calculated from LOI-free compositions normalized to 100 wt. %. q – quartz; c – corundum; or – orthoclase; ab – albite; an – anorthite; lc – leucite; ne – nepheline; di – diopside; hy – hypersthene; ac – acmite; ol – olivine; mt – magnetite; il – ilmenite; hm – hematite; tn – titanite (sphene); ru – rutile; ap – apatite; cc – calcite. Duplicate analyses are given in Table B.1 and analyzed standard values are given in Table B.2. Analytical methods are presented in the Methods section.

	Older Series							Intermediate Series		
element (ppm)	B18-1	M6	M12	M30	M35	M36	M37	M39	B2-1	B5-1
SiO2	44.07	46.00	45.34	47.11	46.74	45.92	45.34	46.54	45.04	45.85
TiO2	2.96	3.23	2.78	2.86	3.12	2.87	3.08	2.93	1.77	1.52
Al2O3	13.64	15.05	13.54	16.14	14.94	14.12	13.88	14.57	13.11	14.68
FeO(T)	11.14	11.80	11.35	10.45	9.87	11.23	11.27	11.88	10.98	12.13
MnO	0.17	0.17	0.17	0.18	0.16	0.17	0.18	0.15	0.15	0.18
MgO	6.57	5.39	7.33	5.53	3.53	6.69	7.11	5.09	9.38	10.94
CaO	10.30	9.92	11.37	8.64	6.82	9.93	9.90	9.63	8.22	10.22
Na2O	2.52	2.77	2.78	3.29	3.89	2.72	2.38	2.65	2.16	2.50
K2O	1.05	1.32	0.93	1.52	1.60	1.08	1.21	1.06	0.42	0.26
P2O5	0.40	0.47	0.35	0.47	0.59	0.38	0.43	0.37	0.20	0.14
Sum	92.82	96.13	95.94	96.20	91.26	95.10	94.78	94.86	91.44	98.42
LOI (%)	5.46	2.39	1.15	1.45	6.31	2.00	3.23	3.12	6.87	0.23
q										
c										
or	6.67	8.09	5.73	9.33	10.39	6.67	7.56	6.55	2.72	1.53
ab	19.96	23.04	16.56	26.90	36.01	23.45	21.22	23.50	20.03	18.09
an	24.56	25.67	22.61	25.76		24.31	24.92	26.14	27.12	28.53
lc					20.37					
ne	1.64	0.75	4.31	1.09		0.40				1.83
di	22.90	18.63	27.92	12.97		20.58	19.72	18.16	13.17	18.08
hy					10.51		1.63	8.51	17.90	
ac					2.67					
ol	17.27	16.33	16.58	17.20		17.96	17.76	10.37	14.88	28.72
mt					12.08					
il	6.06	6.39	5.51	5.66		5.74	6.18	5.87	3.68	2.94
hm					6.50					
tn										
ru										
ap	0.93	1.07	0.79	1.06		0.87	1.00	0.84	0.48	0.30
cc					1.40					
Rock name	OB	OB	AOB	OB	TB	OB	OB	OB	OB	OB

Table 2. *(continued)*

	Intermediate Series									
element (ppm)	B6-1	B6-2	B12-1	B18-2	B18-3	B18-4	B18-5	B18-6	B18-7	B18-8
SiO2	44.19	44.91	43.15	43.45	44.08	45.72	41.37	44.29	45.77	45.75
TiO2	1.64	1.82	1.83	2.06	1.67	1.81	2.53	2.07	1.37	2.16
Al2O3	13.89	14.19	14.48	12.91	13.80	13.45	14.17	15.47	13.69	16.24
FeO(T)	10.84	11.42	11.26	11.76	11.83	11.94	12.46	11.41	12.29	11.68
MnO	0.17	0.17	0.19	0.18	0.18	0.18	0.17	0.18	0.19	0.18
MgO	9.54	9.74	9.29	13.10	12.38	12.34	8.85	8.77	14.19	7.70
CaO	9.85	8.94	9.65	10.12	9.00	10.17	8.55	10.87	9.11	11.12
Na2O	2.07	2.27	2.00	2.15	1.84	2.27	1.34	2.06	2.37	3.00
K2O	0.37	0.37	0.39	0.66	0.33	0.41	0.88	0.34	0.32	0.51
P2O5	0.16	0.20	0.17	0.31	0.19	0.19	0.32	0.20	0.17	0.23
Sum	92.72	94.02	92.40	96.70	95.31	98.48	90.62	95.65	99.47	98.56
LOI (%)	6.14	4.82	6.03	1.47	4.11	0.57	7.64	3.03	0.08	0.20
q										
c										
or	2.36	2.30	2.48	4.01	2.01	2.48	5.73	2.07	1.95	3.07
ab	18.93	20.45	18.26	10.50	16.31	16.57	12.43	18.11	16.64	16.68
an	29.62	29.15	31.81	24.44	29.83	25.63	33.17	33.38	25.90	29.77
lc										
ne				4.48		1.60		0.08	1.89	4.88
di	17.96	13.67	15.41	20.61	12.82	19.87	9.38	17.77	14.99	20.40
hy	4.68	7.73	3.02		5.43		12.49			
ac										
ol	22.71	22.56	24.86	31.23	29.84	29.98	20.72	24.05	35.71	20.54
mt										
il	3.37	3.69	3.77	4.04	3.33	3.50	5.31	4.12	2.61	4.17
hm										
tn										
ru										
ap	0.38	0.46	0.41	0.71	0.45	0.42	0.76	0.46	0.37	0.50
cc										
Rock name	OB	OB	OB	AOB	OB	OB	OB	OB	OB	OB

Table 2. *(continued)*

	Intermediate Series					Younger Series				
element (ppm)	B19-1	B19-2	B19-3	M15	M20	B1-1	B1-2	B1-3	B1-4	B1-5
SiO2	43.13	42.82	43.84	44.97	46.00	46.79	46.95	45.23	44.71	44.78
TiO2	2.26	1.52	2.17	1.86	1.90	1.88	1.72	2.03	1.73	2.02
Al2O3	12.92	11.67	13.13	14.41	15.78	16.70	16.18	14.51	14.58	14.87
FeO(T)	11.89	12.57	11.72	12.69	11.68	11.67	11.61	12.83	11.86	12.06
MnO	0.20	0.19	0.18	0.19	0.18	0.18	0.18	0.19	0.18	0.18
MgO	12.69	15.74	11.52	11.17	8.19	6.97	8.36	11.13	11.70	11.05
CaO	10.28	8.83	10.03	9.90	11.02	10.96	10.69	9.87	10.17	10.54
Na2O	1.85	1.83	1.89	2.78	2.69	2.81	2.88	3.05	2.06	2.77
K2O	0.57	0.31	0.72	0.39	0.37	0.35	0.38	0.52	0.42	0.51
P2O5	0.31	0.19	0.25	0.19	0.17	0.17	0.15	0.27	0.18	0.21
Sum	96.08	95.67	95.45	98.54	97.98	98.47	99.08	99.62	97.58	98.99
LOI (%)	2.78	3.72	3.22	-0.06	0.07	0.67	0.09	-0.55	1.35	-0.10
q										
c										
or	3.48	1.95	4.43	2.30	2.24	2.13	2.24	3.07	2.54	3.07
ab	11.65	12.20	14.61	15.08	18.76	21.86	20.48	14.09	15.41	12.12
an	26.33	23.73	26.40	26.05	30.45	32.41	30.36		30.01	
lc								24.45		26.87
ne	2.48	2.14	1.15	4.79	2.43	1.21	2.23		1.32	
di	20.09	16.85	19.60	18.46	20.03	18.00	18.28	6.38	16.76	6.26
hy								18.83		20.08
ac										
ol	30.84	39.73	28.93	29.35	22.05	20.42	22.80		30.25	
mt								28.76		27.31
il	4.47	3.03	4.33	3.58	3.69	3.62	3.29		3.37	
hm								3.87		3.88
tn										
ru										
ap	0.70	0.44	0.57	0.41	0.38	0.37	0.33		0.39	
cc								0.59		0.46
Rock name	AOB	AOB	OB	AOB	OB	OB	OB	B	OB	B

Table 2. *(continued)*

	Younger Series								
element (ppm)	B6-3	B6-4	B18-9	B19-4	B19-5	M17	M22	M29	M33
SiO2	46.37	45.82	43.05	45.72	46.05	43.98	45.12	44.55	45.85
TiO2	1.63	1.59	2.02	1.82	1.69	2.01	2.60	2.41	1.49
Al2O3	14.90	14.95	14.52	14.61	14.74	14.45	15.50	14.05	15.14
FeO(T)	12.55	12.66	13.21	12.42	12.33	12.55	11.92	13.64	11.90
MnO	0.19	0.19	0.20	0.19	0.19	0.19	0.19	0.21	0.18
MgO	11.00	10.52	11.02	11.53	11.42	10.92	7.53	10.00	10.59
CaO	10.03	9.84	8.16	9.92	9.94	9.96	12.01	10.36	10.08
Na2O	2.85	2.54	1.69	2.70	2.72	2.29	2.97	2.59	2.49
K2O	0.28	0.27	0.40	0.36	0.29	0.44	0.65	0.35	0.27
P2O5	0.15	0.16	0.21	0.18	0.14	0.21	0.29	0.21	0.13
Sum	99.95	98.54	94.48	99.45	99.50	97.01	98.78	98.36	98.12
LOI (%)	-0.65	0.30	4.36	-0.52	-0.75	1.09	0.01	0.08	0.17
q									
c									
or	1.65	1.59	2.48	2.13	1.71	2.72	3.90	2.13	1.65
ab	17.84	19.31	15.13	16.44	17.51	14.78	12.36	15.27	18.95
an	27.05	29.00	32.64	26.80	27.29	28.66		26.11	29.90
lc							27.39		
ne	3.39	1.35		3.55	3.02	2.80		3.77	1.32
di	17.83	15.99	7.18	17.62	17.47	17.10	7.05	20.39	16.57
hy			10.46				25.63		
ac									
ol	28.85	29.35	27.55	29.62	29.50	29.56		27.23	28.46
mt							18.05		
il	3.11	3.07	4.07	3.49	3.23	3.94		4.67	2.90
hm							5.00		
tn									
ru									
ap	0.32	0.35	0.49	0.40	0.31	0.48		0.46	0.29
cc							0.65		
Rock name	AOB	OB	OB	AOB	AOB	AOB	B	AOB	OB

Figure 7. Total alkali versus silica diagram. Symbols after Figure 6 (see text for data references). Alkaline-tholeiitic line after Le Bas et al. (1986). Nearly all Mauritius and Réunion samples plot as alkaline lavas.

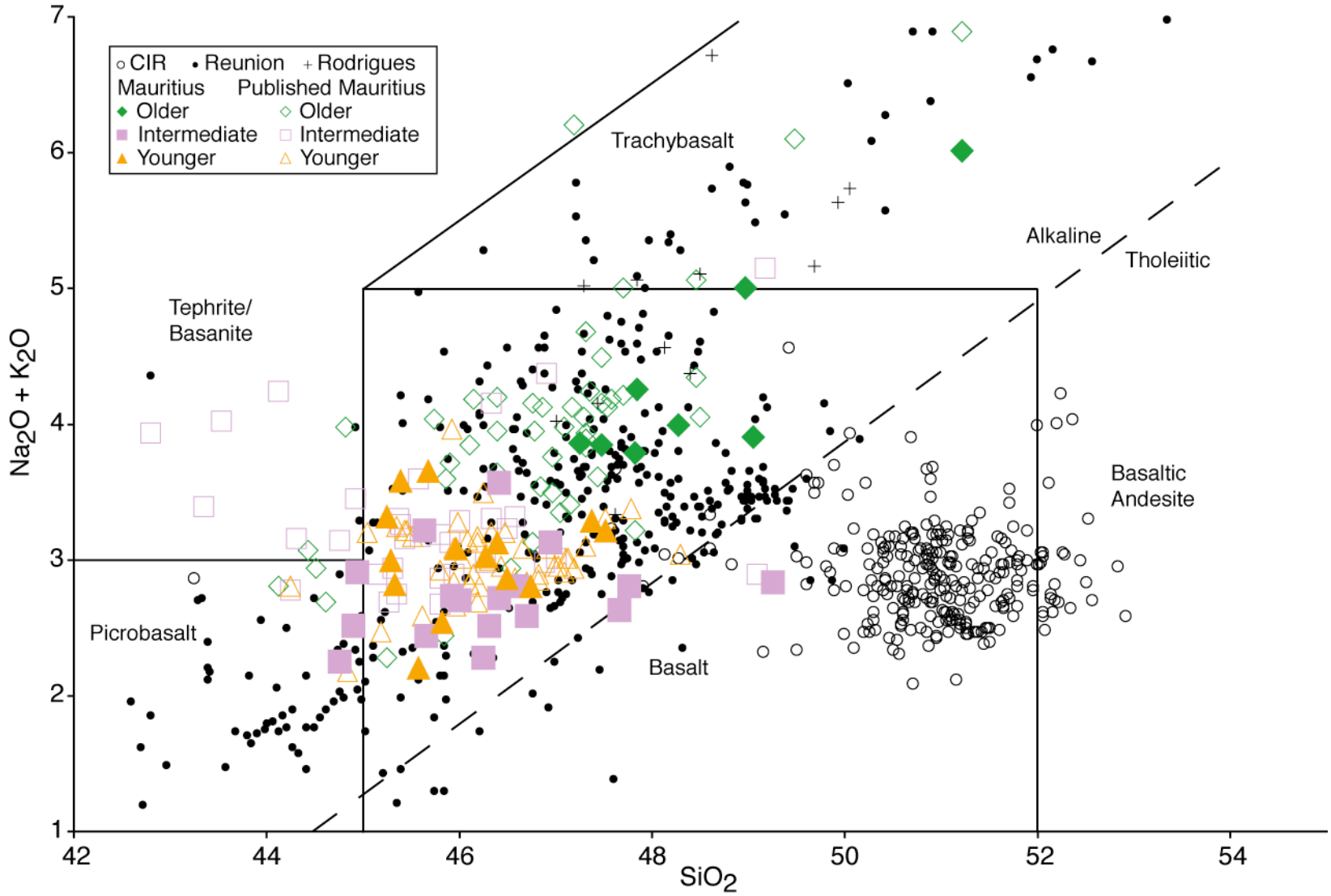
CIR
Reunion
Rodrigues
Mauritius
Older
Intermediate
Younger
Published Mauritius
Older
Intermediate
Younger
Trachybasalt
Alkaline
Tholeiitic
Tephrite/
Basanite
Basaltic
Andesite
Picrobasalt
Basalt
Na2O + K2O
SiO2
7
6
5
4
3
2
1
42
44
46
48
50
52
54

Sheth et al. (2003) were not observed, although sample B18-2 does plot near the basanite-basalt-picrobasalt join.

Grouping by Series

The Older Series lavas have the lowest MgO (3.53 – 7.33 wt. %) of the three Mauritian lava suites, and thus tend to plot relatively distinct from the post-erosional lavas in most major element plots (Figure 6). Older Series lavas are the most differentiated with relatively low Mg# (38.9 – 53.5; Mg# = [atomic Mg / (Mg + Fe^{2+})] • 100, assuming total Fe as Fe^{2+}), towards the lower end of published data for the Older Series (29.6 – 72.9, calculated in the same manner). These lavas have the highest SiO_2, TiO_2, Na_2O, K_2O, and P_2O_5 while having the lowest FeO_T and MnO, on average. The Older Series appear to form a distinct trend from the post-erosional lavas for Al_2O_3, lower alumina at a given MgO. The Older Series also form a distinct trend in CaO, decreasing calcium with decreasing MgO, a result of clinopyroxene fractionation. Each of these trends are consistent with published data (*e.g.* Baxter 1975a, 1976). Older Series lavas are restricted to alkalic compositions and are predominantly basaltic (Figure 7), with the exception of trachybasalt M35 and sample M30, which plots on the basalt-trachybasalt divide. None of the lavas with higher MgO contents (> 8 wt. %) observed in other studies were analyzed for this work.

Lavas of the Intermediate Series overlap significantly with the Younger Series in all oxide-oxide plots, although the Intermediate Series lavas show more intra-series variation. The Intermediate Series lavas show, on average, the highest MgO (7.82 – 16.45 wt. %) with Mg# (54.0 – 69.0) similar to published values. Sample B2-1 has high SiO_2 (49.26 wt. %) for its MgO content (10.26 wt. %), though it tends to be more central in other plots. Two other samples, B6-1 and B6-2, slightly elevated SiO_2 levels at a given MgO, though not so much so in B2-1. Despite overlapping with the Younger Series, the Intermediate Series has on average the highest MgO, the lowest

SiO_2 and Na_2O, and intermediate TiO_2, FeO_T, MnO, CaO, K_2O, and P_2O_5. Intermediate Series lavas do form trends in Al_2O_3, high alumina at a given MgO, and in CaO, decreasing calcium with increasing MgO, that are distinct from the Older Series lavas. Several Intermediate Series samples have elevated K_2O and plot on the high-MgO continuation of trend observed for the Older Series. Intermediate Series lavas are predominantly basaltic in composition, with three samples classified as picrobasalts (B18-2, B19-1, and B19-2). The Intermediate Series basalts straddle the join divide between alkalic and subalkalic, with seven samples falling in to the latter category.

As noted above, the Younger Series overlap significantly with the Intermediate Series. These two lava suites are very similar though, in general, the Younger Series does show a more limited range than the Intermediate Series. On average, the Younger Series has the highest FeO_T, MnO, and CaO, the lowest K_2O and P_2O_5, and intermediate SiO_2, MgO, and Na_2O. A small SiO_2 "gap" exists between the higher MgO and lower MgO samples, but is likely a result of sampling as the published data form a continuum throughout MgO. These lavas have slightly lower Mg# (51.6 – 61.3) than the Intermediate Series. Overall oxide-oxide trends for both post-erosional series lavas are consistent with published data. All Younger Series lavas can be classified as alkali basalts, though sample M33 plots very near to the alkalic-subalkalic divide.

Grouping by Sample Locality

Drill Core Samples

Mauritian lava samples from the measured drill cores have the highest MgO (7.08 – 16.45 wt. %) contents of this Mauritius suite. The drill core lavas show inter-oxide trends consistent with a post-erosional series origin (high MgO; low SiO_2, TiO_2, and alkalis), with the exception of sample B18-1. This sample is the deepest drill core

sample (219.8 m) and has major element concentrations consistent with an Older Series origin, in particular the low Al_2O_3 content (14.70 wt. %) at a given MgO. Drill core lavas have predominantly basaltic compositions, though B18-2, B19-1, and B19-2 are picrobasalts. Additionally, drill core lavas straddle the alkalic-subalkalic divide, with seven samples classified as subalkalic. All subalkalic samples presented in this work are taken from the drill core suite.

Major element oxide concentrations for the measured drill core samples show variation with depth of core, particularly within individual cores. While weak trends with changing depth are observed (*e.g.*, increasing MnO with decreasing depth in core B18), there is little systematic diversity across the core suite as a whole, and thus across the island as a whole.

Cone Samples

Samples from the Intermediate and Younger Series cones span a relatively restricted range of MgO composition (7.62 – 11.34 wt. %), less than the > 7 % intra-core variation observed in MgO for drill core B18. The post-erosional cones are characterized by relatively high Al_2O_3, FeO_T, MnO, CaO, and Na_2O, and low SiO_2 and K_2O, coincident with alkaline basaltic compositions. These compositions are consistent with a post-erosional origin, though, as in other groups, it is difficult to distinguish between the Intermediate and Younger Series solely from major element composition alone. Despite the northeast trend of the cones, no variation is observed with latitude (*i.e.*, location).

Massif Samples

The outcrop samples of the exposed remnants of the edificial massif have a limited range in MgO composition (5.61 – 7.64 wt. %). These samples clearly have high SiO_2, TiO_2, K_2O, and P_2O_5, with low MgO and FeO_T. The massif samples are also characterized by clinopyroxene fractionation, as evidenced by the trend toward

decreasing CaO with decreasing MgO. Together with the low Al_2O_3 at a given MgO that is characteristic of the Older Series, these samples are consistent with an Older Series origin. Apart from sample M30, which plots on the basalt-trachybasalt divide, samples of the remnant massif are alkalic basalts.

Breccia Samples

The samples of breccia were collected from the basal units of the remnant massif, and thus have similar major element characteristics. In particular, the breccia samples have the highest SiO_2 (47.83 – 51.22 wt. %), the lowest MgO (3.86 – 7.50 wt. %), and the Al_2O_3 and CaO trends characteristic of the Older Series lavas. Thus, the samples are relatively differentiated and distinctly non-primitive. The breccia samples are alkalic basalts, with the exception of sample M35, an alkalic trachybasalt.

Trace Elements

In accompaniment to the major element compositions, Baxter (1975a, b; 1976; 1978) utilized trace element concentrations and ratios to characterize the sources and geochemical evolution of the Older, Intermediate and Younger Series. In these works he identified quantifiable distinctions between the three lavas series: higher abundances of incompatible[1] elements and higher degree melts in the Older Series, and variable but low degree melts from a more depleted source resulting in lower abundances of incompatible elements from the Intermediate and Younger Series. Results from more recent work (Mahoney et al., 1996; Sheth et al., 2003; Nohda et al., 2005; Paul et al., 2005) have principally agreed with Baxter's original work, though genetic interpretations have differed.

[1] Incompatible elements are those elements with $D^{s/l} < 1$. Relative compatibility for mantle assemblages is Rb < Ba < Th < Nb < U < La < Ce < Pb < Nd < Sr < P < Sm < Hf < Eu < Ti < Gd < Dy < Y < Er < Lu < Al < Ca < Fe < Si < Mg.

Trace element compositions for the Mauritius samples presented here are presented in Table 3, with errors in Table C.1. As observed with the major element concentrations, trace element concentrations and ratios show similar enrichment and depletion patterns to those in the literature. Table C.2 includes the mean and standard deviation of USGS rock standards BCR-2, BIR-1, and BE-N (n = 28, 4, and 4, respectively), Cornell in-house standard PAL-889 (n = 4), and reference values. Additional information on trace elements can be found in Appendix D.

Grouping by Series

Lavas of the Older Series have the highest incompatible trace element concentrations of the three Mauritian lavas suites. Primitive mantle normalized trace element patterns (Figure 8; McDonough and Sun, 1995) of the Older Series lavas show slight depletions in fluid mobile elements (Cs, Ba, U, and Pb) and slight Nd peaks, though not as severe as those observed in Nohda et al. (2005). Relative depletions common to many OIB are also observed in the high field strength elements (HFSE; Nb, Ta, Zr, Hf), although the trend is more evident in Zr and Hf. Sample M35 is the most highly enriched in incompatible elements, though it appears slightly less enriched in the more compatible elements, where sample M39 has the highest concentrations. Sample B18-1, the only drill core sample of the Older Series, has relatively low trace element abundances. Chondrite normalized rare earth element patterns (REE; Figure 9; McDonough and Sun, 1995) for the Older Series are parallel with moderate enrichment of light rare earth elements (LREE; La = 25.6 – 42.2 ppm) over heavy rare earth elements (HREE; Yb = 2.1 – 2.7 ppm), producing the steepest REE patterns (La/Yb = 11.4 – 16.4) on Mauritius. The ratio of LREE to middle rare earth elements (MREE; Sm = 7.1 – 11.5 ppm) has a relatively limited range (La/Sm = 3.5 – 4.3), and the highest MREE/HREE ratios (Sm/Yb = 3.2 – 4.3 ppm). Of the three series, the Older Series have the highest ratios for more incompatible to less

Table 3. Trace element concentrations for Mauritius samples. Analytical uncertainty given in Table C.1 with analyses of geostandards in Table C.2. Analytical methods are presented in the Methods section.

element	**Older Series**								**Intermediate Series**	
(ppm)	B18-1	M6	M12	M30	M35	M36	M37	M39	B2-1	B5-1
Li	5.03	7.25	7.22	5.27	8.46	5.55	6.08	4.45	3.30	4.39
Be	1.3	1.6	1.2	1.6	2.5	1.4	1.3	1.4	0.6	0.5
B	0.6	0.3	0.7	0.8	0.3	1.3	1.0	0.3	0.2	0.2
Sc	29.34	25.48	32.18	19.99	16.86	29.70	28.46	31.67	25.21	29.42
Ti	16506	19698	16305	18904	21826	15361	17374	19539	8632	8530
V	302.4	340.0	326.4	254.4	281.8	309.2	334.3	393.5	194.1	290.7
Cr	203.4	79.0	394.1	92.7	13.2	143.5	155.4	98.5	280.8	404.0
Co	48.62	45.49	55.73	38.53	31.21	49.99	48.90	41.48	57.86	73.85
Ni	115.71	79.62	137.44	76.97	16.42	112.30	108.52	71.15	265.78	365.99
Cu	110.66	78.75	67.33	40.60	33.10	61.13	59.63	69.84	86.53	100.05
Zn	124.30	124.38	110.86	124.89	129.97	120.64	118.73	114.64	96.41	102.23
Ga	24.96	25.93	22.53	26.91	25.93	25.26	23.97	24.46	18.94	19.99
Rb	25.3	31.7	20.8	36.1	47.2	28.5	27.1	24.4	7.2	4.9
Sr	459.8	522.6	437.8	543.7	831.4	434.4	410.7	404.3	202.5	240.2
Y	28.83	31.95	27.40	33.33	37.18	29.80	28.40	43.15	20.00	20.04
Zr	236.2	282.3	230.8	302.6	459.1	219.8	234.8	241.0	89.0	96.6
Nb	27.12	37.10	25.60	39.79	60.06	27.01	28.34	32.51	9.51	7.87
Cs	0.092	0.206	0.061	0.295	0.665	0.161	0.090	0.089	0.053	0.053
Ba	229.5	331.2	213.5	310.0	309.7	225.8	253.9	255.1	127.6	78.6
La	27.14	32.90	25.55	33.10	42.19	26.72	29.44	42.17	10.69	7.79
Ce	61.83	68.68	57.32	73.78	89.47	59.50	67.45	80.69	23.23	17.52
Pr	7.99	9.10	7.30	9.53	11.11	7.82	8.62	11.64	3.09	2.45
Nd	33.44	37.44	30.54	39.13	45.32	33.01	35.21	50.05	13.81	11.24
Sm	7.70	8.28	7.12	8.80	9.83	7.46	7.85	11.50	3.77	3.15
Eu	2.48	2.71	2.29	2.80	3.09	2.43	2.48	3.60	1.36	1.15
Gd	7.44	7.94	7.06	8.34	9.15	7.39	7.35	11.67	4.32	3.71
Tb	1.06	1.13	1.02	1.20	1.32	1.08	1.05	1.65	0.67	0.61
Dy	5.55	5.95	5.46	6.10	6.40	5.97	5.42	6.81	4.33	3.94
Ho	1.09	1.17	1.08	1.24	1.36	1.15	1.07	1.63	0.78	0.77
Er	2.78	2.91	2.75	3.14	3.43	2.93	2.74	3.97	2.03	2.09
Yb	2.12	2.19	2.17	2.40	2.57	2.35	2.07	2.69	1.68	1.81
Lu	0.30	0.32	0.31	0.34	0.38	0.33	0.30	0.40	0.23	0.26
Hf	5.34	6.15	5.37	6.72	9.05	4.83	5.39	5.60	2.09	2.21
Ta	1.67	2.22	1.59	2.46	3.50	1.59	1.69	1.94	0.49	0.39
Pb	2.68	4.70	4.61	4.89	4.72	3.18	3.25	2.82	20.74	1.92
Th	3.29	3.92	3.31	4.15	5.62	3.08	3.66	2.81	1.21	0.84
U	0.828	0.891	0.644	0.931	1.588	0.750	0.621	0.493	0.113	0.207

Table 3. *(continued)*

element	**Intermediate Series**									
(ppm)	B6-1	B6-2	B12-1	B18-2	B18-3	B18-4	B18-5	B18-6	B18-7	B18-8
Li	3.76	7.81	4.23	4.43	3.90	4.26	7.95	10.14	4.78	5.23
Be	0.5	0.5	0.6	0.9	0.5	0.6	1.2	0.7	0.5	0.7
B	0.5	63.0	0.5	0.4	0.5	0.6	0.9	68.9	0.9	0.6
Sc	27.10	25.86	28.22	28.08	27.05	25.83	26.90	32.15	25.61	31.11
Ti	10794	10950	9529	11932	8559	9270	16433	12805	6677	15199
V	280.0	270.5	274.8	276.7	238.5	277.1	356.7	327.8	212.6	332.1
Cr	443.8	382.0	263.2	552.1	364.2	225.7	396.6	225.3	531.5	127.8
Co	61.81	61.48	56.77	68.51	64.26	67.55	67.45	57.31	79.83	54.28
Ni	263.02	239.42	184.04	357.24	327.14	353.64	216.54	149.61	500.40	108.48
Cu	79.42	71.38	77.90	86.63	67.73	88.65	86.04	84.91	82.77	87.32
Zn	93.17	149.04	92.48	101.92	90.61	97.51	123.34	156.96	104.33	98.51
Ga	18.79	19.43	20.51	19.44	17.43	19.02	23.15	23.55	18.51	22.26
Rb	7.0	6.2	10.8	18.2	6.9	9.1	23.6	5.7	6.4	10.4
Sr	255.8	246.6	672.4	388.8	350.1	340.3	331.6	345.2	262.3	360.0
Y	18.14	19.31	20.82	20.80	18.77	18.52	25.20	22.19	19.42	22.31
Zr	104.0	114.8	90.1	146.6	89.3	104.9	190.2	116.8	91.4	142.9
Nb	12.53	12.78	8.46	27.28	11.17	9.73	34.27	16.87	7.36	22.98
Cs	0.087	0.080	0.058	0.256	0.094	0.062	0.311	0.081	0.072	0.117
Ba	193.2	317.0	114.9	198.6	121.1	129.9	347.0	130.2	96.4	145.5
La	9.41	9.99	10.80	19.50	9.31	11.22	22.21	12.32	9.60	13.52
Ce	21.02	21.92	23.18	40.96	21.06	24.45	46.20	27.11	21.20	29.61
Pr	2.80	2.93	3.11	5.22	2.81	3.24	6.03	3.62	2.83	3.90
Nd	12.39	13.14	13.75	21.12	12.45	14.34	25.56	16.20	12.52	17.20
Sm	3.29	3.47	3.62	4.84	3.28	3.65	5.93	4.14	3.18	4.31
Eu	1.22	1.27	1.30	1.59	1.18	1.27	2.02	1.48	1.14	1.52
Gd	3.68	3.96	4.13	4.82	3.66	4.00	5.95	4.39	3.66	4.61
Tb	0.58	0.63	0.65	0.70	0.58	0.62	0.88	0.69	0.58	0.72
Dy	3.63	3.70	4.20	4.22	3.83	4.03	5.05	4.35	4.09	4.65
Ho	0.67	0.74	0.79	0.77	0.72	0.71	0.90	0.81	0.72	0.84
Er	1.80	1.94	2.12	1.98	1.96	1.87	2.25	2.18	1.96	2.23
Yb	1.49	1.60	1.83	1.66	1.67	1.59	1.75	1.81	1.76	1.88
Lu	0.22	0.23	0.26	0.24	0.25	0.22	0.24	0.26	0.25	0.27
Hf	2.43	2.59	2.11	3.20	2.02	2.44	4.06	2.56	2.02	3.06
Ta	0.69	0.64	0.43	1.53	0.60	0.53	1.84	0.85	0.38	1.11
Pb	7.22	16.64	0.98	1.95	0.80	1.28	2.20	2.16	1.13	1.49
Th	1.09	1.17	1.19	2.54	1.00	1.30	2.67	1.67	0.93	1.48
U	0.224	0.155	0.282	0.627	0.238	0.319	0.508	0.682	0.237	0.352

Table 3. *(continued)*

element	**Intermediate Series**					**Younger Series**				
(ppm)	B19-1	B19-2	B19-3	M15	M20	B1-1	B1-2	B1-3	B1-4	B1-5
Li	3.97	3.72	5.56	6.10	4.36	4.75	4.49	5.31	4.26	3.88
Be	0.8	0.4	0.9	0.7	0.6	0.6	0.5	0.8	0.6	0.6
B	0.6	0.4	0.5	0.9	0.5	0.4	0.4	0.9	0.5	0.7
Sc	25.28	24.65	25.88	28.22	29.60	30.90	28.12	27.76	29.09	30.79
Ti	12149	8747	14231	7590	9161	11166	9497	12998	9868	13986
V	278.1	240.7	344.8	214.6	271.9	311.5	267.0	278.9	290.4	347.6
Cr	496.9	532.6	488.4	387.3	249.4	233.3	217.1	377.3	455.4	212.7
Co	70.26	85.99	66.49	73.21	58.69	53.49	59.61	69.61	73.63	68.28
Ni	346.91	470.55	304.31	323.45	127.11	100.61	137.83	281.51	329.95	279.08
Cu	81.83	67.96	87.32	87.07	77.28	76.06	75.36	89.37	91.97	82.95
Zn	103.86	99.47	112.08	106.80	101.67	100.96	99.73	112.12	106.88	99.11
Ga	20.20	14.02	21.05	20.86	21.28	22.92	21.74	21.26	20.90	19.05
Rb	14.1	6.7	17.6	7.3	6.8	6.3	6.6	10.7	8.5	10.0
Sr	1008.9	272.0	372.7	320.4	336.4	343.2	297.7	370.1	400.1	354.3
Y	19.87	15.97	19.97	21.75	24.62	22.60	21.02	21.83	20.65	21.10
Zr	142.5	89.0	160.3	96.7	88.2	107.2	94.5	135.0	113.7	112.2
Nb	24.08	13.09	25.14	7.50	9.30	10.99	9.47	18.62	11.93	18.28
Cs	0.143	0.063	0.135	0.086	0.043	0.086	0.076	0.092	0.068	0.113
Ba	220.2	118.8	200.9	123.1	102.7	109.2	490.7	140.4	133.0	161.8
La	19.04	11.20	16.39	11.18	10.78	9.80	9.25	13.86	11.39	13.76
Ce	39.95	22.82	35.43	25.31	22.66	21.50	20.38	30.99	25.81	28.71
Pr	5.09	2.91	4.56	3.42	3.18	2.90	2.75	4.07	3.44	3.72
Nd	21.38	12.48	19.66	15.30	14.44	13.25	12.43	17.55	14.74	15.69
Sm	4.87	3.10	4.63	3.95	3.80	3.56	3.34	4.34	3.81	3.94
Eu	1.64	1.10	1.57	1.40	1.37	1.32	1.27	1.48	1.35	1.38
Gd	4.85	3.40	4.58	4.39	4.41	4.17	3.95	4.65	4.11	4.23
Tb	0.71	0.52	0.70	0.68	0.70	0.68	0.64	0.71	0.65	0.66
Dy	3.91	3.34	3.58	4.84	4.12	3.97	4.00	4.90	3.48	3.63
Ho	0.75	0.62	0.75	0.82	0.86	0.85	0.81	0.83	0.78	0.79
Er	1.90	1.65	1.90	2.18	2.33	2.30	2.21	2.20	2.09	2.16
Yb	1.49	1.40	1.41	1.97	1.84	1.87	1.82	1.91	1.65	1.73
Lu	0.21	0.20	0.21	0.28	0.28	0.28	0.27	0.27	0.26	0.27
Hf	3.11	2.06	3.45	2.22	2.05	2.46	2.16	3.03	2.55	2.60
Ta	1.32	0.61	1.41	0.45	0.51	0.54	0.48	1.04	0.56	0.77
Pb	1.88	1.66	1.79	1.25	3.35	1.33	26.46	1.92	1.94	2.04
Th	2.26	1.28	1.96	1.07	1.04	1.11	1.06	1.42	1.19	1.75
U	0.587	0.296	0.504	0.266	0.211	0.216	0.255	0.370	0.255	0.401

Table 3. *(continued)*

element	**Younger Series**								
(ppm)	B6-3	B6-4	B18-9	B19-4	B19-5	M17	M22	M29	M33
Li	4.81	4.65	5.33	4.76	4.29	8.89	4.46	4.94	4.34
Be	0.5	0.5	0.7	0.6	0.5	0.8	0.9	0.6	0.5
B	1.1	0.6	0.5	0.3	0.5	0.9	0.6	11.0	0.6
Sc	28.99	27.50	27.94	25.44	26.83	30.36	31.55	29.21	26.20
Ti	8376	8632	9841	10051	11864	8238	14781	12225	7111
V	248.2	244.6	284.6	260.7	322.5	212.8	353.1	286.0	215.8
Cr	347.2	370.4	394.5	262.7	369.9	381.0	152.5	332.9	337.7
Co	71.34	70.59	73.65	66.76	69.31	79.92	55.01	63.28	69.20
Ni	315.21	322.73	338.30	284.12	300.30	310.61	88.21	246.72	303.89
Cu	98.32	90.93	85.48	76.24	80.91	89.29	95.55	102.02	87.97
Zn	112.39	105.43	112.58	102.47	105.48	116.44	102.82	120.38	98.53
Ga	21.04	20.81	20.70	19.31	19.32	21.26	22.45	20.45	19.69
Rb	5.3	3.5	8.6	6.7	5.1	7.3	13.3	5.3	4.4
Sr	245.7	274.0	291.9	298.0	247.8	358.1	454.0	272.7	249.0
Y	20.70	21.02	21.84	19.10	19.06	22.25	21.73	30.62	18.57
Zr	86.1	99.2	107.5	107.4	100.7	91.7	142.6	104.6	83.1
Nb	5.80	8.43	9.66	11.00	11.50	10.62	22.36	14.33	5.78
Cs	0.045	0.039	0.098	0.060	0.048	0.051	0.080	0.039	0.043
Ba	68.3	92.0	145.5	87.4	71.2	135.7	201.6	129.9	71.7
La	6.93	7.98	13.79	9.22	7.26	12.52	17.92	14.71	7.27
Ce	17.18	18.57	28.78	21.52	17.15	28.25	38.75	28.03	16.96
Pr	2.43	2.64	3.80	2.95	2.43	3.72	4.90	3.95	2.34
Nd	11.40	12.05	16.42	13.21	11.31	16.46	20.64	17.04	10.88
Sm	3.23	3.28	4.12	3.45	3.15	4.17	4.92	4.43	2.97
Eu	1.18	1.19	1.46	1.24	1.16	1.44	1.69	1.54	1.11
Gd	3.78	3.76	4.61	3.73	3.75	4.60	5.04	5.17	3.57
Tb	0.62	0.61	0.71	0.60	0.60	0.71	0.76	0.82	0.58
Dy	3.91	4.05	4.29	3.07	3.90	4.81	4.13	4.76	4.05
Ho	0.77	0.75	0.85	0.71	0.76	0.85	0.83	1.04	0.72
Er	2.11	2.06	2.26	1.91	2.07	2.28	2.17	2.76	1.95
Yb	1.80	1.77	1.88	1.49	1.77	1.97	1.70	2.21	1.71
Lu	0.27	0.26	0.27	0.23	0.26	0.28	0.25	0.34	0.24
Hf	1.99	2.22	2.52	2.39	2.40	2.13	3.17	2.52	1.98
Ta	0.30	0.47	0.51	0.55	0.57	0.58	1.21	0.81	0.31
Pb	1.37	2.39	1.21	0.92	1.44	1.42	2.37	1.22	0.56
Th	0.61	0.72	1.60	0.93	0.71	1.32	2.29	1.45	0.71
U	0.167	0.176	0.373	0.229	0.188	0.295	0.492	0.308	0.167

Figure 8. Primitive mantle normalized spider diagram of trace element data for representative samples of Mauritius lavas categorized by eruptive series (*i.e.*, Older, Intermediate, Younger Series). Colors after Figure 1. Average Réunion data of Albarede et al. (1997) shown in black line. The Older Series lavas from Mauritius are enriched in incompatible trace elements relative to the post-erosional Intermediate and Younger Series lavas, as well as average Réunion lava. This relative enrichment in shield building lavas is unique to Mauritius, and not observed at other islands that exhibit post-erosional volcanism. Primitive mantle of McDonough and Sun (1995).

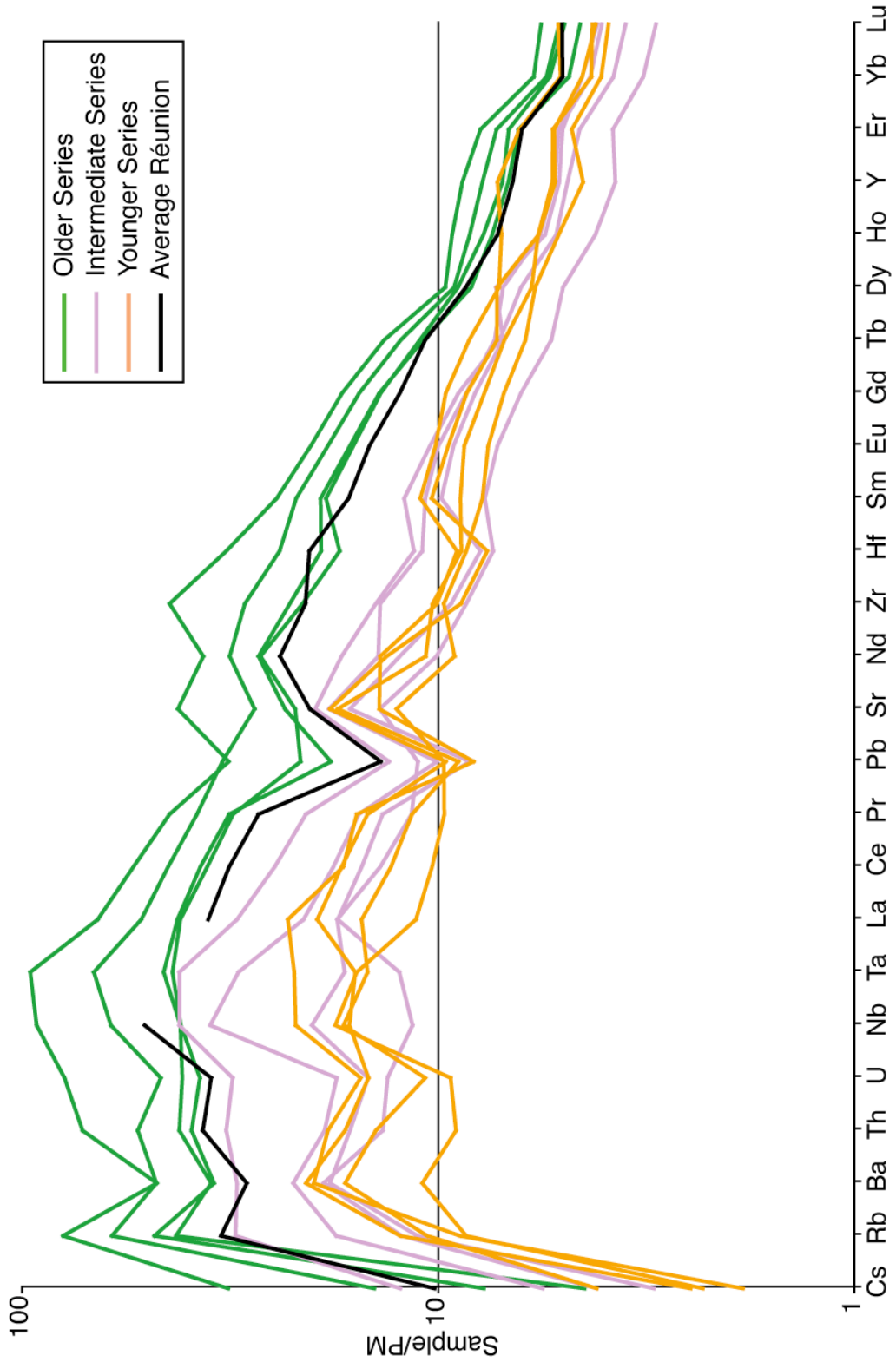
Older Series
Intermediate Series
Younger Series
Average Réunion
100
10
1
Sample/PM
Cs Rb Ba Th U Nb Ta La Ce Pr Pb Sr Nd Zr Hf Sm Eu Gd Tb Dy Ho Y Er Yb Lu

Figure 9. Chondrite mantle normalized rare earth element data for representative samples of Mauritius lavas categorized by eruptive series (*i.e.*, Older, Intermediate, Younger). Symbols after Figure 8. Chondrite of McDonough and Sun (1995).

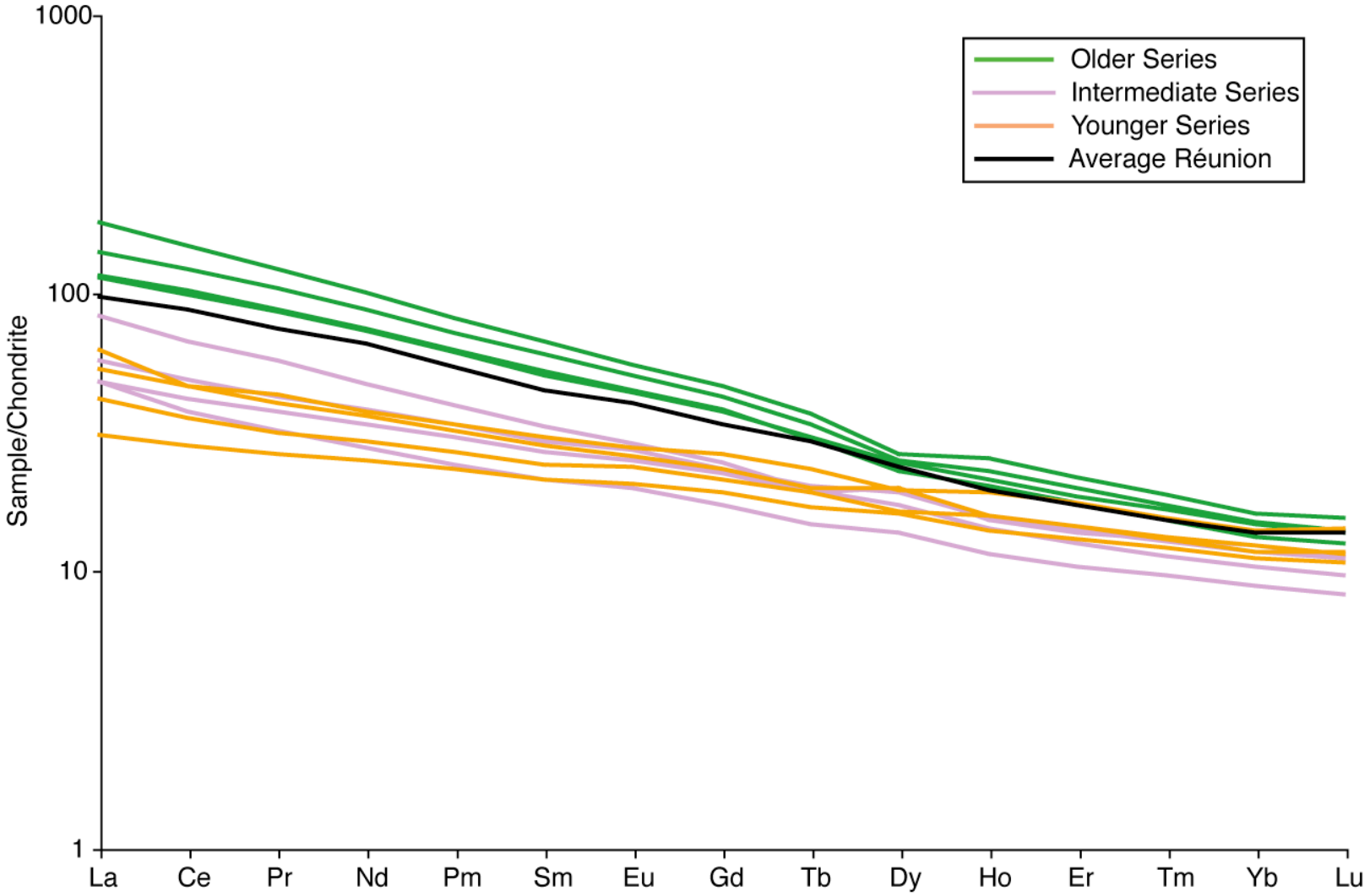
1000
100
10
1
Sample/Chondrite
La
Ce
Pr
Nd
Pm
Sm
Eu
Gd
Tb
Dy
Ho
Er
Tm
Yb
Lu
Older Series
Intermediate Series
Younger Series
Average Réunion

incompatible elements (*e.g.*, La/Sm, Nb/Y). In comparison to the field defined by the post-erosional lavas, the Older Series have high ratios of more/less incompatible elements (La/Sm, Ba/Y) at a given Zr/Nb, except against Ba/La where the Older Series lavas have lower Ba/La. These lavas have virtually nonexistent Eu-anomalies (Eu/Eu* = 0.95 – 1.02; where Eu* = √ ([Sm]*[Gd])). The strong correlation between Sc/Yb and CaO/Al_2O_3 requires clinopyroxene fractionation, as Sc and CaO are removed preferentially over Yb and Al_2O_3.

Primitive mantle normalized trace element patterns for the Intermediate Series are in general very similar to the Older Series, though several important differences exist between the lavas. Intermediate Series lavas have much lower trace element concentrations in the incompatible elements. Whereas the Older Series showed moderate depletions in many of the fluid mobile elements, the Intermediate Series display more severe depletions in U and Pb, with moderate Ba enrichment peaks. In contrast to most of the lavas, samples B2-1 (Pb = 20.7 ppm; Ce/Pb = 1.12; U = 0.11 ppm; Th/U = 10.7) and B6-2 (Pb = 16.6 ppm; Ce/Pb = 1.32; U = 0.15 ppm; Th/U = 7.56; Ba = 317 ppm; Ba/Rb = 51.3) show extreme Pb enrichment with corresponding severe U depletion. B6-2 also shows strong Ba enrichment. Samples B6-1 and M20 also display positive Pb peaks, but have substantially weaker signatures. While most of the Intermediate Series lavas have small Sr peaks (Sr/Nd ≈ 20), samples B12-1 (Sr = 672 ppm; Sr/Nd = 49) and B19-1 (Sr = 1009 ppm; Sr/Nd = 47) are highly enriched in Sr over primitive mantle. Chondrite normalized rare earth element patterns have similar HREE abundances (Yb = 1.4 – 2.0 ppm), but a range of LREE abundances (La = 7.8 – 22.2 ppm). The low but variable La/Yb values (4.3 – 12.8) indicate minor enrichment of LREE with crossing slopes that are generally flatter than the Older Series. The Intermediate Series lavas tend to have intermediate ratios of more/less incompatible elements between the Older Series and Younger Series, but often show

the most variation, both in range and scatter. Together with the Younger Series, the Intermediate lavas form a concave upward array on a plot of Ba/Y vs. Zr/Nb. The Intermediate lavas show the most range along both the ordinate and the abscissa (3.9 – 13.8 and 5.4 – 12.9, respectively). Again, no significant Eu-anomalies (Eu/Eu* = 1.01 – 1.06) are observed.

The Younger Series lavas are quite similar to the Intermediate Series lavas, though in general are slightly less enriched in incompatible elements. Like the Intermediate Series, and unlike the Older Series, the lavas of the Younger Series display enrichment in Ba and Sr, and Pb depletion. Slight depletions are also present for Zr and Hf, but not for Nb and Ta. Minor depletion of uranium is evident, but is not as severe as in the Intermediate Series. Sample M33 (Pb = 0.56 ppm; Ce/Pb = 30.4) displays strong Pb depletion, while sample B1-2 (Pb = 26.5; Ce/Pb = 0.77; Ba = 491; Ba/Rb = 73.9) has extreme enrichment in both Pb and Ba over primitive mantle. Chondrite normalized rare earth element patterns each have similar HREE concentrations (Yb = 1.5 – 2.2 ppm), but a limited range of LREE concentrations (La = 6.9 – 17.9 ppm), similar to the Intermediate Series. These lavas have the flattest rare earth patterns (La/Yb = 3.8 – 10.5) with the smallest amount of LREE enrichment of the three Mauritian lava suites. The Younger Series also show the lowest values of LREE/MREE (La/Sm = 2.1 – 3.6), MREE/HREE (Sm/Yb = 1.7 – 2.9), and more/less incompatible ratios. In plots of Ba/Y vs. Zr/Nb, the Younger Series show considerable variation in Zr/Nb (6.1 – 14.9), but a very limited range in Ba/Y (3.3 – 9.3). Similarly, Ba/Yb shows a exceptionally limited range (38 – 118). There is little to no Eu-anomaly (Eu/Eu* = 0.98 – 1.07) in the Younger Series.

Grouping by Sample Locality

Drill Core Samples

The primitive mantle normalized trace element patterns for the drill core suite of lavas display the greatest range of diversity of all the locality groups (Figures 10 and 11). With few exceptions, the drill core lavas are less enriched in incompatible trace elements than the Older Series breccia and massif lavas, though sample B18-1 has the most enriched abundances for almost all elements. Apart from B18-1, drill core lavas have positive Ba and Sr peaks, and relative depletions in U and Pb. These lavas also display relative enrichments over both primitive mantle and sample B18-1. As discussed above, samples B1-2, B6-1, and B6-2 show severe Ba and Pb enrichments, sample B2-1 displays an extreme Pb enrichment, and samples B12-1 and 19-1 show strong Sr enrichments. Chondrite normalized rare earth element patterns show similar HREE abundances (Yb = 1.4 – 2.1 ppm) with variable LREE abundances (La = 7.3 – 27.1 ppm) producing variable degrees of enrichment and crossing rare earth patterns (La/Yb = 3.8 – 12.8). These lavas have all maintained a Eu/Eu* greater than unity (1.00 – 1.07).

Cone Samples

Samples from the Intermediate and Younger Series post-erosional cones have relatively low primitive mantle normalized trace element patterns with a more limited range than seen in the drill core lavas. Lavas have Pb and U depletions with small Ba and Sr peaks. Sample M20, an Intermediate Series cone, has a small Pb peak, but otherwise consistent with the remainder of the group. Chondrite normalized rare earth element patterns have relatively uniform HREE (Yb = 1.7 – 2.2 ppm) with a broader range of LREE (La = 7.3 – 17.9 ppm). These lavas have generally flat rare earth patterns (La/Yb = 4.3 – 10.5), with no Eu-anomaly (Eu/Eu* = 0.98 – 1.03).

Massif Samples

Outcrop samples from the remnant Older Series massif display relatively enriched primitive mantle normalized trace element patterns. Lavas show minor

Figure 10. Primitive mantle normalized spider diagram of trace element data for representative samples of Mauritius lavas categorized by sampling group (*i.e.*, massif, crater). Top panel—massif and breccia samples (Older Series). Middle panel—post-erosional eruptive craters. Bottom panel—drill core data. Primitive mantle of McDonough and Sun (1995).

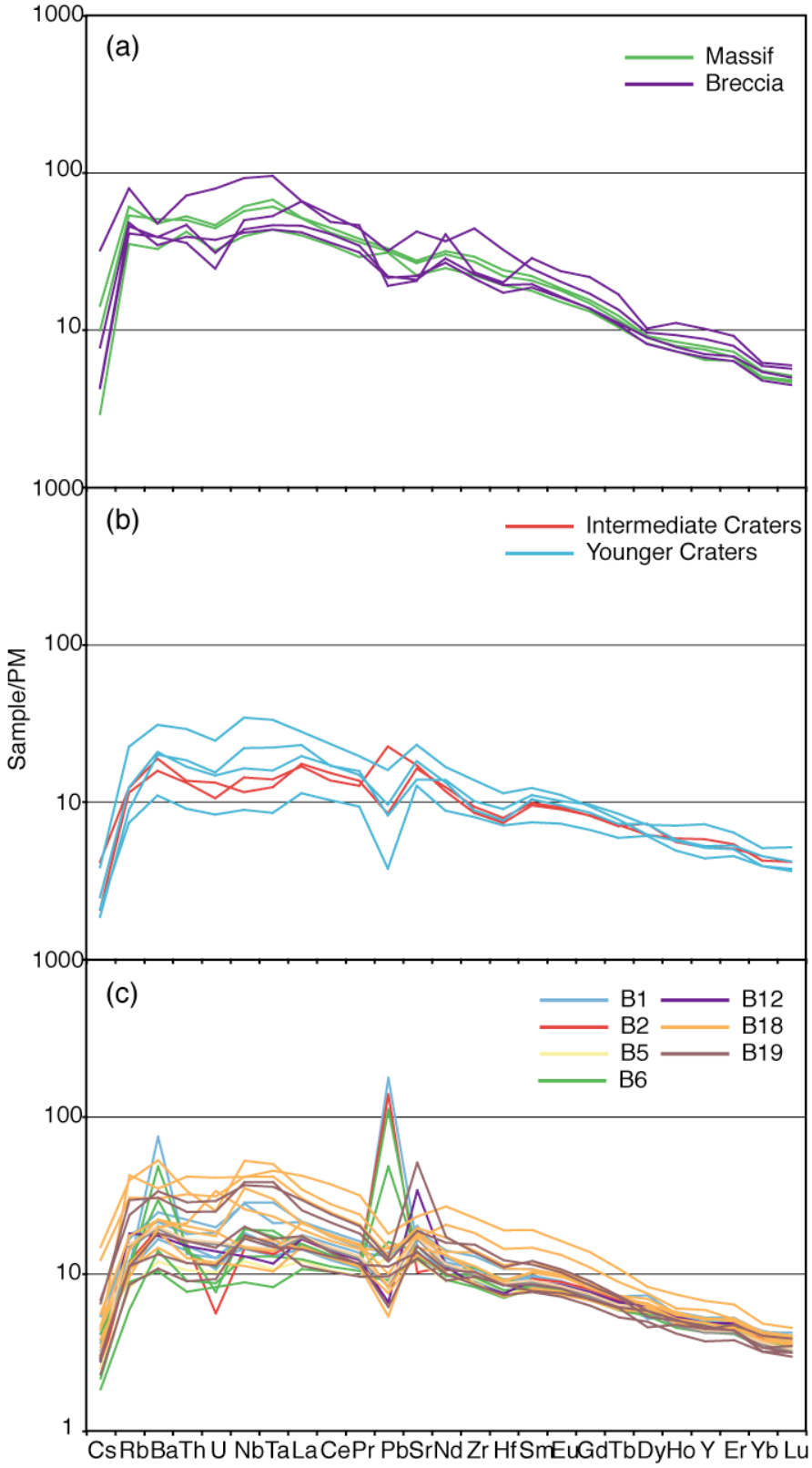
(a)
Massif
Breccia
(b)
Intermediate Craters
Younger Craters
(c)
B1
B2
B5
B6
B12
B18
B19
Sample/PM
1000
100
10
1
Cs Rb Ba Th U Nb Ta La Ce Pr Pb Sr Nd Zr Hf Sm Eu Gd Tb Dy Ho Y Er Yb Lu

Figure 11. Chondrite normalized rare earth element data for representative samples of Mauritius lavas categorized by sampling group (*i.e.*, massif, crater). Top panel—massif and breccia samples (Older Series). Middle panel—craters. Bottom panel—drill core data. Symbols after Figure 10. Chondrite of McDonough and Sun (1995).

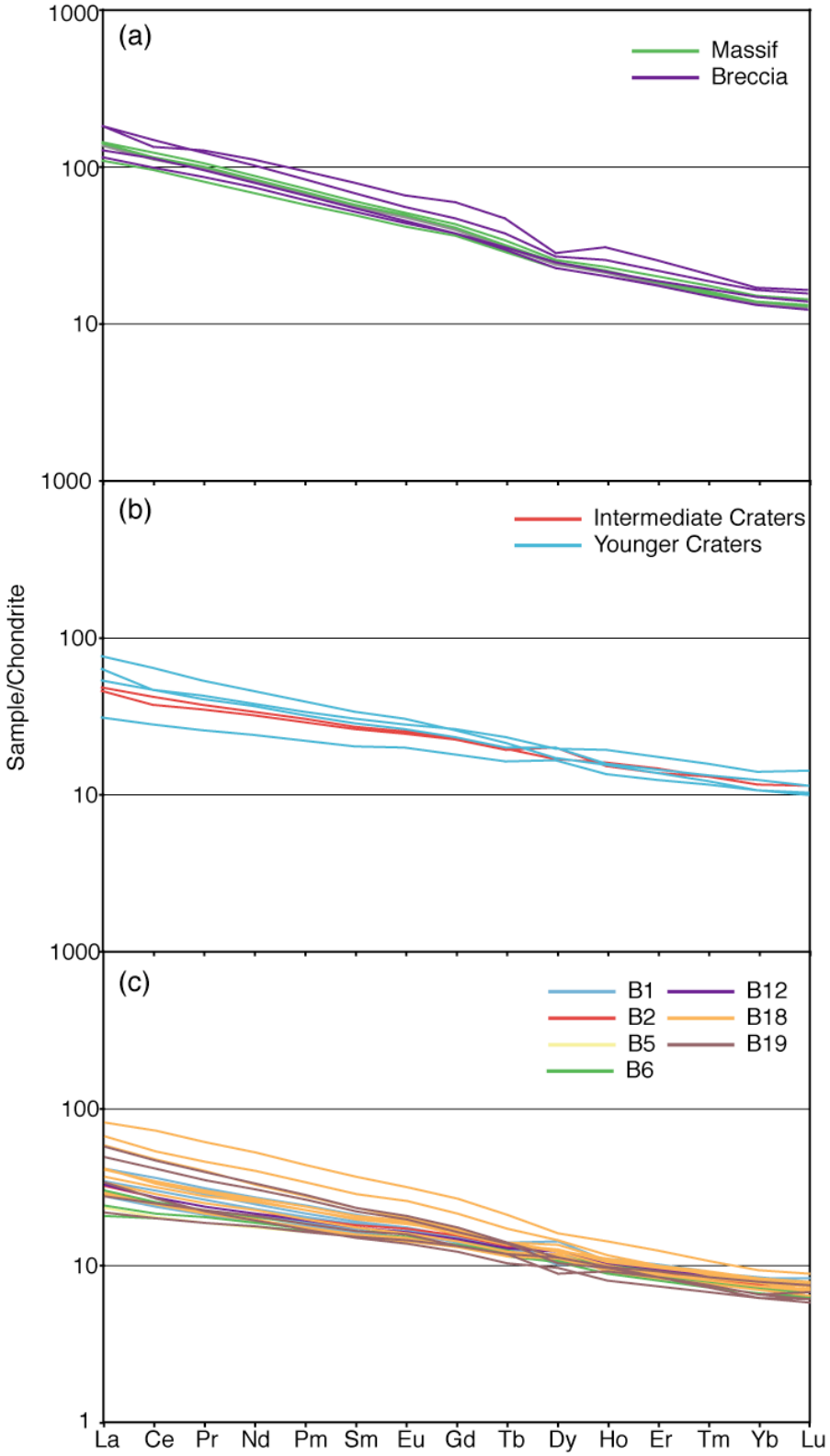
(a)
Massif
Breccia
(b)
Intermediate Craters
Younger Craters
(c)
B1
B2
B5
B6
B12
B18
B19
Sample/Chondrite
1000
100
10
1000
100
10
1000
100
10
1
La
Ce
Pr
Nd
Pm
Sm
Eu
Gd
Tb
Dy
Ho
Er
Tm
Yb
Lu

depletions in U and Sr, with no depletions in Ba or Pb. Any enrichment in Nd is negligible. Chondrite normalized rare earth element patterns have uniform enrichment of LREE (La = 25.6 – 33.1 ppm) over HREE (Yb = 2.2 to 2.4 ppm), producing relatively steep and parallel rare earth patterns (La/Yb = 11.8 – 15.1), with no Eu-anomaly (Eu/Eu* = 0.99 – 1.02).

Breccia Samples

The breccia samples have enriched primitive mantle normalized trace element patterns that are very similar to the massif samples. Lavas show depletions in the fluid mobile elements Ba, U, Pb, and Sr. Small enrichment peaks exist for Nd over primitive mantle, but are more subtle than those described in Nohda et al. (2005). Chondrite normalized rare earth element patterns have uniform enrichment of LREE (La = 26.7 – 42.2 ppm) over HREE (Yb = 2.1 to 2.7 ppm), though are slightly less diverse than the massif samples. Samples have relatively steep and parallel rare earth patterns (La/Yb = 11.4 – 16.4). Like the other Mauritian lavas, no Eu-anomaly exists (Eu/Eu* = 0.95 – 1.00).

Isotopic Composition

Similar to the trends observed through trace elements, the Older Series and post-erosional lavas form separate, but somewhat overlapping, fields in isotope space (Figure 12; *i.e.*, Mahoney et al., 1996; Sheth et al., 2003; Nohda et al., 2005; Paul et al., 2005). The Older Series lavas display the most radiogenic $^{87}Sr/^{86}Sr$ (0.70404 - 0.70433) and Pb isotopic compositions (18.89 - 19.08, 15.58 - 15.62, and 38.95 - 39.32; $^{206}Pb/^{204}Pb$, $^{207}Pb/^{204}Pb$, and $^{208}Pb/^{204}Pb$, respectively) with the lowest ε_{Nd}[2]

[2] $\varepsilon_{Nd} = \left[\frac{^{143}Nd/^{144}Nd)_{sample}}{^{143}Nd/^{144}Nd)_{CHUR}} - 1 \right] * 10^4$, where CHUR (*CH*ondritic *U*niform *R*eservoir) is the age corrected isotope composition for chondrite; $^{143}Nd/^{144}Nd)_{CHUR(0)} = 0.512638$.

Figure 12. Strontium, Nd, and Pb isotopic data for samples from Mauritius. Symbols after Figure 6. The Older Series lavas are enriched in each isotopic system relative to the post-erosional lavas. No overlap occurs between the shield and post-erosional lavas in $^{87}Sr/^{86}Sr$, with little in Pb-isotope space. Though the Intermediate and Younger Series were found to be statistically equivalent in $^{87}Sr/^{86}Sr$, ε_{Nd}, and $^{207}Pb/^{204}Pb$, they were found to be distinct in $^{206}Pb/^{204}Pb$ and $^{208}Pb/^{204}Pb$ (Table 10). Sr- and Nd-isotope data were measured at Cornell University. Pb-isotopes were measured at Max-Planck-Institut für Chemie (MPI) in Mainz, Germany. The detailed analytical methodology can be found in Chapter 2.

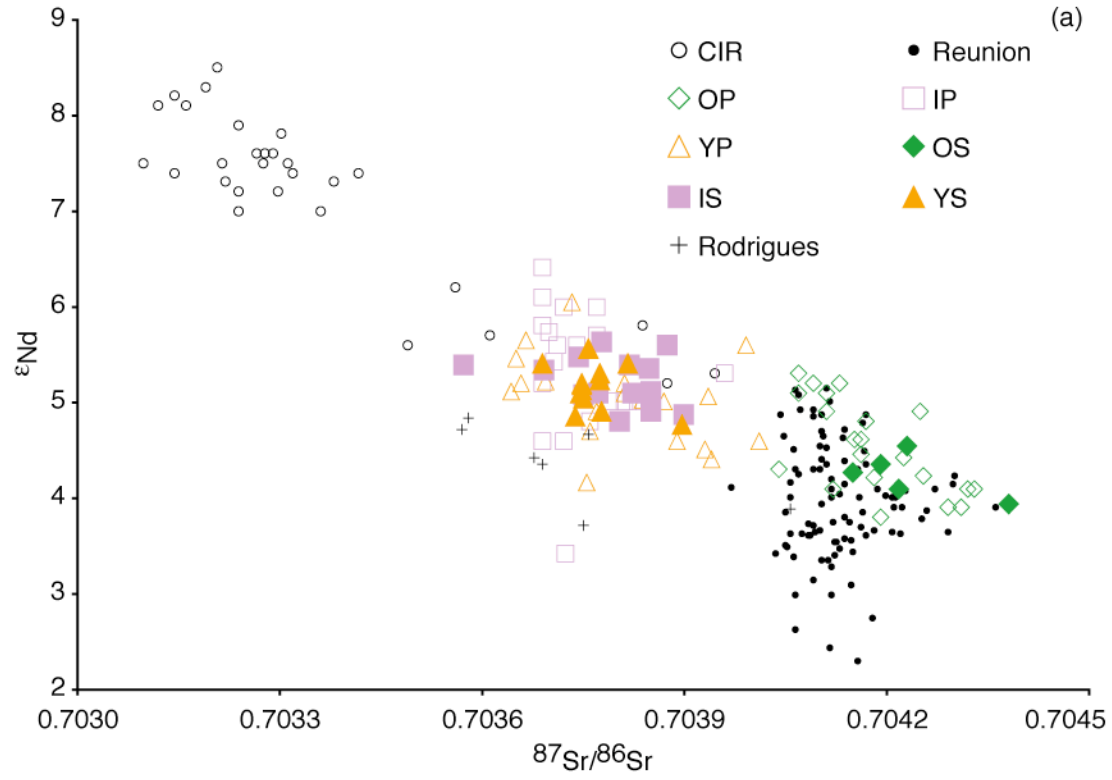
(a)
CIR
Reunion
OP
IP
YP
OS
IS
YS
Rodrigues
εNd
9
8
7
6
5
4
3
2
0.7030
0.7033
0.7036
0.7039
0.7042
0.7045
87Sr/86Sr

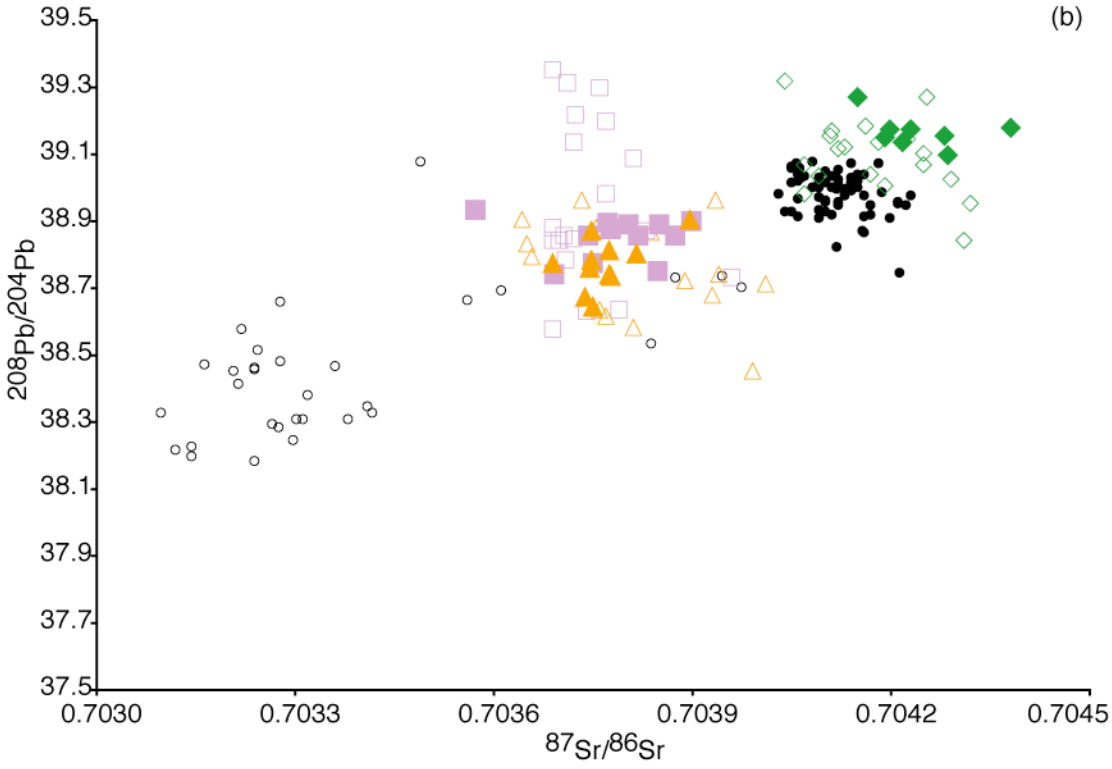
(b)
208Pb/204Pb
39.5
39.3
39.1
38.9
38.7
38.5
38.3
38.1
37.9
37.7
37.5
0.7030
0.7033
0.7036
0.7039
0.7042
0.7045
87Sr/86Sr

Figure 12 (*continued*)

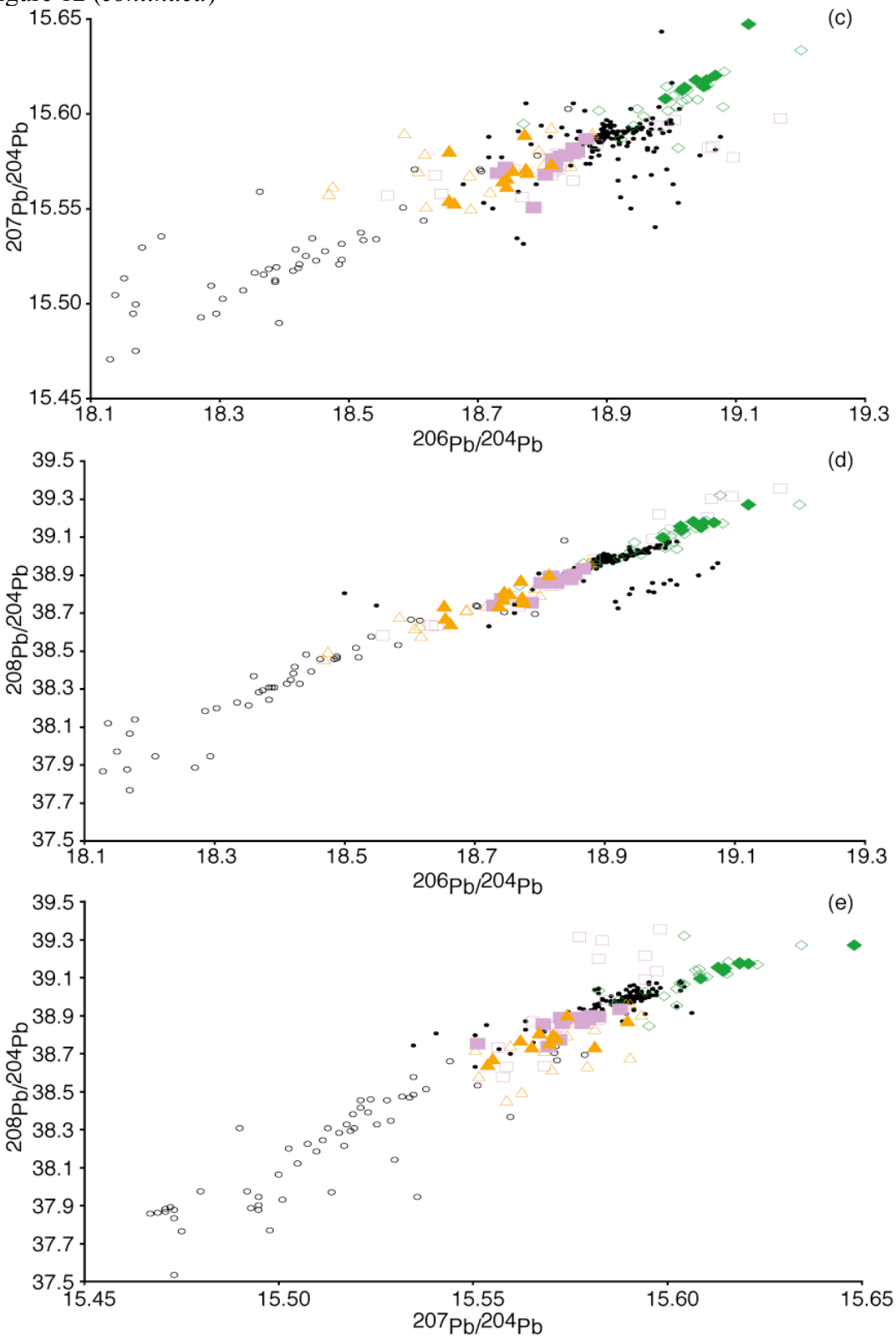

(+3.8 to +5.3) and ε_{Hf}[3] (+8.0 to +10.8) values. Intermediate Series lavas are the most isotopically variable of the lavas, overlapping both the Older and Younger Series in most instances. In particular, Intermediate Series Pb isotopic compositions span almost the entire observed range of Mauritian lavas (18.56 - 19.17, 15.56 - 15.60, 38.58 - 39.35; $^{206}Pb/^{204}Pb$, $^{207}Pb/^{204}Pb$, and $^{208}Pb/^{204}Pb$, respectively). ε_{Nd} (+4.6 to +6.4) and ε_{Hf} (+10.0 to +11.4) values are on average, slightly higher than lavas of the Older and Younger Series, while $^{87}Sr/^{86}Sr$ (0.70369 - 0.70396) are less than and distinct from the Older Series, contained wholly within the Younger Series. Younger Series lavas show the least radiogenic $^{87}Sr/^{86}Sr$ (0.70364 - 0.70401) and Pb isotopic compositions (18.47 - 18.97, 15.55 - 15.59, 38.45 - 38.96; $^{206}Pb/^{204}Pb$, $^{207}Pb/^{204}Pb$, and $^{208}Pb/^{204}Pb$, respectively) with relatively high ε_{Nd} (+4.2 to +6.0) and ε_{Hf} (+9.3 to +11.0) values, greater than the Older Series. It should be emphasized that while the three Mauritian lava series are relatively homogeneous, and thus overlap considerably in ε_{Nd} and all Pb isotopic spaces, the Older Series ($^{87}Sr/^{86}Sr \geq 0.70404$) is everywhere distinct from the Intermediate and Younger Series ($^{87}Sr/^{86}Sr \leq 0.70401$) in the published literature.

Thirty-nine new Sr and Nd and thirty-three new Pb isotopic compositions are presented here for Mauritian lavas collected in 2007 (Table 4). Samples fall under the same classification guidelines as described in the major element section. Overall, the results presented here are consistent with published results (*e.g.*, Sheth et al., 2003; see above), though extend the range of several fields.

Grouping by Series

---

[3] $\varepsilon_{Hf} = \left[\frac{^{176}Hf/^{177}Hf)_{sample}}{^{176}Hf/^{177}Hf)_{CHUR}} - 1 \right] * 10^4$, where CHUR is the same as in ε_{Nd}; $^{176}Hf/^{177}Hf)_{CHUR(0)} = 0.282772$.

Table 4. Strontium, Nd, and Pb isotope ratio errors are 2 standard errors of the mean based on in-run statistics. Standard error is given as (s/√n)/mean, where n is the number of measurements and s is the standard deviation. Errors should be read as the last digit, for example, the Nd isotope ratio for M12 should be read as 0.512840 ± 0.000013. ε_{Nd} is a fractional deviation, in units of parts per 10,000, from the present day chondritic bulk Earth ratio, which is taken as 0.512638 for Nd and 0.70450 for Sr. Errors of standards are given as 2 standard deviations of analytical runs. Accepted values Pb results from Galer and Abouchami (1998; G & A) are given for comparison.

	$^{87}Sr/^{86}Sr$			ε_{Sr}	$^{143}Nd/^{144}Nd$			ε_{Nd}
Older Series								
B18-1	0.70422	±	1	- 4.0	0.512848	±	8	+ 4.09
M6	0.70420	±	1	- 4.3	--			--
M12	0.70438	±	1	- 1.7	0.512840	±	13	+ 3.94
M30	0.70415	±	1	- 5.0	0.512857	±	10	+ 4.27
M35	0.70423	±	1	- 3.8	0.512870	±	13	+ 4.53
M36	0.70429	±	1	- 3.1	--			--
M37	0.70428	±	1	- 3.1	--			--
M39	0.70419	±	1	- 4.4	0.512861	±	10	+ 4.35
Intermediate Series								
B2-1	--				--			--
B5-1	--				--			--
B6-1	0.70385	±	1	- 9.2	0.512912	±	11	+ 5.34
B6-2	0.70387	±	1	- 8.9	0.512925	±	15	+ 5.60
B12-1	--				--			--
B18-2	0.70357	±	2	- 13.2	0.512914	±	8	+ 5.39
B18-3	0.70385	±	1	- 9.2	0.512900	±	9	+ 5.11
B18-4	0.70390	±	1	- 8.5	0.512888	±	16	+ 4.87
B18-5	0.70374	±	1	- 10.8	0.512918	±	12	+ 5.47
B18-6	0.70385	±	1	- 9.2	0.512889	±	12	+ 4.90
B18-7	0.70369	±	1	- 11.5	0.512911	±	10	+ 5.33
B18-8	0.70380	±	1	- 9.9	0.512884	±	9	+ 4.80
B19-1	0.70378	±	1	- 10.3	0.512926	±	10	+ 5.62
B19-2	0.70382	±	1	- 9.6	0.512899	±	12	+ 5.09
B19-3	0.70382	±	1	- 9.7	0.512914	±	9	+ 5.39
M15	0.70375	±	1	- 10.6	0.512898	±	9	+ 5.07
M20	0.70377	±	1	- 10.3	0.512899	±	12	+ 5.09
Younger Series								
B1-1	0.70376	±	1	- 10.5	0.512923	±	13	+ 5.57
B1-2	0.70382	±	1	- 9.7	0.512915	±	11	+ 5.41
B1-3	0.70375	±	1	- 10.7	0.512904	±	13	+ 5.18
B1-4	0.70375	±	1	- 10.7	0.512901	±	8	+ 5.12
B1-5	0.70390	±	1	- 8.6	0.512882	±	8	+ 4.76
B6-3	0.70375	±	1	- 10.7	0.512899	±	12	+ 5.09
B6-4	0.70378	±	1	- 10.3	0.512889	±	15	+ 4.90
B18-9	0.70369	±	2	- 11.5	0.512915	±	13	+ 5.40
B19-4	0.70375	±	1	- 10.7	0.512896	±	11	+ 5.04
B19-5	0.70377	±	1	- 10.3	0.512906	±	9	+ 5.23
M17	0.70374	±	1	- 10.8	0.512887	±	13	+ 4.85
M22	0.70377	±	1	- 10.3	0.512910	±	12	+ 5.31
M29	0.70375	±	1	- 10.7	0.512905	±	13	+ 5.20
M33	0.70374	±	1	- 10.8	--			--
NBS 987	0.71025	±	1	$n = 47$				
Ames Nd					0.512131	±	6	$n = 13$

Table 4. *(continued)*

	$^{206}Pb/^{204}Pb$		$^{207}Pb/^{204}Pb$		$^{208}Pb/^{204}Pb$	
Older Series						
B18-1	19.0199	± 63	15.6152	± 78	39.1338	± 260
M6	19.0532	± 67	15.6195	± 82	39.1730	± 273
M12	19.0374	± 45	15.6192	± 55	39.1765	± 182
M30	19.1205	± 63	15.6491	± 63	39.2682	± 186
M35	19.0678	± 43	15.6218	± 53	39.1747	± 178
M36	18.9896	± 69	15.6094	± 72	39.0961	± 219
M37	19.0163	± 47	15.6137	± 51	39.1518	± 160
M39	19.0494	± 48	15.6156	± 57	39.1495	± 187
Intermediate Series						
B2-1	18.9374	± 78	15.5812	± 88	38.9479	± 288
B5-1	18.8474	± 54	15.5804	± 62	38.8772	± 198
B6-1	18.7864	± 113	15.5515	± 105	38.7515	± 303
B6-2	18.8273	± 67	15.5785	± 81	38.8581	± 270
B12-1	--		--		--	
B18-2	18.8683	± 85	15.5883	± 104	38.9323	± 347
B18-3	--		--		--	
B18-4	18.8538	± 73	15.5810	± 76	38.9007	± 236
B18-5	18.8034	± 51	15.5687	± 63	38.8556	± 209
B18-6	18.8193	± 64	15.5731	± 78	38.8887	± 261
B18-7	18.7302	± 179	15.5699	± 153	38.7381	± 422
B18-8	18.8167	± 65	15.5772	± 81	38.8883	± 271
B19-1	18.8367	± 69	15.5791	± 77	38.8744	± 250
B19-2	--		--		--	
B19-3	18.8169	± 65	15.5734	± 80	38.8572	± 267
M15	18.7430	± 54	15.5727	± 66	38.7719	± 218
M20	18.8486	± 52	15.5829	± 63	38.8954	± 209
Younger Series						
B1-1	--		--		--	
B1-2	18.7548	± 50	15.5712	± 60	38.8031	± 199
B1-3	--		--		--	
B1-4	18.7745	± 95	15.5723	± 96	38.7828	± 286
B1-5	18.8144	± 40	15.5747	± 49	38.9015	± 160
B6-3	18.7758	± 79	15.5703	± 82	38.7583	± 244
B6-4	18.7381	± 49	15.5656	± 59	38.7367	± 195
B18-9	18.7438	± 57	15.5626	± 70	38.7726	± 232
B19-4	18.6641	± 111	15.5541	± 133	38.6434	± 415
B19-5	18.6544	± 119	15.5818	± 124	38.7382	± 378
M17	18.6559	± 77	15.5555	± 74	38.6736	± 225
M22	18.7455	± 45	15.5675	± 51	38.8123	± 160
M29	18.7726	± 46	15.5904	± 57	38.8720	± 189
M33	--		--		--	
NBS 981	16.9436	± 26	15.5016	± 30	36.7316	± 85
G & A	16.9405	± 15	15.4963	± 16	36.7219	± 44

When grouped strictly by eruptive unit, rather than sampling locality, distinct trends emerge from the Sr, Nd and Pb isotopic composition data. The Older Series lavas have the most radiogenic Pb and Sr isotopic compositions and the lowest ε_{Nd} values of all Mauritian lavas ($^{87}Sr/^{86}Sr$ = 0.70419 – 0.70438; ε_{Nd} = +3.94 to +4.53; $^{206}Pb/^{204}Pb$ = 18.9896 – 19.0678; $^{207}Pb/^{204}Pb$ = 15.6094 – 15.6218; $^{208}Pb/^{204}Pb$ = 39.0961 – 39.1765). These lavas span a relatively limited range of compositions, and are distinct from the Intermediate and Younger Series in most isotopic projections. As presented in this work, the Older Series is composed of breccia and massif samples, and a single drill core sample, B18-1. Sample M30, from Motte A Therese, has the most radiogenic Pb isotopic compositions, the least radiogenic $^{87}Sr/^{86}Sr$ and the lowest ε_{Nd} value of all the Older Series lavas, though still falls within the range of published Older Series values.

The Intermediate Series has less enriched isotopic compositions than the Older Series ($^{87}Sr/^{86}Sr$ = 0.70357 – 0.70390; ε_{Nd} = +4.80 to +5.62; $^{206}Pb/^{204}Pb$ = 18.7302 – 18.8683; $^{207}Pb/^{204}Pb$ = 15.5515 – 15.5883; $^{208}Pb/^{204}Pb$ = 38.7381 – 38.9323). The Intermediate Series displays the broadest range among the three series, though it is somewhat more limited here than in other works (*e.g.*, *Paul et al. 2005*) where the series spans nearly the entire extent of all Mauritian lavas. When viewed against depth, an inconsistent picture emerges for the Intermediate Series. Pb isotopic compositions appear to increase with increasing depth (age), with the strongest trend being in $^{206}Pb/^{204}Pb$. However, the bulk of this trend hinges on a single sample, B2-1, which is the deepest and most radiogenic Intermediate Series sample in $^{206}Pb/^{204}Pb$ and $^{208}Pb/^{204}Pb$. Sr isotopic compositions show a slight increase with increasing depth, with the exception of sample B18-2, the least radiogenic Intermediate Series sample ($^{87}Sr/^{86}Sr$ = 0.70357), but also one of the deepest (178 m depth) and presumably earliest. No trends with depth are apparent for ε_{Nd}.

The Younger Series lavas are also less enriched than the Older Series, and overlap almost completely with the Intermediate lavas ($^{87}Sr/^{86}Sr$ = 0.70369 – 0.70390; ε_{Nd} = +4.76 to +5.57; $^{206}Pb/^{204}Pb$ = 18.6544 – 18.8144; $^{207}Pb/^{204}Pb$ = 15.5541 – 15.5904; $^{208}Pb/^{204}Pb$ = 38.6434 – 38.9015). Relative to the Intermediate Series, the Younger Series has slightly elevated $^{207}Pb/^{204}Pb$ values, most evident versus $^{208}Pb/^{204}Pb$. The Younger Series show significant scatter in Pb and Nd isotope spaces, but show almost no variation in Sr isotopic composition. Sampled lavas of the Younger Series are limited to the upper 20 meters of the drill cores and show no apparent variation in any isotopic composition with depth.

Grouping by Sample Locality

Drill Core Samples

Strontium and Nd isotopic compositions for the measured drill core samples show variation with depth of core, particularly within individual cores. While a weak increase toward more radiogenic values with increasing depth is observed, which may be attributed more to a change from Intermediate to Older Series lavas, see below, there is little systematic diversity across the core suite as a whole. With the exception of samples B18-1 and B18-2, all samples fall within the published range for Sr and Nd isotopic compositions ($^{87}Sr/^{86}Sr$ = 0.70369 to 0.70390; ε_{Nd} = +4.76 to +5.62) and are consistent with published values from post-erosional lavas. Sample B18-2 ($^{87}Sr/^{86}Sr$ = 0.70357; ε_{Nd} = +5.39) has the least radiogenic $^{87}Sr/^{86}Sr$ published for Mauritius, and is consistent with the post-erosional lavas as well. Sample B18-1 ($^{87}Sr/^{86}Sr$ = 0.70422; ε_{Nd} = +4.09) has the most radiogenic $^{87}Sr/^{86}Sr$ and lowest ε_{Nd} of all the drill core samples, and represents the only drill core sample to plot within the literature-defined range of the Older Series.

Results of the isotopic composition depth profiles for Pb are similar to those observed from Sr and Nd, though the trend toward increased radiogenic ratios with

depth appears to be somewhat stronger. As with Sr and Nd, all drill core samples overlap with Intermediate and Younger Series lavas ($^{206}Pb/^{204}Pb$ = 18.6544 - 18.9374; $^{207}Pb/^{204}Pb$ = 15.5515 – 15.5883; $^{208}Pb/^{204}Pb$ = 38.6434 – 38.9479), with the exception of a single point. Sample B18-1 ($^{206}Pb/^{204}Pb$ = 19.0199; $^{207}Pb/^{204}Pb$ = 15.6152; $^{208}Pb/^{204}Pb$ = 39.1338) plots has the most radiogenic Pb isotopic composition and is the only drill core sample to plot within the Older Series field. This sample also has the most radiogenic $^{87}Sr/^{86}Sr$ and the lowest ε_{Nd} value. Samples from drill core B19 define most of the variability within the drill core suite, particularly at the unradiogenic end of the Pb isotopic compositions. From the combined major and trace element results, it is important to consider the effects of low-temperature alteration on samples, particularly those at depth.

Cone Samples

Samples from the post-erosional cones show a remarkable degree of homogeneity both within and between lava suites. Strontium isotopic compositions of the Intermediate Series span an incredibly narrow range ($^{87}Sr/^{86}Sr$ = 0.70375 – 0.70377) and are essentially identical to the Younger Series lavas ($^{87}Sr/^{86}Sr$ = 0.70374 - 0.70377). Likewise, the Intermediate Series (ε_{Nd} = +5.07 to +5.09) and Younger Series (ε_{Nd} = +4.85 to +5.31) lavas are indistinguishable by Nd isotopic composition, within error. These results fall squarely within the published range of Sr isotopic compositions and ε_{Nd} values for post-erosional lavas.

Lead isotopic compositions for the post-erosional cones do not show the same homogeneity observed in Sr and Nd isotopes, but span almost the entire range of values seen from all other samples ($^{206}Pb/^{204}Pb$ = 18.6544 – 18.8486; $^{207}Pb/^{204}Pb$ = 15.5555 – 15.5904; $^{208}Pb/^{204}Pb$ = 38.6736 – 38.8954), excluding B18-1. Individually, the samples from Younger Series cones form, on average, the more radiogenic end of the suite, while the Intermediate Series cone samples form the unradiogenic end.

Despite their range, the post-erosional cones as a whole overlap exclusively with the published range of Intermediate and Younger Series lavas values.

Massif Samples

Outcrop samples taken from the eroded massif show the same radiogenic $^{87}Sr/^{86}Sr$ (0.70415 - 0.70438) and low-ε_{Nd} signatures (+3.94 to +4.27) present in published Older Series samples. These results are consistent with an Older Series origin for these samples, as would be expected from their sampling localities. Sample M12, from Tamarin Mountain, has the most radiogenic Sr isotopic composition ($^{87}Sr/^{86}Sr = 0.70438$) of any published Mauritius sample and extends the range of the Older Series field.

The outcrop samples have the most radiogenic Pb isotopic compositions among the samples presented here. Like Sr and Nd, these values ($^{206}Pb/^{204}Pb$ = 19.0374 – 19.1205; $^{207}Pb/^{204}Pb$ = 15.6192 – 15.6491; $^{208}Pb/^{204}Pb$ = 39.1730 – 39.2682) are consistent with an Older Series origin. Sample M30, Motte Á Therese, is the most radiogenic of these samples, but still resides within the field defined by Older Series lavas.

Breccia Samples

Strontium and Nd isotopic compositions for the breccia samples show radiogenic $^{87}Sr/^{86}Sr$ (0.70419 – 0.70429) and low ε_{Nd} values (+4.35 to +4.53). These values, particularly the enriched Sr isotopic composition, are similar to those of known Older Series samples. Sample M36 and its leachate, see Methodology, have identical Sr isotopic compositions ($^{87}Sr/^{86}Sr = 0.704285$ and 0.704265, respectively) within error.

The breccia samples span a relatively restricted range of Pb isotopic compositions ($^{206}Pb/^{204}Pb$ = 18.9896 – 19.0678; $^{207}Pb/^{204}Pb$ = 15.6094 – 15.6218; $^{208}Pb/^{204}Pb$ = 39.0961 – 39.1747), residing within the larger Older Series field. They

overlap with the other radiogenic samples presented here, furthering the case for an unaltered Older Series origin.

K-Ar Age Analysis

The first radiometric ages for Mauritius were published by McDougall and Chamalaun (1969) and delineated the volcanic products into three suites. These results originally established an eruptive period for the shield Older Series lavas of 7.8 – 6.8 Ma, followed by the eruption of more fractionated lavas about 5.5 Ma. The Intermediate Series eruptions followed intermittently from 3.5 – 2.0 Ma, and then the Younger Series from 0.7 to 0.17 Ma. This work confirmed the earlier classifications of Simpson (1950) and positively identified the major eruptive hiatuses between the lava suites. Nohda et al. (2005) conducted further dating, also finding three series of distinct ages. They identified the Older Series lavas as erupting from 6.5 – 5.4 Ma, the Intermediate Series from 3.0 – 1.9 Ma, and the Younger Series as 0.78 – 0.07 Ma. All results were consistent with the previously identified periods, though extending the fields by small amounts. Duncan (unpublished data) dated a small subset of Younger Series lavas from the original collection of Baxter, finding ages from 1.00 to 0.00 Ma, which further extends the duration of the suite.

Eight whole rock samples (two Older Series, three Intermediate Series, and three Younger Series) from Mauritius were dated by ^{40}Ar-^{39}Ar methods (Table 5). The Older Series samples consisted of one core sample, B18-1, and one breccia, M37. Sample B18-1 is the deepest core sample (220 m) and at 8.41 ± 0.08 Ma is the oldest dated basaltic sample from Mauritius. This sample age is determined from total fusion, rather than being a plateau ages like the remainder of the samples. The breccia, M37, is stratigraphically the lowest surficial sample and dates to 8.00 ± 0.07 Ma.

Table 5. ^{40}Ar-^{39}Ar radiometric ages for Mauritius samples

Sample	Total Fusion Age (Ma)	2σ	Plateau Age (Ma)	2σ	*n*	MSWD	Isochron Age (Ma)	2σ	$^{40}Ar/^{36}Ar$ Initial	2σ	*J*
Older Series											
B18-1	**8.41**	0.08	--	--	--	--	--	--	--	--	0.0027507
M37	7.88	0.18	**8.00**	0.07	8/10	0.55	8.00	0.07	295.3	2.4	0.0026437
Intermediate Series											
B6-1	2.43	0.48	**2.07**	0.19	8/9	0.21	2.12	0.25	294.8	2.1	0.0027238
B18-2	3.06	0.15	**2.55**	0.06	8/9	0.18	2.55	0.07	295.6	1.9	0.0025934
B19-1	2.44	0.23	**2.04**	0.12	7/8	0.36	2.07	0.18	294.8	2.7	0.0027733
Younger Series											
B1-5	0.668	0.256	**0.627**	0.117	7/7	0.10	0.614	0.185	295.7	2.4	0.0026187
B18-9	0.666	0.015	**0.671**	0.041	8/8	0.03	0.674	0.048	295.1	3.1	0.0027002
M29	0.202	0.138	**0.192**	0.079	7/7	0.56	0.169	0.090	297.4	6.8	0.0026763

Ages calculated using FCT-3 (28.04 Ma) and the total decay constant λ = 5.530E10/yr. *n* is the number of heating steps (defiring plateau/total); MSWD is an F statistic that compares the variance within step ages with the variance about the plateau age. *J* combines the neutron fluence with the monitor age. Bold values are the reported age for each sample.

The three lavas of the Intermediate Series fall within the published field for the suite. Sample B18-2 is the second deepest sample in its core (178 mbs) and dates to 2.55 ± 0.06 Ma. This represents a stratigraphic separation of 5.86 My between samples B18-1 and B18-2. Sample B6-1 dates to 2.07 Ma ± 0.19 Ma. The final Intermediate Series sample, B19-1, is dated to 2.04 ± 0.12 Ma. This sample is the uppermost sample in core B19.

The Younger Series samples do not extend the range of the published field. Sample B1-5 is the deepest sample in core B1 (152 mbs) and dates to 0.627 ± 0.117 Ma. Based on its depth, this sample was originally identified as Intermediate Series, but has been reclassified along with the four samples stratigraphically above it. Sample B18-9 is the stratigraphically highest sample in its core, dating to 0.671 ± 0.041 Ma. The last Younger Series sample, M29, is from a small, young looking vent near Nouvelle Decouverte. This sample dates to 0.192 ± 0.079 Ma, somewhat older than expected.

The seven samples provided by R. Duncan from the collection of A.N. Baxter date between 0.00 and 1.00 Ma and are all of Younger Series age (Table 6).

Isotopic Composition of Samples from Paul et al. (2007)

Here we present the results of isotopic composition measurements performed on select samples from Paul et al. (2007) measured at both the Max-Planck-Institut für Chemie and Cornell University (Table 7). Eleven Sr, twelve Nd and Hf, and nine Pb isotopic compositions were measured at MPI, and nine Sr and Nd isotopic compositions were measured at Cornell. The distinctions developed by these authors are included in the table, but are not discussed here. Samples broadly fall into two groups: those with radiogenic Sr and Pb isotopic ratios, and those with unradiogenic ratios. These groups overlap with the Older Series and post-erosional lavas,

Table 6. ^{40}Ar-^{39}Ar radiometric ages for Mauritius samples from Duncan

Sample	Age (Ma)	Series
C2	0.29	Younger
C18	0.13	Younger
C46	0.32	Younger
C62	0.32	Younger
C76	1.00	Younger
C78	0.00	Younger
C82	0.73	Younger

Radiometric ages from Mauritius samples provided by Duncan *(unpublished)* Samples are originally from the collection of A.N. Baxter. Methods are similar to those described in Table 6 and the Methodology section.

Table 7. Strontium, Nd, Hf, and Pb isotopic compositions for Mauritius samples presented in Paul et al. (2007). Sample numbers preceded by 'MBP' indicate those samples taken from drill cores, those with 'MP' are from surficial outcrops. Cornell Measurements were conducted by JCM. Samples prepared and analyzed at Cornell University in the same manner as presented in the Methodology section. Mainz samples were prepared and analyzed at the Max-Planck-Institut für Chemie (MPI) in Mainz. Strontium isotopic compositions were corrected for mass fractionation using $^{86}Sr/^{88}Sr = 0.1194$. NIST SRM-987 and La Jolla Nd were used as Sr and Nd standards, respectively, and Sr standard measurements were normalized to 0.710240. Strontium, Nd, and Pb isotope ratio errors are 2 standard errors of the mean based on in-run statistics. Standard error is given as $(s/\sqrt{n})/mean$, where n is the number of measurements and s is the standard deviation. Errors should be read as the last digit. [a]Duplicate analysis of Mainz measurement at Cornell. [b]Average of 2 analyses. [c]Average of 3 analyses.

	$^{87}Sr/^{86}Sr$	$^{143}Nd/^{144}Nd$	ε_{Nd}	$^{176}Hf/^{177}Hf$	ε_{Hf}	$^{206}Pb/^{204}Pb$	$^{207}Pb/^{204}Pb$	$^{208}Pb/^{204}Pb$
Cornell Measurements								
Older Series (Group 1)								
MBP5	0.70372 ± 1	0.512903 ± 12	+ 5.17					
MBP18	0.70386 ± 1	0.512886 ± 10	+ 4.84					
MBP19b[a]	0.70376 ± 1	0.512891 ± 10	+ 4.94					
MBP21	0.70383 ± 1	0.512883 ± 14	+ 4.77					
MBP31b	0.70389 ± 1	0.512893 ± 10	+ 4.98					
Older Differentiated Series (Group 2)								
MP29	0.70415 ± 1	0.512874 ± 14	+ 4.61					
MP42	0.70416 ± 1	0.512866 ± 12	+ 4.45					
Intermediate Series								
MBP6	0.70377 ± 1	0.512900 ± 12	+ 5.11					
Younger Series								
MBP16a[a]	0.70369 ± 1	0.512902 ± 10	+ 5.14					
Mainz Measurements								
Older Series (Group 1)								
MBP-2	0.70371[b]			0.283065	+ 10.46	18.7552	15.5718	38.7852
MBP-16b				0.283057	+ 10.20			
MBP-19b	0.70376[b]		+ 5.38	0.283076	+ 10.86	18.8606	15.5785	38.8939
MBP-25b	0.70366		+ 5.77	0.283085	+ 11.19			
MBP-26b	0.70374		+ 5.45	0.283081	+ 11.03	18.7748	15.5697	38.7980
MBP-30b	0.70376[b]		+ 5.05	0.283086	+ 11.20	18.7638	15.5640	38.7873
Older Differentiated Series (Group 2)								
MP-9	0.70376[c]			0.283104	+ 11.86	18.8636[b]	15.5829[b]	38.9496[b]
MP-50	0.70416		+ 4.61	0.283066	+ 10.51	19.0557	15.6166	39.1812
MP-24	0.70424[c]		+ 4.23[b]	0.283057	+ 10.20	19.2027[b]	15.6365[b]	39.2781[b]
Intermediate Series								
MBP-9	0.70371		+ 5.42	0.283078	+ 10.91	18.8222	15.5801	38.8565
Younger Series								
MBP-13	0.70366		+ 5.65	0.283079	+ 10.95			
MBP-16a	0.70366		+ 5.19	0.283054	+ 10.08	18.8019	15.5748	38.7943

respectively. The four samples (MP-24, MP-29, MP-42, and MP-50) with enriched Sr and Pb isotopic compositions also have lower ε_{Nd} values ($^{87}Sr/^{86}Sr$ = 0.70415 – 0.70424; $^{206}Pb/^{204}Pb$ = 19.0557 – 19.2027; $^{207}Pb/^{204}Pb$ = 15.6166 – 15.6366; $^{208}Pb/^{204}Pb$ = 39.1812 – 39.2781; ε_{Nd} = +4.23 to +4.61) are each taken from the Older Series remnant massif. These samples also have, on average, the lowest ε_{Hf} of the two groups (+10.20 to +10.51). The fields defined by these samples fall squarely within those demarcated by the published data for the Older Series.

The samples that define the unradiogenic Sr and Pb group also have the most radiogenic Nd and Hf isotopic compositions values ($^{87}Sr/^{86}Sr$ = 0.70366 – 0.70389; $^{206}Pb/^{204}Pb$ = 18.7552 – 18.8636; $^{207}Pb/^{204}Pb$ = 15.5640 – 15.5829; $^{208}Pb/^{204}Pb$ = 38.7852 – 38.9496; ε_{Nd} = +4.77 to +5.77; ε_{Hf} = +10.08 to +11.86). These samples overlap with the literature-defined fields for the post-erosional Intermediate and Younger Series lavas. It is worth noting that each of the samples from this group are drill core samples, except for MP-9. This sample defines the most unradiogenic Sr ($^{87}Sr/^{86}Sr$ = 0.70376) and Pb ($^{206}Pb/^{204}Pb$ = 18.8636) compositions and the largest ε_{Hf} value (+ 11.86). While there may be some reason to question the proper classification, sample MP-9 represents the only Older Series sample to overlap with the Sr isotope compositions of the post-erosional lavas ($^{87}Sr/^{86}Sr < 0.7040$).

CHAPTER 4 – DISCUSSION OF ANALYTICAL RESULTS

Low-Temperature Alteration

The chemical effects of low-temperature alteration on ocean island basalt (OIB) lavas have been well documented (*e.g.*, Hofmann and White, 1982a), and will be considered here. Alteration of samples was best observed upon powdering as samples are mostly aphyric, with powder colors ranging from grey (relatively unaltered) to ferrous yellows and reds (more alteration). The presence of secondary growth phases (*e.g.*, calcite and pyrite) and alteration phases (*e.g.*, iddingsite or other clay minerals) was observed in field samples, but was principally limited to those samples taken from the drill cores. Olivine phenocrysts from some samples had visible yellowing and replacement by secondary phases. The presence of these secondary phases is not wholly unexpected as Mauritius has been located subtropically (20° S) throughout its existence and the drill core samples are taken from areas of high hydrologic activity. The cores were originally drilled as part of a study to investigate and characterize the hydrologic domains of Mauritus. Thickened zones of lateritic soil development were observed in the core sections, but care was taken to avoid sampling in these zones.

Chemical evidence for alteration of these lavas is somewhat limited and circumstantial. Some sampled lavas have high loss-on-ignition (LOI) values in major element analyses (> 6 wt. %)because of high H_2O contents in hydrous alteration-phases. There is little systematic variance of LOI with depth, though the Intermediate Series lavas, which compose the bulk of the drill core lavas, do show the most do tend to have the highest average values. Only Na_2O correlates with LOI (decreasing sodium with increasing LOI), and other major elements do not appear affected by alteration.

As discussed previously, the Sr isotopic composition for both breccia sample M36 and its leachate have nearly identical $^{87}Sr/^{86}Sr$ (0.704285 and 0.704265, respectively) within error, indicating a lack of contamination by seawater. Although the Sr isotope system provides no evidence of alteration, the Pb isotope compositions may be more sensitive to these effects. Intra-series scatter within the Pb system may be an indication of significant alteration (Galer, personal communication), as variations observed in this dataset are greater than those expected from the triple-spike method (Galer and Abouchami, 1998; Galer, 1999). Regardless, these isotopic signatures may still be primary as the results fall almost wholly within the established fields for each series, defined exclusively by surficial samples (*e.g.*, Paul et al., 2005). Pb blanks are considered negligible (< 40 pg) and are thus unlikely to be an important factor. There appears to be only nominal correlation between LOI and enrichment in the Pb or Sr isotopic systems ($R^2 < 0.2$ for the data set as a whole, less for most subsets).

In comparing those samples with strong trace element enrichments (Ba: B1-2, B6-1, B6-2; Pb: B1-2, B2-1, B6-1, B6-2, M20; Sr: B12-1, B19-1; U: B18-6) and depletions (U: B2-1, B6-2) to Sr and Pb isotopic compositions, I find very little evidence for enrichment through alteration. For example, sample B1-2 is enriched in Pb approximately 10 times above the other Younger Series lavas yet has a $^{206}Pb/^{204}Pb$ value (18.75) intermediate to its contemporary lavas. With the possible exception of sample B2-1, which has $^{206}Pb/^{204}Pb$ and $^{208}Pb/^{204}Pb$ (18.34 and 38.95, respectively) enriched above the other Intermediate Series lavas, there appears to be no direct association between enriched and/or depleted trace element signatures and isotopic enrichment. This is consistent with the above results from the leaching experiment and seemingly rules out contamination by drilling fluids. There appears to be neither systematic enrichment nor depletion of the fluid mobile elements across a wide area or

throughout a given sampling locality, nor consistent divergence of elements within individual samples. From these results I can conclude that the trace element concentration anomalies are a result of the redistribution of the fluid-mobile elements within the volcanic pile (*i.e.*, Mauritius Island), and not the result of the introduction of external material.

Filtering

In order to more clearly identify and investigate the plume source heterogeneity responsible for the generation of the Mauritius lava suites, I will here attempt to eliminate the effects of low-temperature alteration within the dataset. The task of excluding samples for alteration based on trace elements abundances is relatively subjective, requiring arbitrary determination of cutoffs. Here I use a number of trace element ratios, including the Ba/Rb ratio of Hofmann and White (1982a), to identify and eliminate samples with anomalous values indicative of alteration. Hofmann and White (1982a) demonstrated that modern OIB lavas always had Ba/Rb ratios near 11, and I utilize a cutoff scheme modified from White and Duncan (1996) that excludes all samples with Ba/Rb greater than 20 and less than 6. The arbitrary cutoff of 20 is relatively natural for the dataset, as a small break exists near the value. Values outside the accepted range are principally the anomalous samples discussed in the Results section. Apart from Ba/Rb, other trace element metric and cutoffs include Nb/U (> 55), Ce/Pb (< 10), and Sr/Nd (< 10, > 30). As major elements, isotope compositions, and primitive mantle normalized trace element diagrams do not demonstrate significant deviations outside of the fluid mobile elements, I will only exclude the anomalous elements from subsequent analysis and interpretation (Table 8).

Table 8. Trace element data excluded by spurious ratios and abundances

	Sr		Ba		Pb		U	
Ratio	Sr/Nd		Ba/Rb		Ce/Pb		Nb/U	
Exclusion	> 30		> 20		> 30		> 55	
Range	-		< 6		< 10		-	
			B1-2	(73.9)	B1-2	(0.8)		
					B2-1	(1.1)	B2-1	(84.1)
					B5-1	(9.1)		
			B6-1	(27.5)	B6-1	(2.9)	B6-1	(55.9)
			B6-2	(51.4)	B6-2	(1.3)	B6-2	(82.6)
			B6-4	(25.9)	B6-4	(7.8)		
	B12-1	(48.9)						
							B18-5	(67.4)
			B18-6	(23.0)				
							B18-8	(65.3)
	B19-1	(47.2)						
							B19-5	(61.3)
					M20	(6.8)		
			M29	(24.7)				
					M33	(30.4)		
							M39	(66.0)

Ba/Rb ratio taken from *Hofmann and White (1983)*, range modified from *White and Duncan (1996)*.

Discussion of Analytical Results

At first appearance, the strong geochemical differences between the shield stage Older Series and the post-erosional Intermediate and Younger Series are as striking as the similarity between the post-erosional suites. Although more primitive (*i.e.*, magnesian) Older Series samples were not identified in my analysis, the samples presented here form a low-MgO continuation of published trends (Figure 6). Fractionation trends are evident and dominate the major element Harker diagrams and plots of compatible trace elements, especially for the Older Series lavas. A strong correlation between decreasing CaO with decreasing MgO beginning at approximately 8 wt. % MgO is indicative of clinopyroxene fractionation. The effects of clinopyroxene fractionation in Older Series lavas are also evident from CaO/Al_2O_3 and Sc/Yb ratios, where a strong correlation between the two ratios results from the relative compatibility of CaO and Sc over Al_2O_3 and Yb in clinopyroxene (Figure 13). These signatures are not observed in the Intermediate and Younger Series lavas, which are less evolved and essentially uncorrelated (Baxter, 1976). A strong negative correlation between CaO/Al_2O_3 and FeO/MgO in the Older Series further corroborates the fractionation and removal of clinopyroxene. Nickel and Cr, two elements highly compatible in olivine, both decrease with decreasing MgO content in all three series, and have been highly influenced by the effects of fractionation of olivine (Baxter 1975; 1976).

Incompatible trace element systematics (*e.g.*, La, Nb, Ba) are broadly consistent across the three Mauritius lava suites (Figure 14). Older Series lavas have the highest abundances of incompatible elements. The more evolved Older Series lavas show increasing concentrations with decreasing MgO content, an effect of phenocryst fractionation, though overall abundances are controlled principally by extent of melting and source heterogeneity (Baxter, 1975). Similar processes control

Figure 13. Plot of Sc/Yb vs. CaO/Al_2O_3 for Mauritius lavas. Symbols after Figure 6. The presence of a trend in this plot is suggestive of clinopyroxene removal. Scandium and CaO are more compatible in clinopyroxene than are Yb and Al_2O_3, and are removed preferentially with clinopyroxene fractionation. A strong correlation is observed within the Older Series, while little to no trend is observed for the Intermediate and Younger Series lavas. This is somewhat at odds with the results from the PRIMELT2 algorithm (Herzberg and Asimow, 2008), which suggested extensive clinopyroxene fractionation and removal in all three Mauritian lava suites.

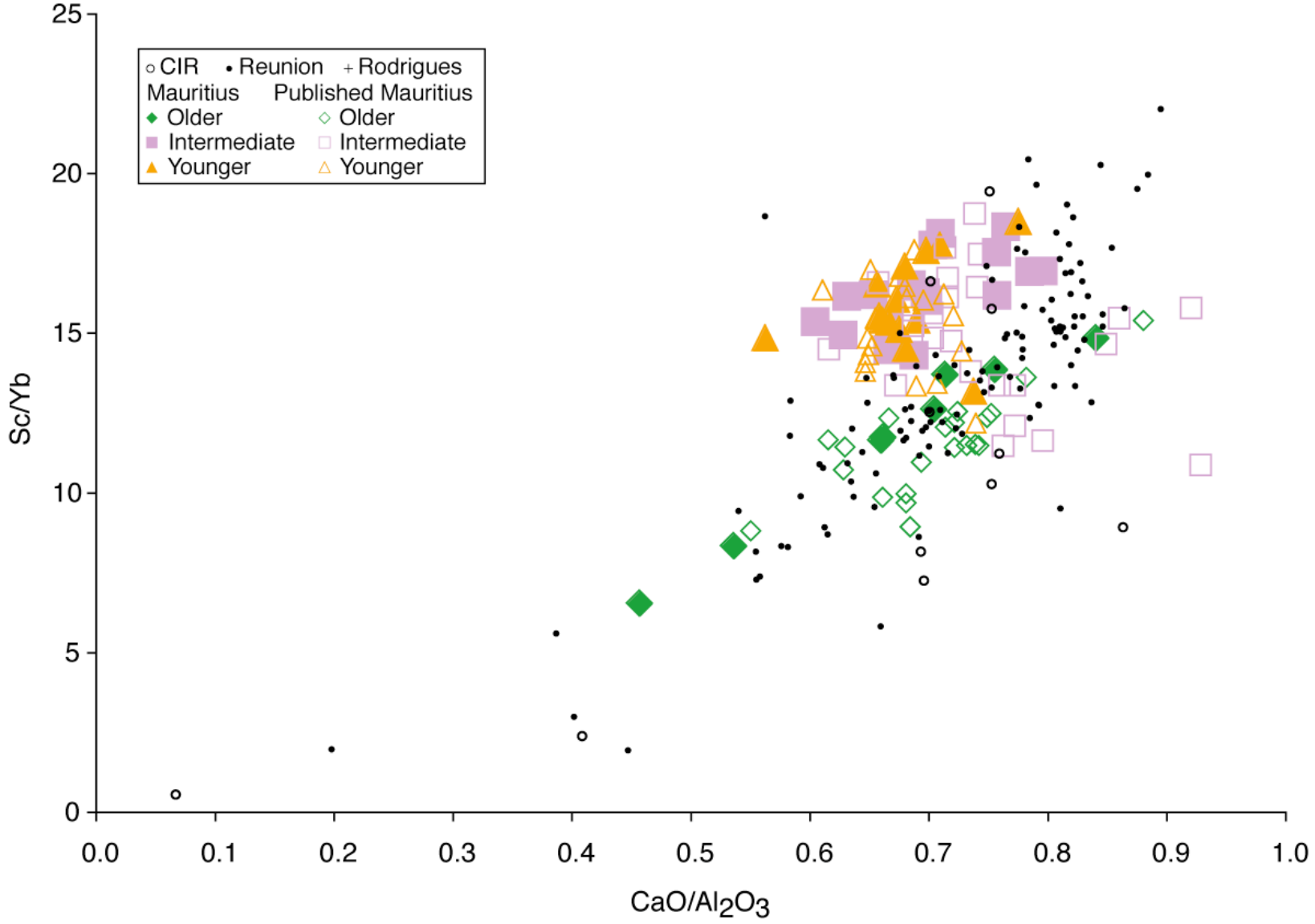
CIR
Reunion
Rodrigues
Mauritius
Older
Intermediate
Younger
Published Mauritius
Older
Intermediate
Younger
Sc/Yb
CaO/Al2O3
0
5
10
15
20
25
0.0
0.1
0.2
0.3
0.4
0.5
0.6
0.7
0.8
0.9
1.0

Figure 14. Incompatible trace element ratios plotted as a function of wt. % MgO. Symbols after Figure 6. Greater concentrations of incompatible elements are observed in the Older Series shield building lavas, relative to the post-erosional Intermediate and Younger Series.

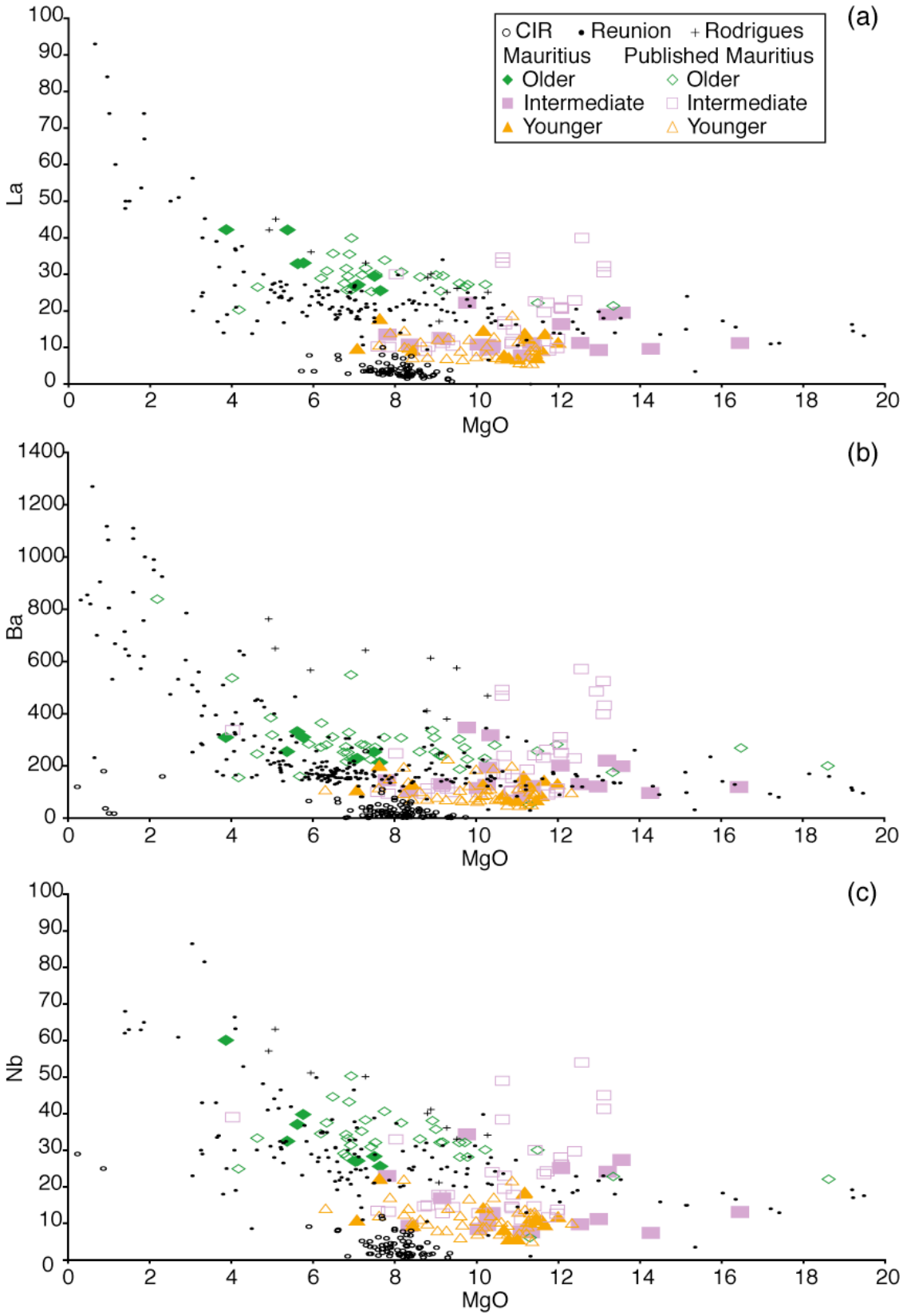
(a)
CIR
Reunion
Rodrigues
Mauritius
Published Mauritius
Older
Intermediate
Younger
Older
Intermediate
Younger
La
MgO
(b)
Ba
MgO
(c)
Nb
MgO

the concentrations of incompatible elements in the post-erosional lavas, which are essentially uncorrelated with MgO content.

The concentrations and ratios of trace elements in the Intermediate and Younger Series lavas are essentially identical. While the Intermediate Series may have, on average, greater concentrations of the most highly incompatible elements (*e.g.*, Cs, Th, Nb), and lower concentrations for the mildly incompatible elements (*e.g.*, Y, HREE), the absolute difference between the means are quite small. For most ratios of more-to-less incompatible elements the Older Series lavas have higher ratios than either of the post-erosional lavas. The steep rare earth patterns (La/Yb = 11.4 – 16.4; Sm/Yb = 3.2 – 4.3) of the Older Series suggest these magmas were produced within the garnet stability field (greater than about 60 km), consistent with being produced from an upwelling plume beneath an ~ 60 My old ocean lithosphere. The post-erosional lavas display more variable but generally shallower rare earth slopes (La/Yb = 3.8 – 12.8; Sm/Yb = 1.7 – 3.4), likely indicating the absence of garnet in their melting region.

In order to quantify the observed similarity between the post-erosional lavas, an analysis of variance (ANOVA) was performed for several key incompatible trace elements concentrations (Sr, Pb, La, Yb, Nb, Zr) and ratios (La/Sm, La/Yb, Sm/Yb, Zr/Nb, Ba/La, Ba/Rb, Ce/Pb). This analysis utilizes an F-test to evaluate whether the means of multiple populations are equal, assuming each population has the same standard deviation (Snedecor and Cochran, 1989). In an F-test, the null hypothesis assumes that the means are equal, while the alternative hypothesis assumes the null hypothesis is false (*i.e.*, the means are not equal). When the calculated F-value (test statistic) exceeds the critical F-value at a given significance level, the null hypothesis is rejected and the means of the populations are concluded to be not equal. A one-way ANOVA test was performed in MATLAB for each of the above trace element

concentrations and ratios at the 95% significance level ($\alpha = 0.05$), with trace element data from each post-erosional series forming the two populations of interest. The F-test failed to reject the null hypothesis for each of the chosen incompatible element concentrations and ratios, indicating the means of the lavas of the Intermediate and Younger Series are statistically equivalent (Table 9).

Apart from the established differences in absolute abundances, several small distinctions exist between the shield and post-erosional lavas. Primitive mantle normalized Older Series lavas do not show positive Ba anomalies $(Ba/Rb)_N$[4] = 0.60 – 0.95), whereas the post-erosional suites have a significant Ba peak $(Ba/Rb)_N$ = 0.97 – 1.68), even after filtering the data for potential effects of alteration. Similarly, Older Series lavas have primitive mantle normalized Nb/Ta ratios less than unity (0.91 – 0.97), while the post-erosional lavas are almost all greater than one $(Nb/Ta)_N$ = 0.93 – 1.33). Lastly, the post-erosional lavas have a small but consistent positive Sr anomaly $(Rb/Sr)_N$ = 0.43 – 2.36), which is not present in the Older Series lavas $(Rb/Sr)_N$ = 1.58 – 2.20).

The few exceptions to the systematic incompatible trace element enrichment of shield lavas over post-erosional lavas are principally restricted to two classes of ratios, those with fluid mobile elements in the numerator (*i.e.*, Ba/La), and those involving HFSE (*e.g.*, Nb/La, Nb/Zr). In ratios of the former (Figures 15 and 16), the differences are most obvious for Ba, wherein the Older Series no longer has the highest ratios of more-to-less incompatible elements. For Ba/La, this suite has the lowest ratios whereas for Ba/Yb the Older Series has ratios intermediate to the post-erosionals. Relative to La, strong trends are not observed for Ba/La in any of the lava suites, though the post-erosional lavas do show positive trends for Ba/Yb, with the

[4] Ratio normalized by the primitive mantle ratio of McDonough and Sun (1995).
Here, $\left(Ba/Rb\right)_N = \left(Ba/Rb\right)_{sample} / \left(Ba/Rb\right)_{primitive\ mantle}$

Table 9. Statistical analysis of trace element equality between representative trace element concentrations and ratios for the Intermediate and Younger Series lavas. A one-way ANOVA was performed at the 95% significance level ($\alpha = 0.05$), with trace element data from each post-erosional series forming the two populations of interest. The null hypothesis for each test assumed equality. When the calculated F-value (test statistic) exceeds the critical F-value at a given significance level, the null hypothesis is rejected and the means of the populations are concluded to be not equal. The F-test failed to reject the null hypothesis for each of the chosen incompatible element concentrations and ratios, indicating the means of the lavas of the Intermediate and Younger Series are statistically equivalent. *SS* – sums of squares. A measure of the variability attributable to variation either between or within groups. *df* – degrees of freedom. *MS* – Mean square. An estimate of the variance, *SS*/*df*. *F* – F-test statistic. *F-crit* – Critical F statistic. *P-value* – Probability the F statistic exceeds the critical F. The analysis shown here is for the data presented in this work, though the results are consistent for all the published data.

La

SUMMARY

Groups	*Count*	*Sum*	*Average*	*Variance*
IS	17	215.0	12.64	17.05
YS	14	155.6	11.12	11.44

ANOVA

Source of Variation	*SS*	*df*	*MS*	*F*	*P-value*	*F crit*
Between Groups	17.90	1	17.90	1.23	0.2762	4.18
Within Groups	421.47	29	14.53			
Total	439.37	30				

Yb

SUMMARY

Groups	*Count*	*Sum*	*Average*	*Variance*
IS	17	28.63	1.68	0.03
YS	14	25.29	1.81	0.03

ANOVA

Source of Variation	*SS*	*df*	*MS*	*F*	*P-value*	*F crit*
Between Groups	0.11	1	0.11	4.07	0.0529	4.18
Within Groups	0.82	29	0.03			
Total	0.93	30				

Zr

SUMMARY

Groups	*Count*	*Sum*	*Average*	*Variance*
IS	17	1953.4	114.9	940.8
YS	14	1485.6	106.1	278.5

ANOVA

Source of Variation	*SS*	*df*	*MS*	*F*	*P-value*	*F crit*
Between Groups	594.0	1	594.0	0.92	0.3448	4.18
Within Groups	18673.2	29	643.9			
Total	19267.2	30				

Table 9. *(continued)*

La/Yb

SUMMARY

Groups	*Count*	*Sum*	*Average*	*Variance*
IS	17	129.6	7.6	7.6
YS	14	86.2	6.2	3.3

ANOVA

Source of Variation	*SS*	*df*	*MS*	*F*	*P-value*	*F crit*
Between Groups	16.6	1	16.6	2.91	0.0988	4.18
Within Groups	165.5	29	5.7			
Total	182.1	30				

Zr/Nb

SUMMARY

Groups	*Count*	*Sum*	*Average*	*Variance*
IS	17	146.3	8.6	6.3
YS	14	135.6	9.7	7.1

ANOVA

Source of Variation	*SS*	*df*	*MS*	*F*	*P-value*	*F crit*
Between Groups	9.0	1	9.0	1.35	0.2552	4.18
Within Groups	193.3	29	6.7			
Total	202.3	30				

Ce/Pb

SUMMARY

Groups	*Count*	*Sum*	*Average*	*Variance*
IS	12	237.3	19.8	13.9
YS	11	190.7	17.3	20.0

ANOVA

Source of Variation	*SS*	*df*	*MS*	*F*	*P-value*	*F crit*
Between Groups	34.1	1	34.1	2.03	0.1686	4.32
Within Groups	352.8	21	16.8			
Total	386.9	22				

Figure 15. Incompatible trace element ratios plotted against La concentration. Symbols after Figure 6. On each plot, the Older Series form a distinct field from the post-erosional lavas. For a given La concentration, the Older Series ahs lower Ba/REE than the Intermediate and Younger Series lavas.

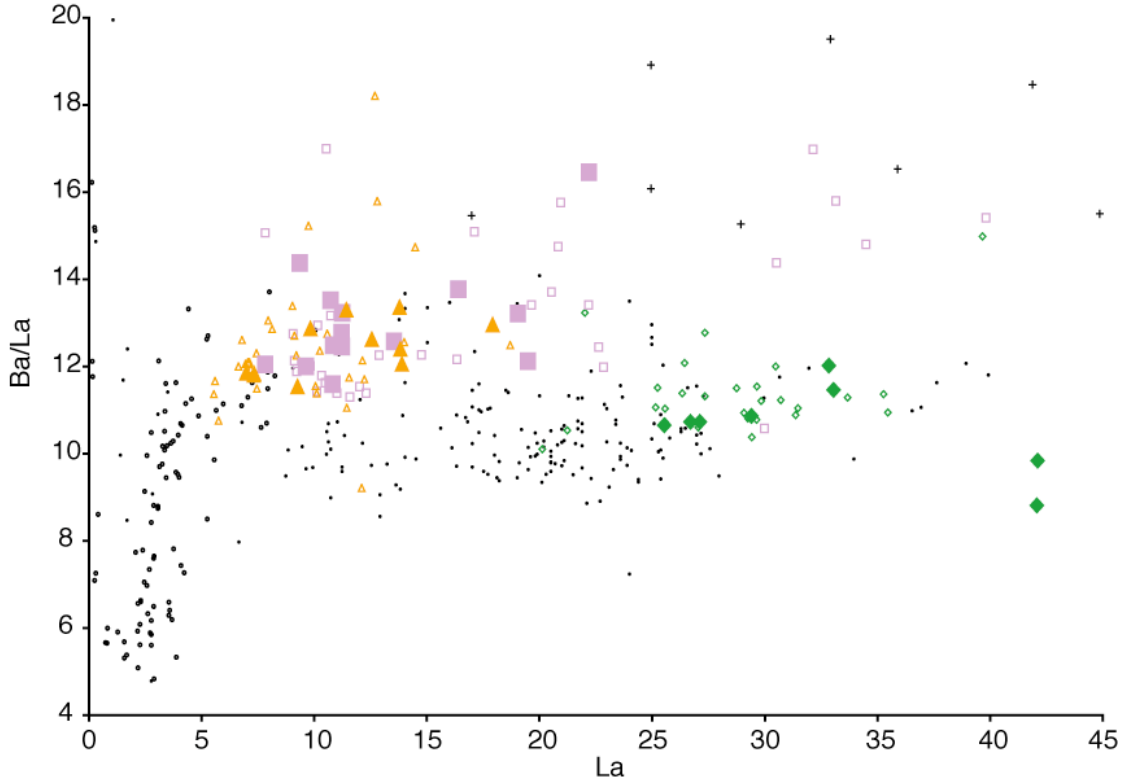
Ba/La
La
20
18
16
14
12
10
8
6
4
0
5
10
15
20
25
30
35
40
45

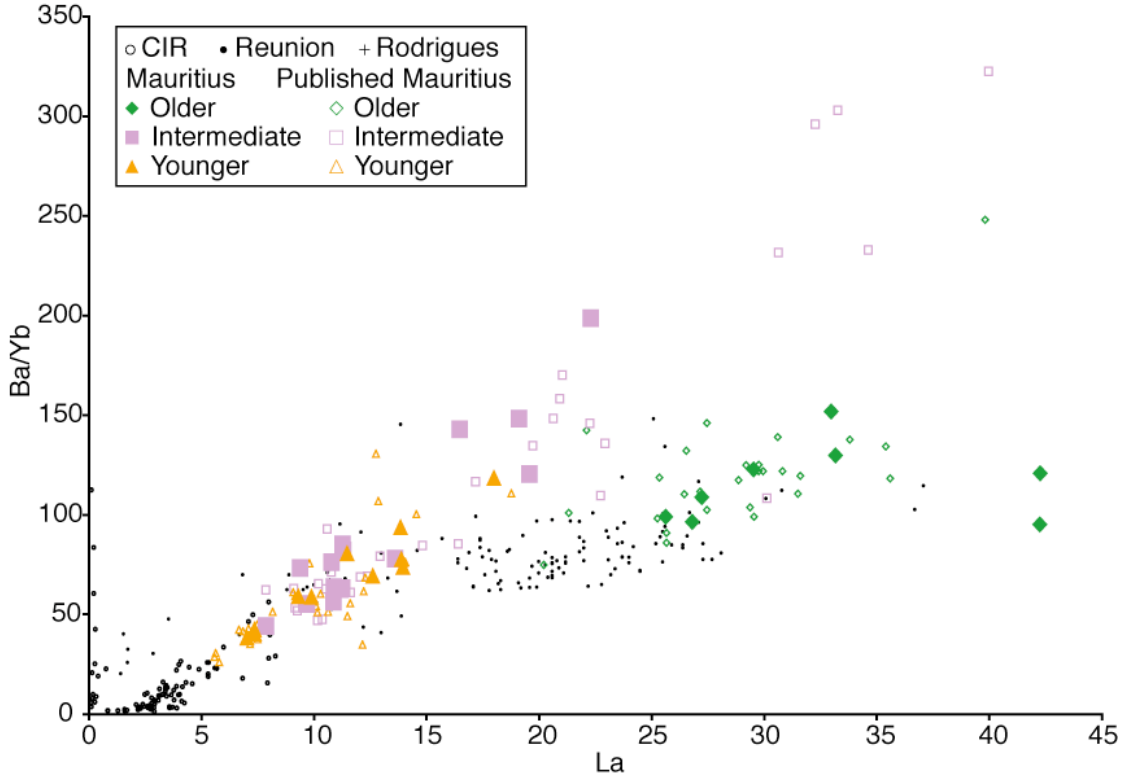
CIR
Reunion
Rodrigues
Mauritius
Older
Intermediate
Younger
Published Mauritius
Older
Intermediate
Younger
Ba/Yb
La
350
300
250
200
150
100
50
0
0
5
10
15
20
25
30
35
40
45

Figure 16. Incompatible trace element ratios of Ba to rare earth elements plotted against a ratio of high field strength elements. Symbols after Figure 6. In the top panel, the Older Series have a lower Ba/LREE ratio than the post-erosional lavas at a given Zr/Nb. In the bottom panel, the Older Series have a higher Ba/HREE ratio than the post-erosional lavas at a given Zr/Nb.

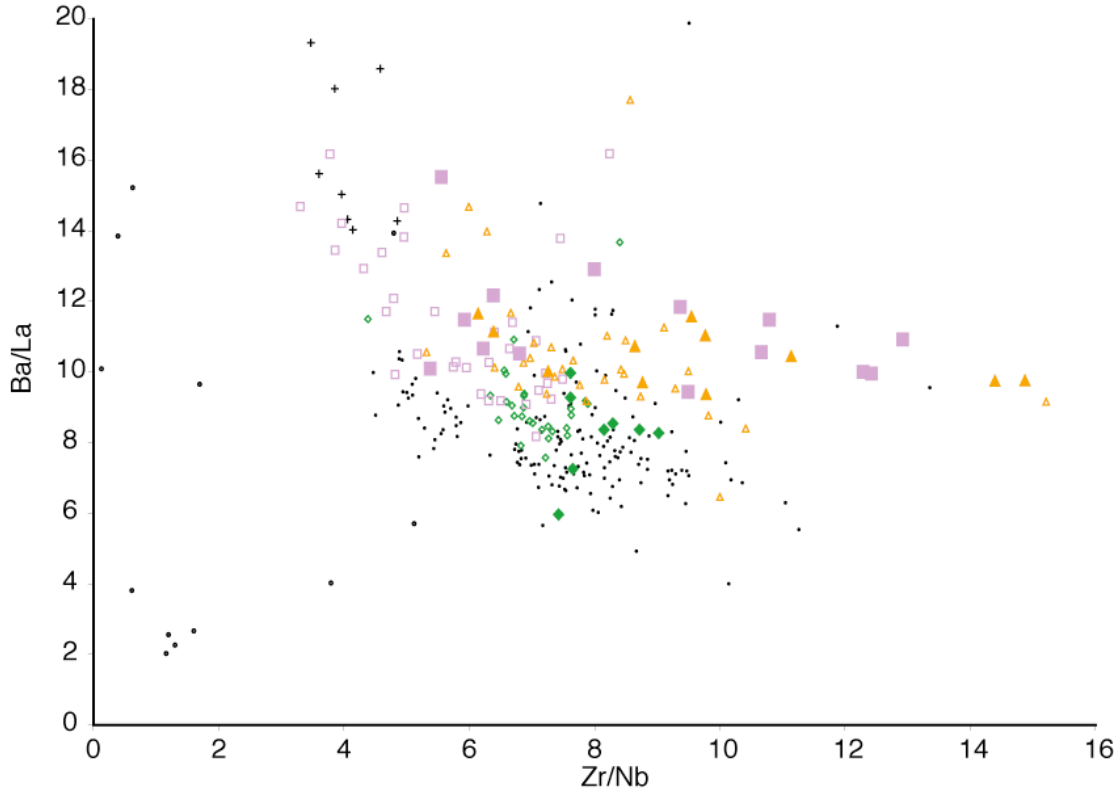
Ba/La
Zr/Nb
0
2
4
6
8
10
12
14
16
18
20

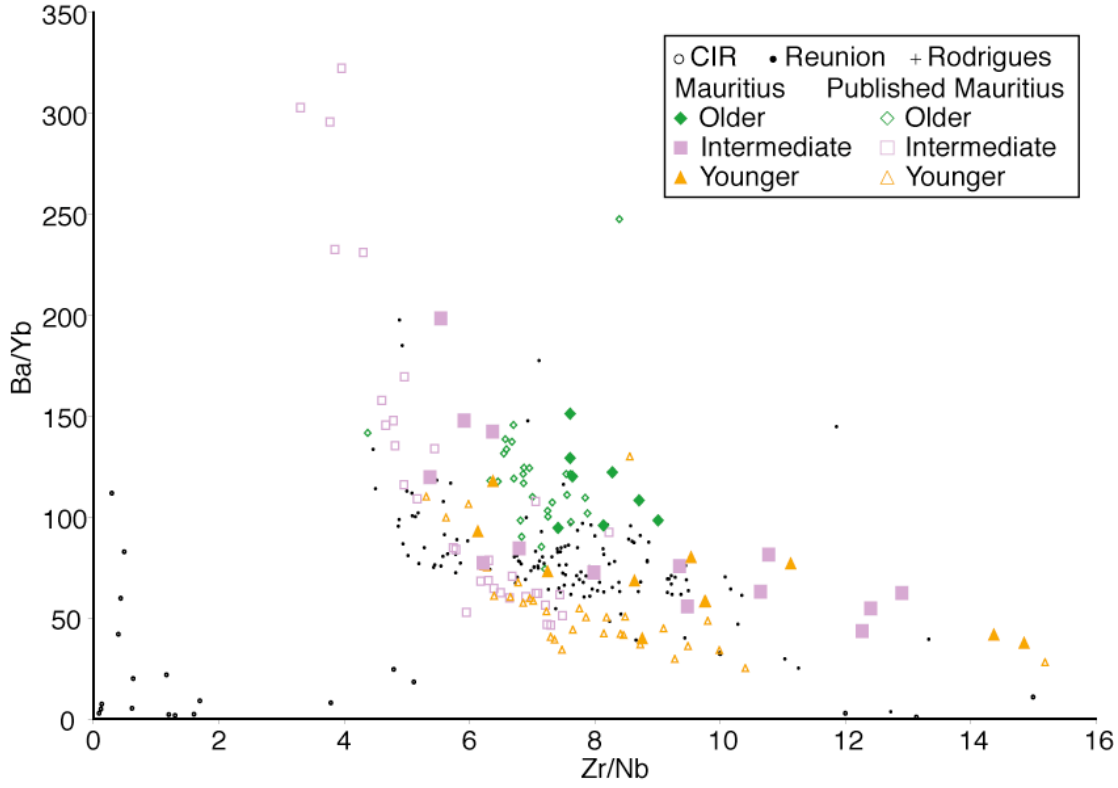
Ba/Yb
Zr/Nb
CIR
Reunion
Rodrigues
Mauritius
Older
Intermediate
Younger
Published Mauritius
Older
Intermediate
Younger
0
50
100
150
200
250
300
350

Older Series limited to a relatively small range (Ba/Yb = 95 – 152). Likewise, ratios involving the HFSE do not follow the incompatible element systematics described above. Relative to the post-erosional lavas, Older Series lavas have either the lowest or intermediate values for both ratios of one HFSE to another (Nb/Zr) and ratios of more-to-less incompatible elements where the HFSE is the more incompatible element (the numerator; Nb/La). However, where the HFSE is the less incompatible element (Th/Nb) the three suites are more consistent with the above systematics.

There exists a small subset of Intermediate (B18-2, B18-5, B19-1, B19-3) and Younger Series (M22) samples that appear to be offset from the bulk of the post-erosional samples, and have certain signatures that are characteristic of the Older Series lavas (Figures 17 and 18). This subset has higher K_2O, TiO_2, and P_2O_5, and is more magnesian. They also have somewhat lower SiO_2, CaO, and Na_2O. Alumina in these samples is lower than the bulk post-erosional lavas, but still higher than the projected Older Series trend at a given MgO. These lavas also have higher abundances of incompatible elements and generally higher ratios for more/less incompatible elements. These samples sometimes appear to plot along the high MgO continuation of trends defined by Older Series lavas (*e.g.*, La vs MgO), but often just have higher concentrations or ratios (high La/Yb at a given Zr/Nb). These samples have slightly enriched Pb isotope compositions and have higher ε_{Nd} relative to the other Intermediate Series lavas, but Sr compositions do not show these enrichment trends. The lavas have intermediate Sr compositions, and sample B18-2 has the least radiogenic composition on record. A limited number of Intermediate and Younger Series lavas from the published literature demonstrate similar characteristics to those discussed here. These unique lavas overlap with the high Ba/Y Intermediate Series samples that *Nohda et al. (2005)* argued are sourced from an EM-like domain, and are quite similar to those from Rodrigues.

Figure 17. Ratio of light rare earth-to-middle rare earth elements plotted against a ratio of middle rare earth-to-heavy rare earth elements. Symbols after Figure 6. Apart from a subset of Older Series-like post-erosional lavas, the Older Series lavas show LREE enrichment and HREE depletion relative to the Intermediate and Younger Series lavas.

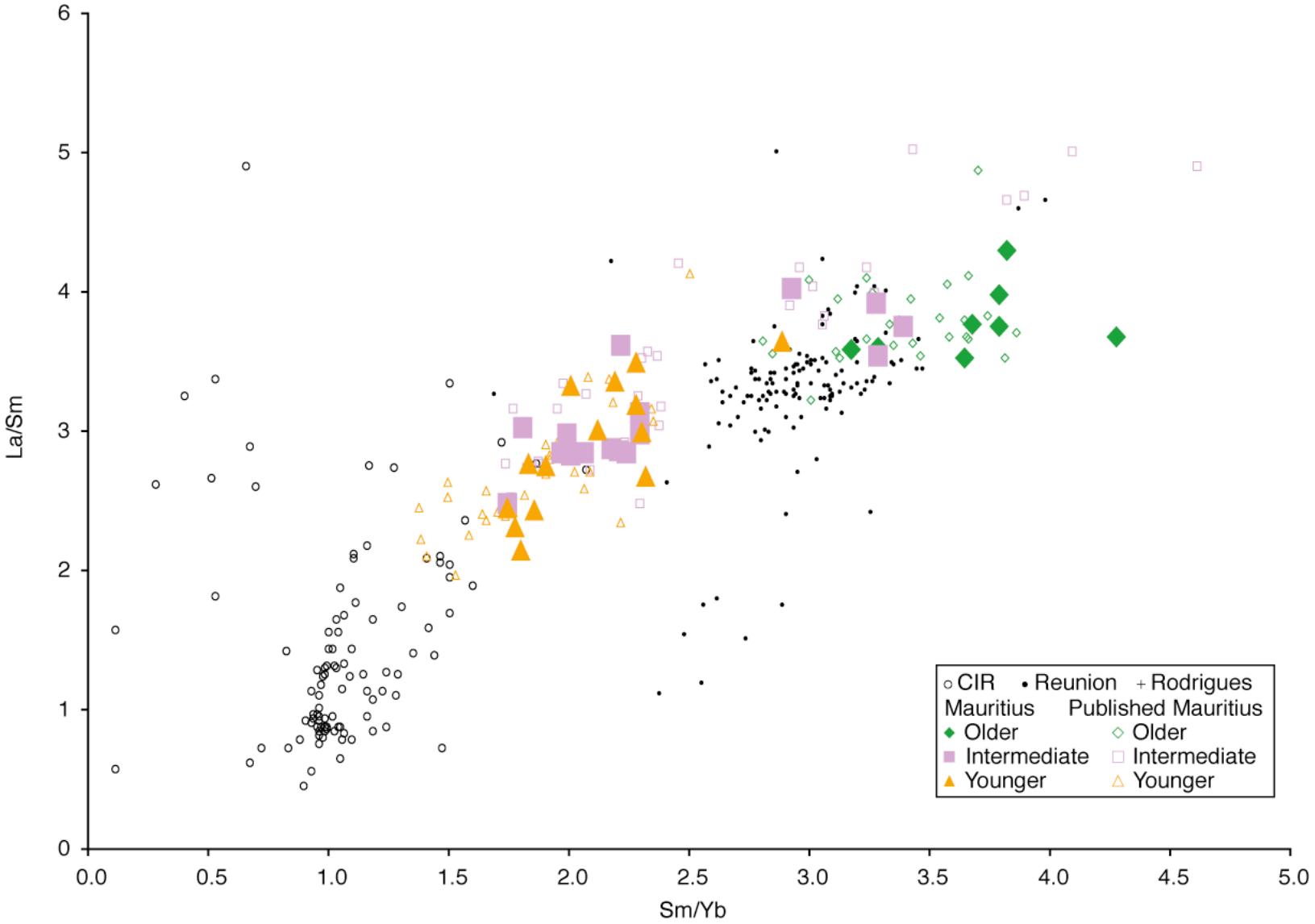
La/Sm
Sm/Yb
0
1
2
3
4
5
6
0.0
0.5
1.0
1.5
2.0
2.5
3.0
3.5
4.0
4.5
5.0
CIR
Reunion
Rodrigues
Mauritius
Published Mauritius
Older
Intermediate
Younger
Older
Intermediate
Younger

Figure 18. Ratio of light rare earth-to-heavy rare earth elements plotted against a LREE, La. Symbols after Figure 6. Apart from a subset of Older Series-like post-erosional lavas, the Older Series lavas have greater LREE/HREE ratios. This ratio is the measure of the steepness of the slope on a chondrite normalized rare earth element plot, and is an indicator of the presence of garnet during melting. Additionally, there is less variation in the Older Series data, typically a sign of larger, and more consistent, degrees of melting.

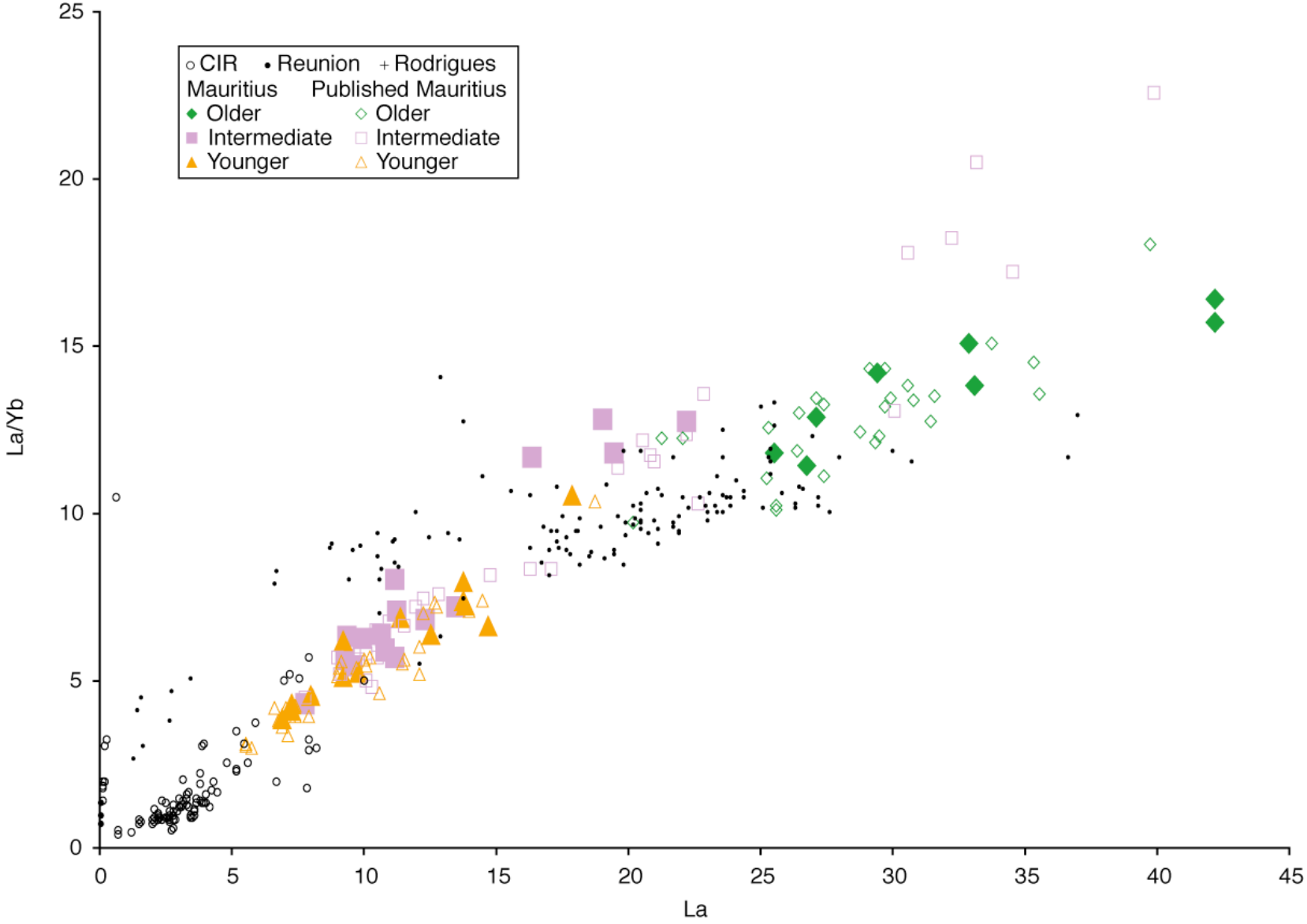
CIR
Reunion
Rodrigues
Mauritius
Older
Intermediate
Younger
Published Mauritius
Older
Intermediate
Younger
La/Yb
La
0
5
10
15
20
25
30
35
40
45

A statistical analysis (ANOVA) was also conducted to determine whether the means of the isotopic ratios of the Intermediate and Younger Series are equivalent. The same procedure was utilized for the isotope ratios as was used for the trace elements. The F-test failed to reject the null hypothesis for $^{87}Sr/^{86}Sr$, $^{143}Nd/^{144}Nd$, and $^{207}Pb/^{204}Pb$ (Table 10), indicating these ratios are statistically equivalent for the post-erosional lavas. The null hypothesis was rejected for $^{206}Pb/^{204}Pb$ and $^{208}Pb/^{204}Pb$, indicating the lavas of the Intermediate and Younger Series are not statistically equivalent for these ratios. Furthermore, the null hypothesis was rejected for both $^{207}Pb/^{206}Pb$ and $^{208}Pb/^{206}Pb$, indicating these ratios are not equivalent for the post-erosional lavas. Analyses of published post-erosional data from Mauritius produce consistent results. That the $^{207}Pb/^{204}Pb$ of the Intermediate and Younger Series are statistically equivalent while the $^{206}Pb/^{204}Pb$ and $^{208}Pb/^{204}Pb$ are not may be related to the limited range of $^{207}Pb/^{204}Pb$ in nature. This assertion may be supported by the extremely low variance of $^{207}Pb/^{204}Pb$ and the low null hypothesis probability for $^{207}Pb/^{206}Pb$ ($F = 17.3$ of 0.04%), $^{208}Pb/^{206}Pb$ ($F = 15.4$ of 0.07%), and $^{208}Pb/^{207}Pb$ ($F = 9.7$ of 0.05%), each of which indicate a strong difference between the post-erosional lavas for all Pb isotope ratios other than $^{207}Pb/^{204}Pb$.

Post-Erosional Comparison

In comparing post-erosional suites from well-studied worldwide occurrences, it is apparent that the post-erosional Intermediate and Younger Series lavas of Mauritius are somewhat distinct from the post-erosional lavas of Hawaii (*i.e.*, Honolulu Series of Oahu, Clague, 1982; Hana volcanics of Haleakala, East Maui, Chen and Frey, 1985; Kauai, Clague and Dalyrmple, 1988), Samoa (south Pacific; Palacz and Saunders, 1986; Wright and White, 1987), Madeira (eastern Atlantic; Geldmacher and Hoernle, 2000), and Tahaa (Society Islands, south Pacific; Brousse et al., 1986; White and

Table 10. Statistical analysis of isotopic composition equality for the Intermediate and Younger Series lavas. See Table 9 for explanation of symbols. The null hypothesis for each test assumed equality. For $^{206}Pb/^{204}Pb$ and $^{208}Pb/^{204}Pb$, the F statistic exceeds the F-crit, the null hypothesis is rejected, demonstrating that the two post-erosional series are distinct. $^{207}Pb/^{206}Pb$, $^{208}Pb/^{206}Pb$, and $^{208}Pb/^{207}Pb$ are also distinct. The analysis shown here is for the data presented in this work, though the results are consistent for all the published data.

$^{87}Sr/^{86}Sr$

SUMMARY

Groups	*Count*	*Sum*	*Average*	*Variance*
Intermediate Series	14	9.85307	0.70379	7E-09
Younger Series	14	9.85269	0.70376	2E-09

ANOVA

Source of Variation	*SS*	*df*	*MS*	*F*	*P-value*	*F crit*
Between Groups	5E-09	1	5E-09	1.08	0.3090	4.23
Within Groups	1E-07	26	5E-09			
Total	1E-07	27				

$^{143}Nd/^{144}Nd$

SUMMARY

Groups	*Count*	*Sum*	*Average*	*Variance*
Intermediate Series	14	7.180678	0.512906	2E-10
Younger Series	13	6.667731	0.512902	1E-10

ANOVA

Source of Variation	*SS*	*df*	*MS*	*F*	*P-value*	*F crit*
Between Groups	7E-11	1	7E-11	0.42	0.5245	4.24
Within Groups	4E-09	25	2E-10			
Total	4E-09	26				

Table 10. *(continued)*

$^{206}Pb/^{204}Pb$

SUMMARY

Groups	*Count*	*Sum*	*Average*	*Variance*
Intermediate Series	13	244.5980	18.8152	0.0017
Younger Series	11	206.0939	18.7358	0.0029

ANOVA

Source of Variation	*SS*	*df*	*MS*	*F*	*P-value*	*F crit*
Between Groups	0.0376	1	0.0376	*16.60*	0.0005	4.30
Within Groups	0.0498	22	0.0023			
Total	0.0874	23				

$^{207}Pb/^{204}Pb$

SUMMARY

Groups	*Count*	*Sum*	*Average*	*Variance*
Intermediate Series	13	202.4768	15.5751	0.0001
Younger Series	11	171.2660	15.5696	0.0001

ANOVA

Source of Variation	*SS*	*df*	*MS*	*F*	*P-value*	*F crit*
Between Groups	0.0002	1	0.0002	1.89	0.1825	4.30
Within Groups	0.0021	22	0.0001			
Total	0.0023	23				

$^{208}Pb/^{204}Pb$

SUMMARY

Groups	*Count*	*Sum*	*Average*	*Variance*
Intermediate Series	13	505.0894	38.8530	0.0037
Younger Series	11	426.4944	38.7722	0.0058

ANOVA

Source of Variation	*SS*	*df*	*MS*	*F*	*P-value*	*F crit*
Between Groups	0.0389	1	0.0389	*8.36*	0.0085	4.30
Within Groups	0.1023	22	0.0047			
Total	0.1412	23				

Table 10. *(continued)*

$^{207}Pb/^{206}Pb$

SUMMARY

Groups	*Count*	*Sum*	*Average*	*Variance*
Intermediate Series	13	10.7614	0.8278	2E-06
Younger Series	11	9.1412	0.8310	5E-06

ANOVA

Source of Variation	*SS*	*df*	*MS*	*F*	*P-value*	*F crit*
Between Groups	6E-05	1	6E-05	*17.30*	0.0004	4.30
Within Groups	8E-05	22	4E-06			
Total	1E-04	23				

$^{208}Pb/^{206}Pb$

SUMMARY

Groups	*Count*	*Sum*	*Average*	*Variance*
Intermediate Series	13	26.8447	2.0650	4E-06
Younger Series	11	22.7637	2.0694	1E-05

ANOVA

Source of Variation	*SS*	*df*	*MS*	*F*	*P-value*	*F crit*
Between Groups	1E-04	1	1E-04	*15.38*	0.0007	4.30
Within Groups	2E-04	22	8E-06			
Total	3E-04	23				

$^{208}Pb/^{207}Pb$

SUMMARY

Groups	*Count*	*Sum*	*Average*	*Variance*
Intermediate Series	13	32.4292	2.4946	9E-06
Younger Series	11	27.3927	2.4902	1E-05

ANOVA

Source of Variation	*SS*	*df*	*MS*	*F*	*P-value*	*F crit*
Between Groups	1E-04	1	1E-04	*9.66*	0.0051	4.30
Within Groups	3E-04	22	1E-05			
Total	4E-04	23				

Duncan, 1996). While absolute consistency amongst these localities should not be expected, relative trace element abundances and ratios appear to differ systematically between the shield lavas and the post-erosional groups for the three island chains (Figure 19a). The Hawaiian Islands are characterized by the relative enrichment of incompatible elements in post-erosional lavas over shield stage lavas, a well-established trend (*e.g.*, Chen and Frey, 1985). This is perhaps best represented at Oahu, where shield lavas display relatively flat REE patterns (La/Yb = 4.2 – 10.9; Frey et al., 1994), compared to the significantly steeper Honolulu Series post-erosional lavas (La/Yb = 9.0 – 60.8; Clague and Frey, 1982; Clague et al., 2006). A similar relationship exists on East Maui, wherein the Hana volcanics have steep REE patterns (La/Yb = 11.2 – 14.3) relative to the associated shield lavas (La/Yb = 4.1 – 7.4; Chen and Frey, 1985). However, in all likelihood the Hana volcanics do not represent true post-erosional lavas (Sherrod and Nishimitsu, 2003), and are very similar to the established post-shield lavas (La/Yb = 10.3 – 14.9). Nonetheless, the relative enrichment of incompatible elements over the shield lavas remains.

Likewise, post-erosional lavas from Samoa and Madeira are also enriched in incompatible elements relative to the shield lavas. Samoan post-erosional lavas are significantly steeper (La/Yb = 32.5 – 42.7) than the shield lavas (La/Yb = 11.7 – 17.3), though the two lava suites come from different islands (Upolu and Tutuila, respectively), possibly complicating direct interpretation. Shield lavas from Madeira (La/Yb = 17.6 – 36.7) are slightly shallower on average than the post-erosional lavas (La/Yb = 19.9 – 27.8), but illustrate more variation than the younger suite. The shield lavas from Tahaa show a slight enrichment in incompatible element concentrations and ratios relative to the post-erosional lavas. The REE slopes for the post-erosional lavas are relatively steep (La/Yb = 24.9 – 25.3), though the variability is difficult to quantify, as the number of measurements is limited ($n = 2$). The shield stage lavas

Figure 19. Trace element and isotopic relationships between worldwide occurrences of islands with post-erosional volcanism. Top Panel: Incompatible trace element ratio La/Yb plotted against La/Sm. Here, Mauritius represents the lone example of an oceanic island wherein the shield lavas show light rare earth enrichment relative to the post-erosional lavas. Other island examples (Hawaii, Madeira, and Tahaa) each show light rare earth enrichment of post-erosional lavas relative to their respective shield lavas. Bottom Panel: ε_{Nd} plotted against $^{87}Sr/^{86}Sr$. Despite the differences in trace element systematics, isotope systematics are consistent across the island chain. Here, shield lavas show isotopic enrichment relative to the post-erosional lavas. Though not shown, systematics are consistent for the Pb-isotope system as well. Trace element and isotope data for Tahaa, Hawaii, and Madeira from GeoRoc database. See text for Mauritius references. Fields labeled PE are post-erosional data for each island.

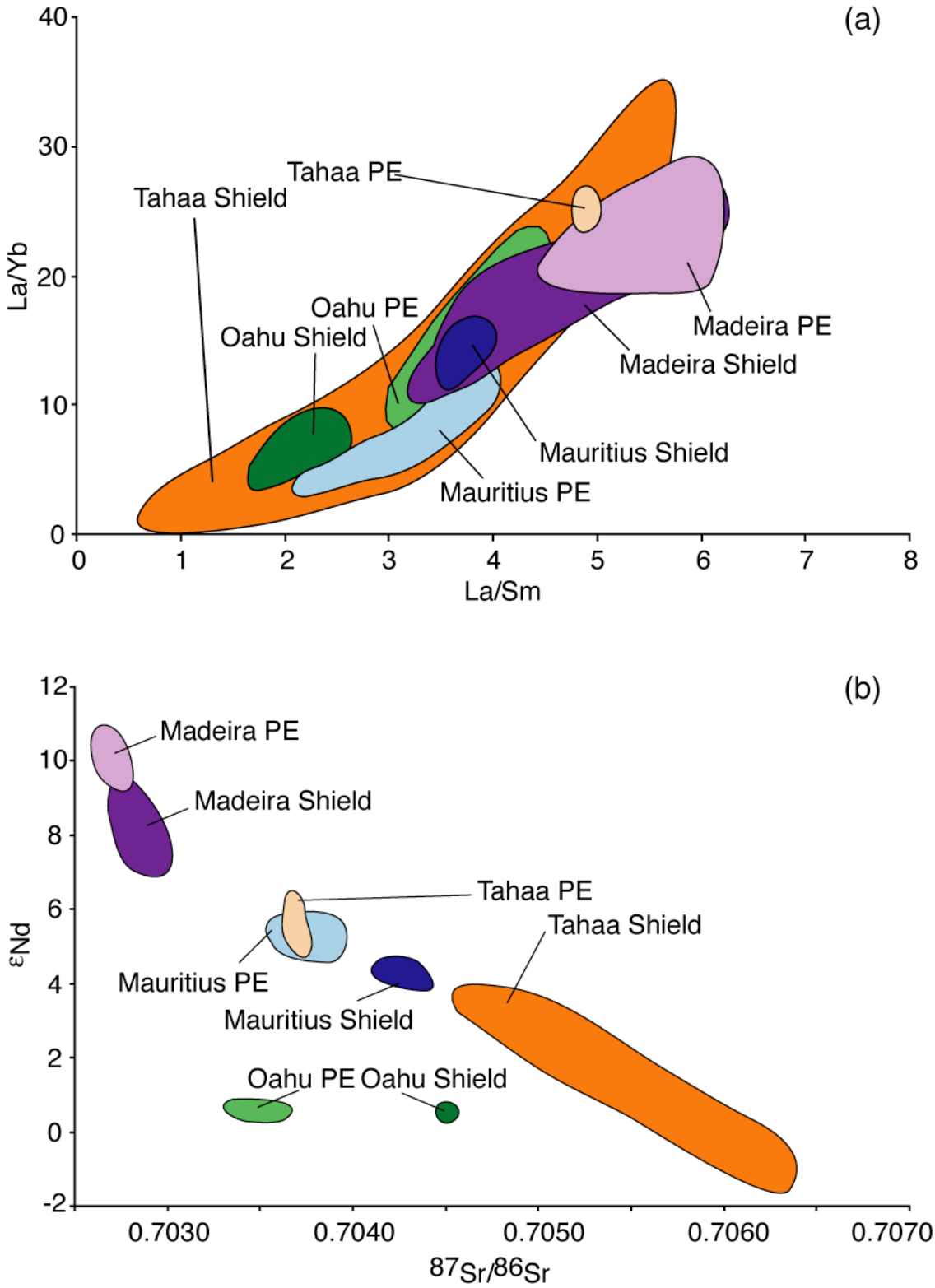
(a)
La/Yb
La/Sm
Tahaa PE
Tahaa Shield
Oahu PE
Oahu Shield
Madeira PE
Madeira Shield
Mauritius Shield
Mauritius PE
(b)
εNd
87Sr/86Sr
Madeira PE
Madeira Shield
Tahaa PE
Tahaa Shield
Mauritius PE
Mauritius Shield
Oahu PE
Oahu Shield

have a relatively wide range of REE slopes (La/Yb = 7.1 – 53.7) that overlap with the post-erosional lavas, but are somewhat higher as well (data for Hawaii, Samoa, Maderia, and Tahaa collected from GeoRef database[5]).

Mauritius lavas show a significant, though not large, absolute difference between the shield stage and post-erosional lavas (Figures 8 and 9). The Older Series shield lavas have higher incompatible element abundances and steeper REE patterns (La/Yb = 11.4 – 16.4), relative to the post-erosional suites. Within the post-erosional lavas, the Intermediate Series (La/Yb = 4.3 – 12.8) are moderately more enriched than the Younger Series (La/Yb = 3.8 – 10.5). From these measurements, it is clear that the relative abundances and steepness of the REE patterns for Mauritius are inconsistent to the trends seen at Hawaii, in particular, and the other islands in general.

Despite the inter-island differences in trace element systematics between Mauritius and other volcanic islands with post-erosional occurrences, overall isotope systematics remain consistent. For each of the volcanic islands, the shield stage lavas have more enriched isotopic signatures (*e.g.*, higher $^{87}Sr/^{86}Sr$ and $^{206}Pb/^{204}Pb$, and lower ε_{Nd}) than their post-erosional counterparts (Figure 19b). The shield lavas for Madeira ($^{87}Sr/^{86}Sr$ = 0.70275 – 0.70299; ε_{Nd} = +7.1 to +9.3; $^{206}Pb/^{204}Pb$ = 18.92 – 19.79) are more enriched than the post-erosional lavas ($^{87}Sr/^{86}Sr$ = 0.70265 – 0.70278; ε_{Nd} = +9.4 to +10.8; $^{206}Pb/^{204}Pb$ = 18.73 – 18.97). However, these lavas do contrast Mauritius, as the two suites are not distinct from one another.

Stratigraphy and Dating

It is at this point worth discussing the results of the radiometric dating and their consequences on the interpretation of the volcanic record. Results for the Older Series

[5] http://georoc.mpch-mainz.gwdg.de/georoc/

lavas are more or less as expected, though interesting nonetheless. Sample B18-1, the deepest sample and the only cutting taken from the drill cores with the chemical signatures of the Older Series, is the oldest sample identified from Mauritius to date, with an age of 8.41 Ma. Therefore, its chemical classification into the Older Series is consistent with the radiometric classification. The breccia sample, M37, was dated to 8.00 Ma, and is the oldest surficial sample thus far dated. Stratigraphically, the breccia is the lowest exposed unit of the remnant massif, and has an appropriately old age.

The lavas of the island of Mauritius have classically been divided into three temporally distinct groups: the Older, Intermediate, and Younger Series (Simpson, 1950). In particular, two groups of lavas have been identified and discussed within the Older Series: the principle shield building lavas and a series of somewhat younger, more evolved trachytic plugs (Baxter, 1975). A third, presumptively older, series was identified near the base of the exposed remnants of the eroded massif (Perroud, 1982). The outcrops observed in 2007 were restricted to stream-cut incisions with facies that consisted of decimeter-scale basaltic blocks in a matrix of weathered clay-like material. Samples M35, M36, and M37 were taken from the footwall of the caldera forming fault along the southwestern foot of Trois Mammelle at elevations of 225 meters. Sample M39 was taken from the foot of Long Mountain at an elevation of approximately 150 meters.

Perroud (1982) suggested the brecciated deposits residing stratigraphically beneath the exposed Older Series massif units were the remains of an episode of phreatic magmatism synchronous with the growth and emergence of the island. Thus, according to Perroud (1982), the breccia represents the deposits of a phreatomagmatic eruption resulting from the interaction of an early pre-emergent phase with seawater.

Radiometric dating of breccia sample M37 indicates that these magmatic deposits are indeed older than the other dated products from the Older Series. With an age of 8.00 Ma, M37 represents the oldest surficial outcrop sampled, in stratigraphic accordance with its relative position beneath the main lava flows of the Older Series, and is consistent with Perroud's hypothesis. This hypothesis also suggests a pre-emergent phreatomagmatic origin, and would necessitate an interaction with seawater. The Sr isotopic composition of seawater is significantly higher than that of oceanic island basalts, and is known to contaminate samples that erupt subaqueously. Lavas deposited proximal to the shore are also known to be affected by salt spray and commonly have artificially high Sr isotopic ratios. The isotopic composition of seawater at 8 Ma ($^{87}Sr/^{86}Sr = 0.7092$; *e.g.*, Hodell et al., 1991) is quite radiogenic in comparison to the range of Older Series lavas ($^{87}Sr/^{86}Sr = .70404 – 0.70438$). Strontium isotopic composition measurements of both the breccia and its leachate are essentially identical, within error, and thus do not show the contamination effects of hi-$^{87}Sr/^{86}Sr$ from interaction with seawater or salt spray.

With the drill core sample B18-1 dating to an older age than the breccia sample and the lack of a seawater $^{87}Sr/^{86}Sr$ signal, the direct interpretation of Perroud (1982) that the breccia represents the deposits of a phreatomagmatic eruption resulting from the interaction of an earlier, more primitive eruptive phase with seawater can be ruled out. These results, however, do not rule out the possible interaction with water and thus a phreatomagmatic origin for the breccia. The interaction of the breccia-forming lavas with meteoric water (*e.g.*, ground water or a caldera lake) would provide the hydrous component necessary for the explosive eruption without the hi-$^{87}Sr/^{86}Sr$ contamination from seawater. This scenario provides a workable alternative for Perroud's phreatomagmatic origin hypothesis for the breccia deposits and effectively explains the observed facies within the prescribed constraints from the Sr isotope

composition data. Moreover, this alternative is capable of explaining the widespread distribution of outcrops throughout the island.

The three Intermediate Series lavas have radiometric dates between 2.55 and 2.04 Ma. The two samples B18-2 and B19-1 date to 2.55 and 2.04 Ma, respectively. These samples comprise a part of the subset of Older Series-like Intermediate lavas. Only two additional Intermediate lavas have both radiometric dates and a full suite of geochemical analyses (major and trace element, isotope composition): samples MR94-04 (1.89 Ma) and MR95-23 (3.03 Ma) of Nohda et al. (2005). These samples cluster tightly with the Older Series-like samples presented here (Figure 20). What is clear from the four samples of this subset is that the enrichment trend towards more Older Series-like compositions is not an ephemeral feature, but rather a long-lived phenomenon spanning the temporal range of the Intermediate lavas and is, at a minimum, highly reproducible. The last Intermediate Series sample dated here, B6-1, dates to 2.07 Ma and is a part of the traditional group of Intermediate lavas that overlap chemically with the Younger Series.

Radiometric dates for the three Younger Series lavas range from 0.671 to 0.192 Ma, within the published range of the series. The most notable aspect of the results is the age of sample B1-5, which dated to 0.627 Ma. Based on sampling depth (153 m), the cross sections of Giorgi et al. (1999), and chemistry, this sample had been classified as Intermediate though the age demonstrates that the sample is certainly young. Consequently, samples B1-3 and B1-4 were also reclassified as Younger Series lavas. The sampling depth for B1-5 definitively demonstrates that the Younger Series lavas are capable of forming flows of substantial thickness, and are not strictly limited to thin sheets of low-volume lavas.

The traditional petrogenetic interpretation of the Mauritian post-erosional lavas (*i.e.*, Baxter, 1976) has focused on the relatively minor chemical differences between

Figure 20. Geochemical trends for Mauritius data with age. Older, Intermediate, and Younger Series symbols after Figure 6. Solid black circles represent published Mauritius samples with radiometric dates and a suite of major and trace element data. Younger Series data from unpublished Duncan data. See text for further references. Open squares are samples from Nohda et al. (2005) and represent samples with radiometric dates, major and trace elements, and radiogenic isotope ratios (*e.g.*, $^{87}Sr/^{86}Sr$ and ε_{Nd}). Top Panel: Age (Ma) plotted against wt. % MgO. Bottom Panel: Age (Ma) plotted against La/Yb. The samples with both radiometric dates and geochemical data do not span the observed range of geochemical data. Consequently, observed trends are not taken as representative.

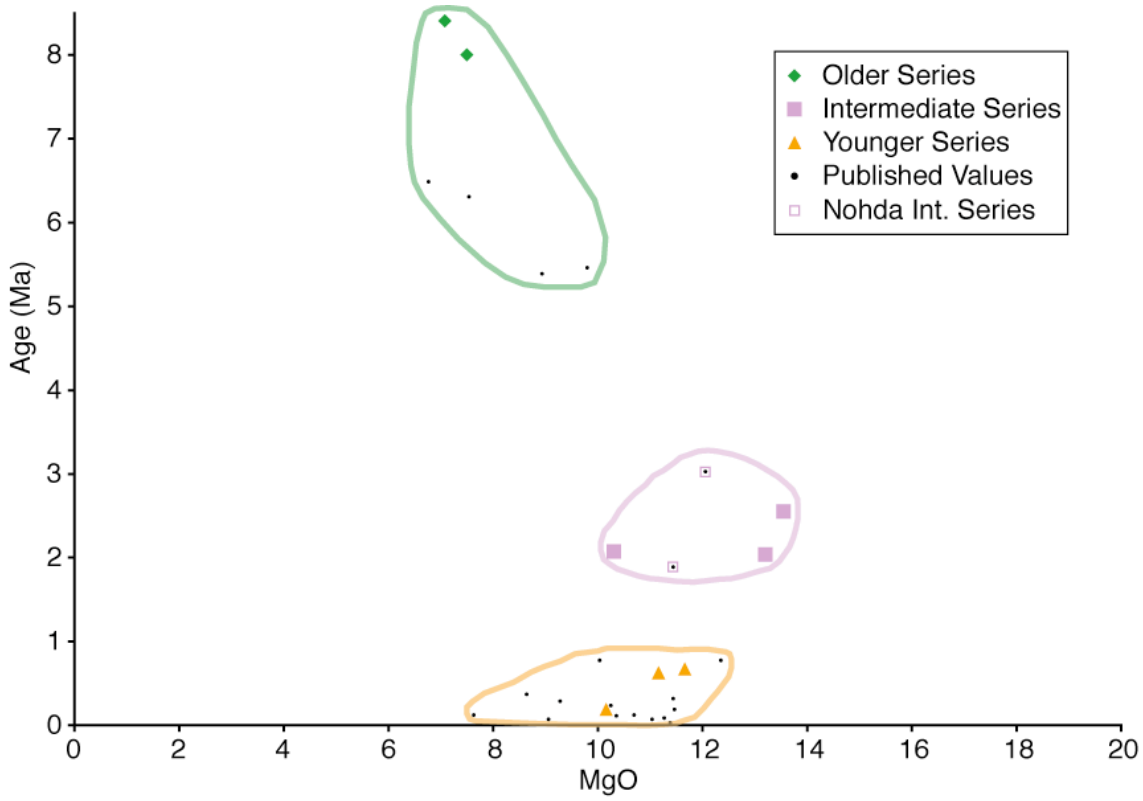
Older Series
Intermediate Series
Younger Series
Published Values
Nohda Int. Series
Age (Ma)
MgO
0
1
2
3
4
5
6
7
8
0
2
4
6
8
10
12
14
16
18
20

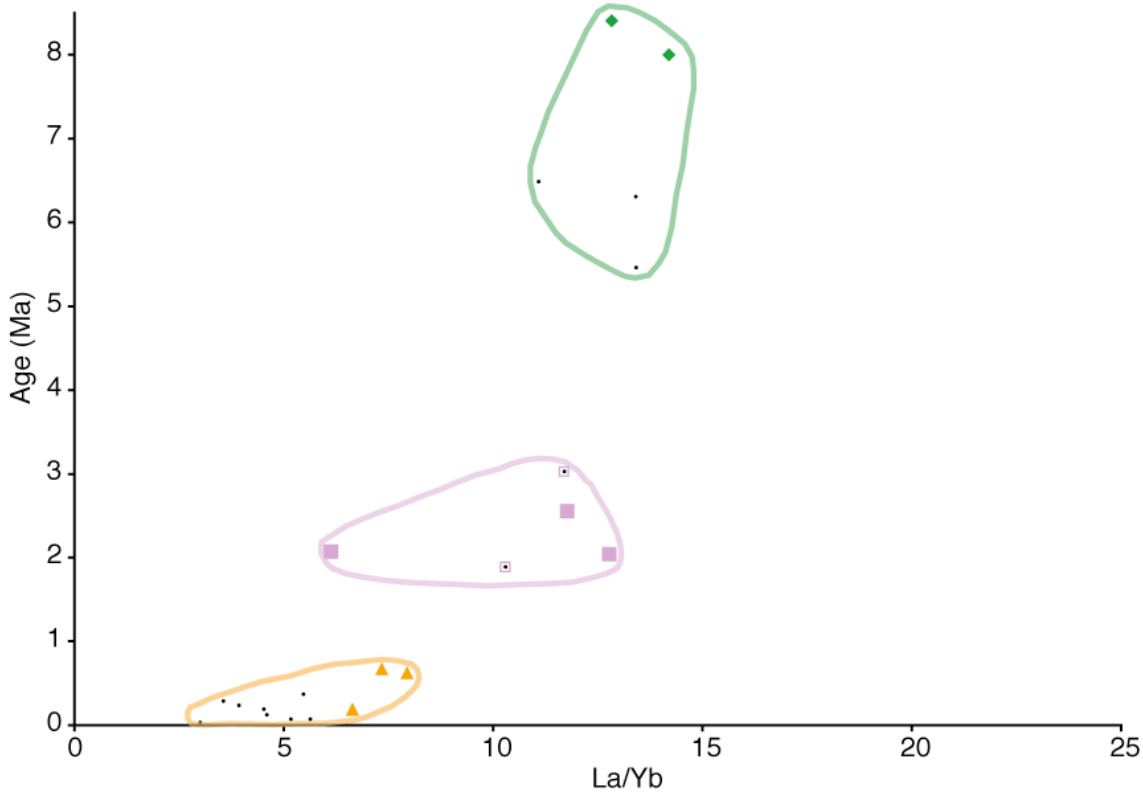
Age (Ma)
La/Yb
0
1
2
3
4
5
6
7
8
0
5
10
15
20
25

the two lava series despite the robust temporal diversity. Discerning between the two post-erosional series in the field is quite difficult, particularly as lava flows of both series commonly have aphyric textures and are weathered. For example, in the earliest geologic maps of Mauritius (Simpson, 1950), Intermediate Series exposures were confined to the southwestern corner of the island. Only recently have more extensive Intermediate Series flows been identified and updated maps published (Giorgi et al., 1999; Paul et al., 2005). Distinguishing between flows of the two series in the field is, at best, difficult and the author was never able to consistently accomplish this task. As might be expected, this difficulty extends to the subsurface lavas as well, and is epitomized by the dating of sample B1-5 to a Younger Series age, 0.63 Ma. Sample B1-5, sampled from 153 meters depth, was taken from a drill core likely used to construct one of the cross sections from Giorgi et al. (1999), which had established the Younger-Intermediate contact near 40 meters depth. By dating this deep sample to a Younger Series age illustrates that simple misinterpretations such as these are likely widespread throughout the island, and quite possibly in published samples as well. Moreover, Simpson's (1950) observation that the Intermediate and Younger Series, formerly the Early and Late Younger Volcanic Series, were separated by an interval of "no great duration" seems consistent with field observations, wherein no definitive unconformity between the post-erosional lavas was observed. In reality, most of the sampled drill cores showed multiple lateritic soil horizons within each profile. These horizons were regularly meters thick, with multiple horizons occurring within a single series. In drill core B18, for example, six meter-scale or larger soil horizons are observed. Thus, even identifying the soil horizon presumed to develop during the 900 ka volcanic hiatus is not as clear-cut as expected.

To date, radiometric dating results have upheld the long-standing convention that the post-erosional lavas are temporally distinct, though it is more difficult to argue

that the two series are chemically so. In review, the Intermediate Series lavas overlap extensively with the Younger Series lavas in all oxide-oxide diagrams and most plots of incompatible elements and ratios, though they do extend to more magnesian compositions and show a greater range of abundances. Small differences emerge when the fields for each series are averaged, though the series remain identical within error. Likewise, similar patterns are present for isotopic compositions. The Younger Series have slightly less enriched isotopic compositions than the Intermediate Series, but the groups overlap considerably. Each series shows sizeable variation beyond analytical error, but their averages are quite similar. Despite these small differences, the two groups are nearly identical within error for most commonly used geochemical tools and, moreover, no single metric can positively distinguish between the two series with any regularity.

The chemical similarity between the post-erosional lavas presents several rather straightforward questions that deserve to be addressed: (1) the likelihood that the Intermediate and Younger Series in actuality represent a single continuous eruptive event, and (2) the possibility that the two series are derived through the same petrogenetic processes. Based on current knowledge from dated Mauritius post-erosional lavas, the temporal gap between the series is upheld. However, the field and chemical observations discussed immediately above demonstrate the profound similarity between the lavas. Extensive radiometric dating of the seemingly youngest and oldest Intermediate and Younger Series lavas, respectively, is currently underway and hopefully will add resolution to this issue. The latter question is better left to the modeling, but can briefly be discussed here. Below, I will propose that the post-erosional lavas are derived principally from a relatively depleted peridotite-like component within the Réunion plume, distinct from the source for the Older Series. This component is hypothesized as forming the bulk of the plume and to melt within

the plume tail, producing the depleted post-erosional lavas. The likelihood that this source and the petrogenetic processes are similar for the two lava suites is largely dependent on the constancy of the melting plume components.

Returning to the diverse trends within the Older Series lavas presented by Paul et al. (2007), a "pre-Older Series" unit was identified from drill core lavas sampled at depth (*i.e.*, older). These deep lavas, "Group 1", were interpreted as erupting prior to the surficial Older Series lavas sampled by all previous studies (*e.g.*, Baxter, 1975), "Group 2" Older Series lavas. The "Group 1" lavas were found to have incompatible trace element patterns more depleted than the surficial "Group 2" Older Series lavas, and closely resemble the post-erosional Intermediate and Younger Series lavas in nearly every key major and trace element metric, and were thus interpreted as sharing a common source. More notably, new isotopic composition data on these samples indicates that all of the drill core samples from Paul et al. (2007) have the low Sr isotope compositions with ($^{87}Sr/^{86}Sr < 0.7040$) and higher ε_{Nd} (+4.77 to +5.17) consistent with the Intermediate and Younger Series lavas (Table 7).

The results of more extensive and systematic sampling of drill core lavas found a dearth of Older Series lavas at depth, with the sole exception of B18-1, the deepest sample measured (Table 5). While these results cannot explicitly rule out the existence of a deep and enriched unit, the available chemical and chronological evidence suggests a more parsimonious solution. The sampling and classification scheme of Paul et al. (2007) assumed the sole presence of Older Series lavas at depths greater than approximately 30 meters, though this is shown to not be the case. The inaccuracy of this assumption is best shown in sample B1-5, which dates to 0.627 ± 0.117 Ma, a Younger Series age, and was taken from a drill core depth of 153 meters. Therefore, the available evidence suggests the interpretation of Paul et al. (2007) is invalid and should be excluded from further analysis.

Post-Erosional Volume Calculations

The volumes of eruptive products on Mauritius (both shield and post-erosional lavas) are calculated here in order to compare relative magnitudes between inter-island chains. These calculations require several assumptions to simplify the process: First, the shield volcano is inferred to extend to the top of the African plate, and to include all material above this surface (Figure 21a). The depth of this surface is defined as the average depth of undisturbed seafloor in the area, approximately 4500 meters below sea level. Second, the construction of a volcanic edifice on an elastic plate results in the downward deflection of the lithosphere around the growing volcano (*e.g.*, Watts, 2001). Shipboard geophysical measurements of the southern Réunion plume track are limited to Réunion Island (*e.g.*, Charvis et al., 1999), and subsequently all geophysical assumption about Mauritius must be inferred. Despite the lack of an observable long-wavelength Hawaiian-style flexural moat surrounding Réunion and the hotspot track (de Voogd et al., 1999), the oceanic crust is depressed approximately 3 km beneath the average depth of the undisturbed seafloor (Gallart et al., 1999; see their Plate 2). As the depth to the top of the ocean crust is now known, the same 3 km depression will be applied to Mauritius. This depression is assumed to be filled with basaltic lava everywhere beneath the island, as defined by the 4500 m surface.

The third assumption entails a vertical contact between Mauritius and the Mascarene Plateau at a small saddle point (Figure 21b), after Bargar and Jackson (1974). It is well established that the assumption of a vertical contact is not adequate as contacts between volcanic edifices occur at shallower angles (DePaolo and Stolper, 1996), however, neither the location nor the nature of this contact is well known. Lastly, Perroud (1982) argued that the flattening and shallowing of dipping lavas beds

Figure 21. Geospatial data from GeoMapApp used in constructing the erupted volume of shield lavas for Mauritius. (a) Solid lines demarcate positions of cross sections A and B illustrated in (b) and (c). Red dashed line demarcates the approximate boundary of the 4500 mbsl contour chosen to represent the depth of the undisturbed seafloor around Mauritius. (b) NE-SW profile Section A. The heavy vertical dashed line indicates the position of the assumed vertical contact between Mauritius and the Mascarene Plateau. The light dashed line shows the extrapolated height of the shield lavas to 1000 m used in the calculation of erupted volume (after Perroud, 1982). (c) NW-SE profile Section B. The light dashed line shows the extrapolated shield height to 1000 m for volume calculations. Shield lavas were calculated to be ~75000 km^3. From drill core observations and the cross-section of Giorgi et al. (1995), the volume of the post-erosional lavas was calculated at ~35 km^3, and represent 0.04% of the island volume.

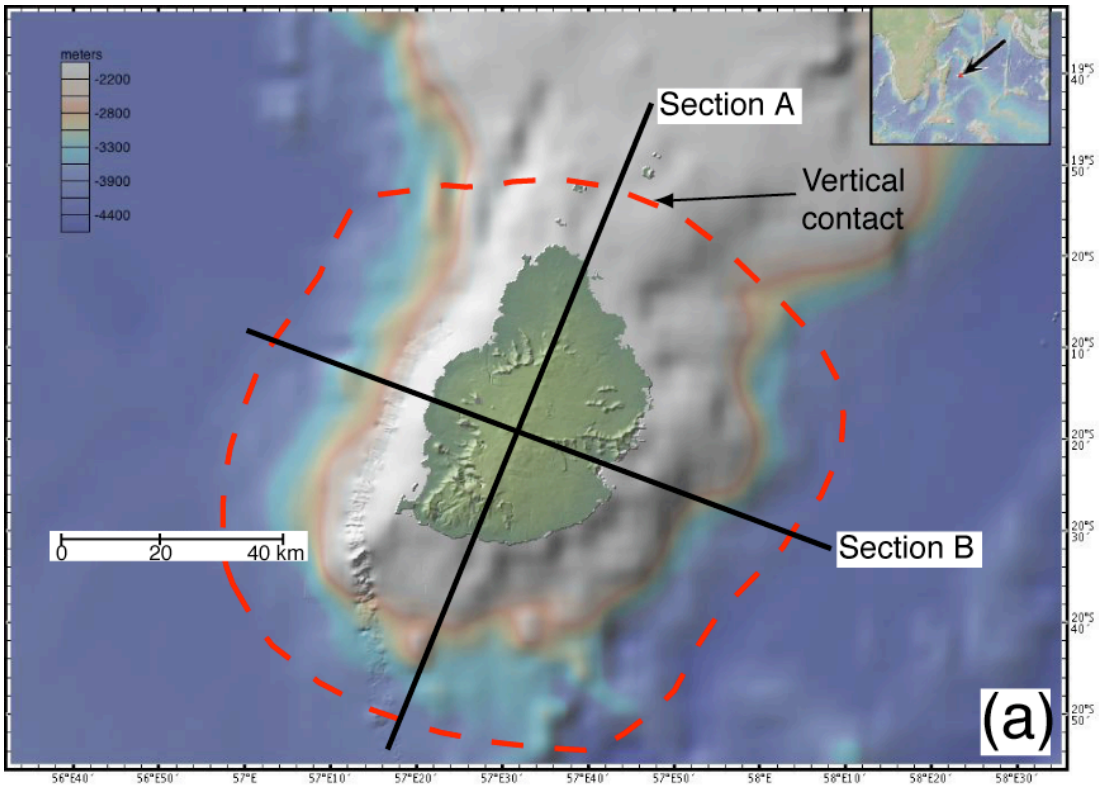
meters
-2200
-2800
-3300
-3900
-4400
Section A
Vertical
contact
Section B
0
20
40 km
(a)

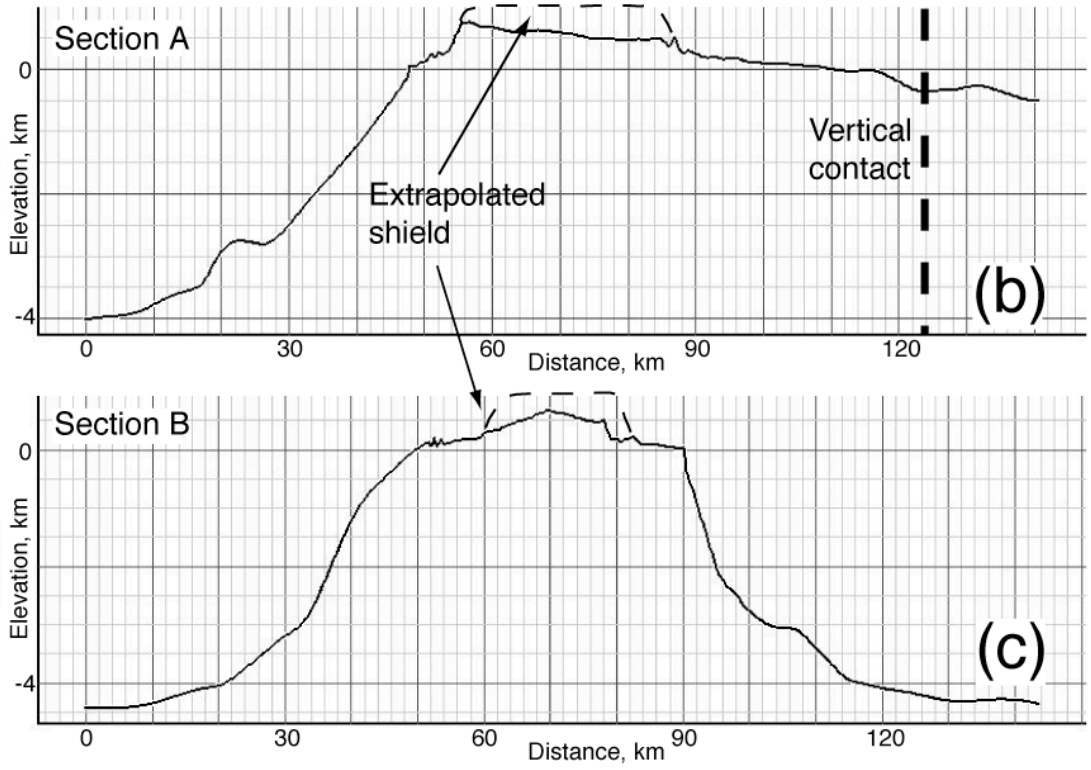
Section A
Vertical
contact
Extrapolated
shield
(b)
Elevation, km
0
-4
0
30
60
90
120
Distance, km
Section B
(c)

in the stratigraphically uppermost lavas of the Older Series massifs implied that it is unlikely the maximum elevation of the island was more than 300 to 350 meters higher than at present day, ~800 m. The maximum elevation for Mauritius was extrapolated to approximately 1000 m within the limits of the central caldera complex (Figure 21c). This elevation is in comparison to Réunion Island, which has a maximum elevation greater than 3000 m. The discrepancy in elevation may indicate the chosen elevation is a poor assumption, although the extent of subsidence and erosion at Mauritius has never been thoroughly quantified. Regardless, under these assumptions, a volume of approximately 75000 km^3 was calculated for Mauritius using topographic profiles collected from GeoMapApp[6].

Just as in calculating the volume of shield lavas, certain assumptions are required to calculate the volume of the post-erosional lavas (combined Intermediate and Younger Series volumes) as well. For the post-erosional lavas, it is important to provide constraints on the thicknesses of the combined lavas. From cross-sections constructed from drill core data (Figure 5) by (Giorgi et al., 1999), radiometric dating, and geochemical results presented here (Figure 22), the Intermediate and Younger Series lavas are commonly 100 meters or more in thickness. However, the regularity of the caldera collapse surface is not known and thicknesses cannot be reliably extended beyond established areas. Therefore, the mean thickness of the post-erosional suite within the caldera complex is assumed to be 50 meters. From field observations and similar arguments, the mean thickness outside of the caldera is assumed to be 10 meters. By determining the area of each area in GeoMapApp and applying the assumed thicknesses, a volume of ~35 km^3 is calculated for the post-

[6] http://www.geomapapp.org/. Data for predicted seafloor topography by Smith and Sandwell (1997); land topography by GTOPO30 and the Marine Geoscience Data System (MGDS; www.marine-geo.org).

Figure 22. Schematic sections created for data based on samples from drill cores with radiometric age dates. Dashed lines are schematic tie-lines and not intended to suggest series contacts. Drill cores indicated by circle with number. Topographic profiles from GeoMapApp. Top Panel: N-S profile through center of island. Intermediate-Older Series tie-line shown. Bottom Panel: NE-SW profile showing Younger-Intermediate and Intermediate-Older Series tie-lines shown.

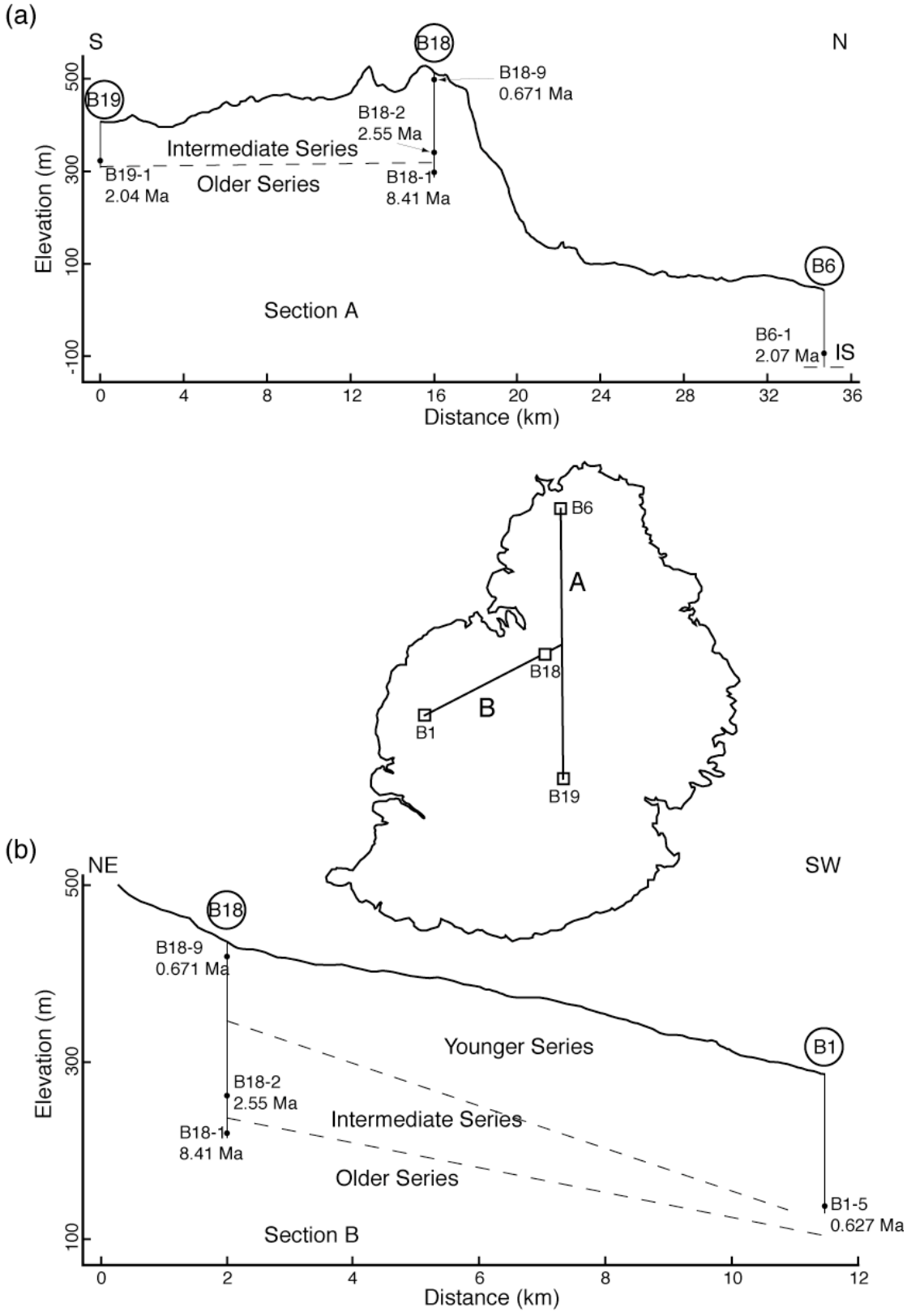
(a)
S
N
B18
B19
B6
B18-9
0.671 Ma
B18-2
2.55 Ma
Intermediate Series
B19-1
2.04 Ma
Older Series
B18-1
8.41 Ma
Section A
B6-1
2.07 Ma
IS
Elevation (m)
500
300
100
-100
0
4
8
12
16
20
24
28
32
36
Distance (km)
B6
A
B18
B
B1
B19
(b)
NE
SW
B18
B18-9
0.671 Ma
Younger Series
B1
B18-2
2.55 Ma
Intermediate Series
B18-1
8.41 Ma
Older Series
B1-5
0.627 Ma
Section B
Elevation (m)
500
300
100
0
2
4
6
8
10
12
Distance (km)

erosional lavas, and is likely a rather conservative value. Thus, the post-erosional lavas of Mauritius represent approximately 0.04% of the total volume of erupted lava.

A systematic study of erupted volumes of worldwide occurrences of post-erosional lava suites has not been conducted. In fact, detailed calculations are limited to the Hawaiian Islands. On the island of Kauai, using extensive data from well cores and outcrops, Gandy et al. (2005; submitted 2008) found the Koloa Volcanics to be approximately 60 km^3 in volume. This value is relative to a volume of 57600 km^3 for the Kauai shield (Robinson and Eakins, 2006), and represents 0.10% of the total lavas. Similarly, Garcia and others (personal communication, 2008) estimated a volume of approximately 20 km^3 for the Honolulu Volcanics, of Oahu. The Oahu shield is calculated to have produced 87600 km^3 of lava (Robinson and Eakins, 2006). The post-erosional lavas thus represent about 0.02% of the total eruptive products.

The eruptive volumes of the three post-erosional series each form only a small proportion of the total volume of their respective islands. A strong negative correlation exists between (1) shield volume and post-erosional volume and (2) shield volume and post-erosional volume proportion (Figure 23). This relationship suggests that as oceanic islands grow larger, the amount of post-erosional lavas produced become less significant. The linear relationships observed between Mauritius, Kauai, and Oahu may indicate that large-scale processes, such as a lithologically heterogeneous plume, govern the generation of post-erosional lavas. However, it is important to consider these relationships are defined by three points, and may not remain robust as data from additional islands is added.

Models of Post-Erosional Volcanism

Having established that the post-erosional Intermediate and Younger Series lavas are chemically and temporally distinct from the Older Series shield lavas and

Figure 23. Calculated volume data for shield and post-erosional lavas for Mauritius, Kauai, and Oahu. Data for Kauai from Gandy et al. (2005; submitted 2008), data for Oahu from Garcia (personal communication). (a) Post-erosional volume plotted against shield volume. Data for Kauai, Mauritius, and Oahu form a strong negative correlation. (b) Volume percentage of the oceanic island formed by the post-erosional lavas plotted against post-erosional volume. A strong positive correlation exists between the three islands. (c) Volume percentage of the oceanic island formed by the post-erosional lavas plotted against shield volume. These relationships suggest that as the oceanic island grows larger, the role of post-erosional volcanism decreases, even as the total erupted post-erosional volume increases. Furthermore, the strong linear relationships may indicate an underlying large-scale process is responsible for the generation of post-erosional lavas worldwide.

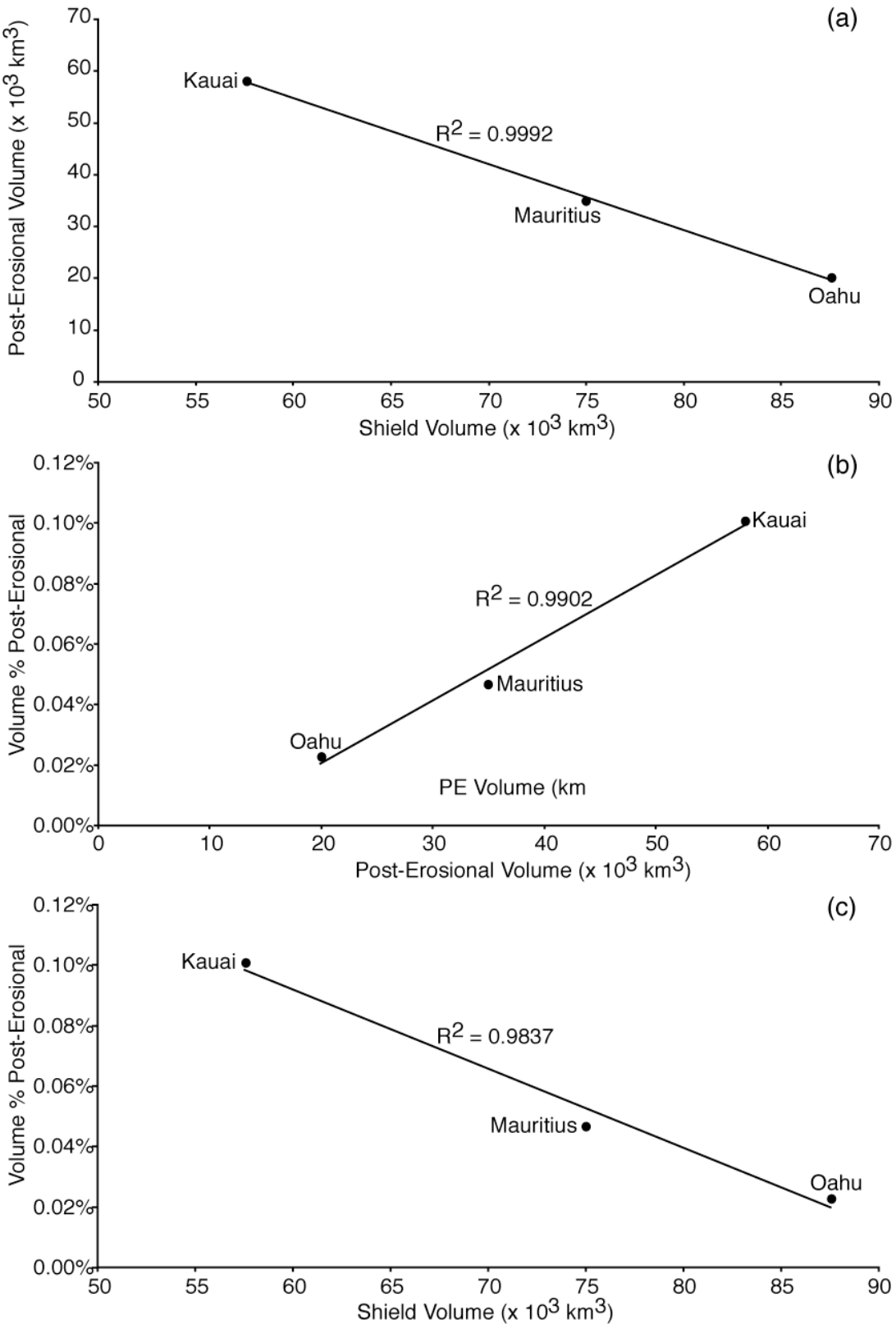
(a)
Post-Erosional Volume (x 10^3 km^3)
70
60
50
40
30
20
10
0
Kauai
R^2 = 0.9992
Mauritius
Oahu
50
55
60
65
70
75
80
85
90
Shield Volume (x 10^3 km^3)
(b)
Volume % Post-Erosional
0.12%
0.10%
0.08%
0.06%
0.04%
0.02%
0.00%
Kauai
R^2 = 0.9902
Mauritius
Oahu
PE Volume (km
0
10
20
30
40
50
60
70
Post-Erosional Volume (x 10^3 km^3)
(c)
Volume % Post-Erosional
0.12%
0.10%
0.08%
0.06%
0.04%
0.02%
0.00%
Kauai
R^2 = 0.9837
Mauritius
Oahu
50
55
60
65
70
75
80
85
90
Shield Volume (x 10^3 km^3)

require a distinct source, the questions of the nature and location of this source begs to be addressed. As stated above, the current models for post-erosional volcanism do not fully address all of the geophysical and geochemical observations associated with these lavas. While a number of mechanistic solutions have been attributed to the generation of the post-erosional lavas, each model has its own unique limitations, restricting each from fulfilling observations completely. Recent works by Paul et al. (2005) and Bianco et al. (2005) have presented the prevailing views on geochemical and geophysical models capable of producing post-erosional lavas, which will be discussed here.

Geochemical models for post-erosional lavas have largely been focused on explaining the differences in major and trace element and isotope compositions between the shield lavas and post-erosional lavas, worrying less about the geophysical requirements. The study of Chen and Frey (1985) on Haleakala, East Maui is considered the classic interpretation of Hawaiian evolution. Their model identifies all magmas as mixtures of plume material and ambient upper mantle (*i.e.*, MORB source), with different compositions produced by differing proportions. The tholeiitic shield lavas are produced centrally over the plume, resulting in the overwhelming dominance of the large degree melts of the enriched plume. The alkalic stages are produced nearer the edges of the plume, such that the magmas are more characterized by the character of the small degree melts of the depleted upper mantle. Thus, the post-erosional magmas are produced most distally, and most closely resemble the ambient upper mantle. It should be noted that dating of lavas from Haleakala has since established a nearly continuous eruptive activity, necessitating its reclassification as a post-shield volcano (Sherrod and Nishimitsu, 2003). Sheth et al. (2003) proposed a model for Mauritus rooted to this model, suggesting that each series is a unique mixture of enriched plume source with enriched plume source variably metasomatized

by small degree melts of a depleted upper mantle source (*i.e.*, MORB source). White and Duncan (1996) modified the model of Chen and Frey by substituting lower mantle material viscously entrained by the rising plume for the depleted source, to better satisfy the isotopic compositions for the Tahaa post-erosional lavas.

When considering the post-erosional problem as a whole, geochemical models of this nature are somewhat insufficient. First, when Sr, Nd and Pb isotopic compositions are each considered simultaneously, it is apparent that post-erosional lavas cannot be simple binary mixtures of MORB source and plume source. Paul et al. (2005) showed this for Mauritius (their Animations 1 & 2), demonstrating that a single line drawn through the three Mauritian lava suites cannot intercept the Central Indian Ridge MORB field. This observation is also discernable, though tougher to visualize, by considering multiple isotope–isotope plots.

In addition to melting of the adiabatically upwelling mantle material within the plume, these models require the melting of an ambient "outside" source to match the range of isotopic compositions observed throughout the volcanic evolution. Detrick and Crough (1978) made a case for the thinning and melting of the lithosphere by conductive heating by the mantle plume, with Gurriet (1987) later arguing for these lithospheric melts as a source for the Haleakala post-erosional lavas. Subsequent work has since demonstrated that neither the overlying lithosphere nor the surrounding asthenosphere (ambient upper mantle) are heated enough by the mantle plume cross their respective solidii and melt (*e.g.*, Ribe and Christensen, 1994; 1999; Farnetani and Richards, 1995), essentially ruling out the model of Chen and Frey (1985). This does not, however, explicitly preclude the model of Lassiter et al. (2000) that argues for Hawaiian post-erosional lavas sourced by the melting of pyroxenite veins in the lower lithosphere as pyroxenites have a lower solidus temperature (*e.g.*, Hirschmann and Stolper, 1996), that is they cross their solidus and begin to melt deeper in the mantle.

Whereas these geochemical models have failed to address the volcanic hiatus between the end of the post-shield volcanism and the onset of post-erosional volcanism, several geophysical models have identified mechanisms capable of explaining the temporal gap. Recognizing the association between post-erosional volcanism and flexural uplift (*e.g.*, Bailey, 1964; Moore, 1970), ten Brink and Brocher (1987) proposed a model in which changing stress conditions within the elastically loaded plate are responsible for shutting off and then reinitiating volcanic activity. As a volcano moves downstream and away from the plume center, new edifices are constructed, altering the orientation of least compressive stress beneath the older volcano from vertical to horizontal, thus presenting an opportunity for magma to reach the surface and erupt. Building further upon the flexure concept, Bianco et al. (2005) modeled decompression melting from mantle flow driven by plate flexure as the source of the post-erosional volcanics. This model generated melts in the proper position and at reasonable volumes when a focus-factor for melt extraction was included. In a three-dimensional variable-viscosity convection model with melting parameterized for the Hawaiian plume, Ribe and Christensen (1999) identified a zone of weak secondary melting 300 – 500 km downstream of the plume stem. This melting zone resulted from decompression melting along a particle path that rises along the edge of the principal melting region, moves downward as a result of the rigidity of the lithosphere, and then upward as the plume tail thins and spreads laterally. The secondary melting zone corresponds to a pulse of volcanism 3.5 – 5.5 Myr after the initial episode, as parameterized for Hawaii. Melting extents are approximately 1% and, assuming a peridotite source, would produce magmas with the strongly alkalic signatures observed from post-erosional volcanics worldwide. However, Jull and Ribe (2002) found this secondary melting zone to be a numerical artifact sensitive to the boundary conditions. Phipps Morgan and Morgan (1999) and

Yamamoto and Phipps Morgan (in prep) found similar results in independent numerical models of the Hawaiian plume, also identifying a region of downstream melting. This secondary melting zone also results from decompression melting as the plume tail thins and spreads laterally. The numerical models differ in that the numerical model of Phipps Morgan and others has a continuous tail extending hundreds of kilometers downstream, rather than a discrete melting zone.

The models I have presented thus far attempted to explain the occurrence of post-erosional volcanism as coming from three principal sources: (1) the surrounding asthenosphere (Chen and Frey, 1985), (2) the overlying lithosphere (Lassiter et al., 2000), and (3) the plume itself (ten Brink and Brocher, 1987; Ribe and Christensen, 1999; Swinnard et al., submitted 2008). The third option is not *a priori* restricted to geophysical modeling, and is gaining a foothold in the geochemical community. Geldmacher and Hoernle (2000) proposed that the underlying mantle plume at Madeira was the source for both the main stage lavas and the post-erosional lavas. Their model included recycled upper oceanic crust as the source for the main stage magmas, and recycled lower oceanic crust and peridotite as the source for the post-erosional magmas. This concept of incorporating recycled (*i.e.*, subducted) materials into mantle plumes as lithologic heterogeneity is a longstanding hypothesis within the geochemical community (*e.g.*, Chase, 1981; Hofmann and White, 1982b; White, 1989), and has long been recognized as necessary to account for the chemical variations observed in oceanic lavas (*e.g.*, White, 1985; Zindler and Hart, 1986). More recent work has established the importance of heterogeneity in the generation of geochemical signatures at Hawaii, and elsewhere (*e.g.*, Hauri, 1996; Sobolev et al., 2005; 2007).

In their flexural decompression model for generating the Hawaiian post-erosional lavas, Bianco et al. (2005) proposed a lithologically heterogeneous plume

consisting of three compositional components. Components were sampled preferentially at the different eruptive localities as a function of differing melt extraction rates at each setting. The main stage magmas are dominated by melts of a pyroxenite (enriched) component, and the post-erosional magmas derived from melts of an anhydrous peridotite (depleted) component. Likewise, Paul et al. (2005) proposed a similar model involving a lithologically heterogeneous plume sourcing both the main stage and post-erosional stage on Mauritius. Though not dynamically driven, an environment is envisioned wherein a low-solidus enriched component (pyroxenite or eclogite) melts preferentially beneath the growing shield volcano, and a depleted component (peridotite) is the dominant source of the downstream post-erosional magmas. Together, these examples reveal growing recognition of the importance of a heterogeneous plume in controlling the entire evolution of oceanic volcanoes.

Numerous geochemical signatures observed in the Mauritius lavas clearly indicate that the post-erosional Intermediate and Younger Series lavas have undergone a different petrogenetic history from the shield building Older Series lavas, and require a distinct source. Major and trace element analyses demonstrate that the Older Series lavas have undergone significant clinopyroxene fractionation and removal. Furthermore, the Older Series are characterized by higher incompatible trace element abundances and greater ratios of more-to-less incompatible elements than the post-erosional lavas. The Older Series lavas also have more enriched isotopic compositions than do the post-erosional lavas. This isotopic enrichment trend is consistent with other worldwide occurrences post-erosional suites, but the relative trace element abundances between shield and post-erosional are opposite to those seen elsewhere. In the next section, I will attempt to model the generation of these lava suites from a lithologically heterogeneous plume.

CHAPTER 5 – MODELING OF A LITHOLOGICALLY HETEROGENEOUS PLUME

Recycling of Earth Materials

The process of subduction is known to transport, or recycle, crustal materials and oceanic lithosphere from the Earth's surface back into the mantle. Whereas the production of oceanic lithosphere by partial melting of an upwelling mantle can be expected to re-homogenize a melting region (*e.g.*, Klein and Langmuir, 1987), subduction re-injects heterogeneity back into the mantle. That is, melting destroys heterogeneity while subduction restores it. This reinjected heterogeneity is thought to be sampled by mantle plume derived ocean island basalts (OIB) lavas, which come in one of several geochemical "flavors": HIMU, EMI, and EMII (*e.g.*, White, 1985; Zindler and Hart, 1986). The geochemical signatures of each of these "end-members" are thought to represent a mixture of deep mantle material with the subducted material that has undergone processing and dehydration in the subduction zone, and long-term storage in the deep mantle.

This subducted lithospheric material is, on average, less mafic than the mantle material it is injected into, and will transform to an eclogitic composition with increasing pressure (Green and Ringwood, 1967). In this work, unless otherwise specified, the term eclogite is used *sensu latu* and refers inclusively to all recycled material (*e.g.,* sediment, continental material, upper and lower ocean crust) that has been subducted to mantle depths ($P \gtrsim 2.0$ GPa), and encompasses lithologies such as websterite, garnet pyroxenite, and eclogite. These lithologies will commonly be olivine-poor and have garnet as a high-pressure aluminous phase. Eclogite in this sense is a chemical rather than mineralogical description, and assemblages are not

required to contain pyralspite garnet[7] and omphacitic clinopyroxene[8]. The collective term eclogite is chosen rather than pyroxenite to prevent confusion with the pyroxene-rich reaction products that will be introduced below (*i.e.*, Sobolev et al., 2005).

Here, two melting scenarios for generating basaltic magmatism from a heterogeneous mantle plume source are modeled using the thermodynamic algorithms of MELTS (Ghiorso and Sack, 1995) and pMELTS (Ghiorso et al., 2002) via the Adiabat_1ph interface (Smith and Asimow, 2005). This approach draws on the modeling of Gaffney et al. (2005) for the young Hawaiian Maui Nui lavas, but differs in the thermodynamic treatment of the plume as an admixture of the enriched and depleted components. This modeling can broadly be dissected into two phases: (1) the shield stage lavas, and (2) the post-erosional lavas. Two methods are modeled here in efforts to explain the geochemical signatures observed on Mauritius, and other oceanic islands. In the first scenario, melts from an enriched component (eclogitic) mix in variable proportions with melts derived from a depleted component (peridotitic) to produce the source for the shield lavas. In the second scenario, melts of the enriched component interact with the surrounding matrix of the depleted component, reacting to form a hybrid pyroxenite. This newly created hybrid pyroxenite subsequently melts, with these melts mixing with those from the depleted component, and possibly the enriched component as well, to form the shield lavas.

---

[7] "Pyralspite" is an abbreviation for the common types of garnet found in the mantle: pyrope ($Mg_3Al_2Si_3O_{12}$), almandine ($Fe_3Al_2Si_3O_{12}$), and spessartine ($Mn_3Al_2Si_3O_{12}$). A Ca-rich component (grossular; $Ca_3Al_2Si_3O_{12}$) is usually found in the garnet solid solution as well. See Appendix E for crystallographic information.

[8] Omphacite is a high-pressure form of clinopyroxene rich in Na and Al (jadeite and diopside components). By definition, eclogite, *sensu stricto*, must contain both omphacitic pyroxene and pyralspite garnet. Appendix E.

Modeling Results and Interpretation

Although the two petrogenetic models presented here are distinct in their treatment of the details of melting and mixing, they each rely on the same underlying hypothesis of a lithologically heterogeneous mantle plume. In this system, defined as mantle material of two or more lithologies within a plume, the mantle plume is assumed to upwell adiabatically (isentropically) from a deep sourced thermal boundary layer (*e.g.*, Davies and Richards, 1992). In order to simplify the modeled system to the greatest extent possible, all plume material is assumed to upwell as a single cohesive unit. The effects of stirring (*e.g.*, Farnetani et al., 2002; Farnetani and Samuel, 2005) and density (*e.g.*, Leitch and Davies, 2001) within the plume are beyond the scope of this project and will not be considered. In this model, the individual components are not assumed to be in chemical equilibrium with each other and, unless explicitly stated, each component (*e.g.*, eclogite or peridotite) is treated as though it were chemically isolated from all other components until mixing is initiated. Melts are derived by batch (equilibrium) melting and maintain equilibrium with their source until extraction. Despite the assumption of chemical disequilibrium, all components (including both solid and melt phases) are assumed to be in thermal equilibrium, and are modeled as such.

Maintaining chemical disequilibrium between mantle components is necessary for explaining the trace element and isotopic signatures observed in mantle derived lavas (*e.g.*, Saal et al., 1998; Kogiso et al., 2004). Once reinjected into the mantle during subduction, recycled crustal and lithospheric materials are entrained in the convecting mantle and subsequently thinned, stretched, and folded (Allègre and Turcotte, 1986). Exposures observed in orogenic lherzolite (peridotite) massifs commonly have eclogitic layers of meter- to decimeter-scale. Hofmann and Hart (1978) demonstrated that bodies as small as centimeter-scale are capable of

maintaining local disequilibrium for periods of 10^8 to 10^9 years under sub-solidus conditions. However, diffusive equilibration is greatly increased when liquid is present (six to seven orders of magnitude), and bodies will equilibrate under partially molten conditions in less than 10^6 years. No special steps are necessary to account for the assumption of chemical disequilibrium during melt. The pMELTS algorithm is designed exclusively to calculate equilibrium assemblages for a single lithology during each analytical run, therefore requiring each component be treated individually.

Phipps Morgan (2001) detailed the thermodynamic interdependence of components within a heterogeneous mantle plume, emphasizing the transfer of heat (conduction) from the higher-solidus component to the lower-solidus component during the early stages of melting. Thermal equilibrium can be maintained between lithologically heterogeneous bodies so long as conductive heat transport exceeds advective heat transport over the lengthscale of the bodies. Sleep (1984) determined this length scale to be on the order of several hundred meters for spherical bodies (*i.e.*, plums within the plume matrix), likely the length scale of long-stored heterogeneities. Unlike chemical disequilibrium, treating the assumption of thermal equilibrium in pMELTS requires special considerations. I have elected to model the thermal evolution of this heterogeneous system by constructing a composite pressure-temperature path from the thermodynamic properties of each component. Were each lithologic component allowed to upwell adiabatically and independently, each would evolve along a different thermal path based on its individual thermodynamic properties (*e.g.*, heat capacity, solidus temperature, productivity). However, allowing each component to evolve along a separate P-T path would not fulfill the requirement for thermal equilibrium. To account for this requirement, a composite pressure-temperature path for the heterogeneous system must be developed. In order to maintain thermal equilibrium between the lithologic components, one or more of these

components must deviate away from their independent P-T paths. From the individual P-T paths, a simple composite path can be constructed by weighting the two (or more) lithologies by their respective modal abundances. Using Adiabat_1ph, the individual components can then be forced along the composite path, providing a common thermal evolution for the entire system. Thus, the concept of an adiabatic path for each component is abandoned in favor of an "adiabatic" path for the system as a whole. This approach represents a reasonable first-order approximation for the combined path, though does not fully account for changes in latent heat consumption from shifting the components off their individual paths.

Model calculations are bracketed in pressure both computationally and physically. The maximal limit on pressure is constrained by the computational parameterization of pMELTS to 4.0 GPa (Ghiorso et al., 2002; Smith and Asimow, 2005). The thickness of the oceanic lithosphere near Mauritius places a physical constraint on the minimal limit of pressure for the model. Upwelling within the plume directly, as well as the vertical ascent of the plume, is assumed to cease when material impinges upon the base of the oceanic lithosphere near 70 km around Mauritius, ~ 2.0 GPa.

Binary Melt-Mixing Model

Shield Lavas

The first melting scenario is constructed as a relatively simple end-member model wherein the two (or more) components that compose the plume are allowed to melt as material ascends adiabatically. These melts are then allowed to mix at some shallower depth, providing the parental magmas for the shield lavas.

For this model, the heterogeneous mantle plume is composed of two lithologic components. The eclogitic component modeled by primitive MORB (Allan et al.,

1989; Ghiorso, 1997; Table 11) is from near the Lamont seamount chain, and taken to represent recycled oceanic lithosphere. This component is chosen to represent the heterogeneous mafic pods, and is modeled as the modally minor component. Partition coefficients for garnet and clinopyroxene are from sample A343 of Pertermann et al. (2004). These partition coefficients were determined experimentally at pressures (3 GPa) and temperatures (1390 °C) appropriate for the modeled conditions, and designed specifically to be consistent with clinopyroxene and garnet in an anhydrous eclogite derived from recycled MORB (Table 12). The eclogitic component is taken to be the isotopically enriched component. There are no explicit geochemical observations that require the low-solidus component be the isotopically enriched component, though it does seem to be the prevalent interpretation (*e.g.*, Sobolev et al., 2005), and a refractory component with an enriched isotopic signature appears to make less geologic sense.

The second component is taken to be peridotitic in nature, and modeled as depleted mantle (DM) of McKenzie and O'Nions (1991; 1995; Table 11). This component is assumed to be the matrix (modally dominant assemblage) within the plume, and is considered to be more refractory than the eclogitic component, with a relatively depleted isotopic signature. Partition coefficients for the depleted component are from DM of McKenzie and O'Nions (1991; 1995), as well (Table 12).

The Réunion plume is estimated to have a potential temperature (T_P; McKenzie & Bickle, 1988) between 1500 and 1575 °C (*e.g.*, Herzberg, 2006; Putirka, 2008)[9]. These calculated potential temperatures rely on assumptions involving equilibrium with a peridotitic source and the addition or subtraction of olivine to reach equilibrium with the mantle. The model under discussion here is based on a

[9] Potential temperature is the temperature a parcel of mantle would achieve were it allowed to rise isentropically to the surface (1 bar) with melting suppressed.

Table 11. Starting compositions for modeling with Adiabat_1ph

Source	Component	SiO2	TiO2	Al2O3	Fe2O3	Cr2O3	FeO	MgO	CaO	Na2O	K2O	P2O5	Mg#[1]
Allan et al. (1989)	Eclogite	48.68	1.01	17.64	0.89	0.03	7.59	9.10	12.45	2.65	0.030	0.08	68
McKenzie and O'Nions (1991; 1995)	Peridotite	45.57	0.17	2.70	0.111	0.44	7.92	40.80	2.41	0.24	0.024	0.014	91

Starting compositions used for modeling in Adiabat_1ph. The eclogitic composition is a primitive MORB from near the Lamont Seamount chain (Allan et al., 1989; Ghiorso, 1997) and is taken to represent recycled oceanic lithosphere embedded in the plume. The peridotite composition is depleted mantle of McKenzie and O'Nions (1991; 1995) and taken to represent the modally dominant peridotite matrix of the plume.

Table 12. Partition coefficients for Adiabat_1ph modeling

	DM Peridotite component *(McKenzie & O'Nions, 1991; 1995)*				MORB Peridotite component *Pertermann et al. (2004)*	
	gt	cpx	ol	opx	gt	cpx
Ba	0.00005	0.0005	0.0003	0.0001	0.005	0.006
La	0.01	0.054	0.0004	0.002	0.012	0.027
Sm	0.217	0.26	0.0013	0.01	0.19	0.19
Yb	4.03	0.28	0.0015	0.049	5.71	0.55
Hf	0.44	0.22	--	0.01	0.22	0.22
Zr	0.32	0.1	0.01	0.03	0.19	0.1
Nb	0.07	0.02	0.005	0.005	0.005	0.005
Sr	0.0006	0.1283	0.00019	0.007	0.01	0.067
Nd	0.087	0.21	0.001	0.0068	0.057	0.122
Pb	0.00001	0.01	0.0001	0.0013	0.056	0.042

Partition coefficients used in Adiabat_1ph for thermodynamic modeling as given by listed authors.

lithologically heterogeneous source, and mixing of melts derived from these sources. When applied to (partially) eclogite sourced lavas, peridotite-based calculations are likely to produce parental magmas that are 2 – 3% too high in MgO and potential temperatures that are content 50 – 70 °C too high (Herzberg and Asimow, 2008). As the potential temperature of the plume is not well constrained, calculations are run in Adiabat_1ph for multiple T_P (~1450 °C, ~1525 °C, and ~1600 °C). For a given potential temperature, isentropic P-T paths are calculated for each component from 4.0 to 2.0 GPa in 0.01 GPa increments (Asimow and Ghiorso, 1998). Batch (equilibrium) melting is assumed, and the system is allowed to evolve without any constraint on oxygen fugacity. From these independent P-T paths, a composite path is constructed by weighting the individual paths by their modal abundances, with eclogite (recycled MORB) proportions of 5, 10, and 15% (Figure 24). Each lithologic component is then forced along this composite P-T path. At 2.0 GPa, melts are assumed to efficiently segregate from each component and are mixed in their respective proportions, calculated from their initial abundance and extent of melting of each component. These melts are thus the parental magmas[10] for the shield building lavas. Subsequent differentiation and fractionation of these magmas at shallower levels is discussed below. The remaining residue is melt-free and assumed to begin traveling downstream through the plume tail to produce the post-erosional lavas.

The construction of a composite P-T path can be seen in Figure 24, as well as the contributions of varying the amount of lithologic heterogeneity in the plume. From the same starting conditions, the P-T path for the eclogite composition is much cooler at a given pressure relative to the peridotite composition. This is largely a result of increased melting of the more fertile composition, and the subsequent cooling

[10] Parental magmas are primitive liquids supplied to higher levels, which will undergo fractional crystallization to produce the erupted lavas.

Figure 24. PT-diagram for a sample calculation illustrating the construction of a composite P-T path from individual eclogite and peridotite paths. The MORB (blue; Allan et al., 1989) and DM (red; McKenzie and O'Nions, 1991; 1995) compositions, which represent the eclogitic and peridotitic component, are allowed to ascend isentropically from starting conditions of 40 kbar (4.0 GPa) and 1550 °C, under batch melting conditions using Adiabat_1ph (Smith and Asimow, 2005). From these individual PT-paths, a composite path is constructed by weighting the MORB and DM components by their modal percentages. Composite P-T paths for modal percentages 5% (yellow), 10% (green), and 15% (purple) MORB are shown.

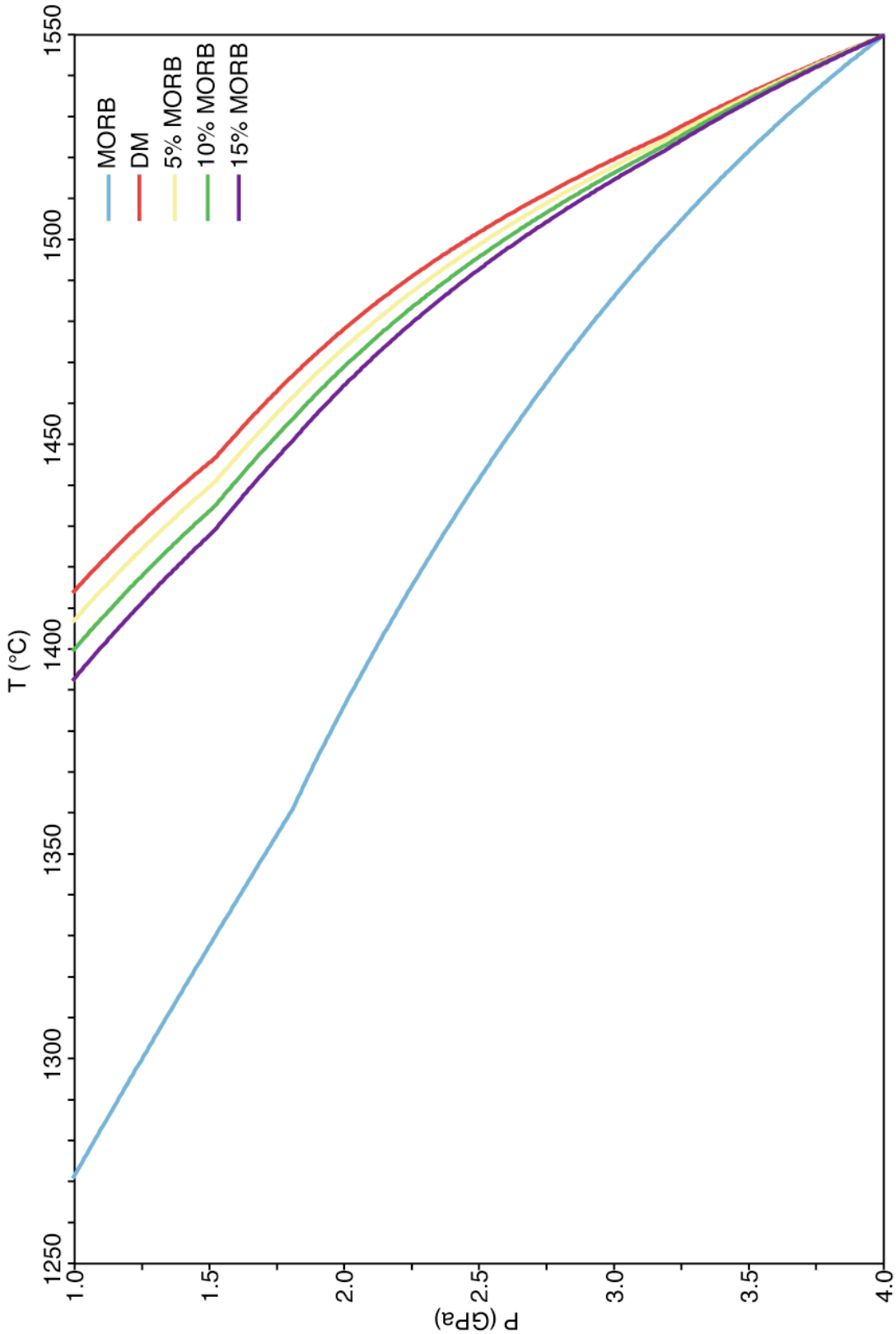
MORB
DM
5% MORB
10% MORB
15% MORB
T (°C)
P (GPa)
1250
1300
1350
1400
1450
1500
1550
1.0
1.5
2.0
2.5
3.0
3.5
4.0

from the endothermic melting reaction. The effects of adding lithologic heterogeneity to the plume are also illustrated, with additional eclogite progressively cooling the P-T path for the composite system. While the thermal effects of varying the amount of eclogite introduced into the system are small, less than 10 °C difference between 5% and 15% eclogite at 2.0 GPa, the effects on the individual components are great. To simulate a system in thermal equilibrium, as discussed above, each component is forced along the composite P-T path for a given eclogite proportion. Thus at 2.0 GPa, the eclogite is approximately 80 °C warmer and the peridotite is 10 °C cooler than their respective individual P-T paths, for 10% eclogite. This will cause the eclogite, the lower solidus component, to melt to a higher degree and the peridotite, the higher solidus component, to melt to a lower degree. The productivities, $-\partial F/\partial P)_S$, of the eclogite and peridotite from their independent and isentropic P-T paths are compared to those when these components are forced along the composite P-T path (Figure 25). The effects of moving the components along the composite P-T path are rather small for the peridotite and quite dramatic for the eclogite. The productivity of the eclogite is greatly increased over pure adiabatic melting, with the component completely melting out at pressures greater than 2.0 GPa. The peridotite component, in contrast, has a lower productivity than determined for the individual isentropic path. These results emulate the predicted enhancement in melt productivity for the lower-solidus component in a heterogeneous mantle of Sleep (1984) and Phipps Morgan (2001). Moreover, reducing the proportion of eclogite in the system from 15 – 5% increases the maximum eclogite productivity, but also decreases the depth where the component crosses its liquidus.

Varying the proportion of eclogitic material introduced into the plume has relatively small effects on major and trace elements at a given potential temperature (Figure 26). The small thermal differences that result from running each model

Figure 25. Melting productivity for a sample calculation illustrating the amount of melt produced for a given change in pressure. Red and blue lines show MORB (eclogitic component) and DM (peridotitic component), respectively, allowed to rise adiabatically. Purple (5% MORB), green (10% MORB), and orange (15% MORB) lines illustrate increased productivity and enhanced melting by forcing the MORB component along composite PT path for the indicated amount of initial eclogite. Yellow line shows decreased productivity of DM component forced along 10% initial eclogite composite path.

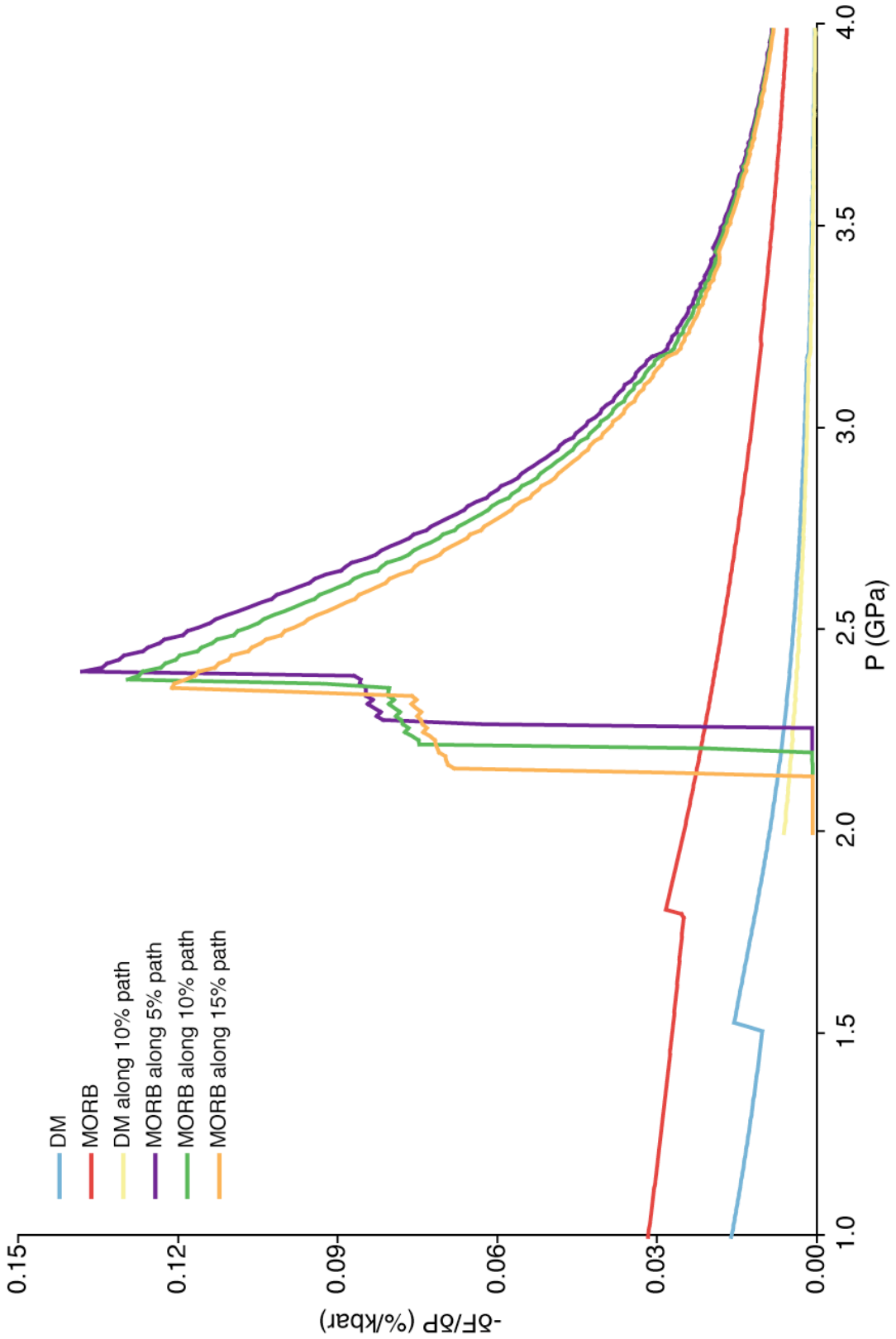
DM
MORB
DM along 10% path
MORB along 5% path
MORB along 10% path
MORB along 15% path
0.15
0.12
0.09
0.06
0.03
0.00
-∂F/∂P (%/kbar)
1.0
1.5
2.0
2.5
3.0
3.5
4.0
P (GPa)

Figure 26. Geochemical evolution of the peridotite and eclogite components in the binary mixing model. Representative major elements plotted against wt. % MgO illustrating the small effect of varying the proportion of initial eclogite in the mantle plume. Black diamond – Older Series lavas. Red circle – Initial peridotite. Green square – Initial eclogite. Red lines – Melting trajectories for peridotite component forced along 5, 10, and 15% initial eclogite composite P-T paths. Green lines – Melting trajectories for eclogite component forced along 5, 10, and 15% initial eclogite composite P-T paths. Blue crosses – Calculated mixtures of peridotite and eclogite melts generated along 5, 10, and 15% initial eclogite composite P-T paths (model shield magma). Blue line – LLOD of model shield magma for 10% initial eclogite P-T path. (a) SiO_2, (b) FeO_T, and (c) CaO plotted against wt. % MgO. Compositional trajectories for each component vary little with changing initial eclogite content, though the extent of mixing changes greatly as the amount of eclogite increases.

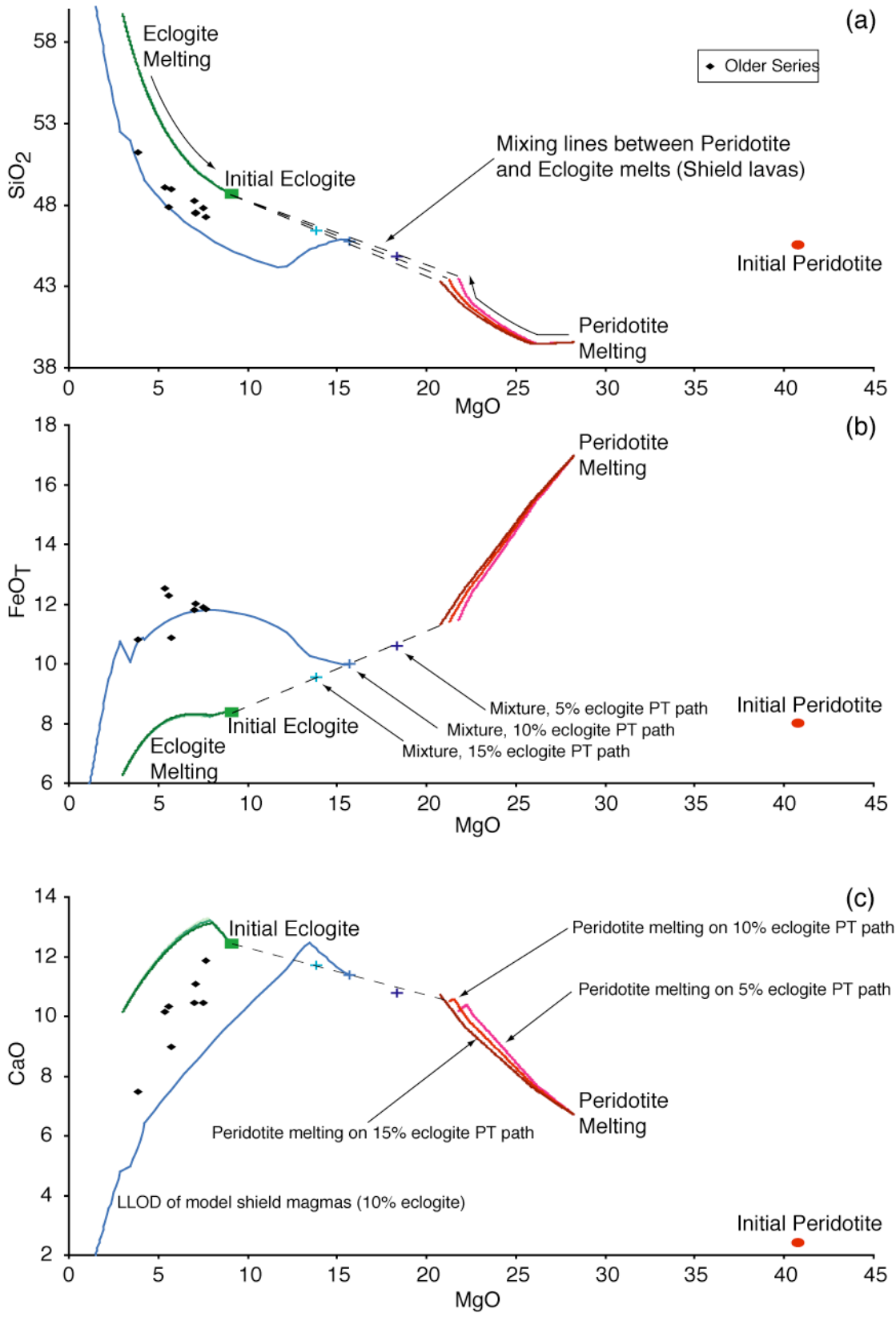
(a)
Eclogite Melting
Older Series
Mixing lines between Peridotite and Eclogite melts (Shield lavas)
Initial Eclogite
Initial Peridotite
Peridotite Melting
SiO2
MgO
(b)
Peridotite Melting
FeOT
Mixture, 5% eclogite PT path
Mixture, 10% eclogite PT path
Mixture, 15% eclogite PT path
Initial Peridotite
Initial Eclogite
Eclogite Melting
MgO
(c)
Initial Eclogite
Peridotite melting on 10% eclogite PT path
Peridotite melting on 5% eclogite PT path
Peridotite Melting
Peridotite melting on 15% eclogite PT path
CaO
LLOD of model shield magmas (10% eclogite)
Initial Peridotite
MgO

component along the three composite P-T paths create only minor chemical differences between model runs, and liquid trajectories for each eclogite proportion of the same component remain sub-parallel. At 10 wt. % CaO, the difference in MgO content between the three peridotite melt paths is ~1 wt. %. Trace elements demonstrate nearly identical characteristics.

Melts derived from the eclogitic and peridotitic model components can be plausibly mixed in any proportion, but the scenario in which they are mixed in the proportions generated by melting along the composite P-T path will be considered here. The proportion of eclogite-derived melt ($X_{F,ecl}$) can be calculated as:

$$X_{F,ecl} = \frac{X_{ecl} \cdot F_{ecl}}{X_{ecl} \cdot F_{ecl} + (1 - X_{ecl}) \cdot F_{per}} \qquad 5.1$$

where X_{ecl} is the proportion of eclogite in the plume, F_{ecl} is the melt fraction of eclogite (the enriched component), and F_{per} is the melt fraction of peridotite (the depleted component). The term $1 - X_{ecl}$ thus represents the proportion of peridotite in the plume, X_{per}.

For each of the composite P-T paths, the enriched eclogitic component melts to completion ($F_{ecl} = 1.00$). The extent of melting for the depleted peridotitic component varies systematically as a function of both potential temperature and initial eclogite percentage (Table 13). In general, increasing the temperature and decreasing the proportion of eclogite increase the degree of melting of the peridotitic component. F_{per} increases from a minimum of 0.04 (T_P = 1450 °C and $X_{ecl} = 0.15$) to a maximum of 0.31 (T_P = 1600 °C and $X_{ecl} = 0.05$). While the proportion of eclogite-derived melt, $X_{F,ecl}$, decreases with increasing F_{per} (Equation 5.1), the amount of eclogitic melt is solely a function of the proportion of initial eclogite in the system.

When comparing compositions derived computationally from pMELTS, it is important to remember the goal of this exercise is not to match precisely the exact

Table 13. Major element concentrations of the modeled shield magmas from the binary mixing model. Results are shown for 5, 10, and 15% initial eclogite in the plume for (a) T_P = 1450 °C, (b) T_P = 1525 °C, and (c) T_P = 1600 °C. The amount of eclogite derived melt in the model shield magma, $X_{F,ecl}$, is given for each computational run and increases with increasing initial eclogite content and decreasing potential temperature. The composition of the shield magma is shown in grey.

(a) 1450°C Potential Temperature

5% Eclogite

	SiO_2	TiO_2	Al_2O_3	Cr_2O_3	MgO	CaO	Na_2O	K_2O	P_2O_5	FeO_T	F
Peridotite	43.23	1.31	11.78	0.20	19.17	9.44	3.24	0.43	0.25	9.89	0.06
Eclogite	48.64	1.01	17.58	0.03	9.08	12.44	2.65	0.03	0.08	7.70	1.00
$X_{F,Ecl}$	SiO_2	TiO_2	Al_2O_3	Cr_2O_3	MgO	CaO	Na_2O	K_2O	P_2O_5	FeO_T	Mg#
0.48	45.85	1.16	14.58	0.12	14.29	10.89	2.96	0.23	0.17	8.83	74

10% Eclogite

	SiO_2	TiO_2	Al_2O_3	Cr_2O_3	MgO	CaO	Na_2O	K_2O	P_2O_5	FeO_T	F
Peridotite	43.31	1.35	11.97	0.21	18.84	9.21	3.55	0.49	0.28	9.75	0.05
Eclogite	48.65	1.01	17.57	0.03	9.07	12.44	2.65	0.03	0.08	7.70	1.00
$X_{F,Ecl}$	SiO_2	TiO_2	Al_2O_3	Cr_2O_3	MgO	CaO	Na_2O	K_2O	P_2O_5	FeO_T	Mg#
0.69	47.01	1.11	15.85	0.08	12.07	11.45	2.92	0.17	0.14	8.33	72

15% Eclogite

	SiO_2	TiO_2	Al_2O_3	Cr_2O_3	MgO	CaO	Na_2O	K_2O	P_2O_5	FeO_T	F
Peridotite	43.31	1.35	11.97	0.21	18.84	9.21	3.55	0.49	0.28	9.75	0.04
Eclogite	48.65	1.01	17.57	0.03	9.07	12.44	2.65	0.03	0.08	7.70	1.00
$X_{F,Ecl}$	SiO_2	TiO_2	Al_2O_3	Cr_2O_3	MgO	CaO	Na_2O	K_2O	P_2O_5	FeO_T	Mg#
0.80	47.63	1.08	16.50	0.06	10.93	11.76	2.89	0.13	0.13	8.07	71

(b) 1525°C Potential Temperature

5% Eclogite

	SiO_2	TiO_2	Al_2O_3	Cr_2O_3	MgO	CaO	Na_2O	K_2O	P_2O_5	FeO_T	F
Peridotite	43.41	0.91	10.04	0.23	21.89	10.14	1.61	0.17	0.10	10.37	0.14
Eclogite	48.60	1.01	17.61	0.03	9.09	12.43	2.65	0.03	0.08	7.71	1.00
$X_{F,Ecl}$	SiO_2	TiO_2	Al_2O_3	Cr_2O_3	MgO	CaO	Na_2O	K_2O	P_2O_5	FeO_T	Mg#
0.27	44.84	0.94	12.12	0.18	18.37	10.77	1.90	0.13	0.09	9.64	77

10% Eclogite

	SiO_2	TiO_2	Al_2O_3	Cr_2O_3	MgO	CaO	Na_2O	K_2O	P_2O_5	FeO_T	F
Peridotite	43.33	0.95	10.27	0.22	21.35	10.47	1.71	0.18	0.11	10.29	0.13
Eclogite	48.60	1.01	17.61	0.03	9.09	12.43	2.65	0.03	0.08	7.71	1.00
$X_{F,Ecl}$	SiO_2	TiO_2	Al_2O_3	Cr_2O_3	MgO	CaO	Na_2O	K_2O	P_2O_5	FeO_T	Mg#
0.46	45.76	0.98	13.65	0.13	15.70	11.37	2.14	0.11	0.09	9.10	75

15% Eclogite

	SiO_2	TiO_2	Al_2O_3	Cr_2O_3	MgO	CaO	Na_2O	K_2O	P_2O_5	FeO_T	F
Peridotite	43.25	0.99	10.51	0.21	20.86	10.68	1.84	0.20	0.12	10.23	0.12
Eclogite	48.60	1.01	17.61	0.03	9.09	12.43	2.65	0.03	0.08	7.71	1.00
$X_{F,Ecl}$	SiO_2	TiO_2	Al_2O_3	Cr_2O_3	MgO	CaO	Na_2O	K_2O	P_2O_5	FeO_T	Mg#
0.60	46.44	1.00	14.74	0.10	13.85	11.72	2.32	0.10	0.09	8.73	74

Table 13. *(continued)*

(c) 1600°C Potential Temperature

5% Eclogite

	SiO_2	TiO_2	Al_2O_3	Cr_2O_3	MgO	CaO	Na_2O	K_2O	P_2O_5	FeO_T	F
Peridotite	44.95	0.51	6.89	0.41	28.73	6.22	0.77	0.08	0.05	10.28	0.31
Eclogite	48.60	1.01	17.61	0.03	9.09	12.43	2.65	0.03	0.08	7.71	1.00
$X_{F,Ecl}$	SiO_2	TiO_2	Al_2O_3	Cr_2O_3	MgO	CaO	Na_2O	K_2O	P_2O_5	FeO_T	Mg#
0.15	45.48	0.58	8.47	0.35	25.85	7.13	1.05	0.07	0.05	9.90	82

10% Eclogite

	SiO_2	TiO_2	Al_2O_3	Cr_2O_3	MgO	CaO	Na_2O	K_2O	P_2O_5	FeO_T	F
Peridotite	44.70	0.55	7.31	0.38	27.87	6.66	0.85	0.09	0.05	10.41	0.28
Eclogite	48.60	1.01	17.61	0.03	9.09	12.43	2.65	0.03	0.08	7.71	1.00
$X_{F,Ecl}$	SiO_2	TiO_2	Al_2O_3	Cr_2O_3	MgO	CaO	Na_2O	K_2O	P_2O_5	FeO_T	Mg#
0.29	45.82	0.68	10.25	0.28	22.50	8.31	1.36	0.07	0.06	9.63	81

15% Eclogite

	SiO_2	TiO_2	Al_2O_3	Cr_2O_3	MgO	CaO	Na_2O	K_2O	P_2O_5	FeO_T	F
Peridotite	44.48	0.59	7.70	0.36	27.04	7.11	0.93	0.09	0.06	10.50	0.25
Eclogite	48.60	1.01	17.61	0.03	9.09	12.43	2.65	0.03	0.08	7.71	1.00
$X_{F,Ecl}$	SiO_2	TiO_2	Al_2O_3	Cr_2O_3	MgO	CaO	Na_2O	K_2O	P_2O_5	FeO_T	Mg#
0.41	46.18	0.76	11.78	0.22	19.65	9.30	1.63	0.07	0.07	9.35	79

compositions of lavas from Mauritius, rather to determine whether the model is capable of reproducing lavas with similar chemical characteristics. Reproducing the lavas in detail would require comprehensive knowledge about the exact components in the plume and the melting history, with the eclogitic and peridotitic components modeled here as only two of a wide variety of hypotheses. The composition of recycled mantle eclogite is dependent on many factors involved in the recycling process, including the initial concentrations of elements, the low-temperature alteration history, the degree of subduction processing, and the history of mixing and residence time in the mantle. Furthermore, the definition of eclogite used here is in itself quite broad and encompasses most of the Earth's surface products. A final factor for uncertainty comes from the pMELTS algorithm itself, which is parameterized exclusively for peridotitic compositions (Ghiorso et al., 2002). The eclogitic composition selected here (*e.g.*, MORB-based eclogite) requires the algorithm to extrapolate beyond its calibrated bounds. However, while individual calculations may not be strictly correct, generalized trends are likely to hold (Smith and Asimow, 2005). Future refinements to the model will be possible with the public release of xMELTS (Ghiorso et al., 2007).

Baxter (1975) suggested that the parental magma for the Older Series lavas can be approximated by the most basic of the observed aphyric lavas, represented by sample A171 (Table 14). More basic lavas are observed within the Older Series (MgO > 18 wt. %), though they are strongly enriched in olivine and clinopyroxene, likely representing cumulate phases (Baxter, 1975). Sobolev and Nikogosian (1994) and Albarède et al. (1997) proposed slightly more magnesian parental magma compositions (MgO ≈ 15 wt. %) for the Réunion shield lavas since 500 ka, lavas that are very similar to those from the Older Series. Calculated mixtures of eclogite and peridotite melts can be compared to this estimated composition as a test of the relative

Table 14. Estimates of parental magma compostions for Mauritius lavas

Source	SiO2	TiO2	Al2O3	FeO_T	MnO	MgO	CaO	K2O	Na2O	P2O5	Mg#[1]
Shield Lavas											
Baxter (1975), A171	46.85	2.54	12.75	11.50	0.16	10.48	10.01	0.95	2.59	0.40	62
Albarede et al. (1997)			11.60	12.30		14.50	12.00				68
Sobolev and Nikogosian (1994)	45.60	2.20	12.40	11.10		15.30	10.30	0.76	2.10		71
Lacroix (1936), Sample 15	46.70	2.50	11.30	9.70	0.16	16.40	9.90	0.60	1.70	0.10	75
primary magma solution	*46.74*	*2.51*	*11.30*	*9.71*	*0.16*	*16.37*	*9.86*	*0.59*	*1.72*	*0.11*	*75*

Estimates of parental magma compositions of Mauritian lavas used to constrain the initial composition of successful model parental shield magmas. Samples considered as parental magmas include sample A171 (Baxter, 1975) from Mauritius and sample 15 (Lacroix, 1936) from Réunion. Two predicted parental magmas are also considered (Sobolev and Nikogosian, 1994; Albarède et al., 1997). Furthermore, the modeled composition for sample 15 of Lacroix, the sole sample from Réunion to provide a successful solution from the PRIMELT2 algorithm (Herzberg and Asimow, 2008), is considered. [1]Total Fe as FeO

suitability of the melting model. For this model, MgO is perhaps the best major oxide to monitor as initial concentrations for the components show the greatest absolute difference between the two components (40.80 wt. % in DM, 9.10 wt. % in MORB). As an example, for a plume with a potential temperature of 1600 °C (T_0 = 1650 °C) and a eclogite proportion of 0.10, melts derived from the eclogite and peridotite components compose 28.6% and 71.4% of the binary melt mixture (Equation 5.1), forming a magma with an MgO of 22.50 wt. % (Table 13). Binary magma calculations for 5% modal eclogite are more magnesian (MgO > 25 wt. %) and the furthest from our parental Older Series melt, whereas an initial proportion of 15% eclogite produces a mixed magma with 19.65 wt. % MgO. As expected, increasing the modal proportion of initial eclogite increases the eclogite-like character of the mixed melts. Decreasing the potential temperature produces less magnesian melts, though the systematics of varying the amount of initial eclogite remains the same. The liquid line of descent[11] (LLOD) for a plume with T_P = 1525 °C and 10% initial eclogite can be observed in Figure 6. Of the three hypothesized parental magmas, the LLOD for sample A171 of Baxter (1975) under these conditions most closely resembles the observed Mauritius data.

However, the MgO content for this parental magma is exceedingly low and the Mg# for the proposed parental magma is only 62 (total Fe as FeO), not in equilibrium with mantle peridotite (Mg# ~70). The parental magma proposed by Sobolev and Nikogosian (1994) and Albarède et al. (1997) have higher MgO contents (14.5 and 15.3 wt. %, respectively) and Mg#s of 68 and 71, respectively, more in equilibrium

[11] LLOD calculation by MELTS (Ghiorso and Sack, 1995). Based on the observed mineralogy assemblage of the Older Series (olivine + clinopyroxene ± plagioclase feldspar; Baxter, 1975) and the phase diagram constructed by Albarède et al. (1997; their Figure 21) for the analogous lavas of Piton de la Fournaise (Réunion), lavas were allowed to undergo isobaric fractional crystallization at 0.8 GPa, with f_{O_2} = QFM+2 (Horn et al., 1994).

with the mantle. These MgO contents are somewhat lower than estimated parental magmas from other plume localities (*e.g.*, 17 – 22 wt. % MgO for Mauna Loa, Hawaii; 17 – 20 wt. % for Pitcairn; Herzberg and Asimow, 2008), but may be satisfactory nevertheless. Despite producing a LLOD similar to the observed Mauritius Older Series lavas, sample A171 of Baxter (1975) is not in equilibrium with the mantle and is likely an unsuitable composition for the parental magma for the Older Series lavas, though three additional parental magma candidates remain.

In their attempt to model the potential temperature of the Réunion plume using PRIMELT2, Herzberg and Asimow (2008) found that nearly all shield lavas from Piton de la Fournaise (Réunion Island) were compromised by clinopyroxene fractionation, and thus unable to provide model solutions. Herzberg (2006) found the lavas from Piton de la Fournaise to be too deficient in CaO to be primary melts of a peridotite source, and required fractionation of clinopyroxene to explain the low CaO values observed in erupted lavas. The conclusion that clinopyroxene fractionation was key in the evolution of the Réunion shield lavas is consistent with the interpretation of Albarède et al. (1997), who argued for the role of cumulate formation from high-pressure (>0.8 GPa) fractionation of clinopyroxene during ascent through the lithosphere. If clinopyroxene fractionation is not accounted for in the models of potential temperature as well as olivine, the resulting primary magmas will be too rich in MgO (up to 4 wt. %). The removal of augitic pyroxene[12] (+ olivine) from the system reduces the CaO of the residual liquid but also increases the FeO content, which in turn requires higher MgO concentrations (via olivine addition) to reach equilibrium with the mantle. Errors introduced by ignoring clinopyroxene fractionation can propagate to an ~100 °C excess in potential temperature (Herzberg

[12] Augite is a calcic clinopyroxene with extensive solid solution between Ca^{2+}, Mg^{2+}, and Fe^{2+}, and between Al^{4+} and Si^{4+}. See Appendix E.

and Asimow, 2008). Of the Réunion samples tested by the PRIMELT2 model, only one sample produced a satisfactory primary magma solution, sample 15 of Lacroix (1936), with an MgO content of 16.4 wt. % (Table 14) and a T_P = 1493 °C. Primary magma calculations were performed for all thirty-nine new Mauritius lavas, as well as Baxter's parental A171 composition, using the recommended condition that Fe_2O_3/TiO_2 = 0.5 in the primary magma. Acceptable solutions within the framework of PRIMELT2 were not obtained for any of the samples as each was flagged as potentially being compromised by clinopyroxene fractionation. Furthermore, thirty-three of the new Mauritius samples, including seven of eight Older Series lavas, were tagged as potentially forming from pyroxenite sources. Similar to the effects of clinopyroxene fractionation, lavas derived from a pyroxenite source will have estimated MgO contents 2 – 3% too high and potential temperatures ~50 – 70 °C too high (Herzberg and Asimow, 2008).

For the binary melt-mixing model with T_P = 1525 °C and 10% initial eclogite, the modeling of the major elements are shown in Figures 26 and 27 for the model shield magmas. The compositions of the initial peridotite and eclogite are depicted in the figures and Table 14. Looking at panel (a) in each figure, the initial peridotite has higher MgO (40.80 wt. %) and lower SiO_2 (45.57 wt. %) than the initial eclogite composition (MgO = 9.10 and SiO_2 = 48.68 wt. %). When melting commences at 4.0 GPa, the peridotite-derived melts are lower in both MgO and SiO_2 than the initial composition, and increase with extent of melting. Likewise, the first melts of the eclogitic component have lower MgO, but have higher SiO_2 contents (andesitic) than the initial composition. As melting continues, the SiO_2 content of the eclogite-derived melt continues to decrease, while the MgO increases. The compositional trajectories for the melts of each component are shown in Figure 26. In Figure 27, and all figures hereafter, only the composition of the final melt of each component is shown. The

Figure 27. Representative major element compositions for the geochemical evolution of the binary mixing model with T_P = 1525 °C and a maximum vertical ascent of the post-erosional source in the plume stem to 3.0 GPa, for a plume with 10% initial eclogite. Black diamond – Older Series lavas. Open black diamond – Post-erosional lavas. Green square – Initial eclogite. Open green square – Eclogite melt at 2.0 GPa. Small light green square – Residual eclogite melt at 2.7 GPa. Red circle – Initial peridotite (not visible, MgO = 40.8 wt. %). Open red circle – Peridotite melt at 2.0 GPa. Small pink circle – Residual peridotite melt at 2.7 GPa. Light blue cross – Model shield magma. Dark blue cross – Model post-erosional magma. Light blue line – LLOD of model shield magma at 0.8 GPa (after Albarède et al., 1997). Dark blue line – LLOD of model post-erosional magma at 0.8 GPa. Dashed lines represent mixing lines between peridotite and eclogite melts at 2.0 GPa and residual eclogite and residual peridotite melts at 2.7 GPa, respectively. In the binary mixing model, the peridotitic and eclogitic component are each allowed to rise along the 10% initial eclogite composite P-T path from 4.0 to 2.0 GPa. The melts of each component generated by this decompression are mixed, producing the model shield magma. At 2.0 GPa, the eclogitic component has melted completely and the melt has the same composition as the initial eclogite, and plot together. The model post-erosional lavas are generated in a very similar manner. The two plume component rise along the 10% initial eclogite composite P-T path from 4.0 to 3.0 GPa where any melts are extracted. The residual components then continue decompression through the plume tail from 3.0 to 2.7 GPa (after Ribe and Christensen, 1999). Any melts generated in this region are mixed to form the model post-erosional magma. See text for full description. (a) SiO_2, (b) FeO_T, and (c) CaO plotted against wt. % MgO. The model shield magma composition reproduces SiO_2 and FeO_T well, though CaO is low for a given MgO content. The model post-erosional lava has an MgO content (9.6 wt. %) too low to produce the bulk of the observed Intermediate and Younger Series lava via fractional crystallization.

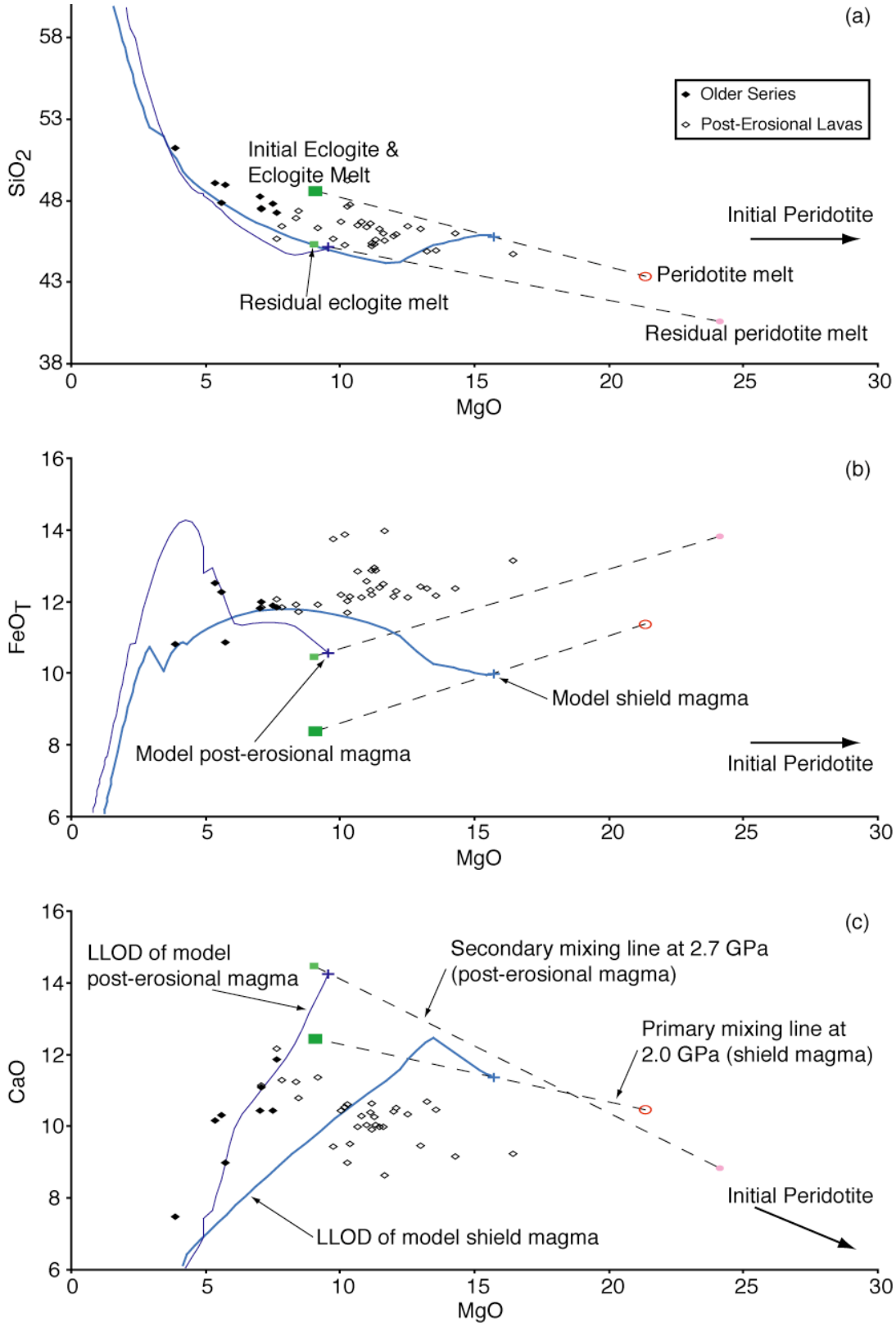
(a)
Older Series
Post-Erosional Lavas
Initial Eclogite &
Eclogite Melt
Initial Peridotite
Peridotite melt
Residual eclogite melt
Residual peridotite melt
SiO2
MgO
(b)
Model shield magma
Model post-erosional magma
Initial Peridotite
FeOT
MgO
(c)
LLOD of model
post-erosional magma
Secondary mixing line at 2.7 GPa
(post-erosional magma)
Primary mixing line at
2.0 GPa (shield magma)
Initial Peridotite
LLOD of model shield magma
CaO
MgO

system continues melting until 2.0 GPa, when the plume intersects the base of the oceanic lithosphere. The peridotitic component melts 13% to a picritic composition (MgO = 21.35 and SiO_2 = 43.33 wt. %). The eclogitic component melts completely (F_{ecl} = 1), giving the final melt the same composition as the initial eclogite. The melts generated from each component are then mixed in the respective proportions in which they are produced during melting (Equation 5.1) to produce the modeled parental magma for the shield lavas, which are balanced between the peridotite- and eclogite-derived melts ($X_{F,ecl}$ = 0.46). This model shield magma can then be used to calculate the LLOD and compare the modeled magma to the observed Older Series data. An identical procedure can be applied to the 5 and 15% initial eclogite models (Table 13).

As both the appropriateness of applying peridotite-based primary magma calculations to lavas with extensive clinopyroxene fractionation (Herzberg and Asimow, 2008) and the relative accuracy of pMELTS calculations for basaltic compositions are uncertain (Ghiorso et al., 2002), only modeled lavas with < 20 wt. % MgO will be considered as the parental magmas for the Mauritian shield lavas (Table 13). The majority of lavas with a potential temperature of 1600 °C remain overly magnesian as melt fractions for the peridotite component are large (F_{per} > 0.25). The model with 15% initial eclogite is the lone exception, which has an elevated but allowable MgO content of 19.7 wt. %. All three compositions from the T_P = 1525 °C models are within the established parameters for MgO (13.9 – 18.4 wt. %), as is the 5% eclogite model for a potential temperature of 1450 °C. Select liquid lines of descent are shown in Figure 27 for T_P = 1525 °C at 10% initial eclogite. These LLODs demonstrate that the modeled major element oxides, though far from perfect, follow similar trends to the Older Series lavas and are generally consistent with the observed range of compositions. Modeled TiO_2 and K_2O contents (not shown) are low relative to the observed data (a factor of 3 and an order of magnitude,

respectively), both related primarily to the extensive melting of the eclogitic component, $F_{ecl} = 1$, at all combinations of temperature and eclogite proportion. An additional factor for the low model-TiO_2 may stem from the parameterization of pMELTS, which does not include a titanium-component in the garnet solid solution model (Ghiorso et al., 2002), where Ti^{4+} commonly substitutes into the normally trivalent garnet Y-site (Meagher, 1980; Pertermann et al., 2004).

Using Adiabat_1ph, trace element partitioning is integrated into the MELTS and pMELTS algorithms, allowing for the detailed tracking of the trace element evolution of a system. Here I utilize this functionality to iteratively fit the initial (source) concentrations required for each component to the Older Series shield lavas as 2.0 GPa parental magmas (Table 15). The initial iteration used N-MORB of Hofmann (1988) as an analogue for the eclogitic component, and DM of McKenzie and O'Nions (1991; 1995) for the peridotitic component.

Calculations can be made for the trace element and isotope ratios for the model shield elements, and are identical to the procedure described above for the major elements. Figure 28 shows the trace element results for the binary melt-mixing model with T_P = 1525 °C and 10% initial eclogite. The initial peridotite has lower La/Sm (3.00) and Sm/Yb (2.73) than the initial eclogite (La/Sm = 4.47 and Sm/Yb = 4.47, a coincidence; Table 15a). These compositions have been fit to the two components such that the model shield magma reproduces the observed Older Series values. When melting commences at 4.0 GPa, the first melts of the peridotite- (La/Sm = 4.14 and Sm/Yb = 7.92) and eclogite-derived melts (La/Sm = 6.36 and Sm/Yb = 28.88) are greater than their respective initial components, but decrease as the degree of melting increases (not shown). When melting ceases at 2.0 GPa, the peridotitic component has melted 13% with melts enriched slightly over the initial concentration (3.07 and 2.97). The eclogitic component has melted completely ($F_{ecl} = 1$) and has the same trace

Table 15. Binary melt-mixing model shield lava trace elements, 10% eclogite

(a) 1525°C Potential Temperature, $P_{max,PE}$ = 3.0 GPa

Init. Conc.	La	Sm	Yb	Hf	Zr	Nb	Sr	Nd	Pb	Ba	La/Sm	Sm/Yb	Hf/Zr	Sr/Nd	La/Nb	Pb/Yb	Zr/Nb	Ba/La	
Peridotite	0.90	0.30	0.11	0.26	12.00	1.30	16.00	0.75	0.27	12.00	3.00	2.73	0.022	21.33	0.69	2.45	9.23	13.33	
Eclogite	17.00	3.80	0.85	2.30	104.00	14.00	113.00	15.00	0.70	90.00	4.47	4.47	0.022	7.53	1.21	0.82	7.43	5.29	
	La	Sm	Yb	Hf	Zr	Nb	Sr	Nd	Pb	Ba	La/Sm	Sm/Yb	Hf/Zr	Sr/Nd	La/Nb	Pb/Yb	Zr/Nb	Ba/La	*F*
Peridotite	6.86	2.24	0.75	1.95	82.88	9.67	120.85	5.64	2.07	92.04	3.07	2.97	0.024	21.42	0.71	2.74	8.57	13.41	0.13
Eclogite	17.00	3.80	0.85	2.30	104.00	14.00	113.00	15.00	0.70	90.00	4.47	4.47	0.022	7.53	1.21	0.82	7.43	5.29	1.00
$X_{F,ecl}$	La	Sm	Yb	Hf	Zr	Nb	Sr	Nd	Pb	Ba	La/Sm	Sm/Yb	Hf/Zr	Sr/Nd	La/Nb	Pb/Yb	Zr/Nb	Ba/La	
0.46	11.53	2.96	0.80	2.11	92.60	11.66	117.23	9.95	1.44	91.10	3.90	3.71	0.023	11.78	0.99	1.80	7.94	7.90	

(b) 1525°C Potential Temperature, $P_{max,PE}$ = 2.5 GPa

Init. Conc.	La	Sm	Yb	Hf	Zr	Nb	Sr	Nd	Pb	Ba	La/Sm	Sm/Yb	Hf/Zr	Sr/Nd	La/Nb	Pb/Yb	Zr/Nb	Ba/La	
Peridotite	1.35	0.30	0.15	0.17	7.35	1.05	18.00	0.72	0.38	25.00	4.50	2.00	0.023	25.00	1.29	2.50	7.00	18.52	
Eclogite	13.00	3.80	0.64	3.40	160.00	18.00	135.00	15.00	0.20	20.00	3.42	5.94	0.021	9.00	0.72	0.31	8.89	1.54	
	La	Sm	Yb	Hf	Zr	Nb	Sr	Nd	Pb	Ba	La/Sm	Sm/Yb	Hf/Zr	Sr/Nd	La/Nb	Pb/Yb	Zr/Nb	Ba/La	*F*
Peridotite	10.30	2.24	1.03	1.28	50.76	7.81	135.95	5.42	2.87	191.75	4.60	2.18	0.025	25.10	1.32	2.79	6.50	18.63	0.13
Eclogite	13.00	3.80	0.64	3.40	160.00	18.00	135.00	15.00	0.20	20.00	3.42	5.94	0.021	9.00	0.72	0.31	8.89	1.54	1.00
$X_{F,ecl}$	La	Sm	Yb	Hf	Zr	Nb	Sr	Nd	Pb	Ba	La/Sm	Sm/Yb	Hf/Zr	Sr/Nd	La/Nb	Pb/Yb	Zr/Nb	Ba/La	
0.46	11.54	2.96	0.85	2.25	101.06	12.50	135.51	9.83	1.64	112.66	3.90	3.48	0.022	13.79	0.92	1.93	8.08	9.76	

Trace elements for the binary melt-mixing model shield magma with 10% initial eclogite. Results are shown for both the $P_{max,PE}$ = (a) 3.0 and (b) 2.5 GPa models. Although these pressures do not affect the shield magmas, the trace elements were adjusted for each of the post-erosional models to better fit the entire suite of data. F is the degree of melting for each component when adiabatic decompression ceases at 2.0 GPa. The proportion of eclogite melt, $X_{F,ecl}$, composing the magma is given. The composition of the shield magma is shown in grey.

Figure 28. Representative incompatible trace element composition for the geochemical evolution of the binary mixing model with T_P = 1525 °C and a maximum vertical ascent of the post-erosional source in the plume stem to 3.0 GPa, for a plume with 10% initial eclogite. Symbols after Figure 27. Solid curves represent mixing lines between peridotite and eclogite melts at 2.0 GPa and residual eclogite and residual peridotite melts at 2.7 GPa, respectively. Vertical and horizontal dashed lines represent trace element ratio of Primitive Mantle (McDonough and Sun, 1995). La/Sm plotted against Sm/Yb. Incompatible trace element compositions of the initial eclogite and initial peridotite are chosen such that the model shield magma fits the observed Older Series trace element data. Trace element compositions of the initial compositions are kept constant for the post-erosional lavas. In this model, the post-erosional magma consists of 96% melts of the eclogitic residue and does not represent the observed post-erosional data.

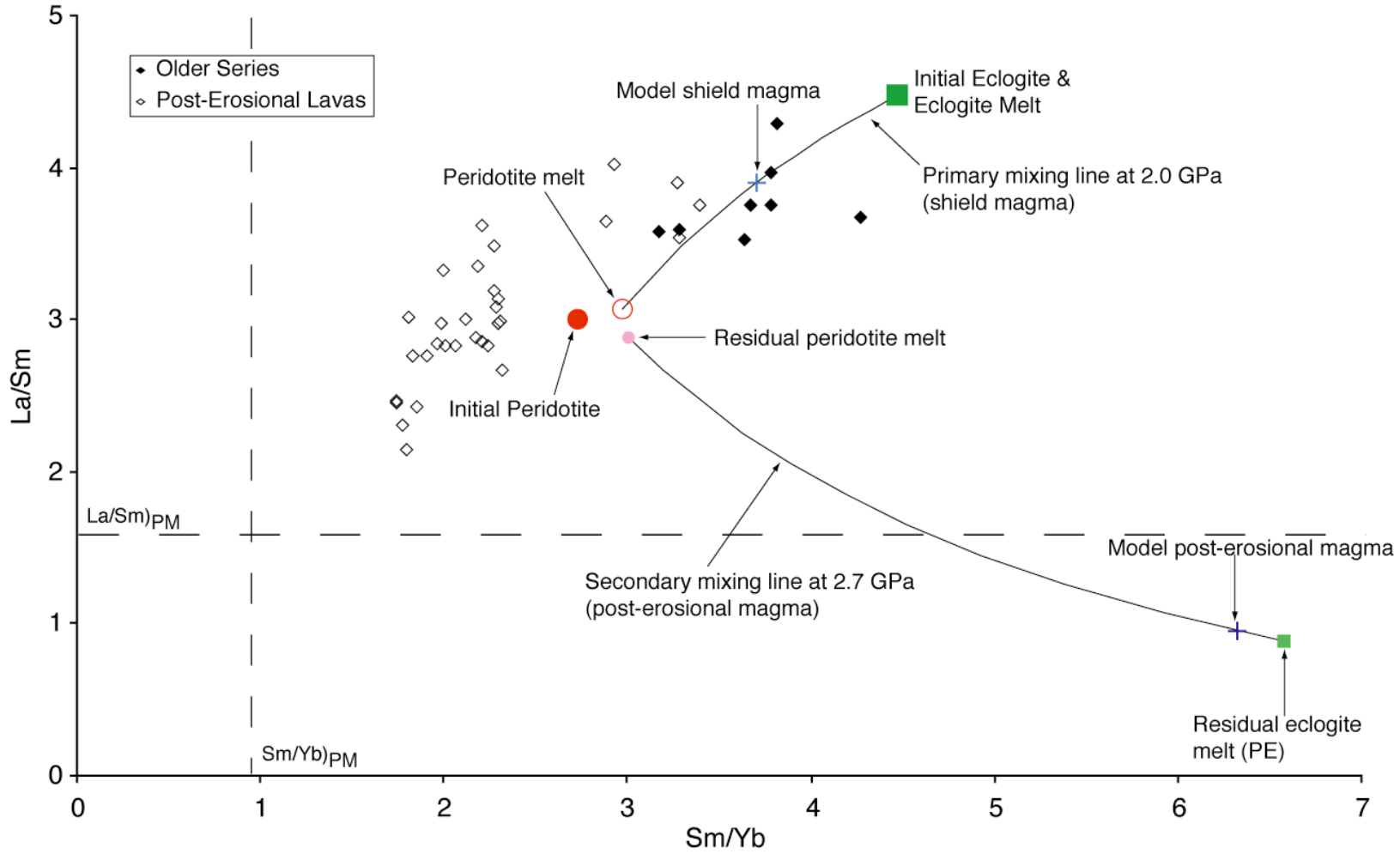
Older Series
Post-Erosional Lavas
Model shield magma
Initial Eclogite &
Eclogite Melt
Peridotite melt
Primary mixing line at 2.0 GPa
(shield magma)
Residual peridotite melt
Initial Peridotite
La/Sm)PM
Model post-erosional magma
Secondary mixing line at 2.7 GPa
(post-erosional magma)
Residual eclogite
melt (PE)
Sm/Yb)PM
La/Sm
Sm/Yb
0
1
2
3
4
5
6
7

element ratios as the initial component. The two melts are then combined ($X_{F,ecl}$ = 0.46) to produce the model shield magma (Figure 28). In an effort to maintain clarity and simplicity, the discussion of trace element and isotopic results (Figure 29; Table 16) for the shield lavas will focus on models with T_P = 1525 °C and 10% initial eclogite, unless otherwise specified.

Perhaps the most compelling feature of the binary melt-mixing model for the shield magmas is the extensive melting of the plume components (*e.g.*, Table 13). In each of the binary models, the eclogitic component melts completely, F_{ecl} = 1.00. Comparatively, the more refractory peridotitic component melts from 4 to 31%, with the degree of melt increasing as the initial eclogite content of the plume decreases and the potential temperature of the plume increases. The complete melting of the eclogitic component modeled here is contradictory to the assumption of Sobolev et al. (2005) about the extent to which this component will melt. Based on work by Kushiro (2001), Sobolev argued that because melting in the mantle occurs (near-) fractionally, the eclogitic residue will become refractory once the melt fraction reaches approximately 0.5. At this point, the component becomes inert and its contributions to the melt cease. However, under the batch (equilibrium) melting conditions modeled in this work, the melt fraction for the eclogitic component was found to reach 1.0, consistent with experimental data for melting under conditions appropriate for Hawaii (Takahashi et al., 2002). Early forms of this model attempted to include near-fractional melting, ϕ = 0.005 – 0.01 (where ϕ is the retained melt fraction, *e.g.* Albarède, 1995), and produced lower melt fractions at a given temperature, though computational instability derailed these efforts.

A consequence of completely melting the eclogitic component is that the composition of the final melt is equivalent to the initial eclogitic composition. As observed in Figure 26, the SiO_2 content of the melt decreases as the extent of melting

Figure 29. Isotope ratios systematics for the geochemical evolution of the binary mixing model with T_P = 1525 °C and a maximum vertical ascent of the post-erosional source in the plume stem to 3.0 GPa, for a plume with 10% initial eclogite. Symbols after Figure 27 and 28. End-member isotope compositions are chosen to reflect the observed range of Mauritius lavas. Plots of Sm/Yb against (a) $^{87}Sr/^{86}Sr$, (b) ε_{Nd}, and (c) $^{206}Pb/^{204}Pb$. Trace element concentrations for mixing are taken from compositions of the model shield and post-erosional magmas. Model shield magmas reproduce Sr- and Nd-isotopes well, but do not fit Pb-isotopes. Model post-erosional magmas are dominated by the enriched melts of the eclogitic residue ($X_{F,ecl}$ = 0.96) and are not representative of the observed data.

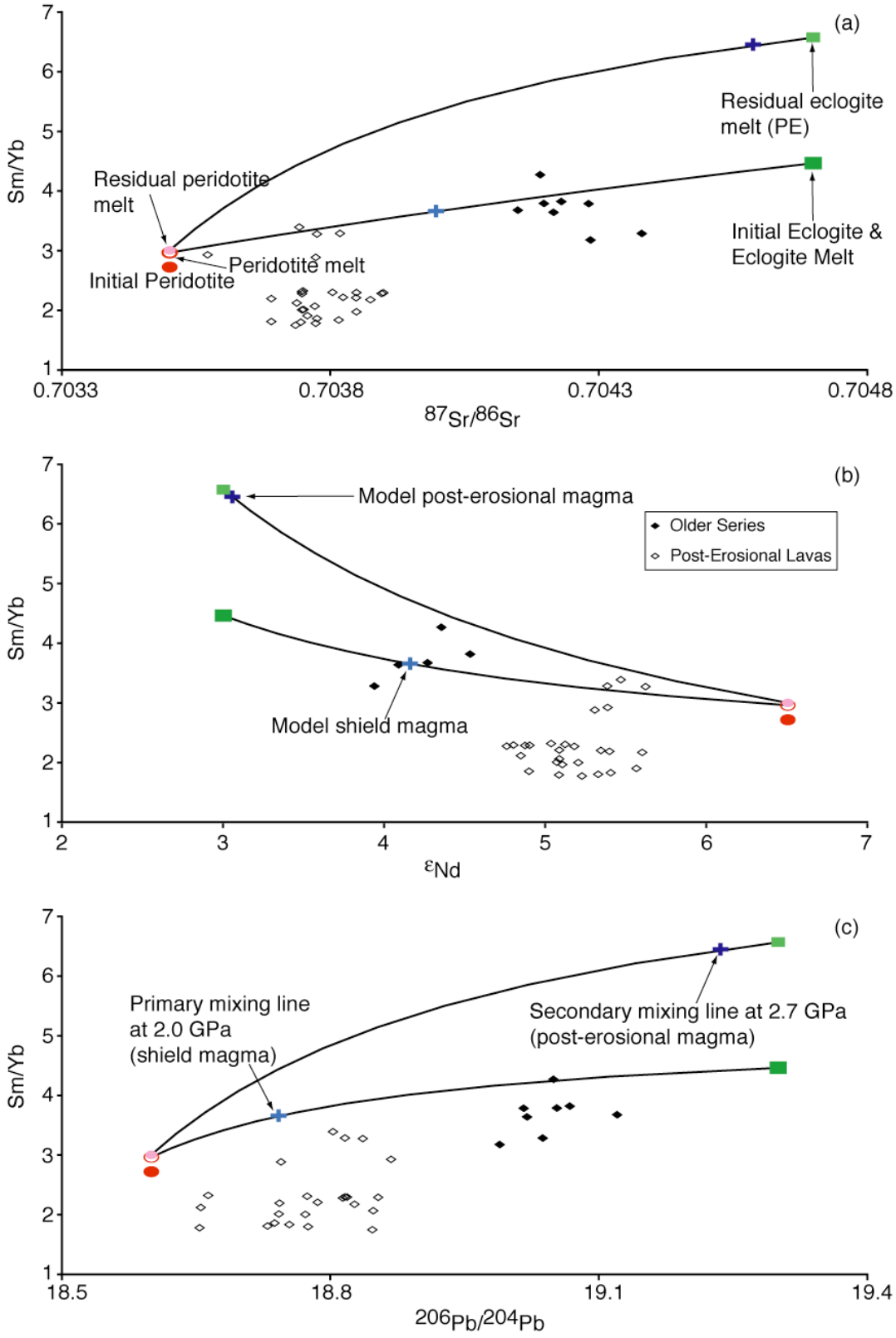
(a)
Residual eclogite melt (PE)
Residual peridotite melt
Initial Eclogite & Eclogite Melt
Peridotite melt
Initial Peridotite
Sm/Yb
$^{87}Sr/^{86}Sr$
0.7033
0.7038
0.7043
0.7048
(b)
Model post-erosional magma
Older Series
Post-Erosional Lavas
Model shield magma
Sm/Yb
εNd
(c)
Primary mixing line at 2.0 GPa (shield magma)
Secondary mixing line at 2.7 GPa (post-erosional magma)
Sm/Yb
$^{206}Pb/^{204}Pb$
18.5
18.8
19.1
19.4

Table 16. Binary mixing model shield magma isotope ratios

(a) 1525 °C Potential Temperature, $P_{max,PE}$ = 3.0 GPa

1525°C Potential Temperature, 10% Eclogite						
	Sr	Nd	Pb	$^{87}Sr/^{86}Sr$	εNd	$^{206}Pb/^{204}Pb$
Peridotite	120.85	5.64	2.07	0.70350	6.50	18.60
Eclogite	113.00	15.00	0.70	0.70470	3.00	19.30
$X_{F,Ecl}$	Sr	Nd	Pb	$^{87}Sr/^{86}Sr$	εNd	$^{206}Pb/^{204}Pb$
0.46	117.23	9.95	1.44	0.70400	4.16	18.74

(b) 1525 °C Potential Temperature, $P_{max,PE}$ = 2.5 GPa

1525°C Potential Temperature, 10% Eclogite						
	Sr	Nd	Pb	$^{87}Sr/^{86}Sr$	εNd	$^{206}Pb/^{204}Pb$
Peridotite	135.95	5.42	2.87	0.70350	6.50	18.60
Eclogite	135.00	15.00	0.20	0.70470	3.00	19.30
$X_{F,Ecl}$	Sr	Nd	Pb	$^{87}Sr/^{86}Sr$	εNd	$^{206}Pb/^{204}Pb$
0.46	135.51	9.83	1.64	0.70419	3.73	18.66

Isotope ratios for the binary melt-mixing model shield magma with 10% initial eclogite. (a) Model with initial trace element ratios for post-erosional ascent to 3.0 GPa. (b) Model with initial trace element ratios for post-erosional ascent to 2.5 GPa. Trace element differences reflect the different starting compositions for the two models. The composition of the shield magma is shown in grey.

of the eclogitic component increases. Once the component is completely melted, the melt has the SiO_2 content of the initial eclogite (48.68 wt. %; Table 11). The compositions and melting trajectories of the peridotite-derived melts are also shown, and demonstrate the potential differences in compositions between lower-degree melts (F_{per} = 0.12 – 0.14) and the initial component.

The implications of the extensive eclogitic melting on the binary melt-mixing model are best observed from trace element ratios (*e.g.*, Figure 28). As the extent of melting of the eclogitic component grows large in the shield model, both the abscissa (*e.g.*, La/Sm) and ordinate (*e.g.*, Sm/Yb) ratios converge toward and eventually reach their initial values. As there is a rather limited range of La/Sm for the Older Series shield lavas (3.5 – 4.3), the extensive melting provides certain constraints on the initial trace element ratios in both components, eclogitic and peridotitic. The relative constancy of the LREE slope in the shield lavas requires a relatively shallow slope for the mixing line between the eclogite- and peridotite-derived melts. Thus, the La/Sm ratios of these melts, of large and small degrees, respectively, must not differ greatly. Therefore, both the initial La/Sm ratio for eclogite and the final melt fraction of the peridotite component must be near the average La/Sm of the Older Series (La/Sm = 3.77). Indeed, the observation that the initial trace element ratios of the eclogitic component are equivalent to the eclogite-derived melt allows ratios for this component to be set, allowing the ratios and concentrations of the initial peridotite the degrees of freedom necessary to be iteratively adjusted until the model shield magma (Equation 5.1) fits the Older Series data.

It is important to emphasize that this modeling attempts to fit model shield magmas to the observed Mauritius Older Series lavas by forward modeling of the initial incompatible trace element ratios in the component sources (*i.e.*, eclogite and peridotite) via Adiabat_1ph. Primitive mantle (PM) normalized trace element patterns

for the initial trace element concentrations are shown in Figure 30a along with the published values for Depleted Mantle (reference for peridotite component; DM of McKenzie and O'Nions, 1991; 1995) and N-MORB (reference for eclogite component; Hofmann, 1988). Incompatible trace element ratios, rather than absolute abundances, were utilized for fitting the model to the observed shield lavas. This approach does require at least one element to be fixed, allowing the other elements to be adjusted accordingly. Here, I elected to fix Sm to a value near the reference value for each component (Sm_{DM} = 0.299 and $Sm_{N\text{-}MORB}$ = 3.752 ppm; Table 15). No further attempt was made to scale the initial element abundances such that the model shield magma would reproduce the concentrations of the Older Series shield lavas. Regardless, the observed PM normalized patterns can be compared directly to the reference values. In Figure 30a and Table 15, two distinct sets of trace element patterns are given for the binary melt-mixing model. The differences between these patterns are related to the maximum pressure of adiabatic ascent in generating the model post-erosional magmas ($P_{max,PE}$ = 2.5 and 3.0 GPa), and are simply minor modifications made to the initial concentrations to better fit the observed post-erosional lavas. Results for the post-erosional models associated with each of these parameter combinations will be discussed in detail below. Despite these modifications, the two sets of initial concentrations for the peridotitic and eclogitic components are broadly consistent.

Several key observations about the modeled initial trace element concentrations are evident from Figure 30a. First, the model peridotitic components are strongly enriched in the most incompatible elements relative to DM (McKenzie and O'Nions, 1991; 1995), but broadly consistent throughout the moderately incompatible elements. Both peridotite components have lower Yb than DM. Positive Pb anomalies are observed, whereas DM has a strong negative anomaly.

Figure 30. Primitive mantle normalized trace element concentrations of modeled source components. (a) Binary melt-mixing model. Solid dark blue – Eclogite component with $P_{max,PE}$ = 2.5 GPa. Dashed dark blue – Eclogite component with $P_{max,PE}$ = 3.0 GPa. Solid red – Peridotite component with $P_{max,PE}$ = 2.5 GPa. Dashed red – Peridotite component with $P_{max,PE}$ = 3.0 GPa. Dark grey – N-MORB of Hofmann (1988). Light grey – DM of McKenzie and O'Nions (1991; 1995). Light blue – Subduction processed N-MORB by method of Kogiso et al. (1997). The modeled source compositions of the eclogite and peridotite components are based no the compositions of N-MORB and DM, respectively, by fixing the model Sm concentration to a value near these reference values. N-MORB is taken to be an eclogitic analogue and DM as a peridotitic analogue. The $P_{max,PE}$ = 2.5 GPa values (solid lines) are the best fit models. The model requires an enrichment of the most incompatible elements relative to N-MORB and DM, though the concentrations of the moderately incompatible elements are similar. (b) Hybrid melting model. Solid blue line – Eclogite component. Solid red line – Peridotite component. Both components are for the $P_{max,PE}$ = 2.5 GPa model. N-MORB and DM as in (a). Model result also require enrichment of the most incompatible elements. Primitive mantle of McDonough and Sun (1995).

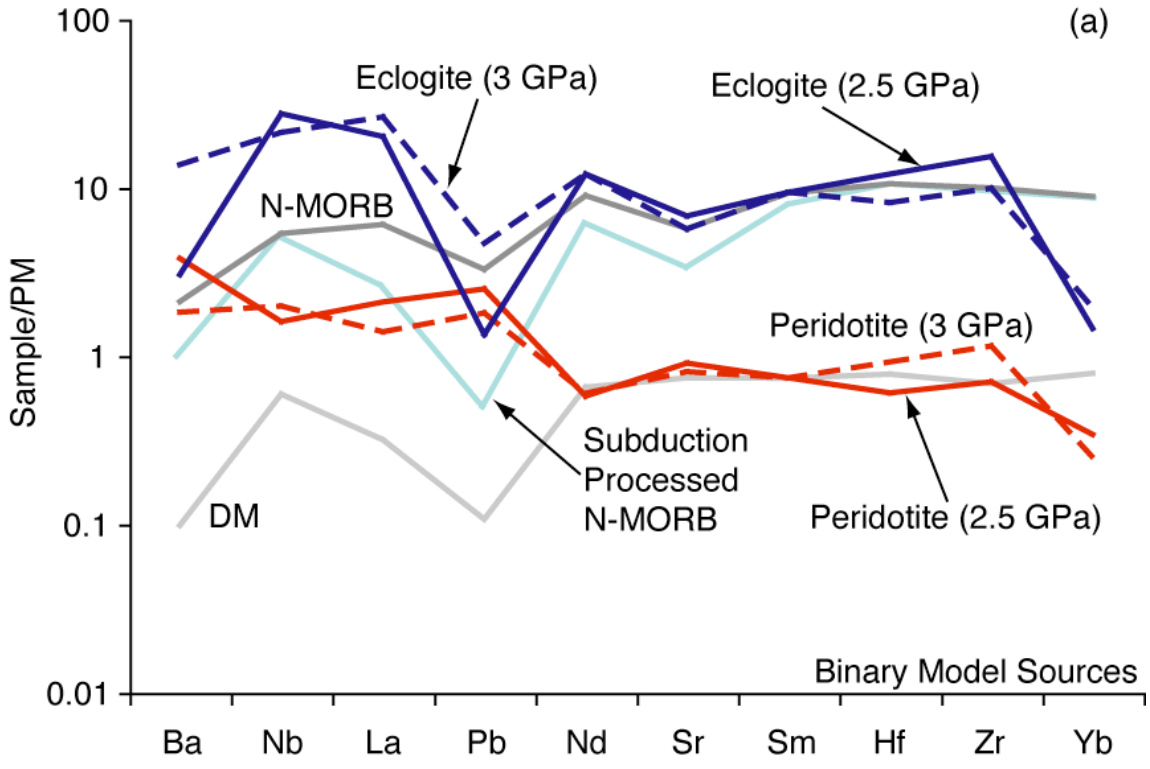
(a)
100
10
1
0.1
0.01
Sample/PM
Eclogite (3 GPa)
Eclogite (2.5 GPa)
N-MORB
Peridotite (3 GPa)
Subduction
Processed
N-MORB
DM
Peridotite (2.5 GPa)
Binary Model Sources
Ba
Nb
La
Pb
Nd
Sr
Sm
Hf
Zr
Yb

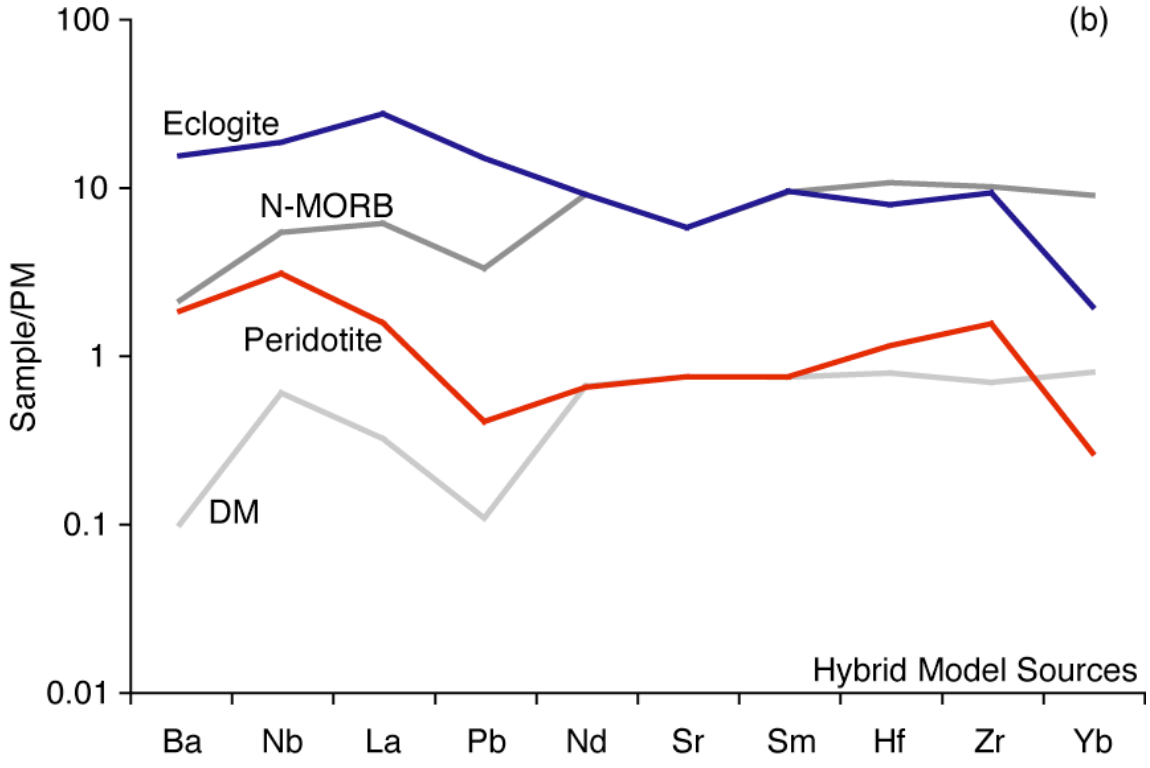
(b)
100
10
1
0.1
0.01
Sample/PM
Eclogite
N-MORB
Peridotite
DM
Hybrid Model Sources
Ba
Nb
La
Pb
Nd
Sr
Sm
Hf
Zr
Yb

Second, the model eclogitic components are also enriched in the most incompatible elements over N-MORB (Hofmann, 1988). Each eclogitic component has a negative Ba anomaly, though of varying degrees. Strong negative Pb anomalies are also observed. Similar to the model peridotitic components, the eclogitic components are broadly consistent with N-MORB for the moderately incompatible elements, but have lower Yb. Finally, each of these model results have steep normalized REE patterns $(La/Sm)_N$, $Sm/Yb)_N$, and $La/Yb)_N > 1$), which differs from the reference values for each source $(La/Sm)_N$ and $La/Yb)_N < 1$ and $Sm/Yb)_N \approx 1$). In all cases, $Zr/Nb)_N < 1$, where reference values are greater than unity.

Though the two source models are broadly consistent, significant differences exist within each component (Figure 30a). For both the peridotitic and eclogitic components, the differences between the models are greatest for the most incompatible, and to a lesser degree, the least incompatible trace elements. Concentrations in the moderately incompatible elements are very similar. The 3.0 GPa models have somewhat lower concentrations of highly incompatible elements and slightly higher concentrations of less incompatible elements, producing a flatter trace (less steep) spider diagram.

While certain aspects of these normalized trace element patterns for each component are dictated by the choice of major element composition and thermodynamic algorithm, and are thus necessary (*e.g.*, relatively steep REE slope), these solutions are decidedly non-unique. Ideally a more rigorous mathematical treatment (*e.g.*, the inverse modeling method of White and McKenzie, 1995) could be integrated into Adiabat_1ph, potentially providing further constraints on the range of initial concentrations and ratios for each component within a given set of parameters.

Before further discussion of the implications of these modeled results for the binary shield magmas, it is worth reiterating that for this work, the eclogitic component is taken to be the isotopically enriched component. Again, there are no explicit geochemical observations that require the low-solidus (eclogitic) component be the isotopically enriched component, though it does seem to be the prevalent interpretation (*e.g.*, Hauri, 1996), and a refractory component with an enriched isotopic signature appears to make less geologic sense. The model isotopic ratios for the depleted peridotitic ($^{87}Sr/^{86}Sr = 0.70350$; $\varepsilon_{Nd} = +6.50$; $^{208}Pb/^{204}Pb = 18.60$) and the enriched eclogitic sources ($^{87}Sr/^{86}Sr = 0.70450$; $\varepsilon_{Nd} = +3.00$; $^{208}Pb/^{204}Pb = 19.30$) are chosen to represent the fictive endpoints of the Mauritian isotopic array (*i.e.*, Figure 12). These values are held consistent throughout this work, including the post-erosional and hybrid models. The range of these endpoints is relatively restricted, as is the range of lavas associated with the modern Réunion hotspot track (*e.g.*, White et al., 1990), especially when compared to the known range of OIB lavas (*e.g.*, Zindler and Hart, 1986).

Using the chosen isotopic compositions for the depleted and enriched components, the isotopic results of the binary model shield magmas are calculated for the modeled initial trace element compositions (Table 15). In the first model ($P_{max,PE} = 3.0$ GPa), the model $^{87}Sr/^{86}Sr$ and $^{206}Pb/^{204}Pb$ are each lower than the observed Older Series lavas (Figure 29), and each would benefit from a more enriched depleted component ($^{87}Sr/^{86}Sr \approx 0.70370$ and $^{206}Pb/^{204}Pb \approx 19.00$). Despite being somewhat depleted, the model Sr-isotope ratio does maintain some of the enriched measure of the Older Series lavas (*i.e.*, $^{87}Sr/^{86}Sr > 0.70400$). The Pb-isotopic ratio is strongly depleted relative to the Older Series lavas ($^{206}Pb/^{204}Pb = 18.74$), a function of the melts of the isotopically enriched eclogitic component being depleted in Pb (0.70 ppm), an

order of magnitude less than the peridotitic melts (2.07 ppm). The model ε_{Nd} accurately reproduces the Older Series lavas (+4.16).

The results of the second binary model shield magmas ($P_{max,PE}$ = 2.5 GPa) successfully reproduce the $^{87}Sr/^{86}Sr$ and, to a lesser extent, the ε_{Nd} values of the Older Series lavas from the chosen isotopic compositions. A small increase in the isotopic composition of either component would better fit the model magma to the observed lavas. Again, the model Pb-isotopic ratio is dominated by the relatively Pb-rich melts (2.87 ppm) of the depleted peridotite-derived melts versus the Pb-poor melts (0.20 ppm) of the enriched eclogitic melts.

Overall, it is apparent that, apart from the Pb-isotopes, the assumption of choosing isotopic endpoints from the spread of Mauritius isotopic data is reasonable. The misfit in the model Pb relates to the low concentrations in the eclogitic melts, which is directly related to the extensive melting experienced by the eclogitic component.

Comparatively, each of the two model shield magmas produced by the binary model are very similar (Figure 31). The $P_{max,PE}$ = 2.5 GPa model is more enriched than the 3.0 GPa model in all elements except Nd (9.83 versus 9.95 ppm, respectively). Both model magmas are essentially parallel to the Older Series lavas, though absolute concentrations are lower by a factor of 3 to 4. This relative depletion relates to the fact that trace element ratios were modeled rather than absolute concentrations, although abundances may be affected by the assumption of batch melting as well.

Post-Erosional Lavas

While extensive numerical modeling has been conducted on the generation of shield lavas at ocean island localities worldwide (*e.g.*, Farnetani et al., 2002; Ito and

Figure 31. Primitive mantle normalized trace element concentrations of modeled magmas. Solid red – Binary shield magma from $P_{max,PE}$ = 2.5 GPa model. Dashed red – Binary shield magma from $P_{max,PE}$ = 3.0 GPa model. Pink – Binary post-erosional magma from $P_{max,PE}$ = 2.5 GPa model. Solid blue – Hybrid shield magma. Light blue – Hybrid post-erosional magma. Dark grey field – range of Older Series shield lavas. Light grey field – range of Intermediate and Younger Series lavas. Both hybrid magmas from $P_{max,PE}$ = 2.5 GPa models. Modeled shield magmas are similar across the two models, though the hybrid have slightly lower concentrations. Both models reproduce the intra-elements slopes, though the overall concentrations are lower than the Older Series lavas, likely a product of model assumptions about melting. The model post-erosional magmas also have lower concentrations than the Intermediate and Younger Series lavas. The binary model produces a smoother pattern than the hybrid model, though each reproduce the overall pattern of the post-erosional lavas. Primitive mantle of McDonough and Sun (1995).

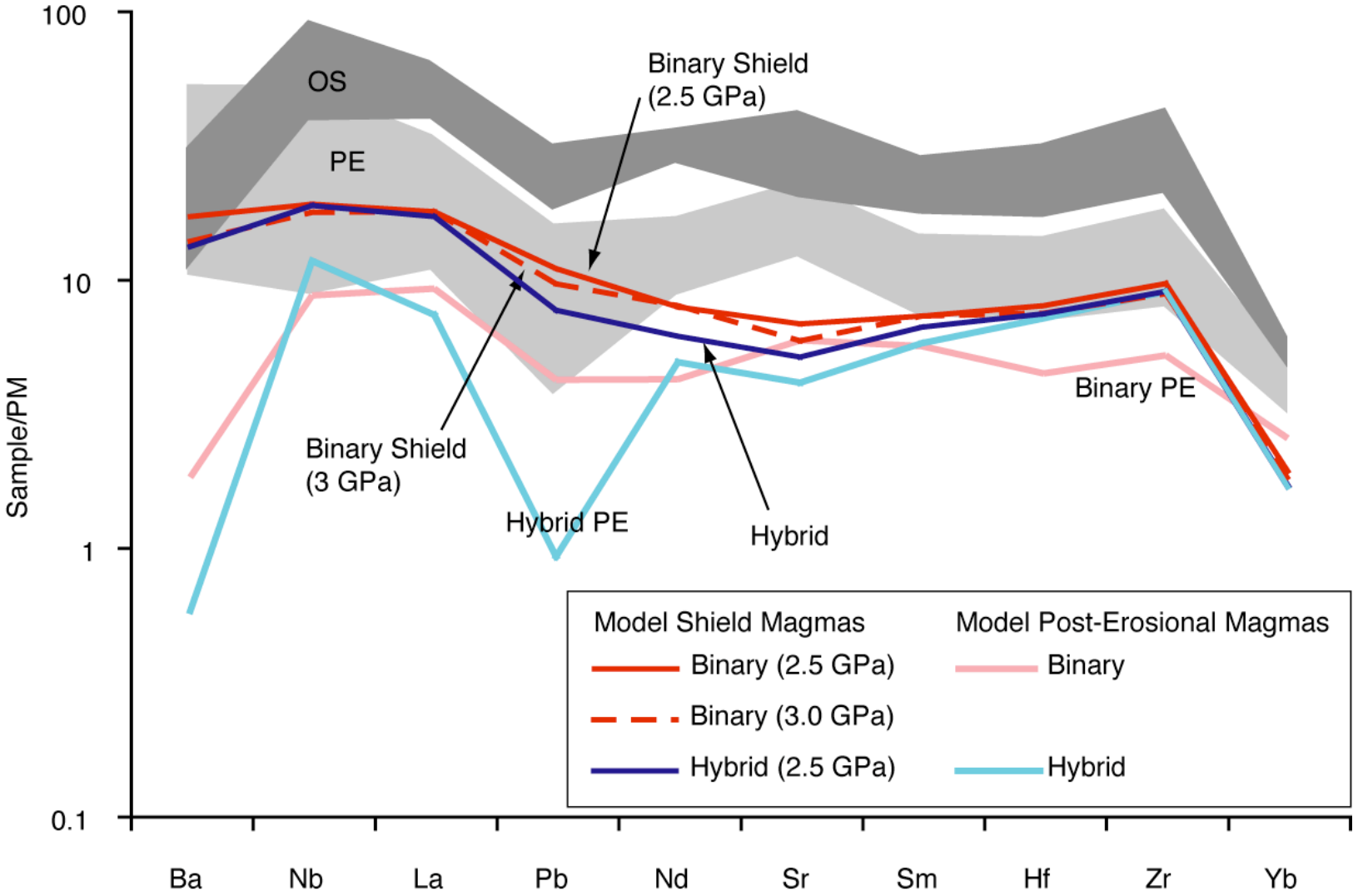
100
10
1
0.1
Sample/PM
OS
PE
Binary Shield
(2.5 GPa)
Binary Shield
(3 GPa)
Hybrid PE
Hybrid
Binary PE
Model Shield Magmas
Binary (2.5 GPa)
Binary (3.0 GPa)
Hybrid (2.5 GPa)
Model Post-Erosional Magmas
Binary
Hybrid
Ba
Nb
La
Pb
Nd
Sr
Sm
Hf
Zr
Yb

Mahoney, 2005a,b), the role of melting and re-melting as materials pass downstream through the plume tail has received little attention. Studies that have included models for the plume tail have presented conflicting scenarios for the thermal history of material passing through these zones. The study of Ribe and Christensen (1999) identified a secondary melting zone within the plume tail wherein the material ascends and decompresses as the tail spreads laterally, producing small degree melts. Interpreting from their Figure 5, this material undergoes approximately 10 km of decompression (vertical ascent) and cools by approximately 50 °C, a non-adiabatic PT-path. In this model scenario, a temperature decrease of 50 °C is prescribed over a vertical ascent of 10 km, producing an average thermal ascent profile of 0.006 GPa/°C.

Alternatively, the studies of Phipps Morgan and Morgan (1999) and Yamamoto and Phipps Morgan (in prep) also found decompression (vertical ascent) to occur within the plume tail as it spread laterally. However, material ascending through the axis of the tail was found to behave nearly-adiabatically. In this scenario, temperatures decrease only ~15 °C over the 10 km vertical ascent, for an average thermal ascent profile of 0.019 GPa/°C. These authors did not expressly predict post-erosional volcanism with their models, though the possibility of an eruptible product cannot be precluded. The contrasting thermal solutions provide very different results when applied to the melting models in this work. Here, I will discuss the implementation and results of these models of the plume tail for both the binary melt-mixing model, as well as the hybrid model.

The post-erosional particle paths identified by Ribe and Christensen (1999) and mimicked by Phipps Morgan and Morgan (1999) and Yamamoto and Phipps Morgan (in prep) are distinct from those that form the shield lavas. These particle

paths exist toward the periphery of the plume, and consequently ascend to lower pressures than do the shield magma source rocks (Figure 32). As a result, the post-erosional lavas are modeled separately from the shield lavas, though many of the characteristics of modeling are similar.

Modeling the post-erosional lavas does not differ widely from the methods used to model the shield lavas, though small changes in pressure and temperature steps result in significant geochemical disparity. Just as for the models of the shield lavas with T_P = 1525 °C and 10% initial eclogite, the thermodynamic models output data for the evolution of the major (Figure 27) and trace elements (Figure 28), and isotopic ratios (Figure 29). Here, the procedure for the trace element ratios will be discussed in detail. In order to maintain geochemical consistency between the shield and post-erosional models, the trace element ratios determined for each component for the shield lavas are applied to the models of the post-erosional. The initial peridotite has lower La/Sm (3.00) and Sm/Yb (2.73) than the initial eclogite (La/Sm = 4.47 and Sm/Yb = 4.47; Table 15a). The plume material then ascends adiabatically along the 10 % initial eclogite composite P-T path from 4.0 GPa to the level where the plume begins to flatten out from intersecting the base of the lithosphere. For the post-erosional magmas, this level is deeper than that of the shield lavas because material from the upstream and axial portions of the plume impinge on the base of the lithosphere and fold over, increasing the effective thickness of the upper boundary layer on the downstream side of the plume and limiting the amount of vertical ascent (Figure 32). In this model, the maximum level of vertical ascent within the plume stem, $P_{max,PE}$, is 3.0 GPa. At this point the peridotitic component has melted 7% and the melts have La/Sm = 3.59 and Sm/Yb = 3.10, greater than the initial ratios (not shown in Figure 28). The eclogitic component has melted to a much greater extent (F_{ecl} = 0.71), though the La/Sm (4.79) and Sm/Yb (10.84) are still greater than the

Figure 32. Idealized melting structure of the Réunion mantle plume (modified from Paul et al., 2005). The eclogitic and hybrid pyroxenite bodies (plums) within the plume cross their respective solidii at greater depths and begin to melt earlier than the peridotite matrix. This produces a graded melting zone with the different components contributing to lavas samples from different depths. Particle paths for the shield magmas (red line) and post-erosional magmas (black line) are from Ribe and Christensen (1999) and represent the generalized spatial and pressure-temperature paths for the mantle material that generate each series. The shield path passes through the hotter center of the plume and experiences greater degrees of melting, while the post-erosional path passes along a potentially cooler path closer to the periphery of the plume. This path enters the downstream plume tail at a greater depth (larger pressure) and experiences less decompression, and thus lower degrees of melting. The downstream side of the plume represents the side of the plume where the plume tail has formed, and the upstream representing the side without the plume tail.

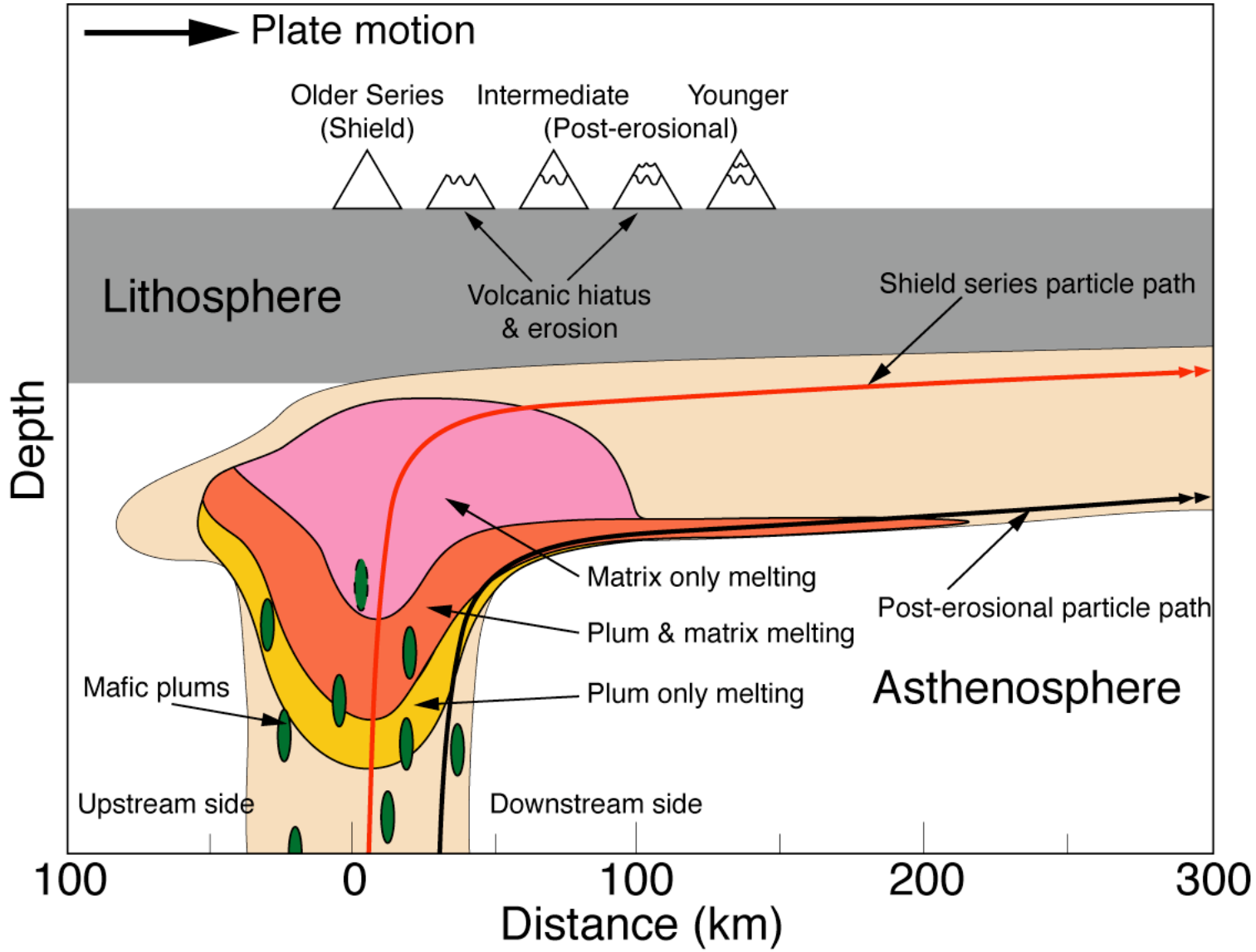
Plate motion
Older Series
(Shield)
Intermediate
(Post-erosional)
Younger
Lithosphere
Volcanic hiatus
& erosion
Shield series particle path
Depth
Matrix only melting
Post-erosional particle path
Plum & matrix melting
Mafic plums
Plum only melting
Asthenosphere
Upstream side
Downstream side
100
0
100
200
300
Distance (km)

ratios of the initial component. The peridotite-derived residue has La/Sm = 0.86 and Sm/Yb = 2.07, while the eclogitic-derived residue has La/Sm = 0.43 and Sm/Yb = 0.44. At this point, the melt-free residues produced by extraction of melt from 4.0 to 3.0 GPa become the sources for the model post-erosional parental magma as they enter the plume tail. When the source material is assumed to pass adiabatically through the plume tail (*e.g.*, Phipps Morgan and Morgan, 1999; Yamamoto and Phipps Morgan, in prep) the material along the post-erosional particle path ascends approximately 10 km, or 0.3 GPa where 1 GPa is taken to be approximately 35 km. Therefore, melting in the plume tail occurs between 3.0 and 2.7 GPa. Under these conditions, the peridotite-derived residue melts 0.2%, producing La/Sm = 2.89 and Sm/Yb = 3.01. Each of these ratios are larger than the source, though the Sm/Yb is larger and the La/Sm smaller than the ratio of the initial component. The melts of the eclogite-derived residue (La/Sm = 0.88 and Sm/Yb = 6.58) are also greater than the source, and have a smaller La/Sm and larger Sm/Yb than the initial eclogite ratio. Mixing the melts, the melts of the eclogite-derived residue compose 96% of the total model post-erosional parental magma.

The amount of melt generated by the peridotitic component that contributes to the model post-erosional parental magma at 2.7 GPa, $F_{per,27}$, can be calculated as:

$$F_{per,27} = X_{per}\left(1 - F_{per,43}\right) \cdot F_{per,327} \qquad 5.2$$

where X_{per} is the proportion of peridotite initially in the plume, $F_{per,43}$ is the melt fraction of peridotite from 4.0 to 3.0 GPa, and $F_{per,327}$ is the melt fraction of the peridotite residue from 3.0 to 2.7 GPa. The first term represents the proportion of the residual peridotite. A similar expression can be written for the eclogitic component. This scenario can also be considered to model a plume that produces a relatively thick plume tail or a particle path closer to the periphery of the plume.

To investigate the effect of decreasing the thickness of the effective upper boundary layer on the post-erosional particle paths, $P_{max,PE}$ is changed to 2.5 GPa. The initial peridotite has La/Sm = 4.50 and Sm/Yb = 2.00, and the initial eclogite has La/Sm = 3.42 and Sm/Yb = 5.94. These ratios are different than the above model, a consequence of slightly different trace element ratios being fit for the lower pressure model (Table 15b). The plume material then ascends adiabatically along the 10 % initial eclogite composite P-T path from 4.0 GPa to the level where the plume begins to flatten out from intersecting the base of the lithosphere. In this model, this level is 2.5 GPa. At this point the peridotitic component has melted 9% and the melts have La/Sm = 5.04 and Sm/Yb = 2.24, greater than the initial ratios (not shown in Figure 33). The eclogitic component has melted completely and has the trace element ratios of the initial eclogite composition. The peridotite-derived residue has La/Sm = 1.11 and Sm/Yb = 1.20, while no eclogitic residue is present. At this point, the melt-free residue of the peridotitic component produced by extraction of melt from 4.0 to 2.5 GPa becomes the sole source for the model post-erosional parental magma as it enters the plume tail. Therefore, melting in the plume tail occurs between 2.5 and 2.2 GPa. Under these conditions, the peridotite-derived residue melts 0.5%, producing La/Sm = 2.62 and Sm/Yb = 2.03. Each of these ratios are larger than the source, though the Sm/Yb is larger and the La/Sm smaller than the ratio of the initial component. As no eclogitic residue remains, the melts of the peridotite-derived residue compose 100% of the model post-erosional parental magma.

The amount of melt generated by the peridotitic component that contributes to the model post-erosional parental magma at 2.2 GPa, $F_{per,22}$, can be calculated as:

$$F_{per,22} = X_{per}\left(1 - F_{per,425}\right) \cdot F_{per,2522} \qquad 5.3$$

where X_{per} is the proportion of peridotite initially in the plume, $F_{per,425}$ is the melt fraction of peridotite from 4.0 to 2.5 GPa, and $F_{per,2522}$ is the melt fraction of the

Figure 33. Representative incompatible trace element composition for the geochemical evolution of the binary mixing model with T_P = 1525 °C and a maximum vertical ascent of the post-erosional source in the plume stem to 2.5 GPa, for a plume with 10% initial eclogite. Black diamond – Older Series lavas. Open black diamond – Post-erosional lavas. Green square – Initial eclogite. Open green square – Eclogite melt at 2.0 GPa. Small light green square – Residual eclogite melt at 2.2 GPa. Red circle – Initial peridotite (not visible, MgO = 40.8 wt. %). Open red circle – Peridotite melt at 2.0 GPa. Small pink circle – Residual peridotite melt at 2.2 GPa. Light blue cross – Model shield magma. Dark blue cross – Model post-erosional magma. Light blue line – LLOD of model shield magma at 0.8 GPa (after Albarède et al., 1997). Dark blue line – LLOD of model post-erosional magma at 0.8 GPa. In this version of the binary mixing model, the shield lavas are generated in the same manner, but for the post-erosional lavas the initial peridotite and eclogite and allowed to rise to 2.5 GPa before ceasing vertical ascent in the plume stem. The residual peridotite and eclogite components then continue decompression through the plume tail from 2.5 to 2.2 GPa. Any melts generated in this region are mixed to form the model post-erosional magma. Solid curves represent mixing lines between peridotite and eclogite melts at 2.0 GPa and residual eclogite and residual peridotite melts at 2.2 GPa, respectively. The horizontal dashed line represents the trace element ratio of Primitive Mantle (McDonough and Sun, 1995). (a) La/Sm, (b) La/Nb, and (c) Zr/Nb plotted against Sm/Yb. Incompatible trace element compositions of the initial eclogite and initial peridotite are chosen such that the model shield magma fits the observed Older Series trace element data. Trace element compositions of the initial compositions are kept constant for the post-erosional lavas. In this model, the eclogitic residue does not melt in the plume tail, leaving the model post-erosional magma with the trace element composition of the peridotitic

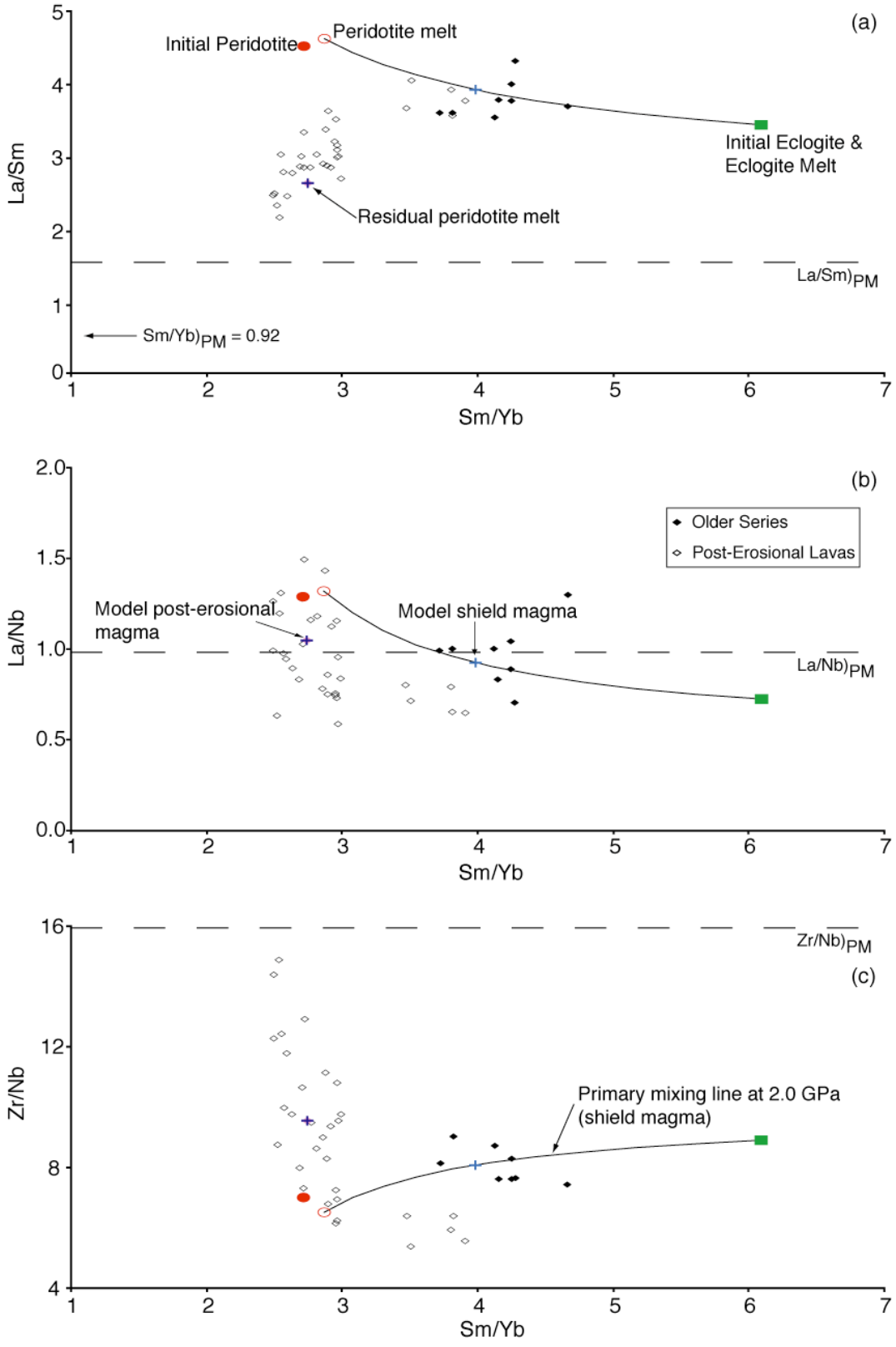
(a)
Initial Peridotite
Peridotite melt
Initial Eclogite &
Eclogite Melt
Residual peridotite melt
La/Sm)PM
Sm/Yb)PM = 0.92
La/Sm
Sm/Yb
(b)
Older Series
Post-Erosional Lavas
Model post-erosional
magma
Model shield magma
La/Nb)PM
La/Nb
Sm/Yb
Zr/Nb)PM
(c)
Primary mixing line at 2.0 GPa
(shield magma)
Zr/Nb
Sm/Yb

peridotite residue from 2.5 to 2.2 GPa. The first term represents the proportion of the residual peridotite. A similar expression can be written for the eclogitic component. This scenario can also be considered to model a plume that produces a relatively thinner tail or a particle path closer to the plume stem.

The excess temperature of mantle plumes relative to the surrounding asthenosphere is on the order of 200 °C (*e.g.*, Sleep, 1990). Though the plume loses little heat to the asthenosphere by conduction, the periphery of the plume is likely to be cooler than the axis (*e.g.*, Phipps Morgan, 2001). The post-erosional particle paths of Ribe and Christensen (1999) are depicted as 50 – 75 °C cooler than the central axis of the plume. To account for the radially decreasing temperature structure of the plume, the post-erosional particle paths are also modeled as having a potential temperature 75 °C cooler than the axially formed shield magmas (T_P = 1450 °C) for both maximal pressure levels, $P_{max,PE}$ = 2.5 and 3.0 GPa. Deviations in the thermal profile for the post-erosional particle paths do not alter the procedure from that described above, but will change the degree of melting and extent of fractionation.

Finally, if the non-adiabatic thermal profile prescribed exactly by the post-erosional particle path in Figure 5 of Ribe and Christensen (1999) is adopted, a temperature decrease of 50 °C over the 10 km vertical ascent produces an average thermal ascent profile of 0.006 GPa/°C. Under this profile, no additional melting of either component occurs for any of the pressure and temperature conditions described above. Given the rapid loss of heat from the system (non-adiabatic), both the eclogite and peridotite components are too refractory for further melting. Each simply passes through the secondary melting zone. Therefore, this scenario, as modeled, is an unsatisfactory solution.

The adiabatic thermal profile through the plume tail, as suggested by Phipps Morgan and others, can be combined with the pressure and thermal constraints

proposed above and developed into a series of models. When imposing an effective upper boundary layer of 3.0 GPa and a uniform plume temperature of T_P = 1525 °C, the post-erosional parental magmas are dominated by melts of the eclogitic component ($X_{F,ecl}$ = 0.96; Tables 17a, 18a, and 19a). This model is identical to the first post-erosional magma scenario described above. The modeled post-erosional melts from the eclogitic component are the product of moderate degree melts, $F_{ecl,327}$ = 0.13, of a highly depleted eclogite-derived residue, $F_{ecl,43}$ = 0.71. Melts from the peridotitic component are very low degree melts, $F_{per,327}$ = 0.002, of a slightly depleted peridotite-derived residue, $F_{per,43}$ = 0.07. The post-erosional parental magmas are much too low in MgO (9.57 wt. %) to be a true parental magma for the bulk of the Intermediate and Younger Series lavas (Figure 27). When trace element ratios are considered (Figure 28), the model post-erosional magma is much too low in La/Sm (0.95) and high in Sm/Yb (6.33), a product of being sourced almost exclusively by melts of the eclogite-derived residue. Similarly, the isotopic ratios for the model post-erosional magma are enriched ($^{87}Sr/^{86}Sr$ = 0.70459, ε_{Nd} = +3.06, and $^{206}Pb/^{204}Pb$ = 19.24), with near-eclogitic values (Figure 29). To fit this model to the observed data, the eclogitic component would need to be isotopically depleted, completely contradictory to the general modeling assumptions. This model would appear to provide an unsatisfactory solution.

Keeping with a uniform plume temperature of T_P = 1525 °C, but decreasing the effective upper boundary layer to 2.5 GPa, the post-erosional parental magmas are formed entirely from melts of the residual peridotite component (Tables 17b, 18b, and 19b). This model is identical to the second post-erosional magma scenario described above. The eclogitic component melts completely by 2.5 GPa ($F_{ecl,425}$ = 1.00), and consequently plays no role in the formation of the model post-erosional parental magmas in this scenario. Melts from the peridotitic component are very low degree

Table 17. Binary melt-mixing model for PE major elements, 10% eclogite

(a) 1525 °C Potential Temperature, $P_{max,PE}$ = 3.0 GPa

											$X_{F,ecl}$	0.96
	SiO_2	TiO_2	Al_2O_3	Cr_2O_3	MgO	CaO	Na_2O	K_2O	P_2O_5	FeO_T	F_{43}	F_{327}
Peridotite	40.60	1.07	8.88	0.19	24.12	8.84	2.46	0.00	0.00	13.82	0.13	0.00
Eclogite	45.35	0.87	17.30	0.01	9.02	14.46	2.39	0.00	0.00	10.45	1.00	0.13
	SiO_2	TiO_2	Al_2O_3	Cr_2O_3	MgO	CaO	Na_2O	K_2O	P_2O_5	FeO_T	Mg#	
	45.18	0.88	16.99	0.01	9.57	14.25	2.40	0.00	0.00	10.57	62	

(b) 1525 °C Potential Temperature, $P_{max,PE}$ = 2.5 GPa

											$X_{F,ecl}$	0.00
	SiO_2	TiO_2	Al_2O_3	Cr_2O_3	MgO	CaO	Na_2O	K_2O	P_2O_5	FeO_T	F_{425}	F_{2522}
Peridotite	40.60	1.07	8.88	0.19	24.12	8.84	2.46	0.00	0.00	13.82	0.09	0.01
Eclogite	--	--	--	--	--	--	--	--	--	--	1.00	0.00
	SiO_2	TiO_2	Al_2O_3	Cr_2O_3	MgO	CaO	Na_2O	K_2O	P_2O_5	FeO_T	Mg#	
	40.60	1.07	8.88	0.19	24.12	8.84	2.46	0.00	0.00	13.82	76	

(c) 1450 °C Potential Temperature, $P_{max,PE}$ = 3.0 GPa

											$X_{F,ecl}$	1.00
	SiO_2	TiO_2	Al_2O_3	Cr_2O_3	MgO	CaO	Na_2O	K_2O	P_2O_5	FeO_T	F_{43}	F_{327}
Peridotite	--	--	--	--	--	--	--	--	--	--	0.02	0.00
Eclogite	47.28	1.44	17.49	0.03	6.22	11.14	4.57	0.00	0.00	11.76	0.37	0.07
	SiO_2	TiO_2	Al_2O_3	Cr_2O_3	MgO	CaO	Na_2O	K_2O	P_2O_5	FeO_T	Mg#	
	47.28	1.44	17.49	0.03	6.22	11.14	4.57	0.00	0.00	11.76	49	

(d) 1450 °C Potential Temperature, $P_{max,PE}$ = 2.5 GPa

											$X_{F,ecl}$	0.97
	SiO_2	TiO_2	Al_2O_3	Cr_2O_3	MgO	CaO	Na_2O	K_2O	P_2O_5	FeO_T	F_{425}	F_{2522}
Peridotite	42.35	1.40	11.39	0.25	20.03	8.36	4.35	0.00	0.00	11.85	0.03	0.00
Eclogite	47.13	0.81	18.06	0.00	10.07	12.14	2.01	0.00	0.00	9.68	0.73	0.29
	SiO_2	TiO_2	Al_2O_3	Cr_2O_3	MgO	CaO	Na_2O	K_2O	P_2O_5	FeO_T	Mg#	
	46.98	0.83	17.86	0.01	10.38	12.02	2.08	0.00	0.00	9.75	65	

Major element contents for the binary melt-mixing model post-erosional magmas with 10% initial eclogite. Results are shown for both the (a) T_P = 1525 °C and $P_{max,PE}$ = 3.0, (b) T_P = 1525 °C and $P_{max,PE}$ = 2.5, (a) T_P = 1450 °C and $P_{max,PE}$ = 3.0, and (a) T_P = 1450 °C and $P_{max,PE}$ = 2.5 GPa models. The proportion of eclogite melt, $X_{F,ecl}$, composing the magma is given as well as the melt fraction for each melting stage.

Table 18. Trace element concentrations for the binary melt-mixing model post-erosional magmas with 10% initial eclogite. Results are shown for both the (a) T_P = 1525 °C and $P_{max,PE}$ = 3.0, (b) T_P = 1525 °C and $P_{max,PE}$ = 2.5, (a) T_P = 1450 °C and $P_{max,PE}$ = 3.0, and (a) T_P = 1450 °C and $P_{max,PE}$ = 2.5 GPa models. The proportion of eclogite melt, $X_{F,ecl}$, composing the magma is given as well as the melt fraction for each melting stage.

(a) 1525 °C Potential Temperature, $P_{max,PE}$ = 3.0 GPa

																		$X_{F,ecl}$	0.96
Init. Conc.	La	Sm	Yb	Hf	Zr	Nb	Sr	Nd	Pb	Ba	La/Sm	Sm/Yb	Hf/Zr	Sr/Nd	La/Nb	Pb/Yb	Zr/Nb	Ba/La		
Peridotite	0.90	0.30	0.11	0.26	12.00	1.30	16.00	0.75	0.27	12.00	3.00	2.73	0.022	21.33	0.69	2.45	9.23	13.33		
Eclogite	17.00	3.80	0.85	2.30	104.00	14.00	113.00	15.00	0.70	90.00	4.47	4.47	0.022	7.53	1.21	0.82	7.43	5.29		
	La	Sm	Yb	Hf	Zr	Nb	Sr	Nd	Pb	Ba	La/Sm	Sm/Yb	Hf/Zr	Sr/Nd	La/Nb	Pb/Yb	Zr/Nb	Ba/La	F_{43}	F_{327}
Peridotite	8.52	2.95	0.98	2.61	117.96	12.87	164.75	7.58	1.51	21.88	2.89	3.01	0.022	21.74	0.66	1.54	9.16	2.57	0.07	0.00
Eclogite	2.80	3.19	0.48	2.03	80.32	0.73	29.98	8.20	0.28	4.97	0.88	6.58	0.025	3.66	3.86	0.58	110.73	1.78	0.71	0.13
	La	Sm	Yb	Hf	Zr	Nb	Sr	Nd	Pb	Ba	La/Sm	Sm/Yb	Hf/Zr	Sr/Nd	La/Nb	Pb/Yb	Zr/Nb	Ba/La		
	3.01	3.18	0.50	2.05	81.69	1.17	34.89	8.18	0.33	5.59	0.95	6.33	0.025	4.27	2.58	0.65	69.96	1.9		

(b) 1525 °C Potential Temperature, $P_{max,PE}$ = 2.5 GPa

																		$X_{F,ecl}$	0.00
Init. Conc.	La	Sm	Yb	Hf	Zr	Nb	Sr	Nd	Pb	Ba	La/Sm	Sm/Yb	Hf/Zr	Sr/Nd	La/Nb	Pb/Yb	Zr/Nb	Ba/La		
Peridotite	1.35	0.30	0.15	0.17	7.35	1.05	18.00	0.72	0.38	25.00	4.50	2.00	0.023	25.00	1.29	2.50	7.00	18.52		
Eclogite	13.00	3.80	0.64	3.40	160.00	18.00	135.00	15.00	0.20	20.00	3.42	5.94	0.021	9.00	0.72	0.31	8.89	1.54		
	La	Sm	Yb	Hf	Zr	Nb	Sr	Nd	Pb	Ba	La/Sm	Sm/Yb	Hf/Zr	Sr/Nd	La/Nb	Pb/Yb	Zr/Nb	Ba/La	F_{425}	F_{2522}
Peridotite	5.94	2.27	1.12	1.25	54.15	5.68	116.86	5.25	0.63	11.98	2.62	2.03	0.023	22.27	1.04	0.56	9.53	2.02	0.09	0.01
Eclogite	--	--	--	--	--	--	--	--	--	--	--	--	--	--	--	--	--	--	1.00	0.00
	La	Sm	Yb	Hf	Zr	Nb	Sr	Nd	Pb	Ba	La/Sm	Sm/Yb	Hf/Zr	Sr/Nd	La/Nb	Pb/Yb	Zr/Nb	Ba/La		
	5.94	2.27	1.12	1.25	54.15	5.68	116.86	5.25	0.63	11.98	2.62	2.03	0.023	22.27	1.04	0.56	9.53	2.02		

Table 18. *(continued)*

(c) 1450 °C Potential Temperature, $P_{max,PE}$ = 3.0 GPa

																		$X_{F,ecl}$	1.00
Init. Conc.	La	Sm	Yb	Hf	Zr	Nb	Sr	Nd	Pb	Ba	La/Sm	Sm/Yb	Hf/Zr	Sr/Nd	La/Nb	Pb/Yb	Zr/Nb	Ba/La		
Peridotite	0.90	0.30	0.11	0.26	12.00	1.30	16.00	0.75	0.27	12.00	3.00	2.73	0.022	21.33	0.69	2.45	9.23	13.33		
Eclogite	17.00	3.80	0.85	2.30	104.00	14.00	113.00	15.00	0.70	90.00	4.47	4.47	0.022	7.53	1.21	0.82	7.43	5.29		
	La	Sm	Yb	Hf	Zr	Nb	Sr	Nd	Pb	Ba	La/Sm	Sm/Yb	Hf/Zr	Sr/Nd	La/Nb	Pb/Yb	Zr/Nb	Ba/La	F_{43}	F_{327}
Peridotite	--	--	--	--	--	--	--	--	--	--	--	--	--	--	--	--	--	--	0.02	0.00
Eclogite	10.66	6.02	0.47	3.64	160.80	2.59	114.47	21.10	0.74	18.48	1.77	12.92	0.023	5.42	4.12	1.60	62.17	1.73	0.37	0.07
	La	Sm	Yb	Hf	Zr	Nb	Sr	Nd	Pb	Ba	La/Sm	Sm/Yb	Hf/Zr	Sr/Nd	La/Nb	Pb/Yb	Zr/Nb	Ba/La		
	10.66	6.02	0.47	3.64	160.80	2.59	114.47	21.10	0.74	18.48	1.77	12.92	0.023	5.42	4.12	1.60	62.17	1.73		

(d) 1450 °C Potential Temperature, $P_{max,PE}$ = 2.5 GPa

																		$X_{F,ecl}$	0.97
Init. Conc.	La	Sm	Yb	Hf	Zr	Nb	Sr	Nd	Pb	Ba	La/Sm	Sm/Yb	Hf/Zr	Sr/Nd	La/Nb	Pb/Yb	Zr/Nb	Ba/La		
Peridotite	1.35	0.30	0.15	0.17	7.35	1.05	18.00	0.72	0.38	25.00	4.50	2.00	0.023	25.00	1.29	2.50	7.00	18.52		
Eclogite	13.00	3.80	0.64	3.40	160.00	18.00	135.00	15.00	0.20	20.00	3.42	5.94	0.021	9.00	0.72	0.31	8.89	1.54		
	La	Sm	Yb	Hf	Zr	Nb	Sr	Nd	Pb	Ba	La/Sm	Sm/Yb	Hf/Zr	Sr/Nd	La/Nb	Pb/Yb	Zr/Nb	Ba/La	F_{425}	F_{2522}
Peridotite	28.12	4.71	1.99	2.88	127.57	21.91	355.68	12.41	4.64	81.64	5.96	2.37	0.023	28.65	1.28	2.33	5.82	2.90	0.03	0.00
Eclogite	1.33	2.22	0.97	2.17	71.98	0.42	28.45	5.65	0.04	0.54	0.60	2.28	0.030	5.04	3.15	0.04	170.44	0.40	0.73	0.29
	La	Sm	Yb	Hf	Zr	Nb	Sr	Nd	Pb	Ba	La/Sm	Sm/Yb	Hf/Zr	Sr/Nd	La/Nb	Pb/Yb	Zr/Nb	Ba/La		
	2.16	2.29	1.00	2.19	73.69	1.08	38.54	5.85	0.18	3.04	0.94	2.28	0.030	6.58	1.99	0.18	67.93	1.41		

Table 19. Binary melt-mixing model for post-erosional isotope ratios, 10% eclogite

(a) 1525 °C Potential Temperature, $P_{max,PE}$ = 3.0 GPa

							$X_{F,ecl}$	0.96
	Sr	Nd	Pb	$^{87}Sr/^{86}Sr$	εNd	$^{206}Pb/^{204}Pb$	F_{43}	F_{327}
Peridotite	164.75	7.58	1.51	0.70350	6.50	18.60	0.13	0.00
Eclogite	29.98	8.20	0.28	0.70470	3.00	19.30	0.71	0.13
	Sr	Nd	Pb	$^{87}Sr/^{86}Sr$	εNd	$^{206}Pb/^{204}Pb$		
	34.89	8.18	0.33	0.70459	3.06	19.24		

(b) 1525 °C Potential Temperature, $P_{max,PE}$ = 2.5 GPa

							$X_{F,ecl}$	0.00
	Sr	Nd	Pb	$^{87}Sr/^{86}Sr$	εNd	$^{206}Pb/^{204}Pb$	F_{425}	F_{2522}
Peridotite	116.86	5.25	0.63	0.70350	6.50	18.60	0.09	0.01
Eclogite	--	--	--	0.70470	3.00	19.30	1.00	0.00
	Sr	Nd	Pb	$^{87}Sr/^{86}Sr$	εNd	$^{206}Pb/^{204}Pb$		
	116.86	5.25	0.63	0.70350	6.50	18.60		

(c) 1450 °C Potential Temperature, $P_{max,PE}$ = 3.0 GPa

							$X_{F,ecl}$	1.00
	Sr	Nd	Pb	$^{87}Sr/^{86}Sr$	εNd	$^{206}Pb/^{204}Pb$	F_{43}	F_{327}
Peridotite	--	--	--	0.70350	6.50	18.60	0.02	0.00
Eclogite	114.47	21.10	0.74	0.70470	3.00	19.30	0.37	0.07
	Sr	Nd	Pb	$^{87}Sr/^{86}Sr$	εNd	$^{206}Pb/^{204}Pb$		
	114.47	21.10	0.74	0.70470	3.00	19.30		

(d) 1450 °C Potential Temperature, $P_{max,PE}$ = 2.5 GPa

							$X_{F,ecl}$	0.97
	Sr	Nd	Pb	$^{87}Sr/^{86}Sr$	εNd	$^{206}Pb/^{204}Pb$	F_{425}	F_{2522}
Peridotite	355.68	12.41	4.64	0.70350	6.50	18.60	0.03	0.00
Eclogite	28.45	5.65	0.04	0.70470	3.00	19.30	0.73	0.29
	Sr	Nd	Pb	$^{87}Sr/^{86}Sr$	εNd	$^{206}Pb/^{204}Pb$		
	38.54	5.85	0.18	0.70450	3.12	18.84		

Isotope compositions for the binary melt-mixing model post-erosional magmas with 10% initial eclogite. Results are shown for both the (a) T_P = 1525 °C and $P_{max,PE}$ = 3.0, (b) T_P = 1525 °C and $P_{max,PE}$ = 2.5, (a) T_P = 1450 °C and $P_{max,PE}$ = 3.0, and (a) T_P = 1450 °C and $P_{max,PE}$ = 2.5 GPa models. The proportion of eclogite melt, XF,ecl, composing the magma is given as well as the melt fraction for each melting stage. The composition of the post-erosional magma is shown in grey.

melts, $F_{per,2522}$ = 0.01, of a slightly depleted peridotite-derived residue, $F_{per,425}$ = 0.09. The model post-erosional parental magmas are very high in MgO (24.12 wt. %) and FeO_T (13.82 wt. %), producing an Mg# slightly more ultramafic than in equilibrium with the mangle (75.7). Apart from CaO, fractionation paths for the model post-erosional parental magma do not reproduce the Intermediate and Younger Series well (Figure 34). Trace elements ratios for the post-erosional magma plot squarely within the range of observed post-erosional lavas (Figure 33). The model post-erosional magma is derived completely from the depleted peridotitic component and can easily reproduce the $^{87}Sr/^{86}Sr$ and ε_{Nd} of the Intermediate and Younger Series with small enrichments to the chosen isotopic end-members (*e.g.*, $^{87}Sr/^{86}Sr \approx 0.7037$, $\varepsilon_{Nd} \approx +5.5$, and $^{206}Pb/^{204}Pb \approx 18.8$; Figure 35). Despite the poor reproducibility of the major elements, this model remains in consideration as a satisfactory solution.

Returning to an effective upper boundary layer of 3.0 GPa for the post-erosional source components, but running the components along the cooler T_P = 1450 °C particle path, the post-erosional lavas are sourced solely from the eclogitic component (Tables 17c, 18c, and 19c). Whereas the peridotite-derived residue is too refractory to melt between 3.0 and 2.7 GPa, the melts from the eclogitic component are the product of moderate degree melts, $F_{ecl,327}$ = 0.07, of a strongly depleted eclogite-derived residue, $F_{ecl,43}$ = 0.37. The model post-erosional parental magma has an exceptionally low MgO (6.22 wt. %) and Mg# (49), much too low to be a true parental magma for the Intermediate and Younger Series lavas (Figure 36). The high Sm/Yb (12.92) and low La/Sm (1.78) of the melt from the eclogite-derived residue are evident in the model post-erosional magma and do not reflect the observed data (Figure 37). Similarly, the isotopic ratios for the model post-erosional magma are that of the enriched eclogitic source ($^{87}Sr/^{86}Sr$ = 0.70470, ε_{Nd} = +3.00, and $^{206}Pb/^{204}Pb$ =

Figure 34. Representative major element compositions for the geochemical evolution of the binary mixing model with T_P = 1525 °C and a maximum vertical ascent of the post-erosional source in the plume stem to 2.5 GPa, for a plume with 10% initial eclogite. Symbols after Figure 33. Dashed lines represent mixing lines between peridotite and eclogite melts at 2.0 GPa and residual eclogite and residual peridotite melts at 2.2 GPa, respectively. In this version of the binary mixing model, the shield lavas are generated in the same manner, but for the post-erosional lavas the initial peridotite and eclogite and allowed to rise to 2.5 GPa before ceasing vertical ascent in the plume stem. The residual peridotite and eclogite components then continue decompression through the plume tail from 2.5 to 2.2 GPa. Any melts generated in this region are mixed to form the model post-erosional magma. See text for full description. (a) SiO_2, (b) FeO_T, and (c) CaO plotted against wt. % MgO. The model shield magma composition reproduces SiO_2 and FeO_T well, though CaO is low for a given MgO content. From the LLOD for the model post-erosional magma, the SiO_2 is much too low and the FeO_T much to high to reproduce the observed lavas.

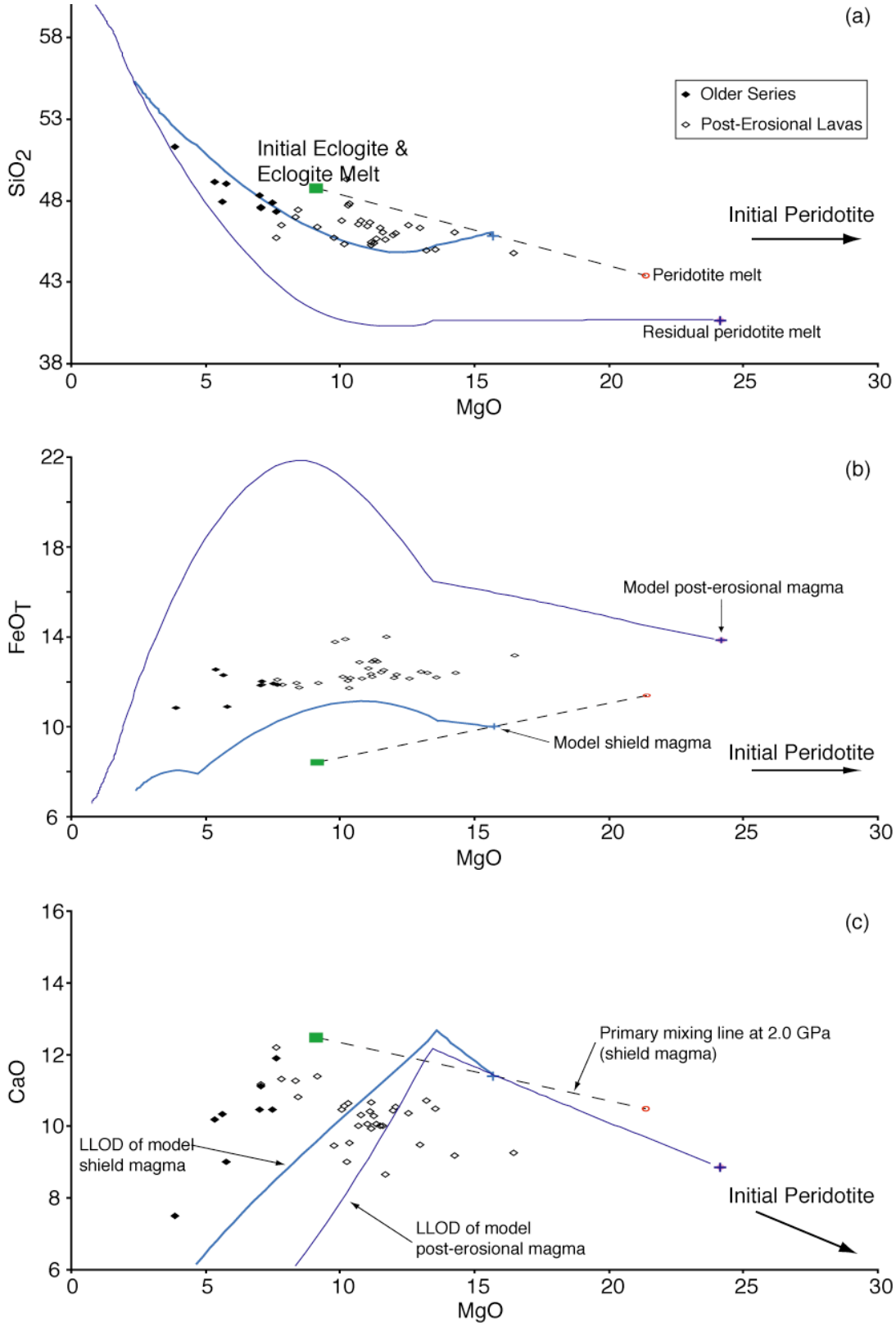
(a)
Older Series
Post-Erosional Lavas
Initial Eclogite &
Eclogite Melt
Initial Peridotite
Peridotite melt
Residual peridotite melt
SiO2
MgO
(b)
Model post-erosional magma
Model shield magma
Initial Peridotite
FeOT
MgO
(c)
Primary mixing line at 2.0 GPa
(shield magma)
LLOD of model
shield magma
LLOD of model
post-erosional magma
Initial Peridotite
CaO
MgO

Figure 35. Isotope ratios systematics for the geochemical evolution of the binary mixing model with T_P = 1525 °C and a maximum vertical ascent of the post-erosional source in the plume stem to 3.0 GPa, for a plume with 10% initial eclogite. Symbols after Figure 33 and 34. End-member isotope compositions are chosen to reflect the observed range of Mauritius lavas. Plots of Sm/Yb against (a) $^{87}Sr/^{86}Sr$, (b) ε_{Nd}, and (c) $^{206}Pb/^{204}Pb$. Trace element concentrations for mixing are taken from compositions of the model shield and post-erosional magmas. Model shield magmas reproduce Sr- and Nd-isotopes well, but do not fit Pb-isotopes. In this model, the eclogitic residue does not melt in the plume tail, leaving the model post-erosional magma with the isotope ratios of the peridotitic residue. These isotope ratios are much too depleted in ε_{Nd} and $^{206}Pb/^{204}Pb$ to form the post-erosional lavas.

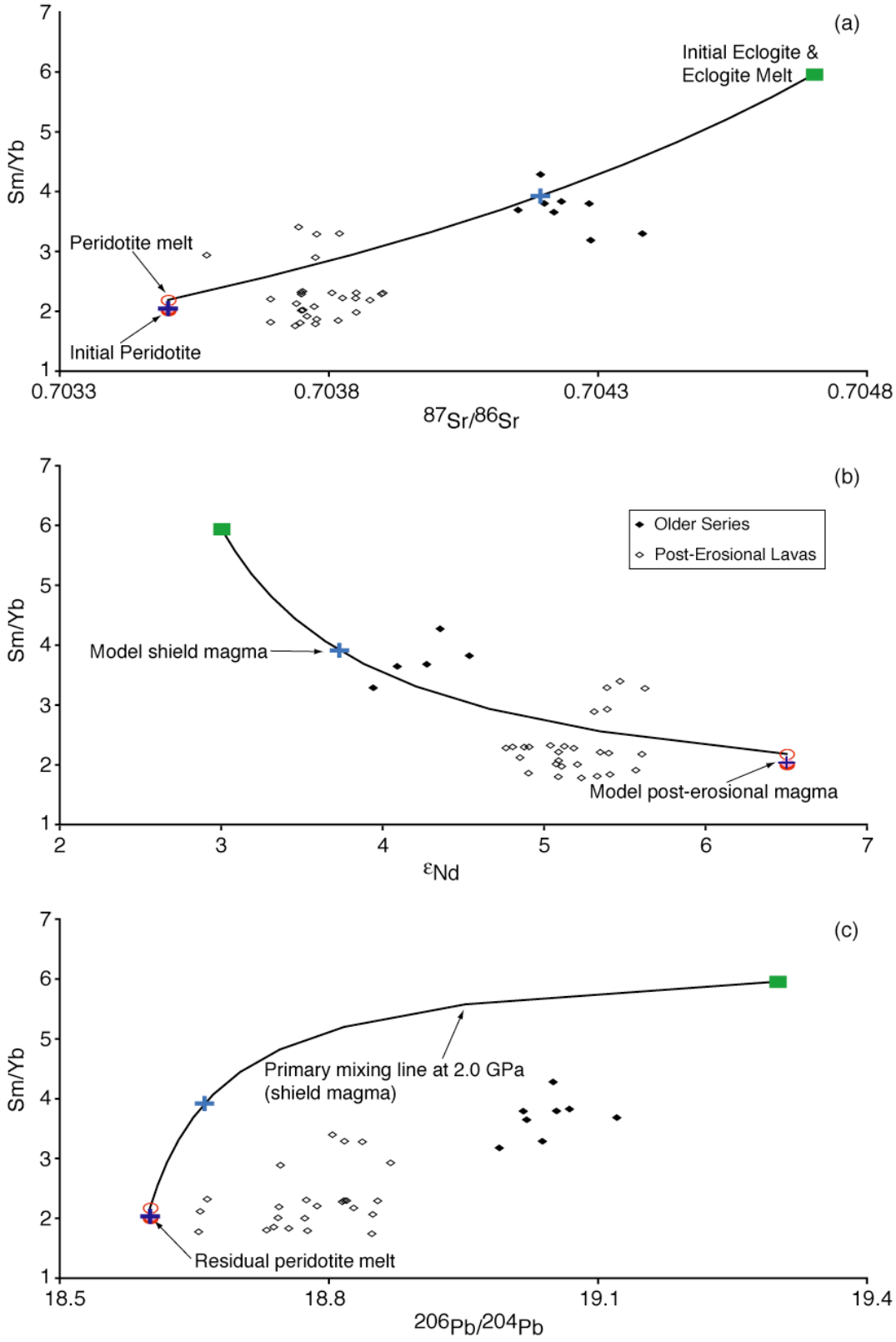
(a)
Initial Eclogite &
Eclogite Melt
Peridotite melt
Initial Peridotite
Sm/Yb
$^{87}Sr/^{86}Sr$
0.7033
0.7038
0.7043
0.7048
(b)
Older Series
Post-Erosional Lavas
Model shield magma
Model post-erosional magma
Sm/Yb
εNd
(c)
Primary mixing line at 2.0 GPa
(shield magma)
Residual peridotite melt
Sm/Yb
$^{206}Pb/^{204}Pb$
18.5
18.8
19.1
19.4

Figure 36. Representative major element compositions for the geochemical evolution of the binary mixing model with T_P = 1525 °C for the shield lavas, T_P = 1450 °C for the post-erosional lavas, and a maximum vertical ascent of the post-erosional source in the plume stem to 3.0 GPa, for a plume with 10% initial eclogite. Symbols after Figure 27. In this version of the binary mixing model, the shield lavas are produced identically as in Figure 27, except the post-erosional lavas have a cooler potential temperature of T_P = 1450 °C. See text for full description. (a) SiO_2, (b) FeO_T, and (c) CaO plotted against wt. % MgO. The model shield magma composition reproduces SiO_2 and FeO_T well, though CaO is low for a given MgO content. The model post-erosional magmas are the product of melts of the eclogite-derived residue alone as the peridotitic residue does not melt in the plume tail. Consequently, the MgO content is very low (6.2 wt. %) and is not representative of the observed lavas.

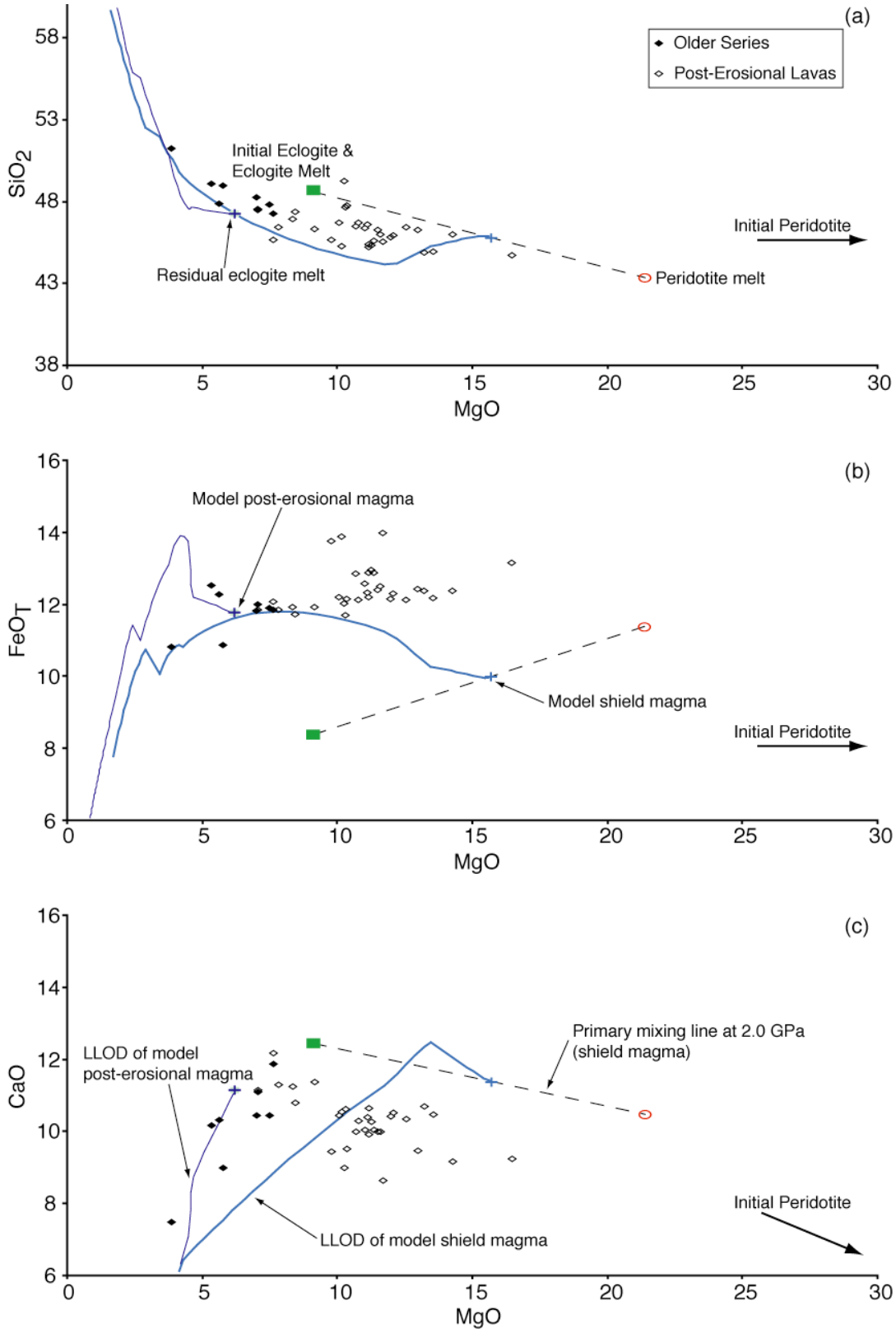
(a)
Older Series
Post-Erosional Lavas
Initial Eclogite &
Eclogite Melt
Residual eclogite melt
Initial Peridotite
Peridotite melt
SiO2
MgO
(b)
Model post-erosional magma
Model shield magma
Initial Peridotite
FeOT
MgO
(c)
LLOD of model
post-erosional magma
Primary mixing line at 2.0 GPa
(shield magma)
LLOD of model shield magma
Initial Peridotite
CaO
MgO

Figure 37. Representative incompatible trace element composition for the geochemical evolution of the binary mixing model with T_P = 1525 °C for the shield lavas, T_P = 1450 °C for the post-erosional lavas, and a maximum vertical ascent of the post-erosional source in the plume stem to 3.0 GPa, for a plume with 10% initial eclogite. Symbols after Figure 27. Solid curves represent mixing lines between peridotite and eclogite melts at 2.0 GPa and residual eclogite and residual peridotite melts at 2.7 GPa, respectively. Vertical and horizontal dashed lines represent trace element ratio of Primitive Mantle (McDonough and Sun, 1995). La/Sm plotted against Sm/Yb. Incompatible trace element compositions of the initial eclogite and initial peridotite are chosen such that the model shield magma fits the observed Older Series trace element data. Trace element compositions of the initial compositions are kept constant for the post-erosional lavas. In this model, the post-erosional magma consists entirely of melts of the eclogite-derived residue and have large a Sm/Yb (12.9) that well exceeds the uppermost bound of the observed post-erosional lavas.

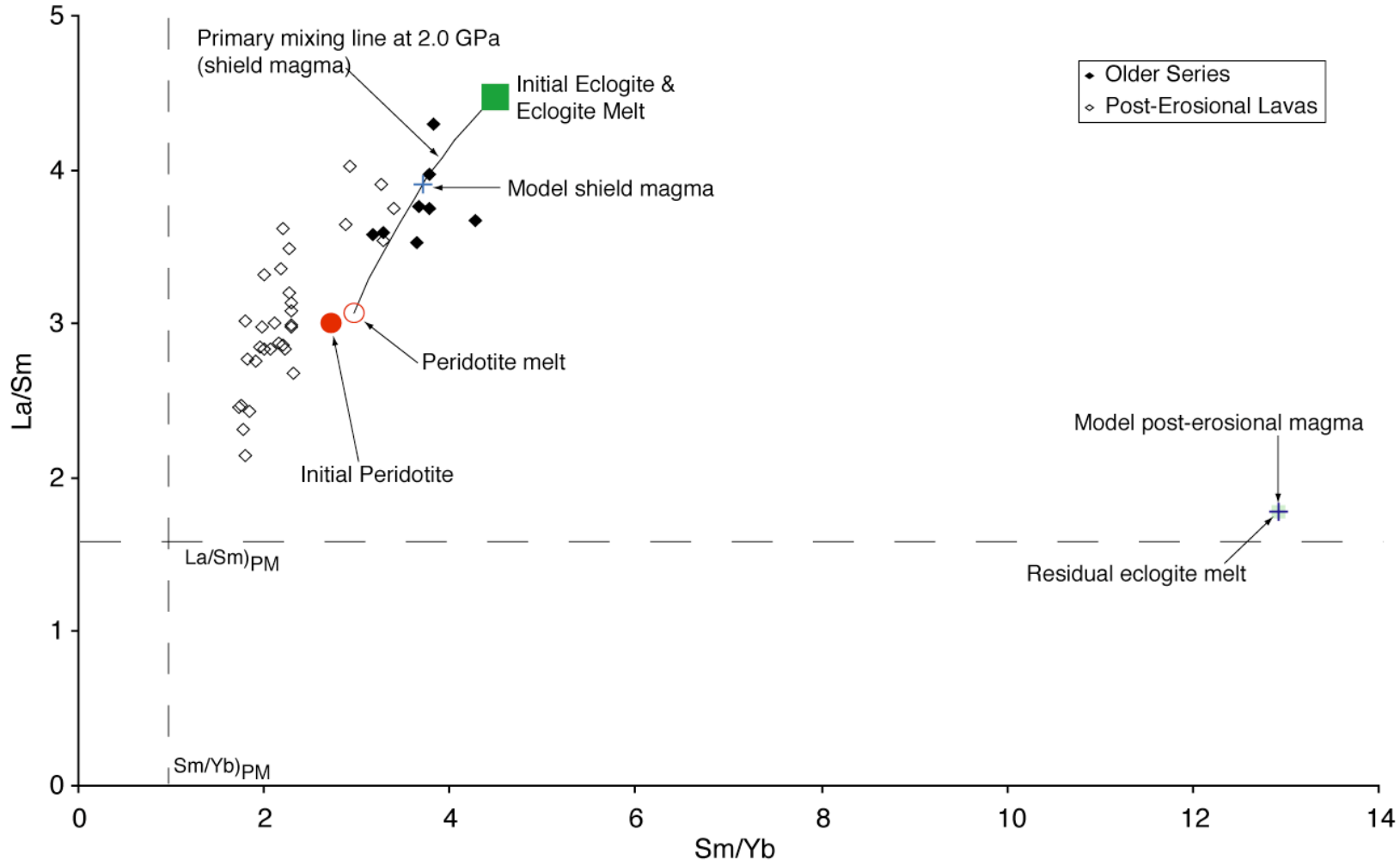
Primary mixing line at 2.0 GPa
(shield magma)
Initial Eclogite &
Eclogite Melt
Model shield magma
Peridotite melt
Initial Peridotite
Older Series
Post-Erosional Lavas
Model post-erosional magma
Residual eclogite melt
La/Sm)PM
Sm/Yb)PM
La/Sm
Sm/Yb
0
1
2
3
4
5
0
2
4
6
8
10
12
14

19.30), not of the depleted Intermediate and Younger Series lavas (Figure 38). Consequently, this model provides an unsatisfactory solution.

The final iteration of temperature and pressure for the post-erosional lavas in the binary melt-mixing model decreases the effective upper boundary layer to 2.5 GPa and uses the cooler temperature of T_P = 1450 °C (Tables, 17d, 18d, and 19d). The modeled post-erosional melts from the eclogitic component are the product of moderate degree melts, $F_{ecl,2522}$ = 0.29, of a highly depleted eclogite-derived residue, $F_{ecl,425}$ = 0.73. Melts from the peridotitic component are very low degree melts, $F_{per,2522}$ = 0.003, of a slightly depleted peridotite-derived residue, $F_{per,425}$ = 0.03. This parental magma has a relatively low MgO content (10.38 wt. %; Mg# = 65) that is intermediate to the other models (Figure 39). However, this model magma remains too low in MgO to be the parental magma for the entire suite of post-erosional lavas. Once again, the model post-erosional magma is dominated by melts of the eclogitic component ($X_{F,ecl}$ = 0.97). Due to the large extent of melting of the eclogite-derived residue between 2.5 and 2.2 GPa, the model post-erosional magma has a low Sm/Yb (0.60) broadly consistent with the Intermediate and Younger Series lavas. The La/Sm is somewhat low though (2.28), and it is difficult to assess the viability of the model from the trace elements alone (Figure 40). However, isotopic ratios for the model post-erosional magma are dominated by the enriched eclogitic source ($^{87}Sr/^{86}Sr$ = 0.70450, and ε_{Nd} = +3.12). The Pb-isotopes are reproduced well ($^{206}Pb/^{204}Pb$ = 18.84), though the Pb trace element systematics are different than for Sr and Nd (Figure 41). Here, the modal dominance of the contributions from the eclogitic component ($X_{F,ecl}$ = 0.97; Pb = 0.04 ppm) are overwhelmed by the small contributions from the peridotitic component (Pb = 4.64 ppm). Nevertheless, the model provides an unsatisfactory solution based on major element and isotopic evidence.

Figure 38. Isotope ratios systematics for the geochemical evolution of the binary mixing model with T_P = 1525 °C for the shield lavas, T_P = 1450 °C for the post-erosional lavas, and a maximum vertical ascent of the post-erosional source in the plume stem to 3.0 GPa, for a plume with 10% initial eclogite. Symbols after Figure 27 and 28. End-member isotope compositions are chosen to reflect the observed range of Mauritius lavas. Plots of Sm/Yb against (a) $^{87}Sr/^{86}Sr$, (b) ε_{Nd}, and (c) $^{206}Pb/^{204}Pb$. Trace element concentrations for mixing are taken from compositions of the model shield and post-erosional magmas. Model shield magmas reproduce Sr- and Nd-isotopes well, but do not fit Pb-isotopes. Model post-erosional magmas are completely sourced by the enriched melts of the eclogitic residue and are not representative of the observed data.

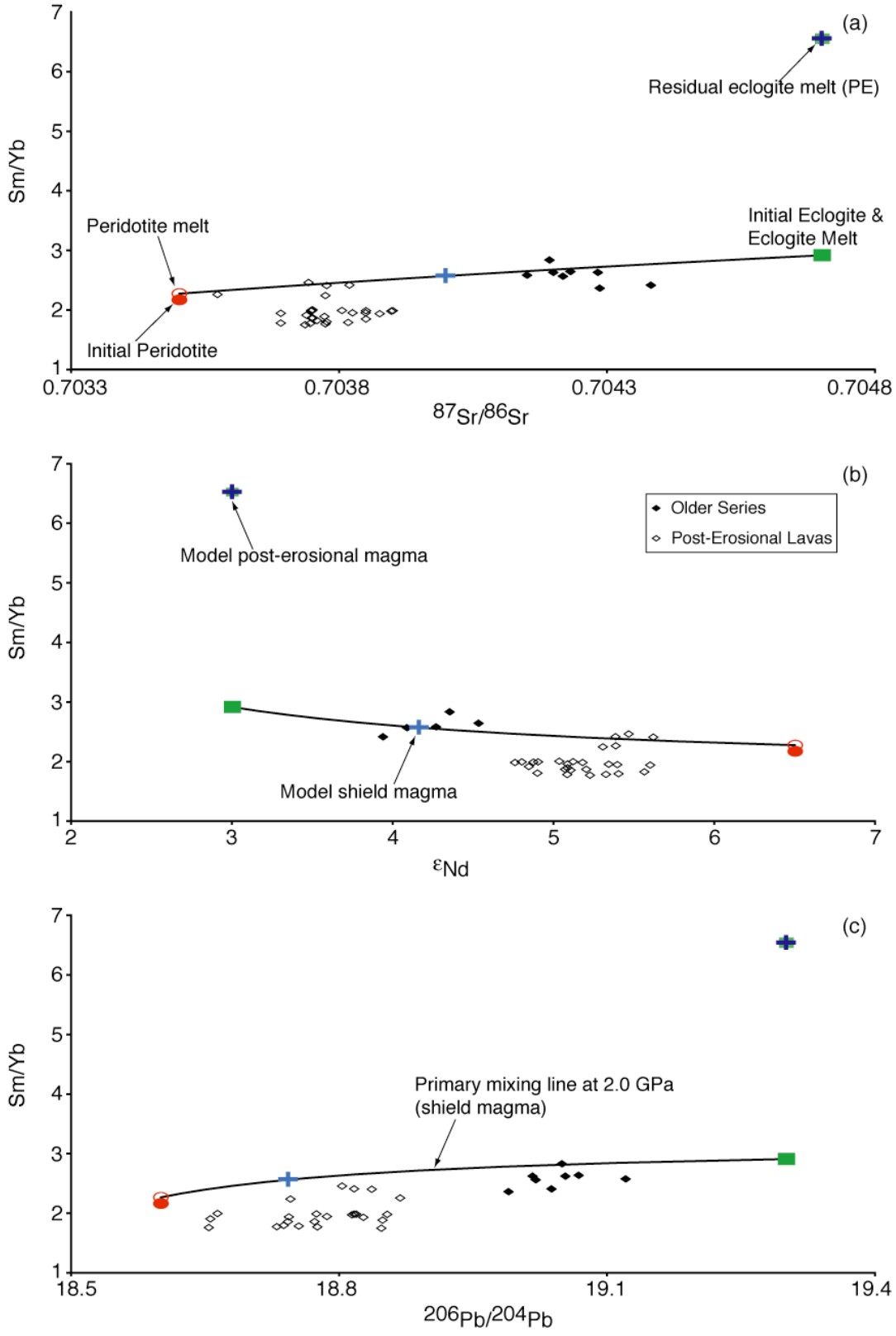
(a)
Residual eclogite melt (PE)
Peridotite melt
Initial Eclogite &
Eclogite Melt
Initial Peridotite
Sm/Yb
$^{87}Sr/^{86}Sr$
0.7033
0.7038
0.7043
0.7048
(b)
Older Series
Post-Erosional Lavas
Model post-erosional magma
Model shield magma
Sm/Yb
εNd
(c)
Primary mixing line at 2.0 GPa
(shield magma)
Sm/Yb
$^{206}Pb/^{204}Pb$
18.5
18.8
19.1
19.4

Figure 39. Representative major element compositions for the geochemical evolution of the binary mixing model with T_P = 1525 °C for the shield lavas, T_P = 1450 °C for the post-erosional lavas, and a maximum vertical ascent of the post-erosional source in the plume stem to 2.5 GPa, for a plume with 10% initial eclogite. Symbols after Figure 33. In this version of the binary mixing model, the shield lavas are generated in the same manner, but for the post-erosional lavas the initial peridotite and eclogite and allowed to rise to 2.5 GPa before ceasing vertical ascent in the plume stem of T_P = 1450 °C. The residual peridotite and eclogite components then continue decompression through the plume tail from 2.5 to 2.2 GPa. Any melts generated in this region are mixed to form the model post-erosional magma. See text for full description. (a) SiO_2, (b) FeO_T, and (c) CaO plotted against wt. % MgO. The model shield magma composition reproduces SiO_2 and FeO_T well, though CaO is low for a given MgO content. The MgO content of the model post-erosional magma (10.4 wt. %) is low relative to many of the post-erosional samples, and does a particularly poor job of reproducing FeO_T.

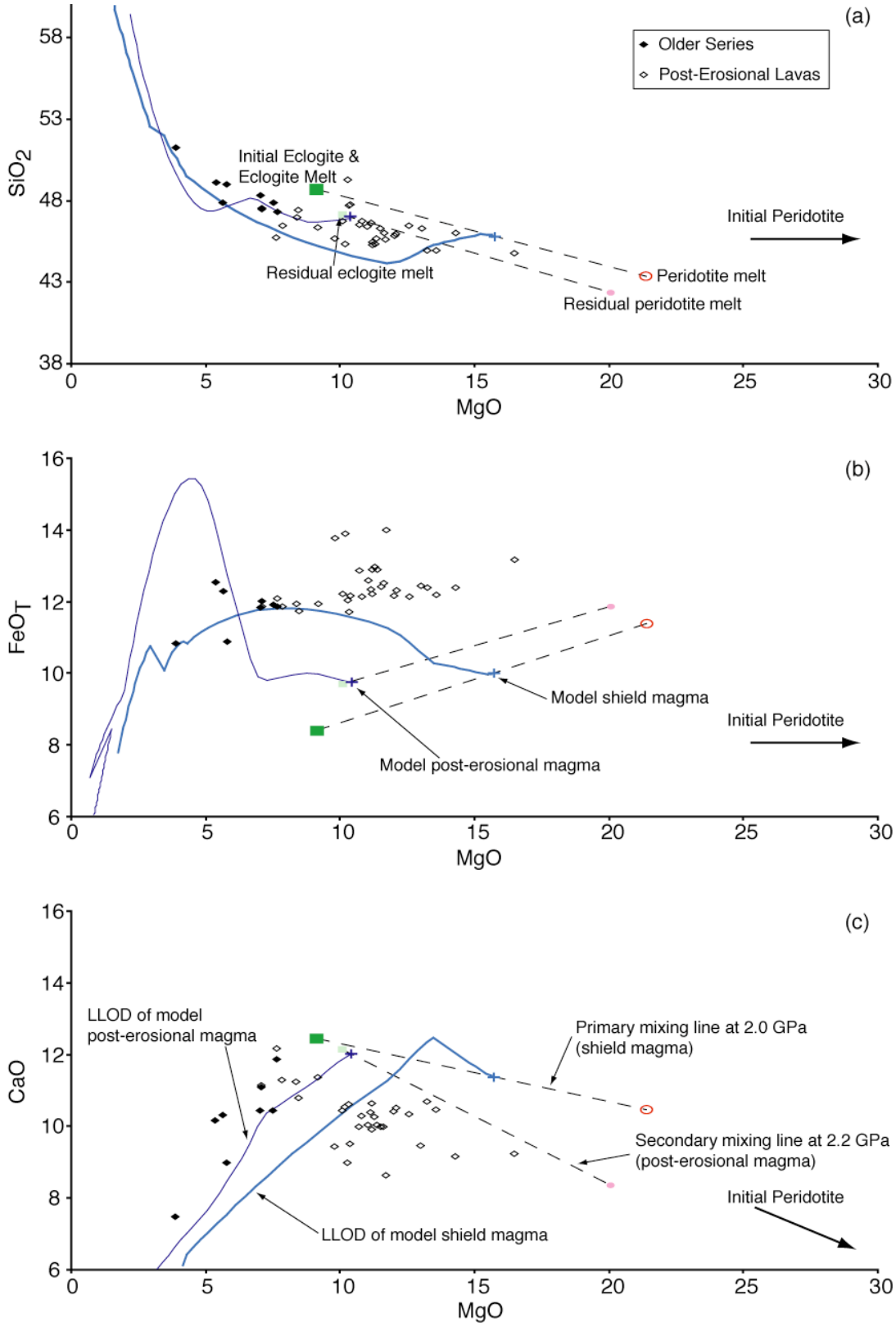
(a)
Older Series
Post-Erosional Lavas
Initial Eclogite &
Eclogite Melt
Residual eclogite melt
Initial Peridotite
Peridotite melt
Residual peridotite melt
SiO2
MgO
(b)
Model shield magma
Model post-erosional magma
Initial Peridotite
FeOT
MgO
(c)
LLOD of model
post-erosional magma
Primary mixing line at 2.0 GPa
(shield magma)
Secondary mixing line at 2.2 GPa
(post-erosional magma)
Initial Peridotite
LLOD of model shield magma
CaO
MgO

Figure 40. Representative incompatible trace element composition for the geochemical evolution of the binary mixing model with T_P = 1525 °C for the shield lavas, T_P = 1450 °C for the post-erosional lavas, and a maximum vertical ascent of the post-erosional source in the plume stem to 2.5 GPa, for a plume with 10% initial eclogite. Symbols after Figure 33. Solid curves represent mixing lines between peridotite and eclogite melts at 2.0 GPa and residual eclogite and residual peridotite melts at 2.2 GPa, respectively. The horizontal dashed line represents the trace element ratio of Primitive Mantle (McDonough and Sun, 1995). (a) La/Sm, (b) La/Nb, and (c) Zr/Nb plotted against Sm/Yb. Incompatible trace element compositions of the initial eclogite and initial peridotite are chosen such that the model shield magma fits the observed Older Series trace element data. Trace element compositions of the initial compositions are kept constant for the post-erosional lavas. In this model, Sm/Yb values are appropriate for the post-erosional lavas (2.3), though other ratios show extensive fractionation in the melts of the eclogite-derived residue (*i.e.,* Zr/Nb = 170.4), which composes 97% of the model post-erosional magma.

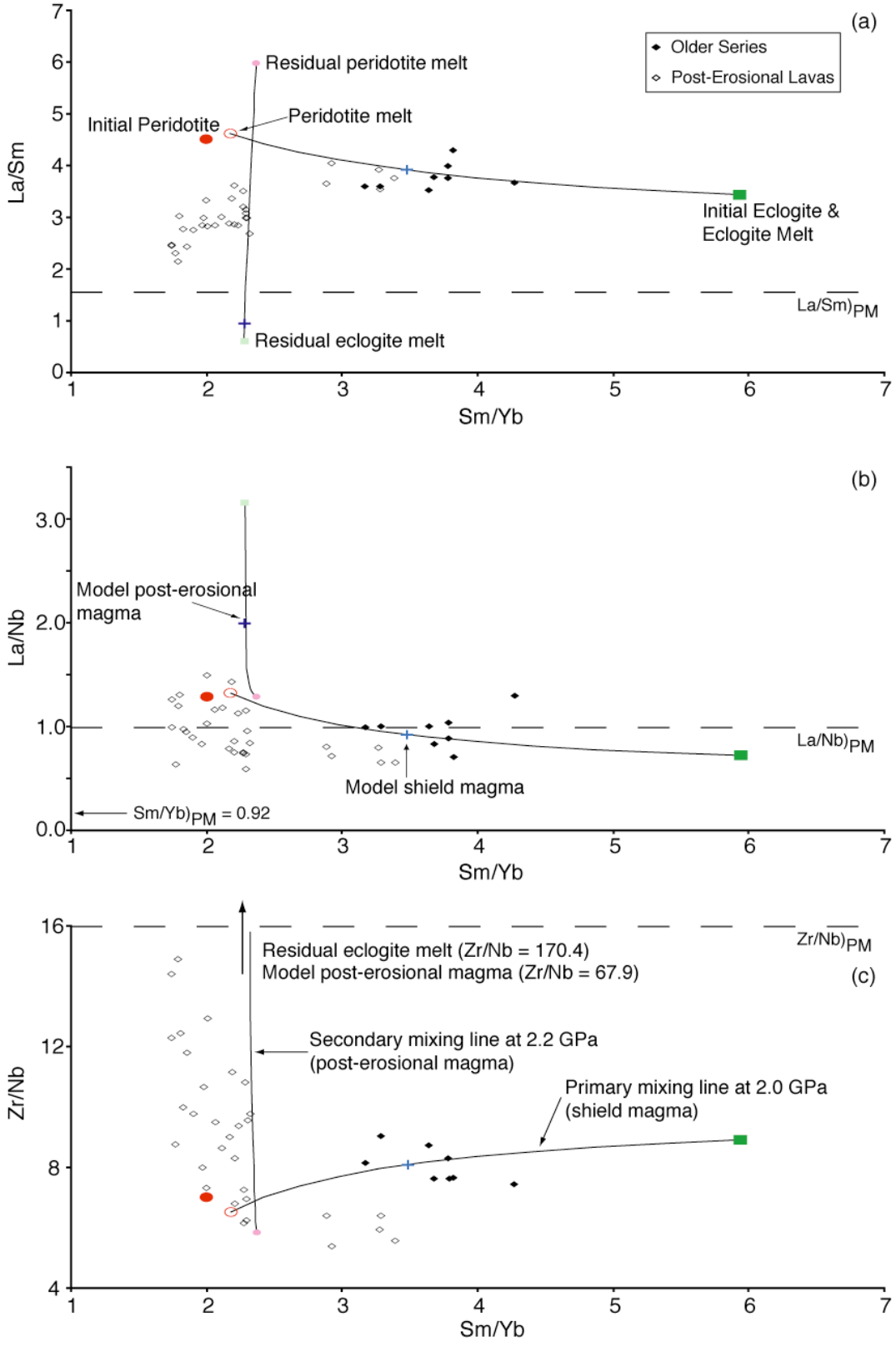
(a)
Older Series
Post-Erosional Lavas
Residual peridotite melt
Initial Peridotite
Peridotite melt
Initial Eclogite &
Eclogite Melt
La/Sm)PM
Residual eclogite melt
La/Sm
Sm/Yb
(b)
Model post-erosional
magma
La/Nb)PM
Model shield magma
Sm/Yb)PM = 0.92
La/Nb
Sm/Yb
Zr/Nb)PM
(c)
Residual eclogite melt (Zr/Nb = 170.4)
Model post-erosional magma (Zr/Nb = 67.9)
Secondary mixing line at 2.2 GPa
(post-erosional magma)
Primary mixing line at 2.0 GPa
(shield magma)
Zr/Nb
Sm/Yb

Figure 41. Isotope ratios systematics for the geochemical evolution of the binary mixing model with T_P = 1525 °C for the shield lavas, T_P = 1450 °C for the post-erosional lavas, and a maximum vertical ascent of the post-erosional source in the plume stem to 2.5 GPa, for a plume with 10% initial eclogite. Symbols after Figure 33 and 34. End-member isotope compositions are chosen to reflect the observed range of Mauritius lavas. Plots of Sm/Yb against (a) $^{87}Sr/^{86}Sr$, (b) ε_{Nd}, and (c) $^{206}Pb/^{204}Pb$. Trace element concentrations for mixing are taken from compositions of the model shield and post-erosional magmas. Model shield magmas reproduce Sr- and Nd-isotopes well, but do not fit Pb-isotopes. In this model, the peridotitic component contributes little to the model post-erosional magma ($X_{F,per}$ = 0.03), and the isotopic compositions of the model lavas are not representative of the observed Intermediate and Younger Series.

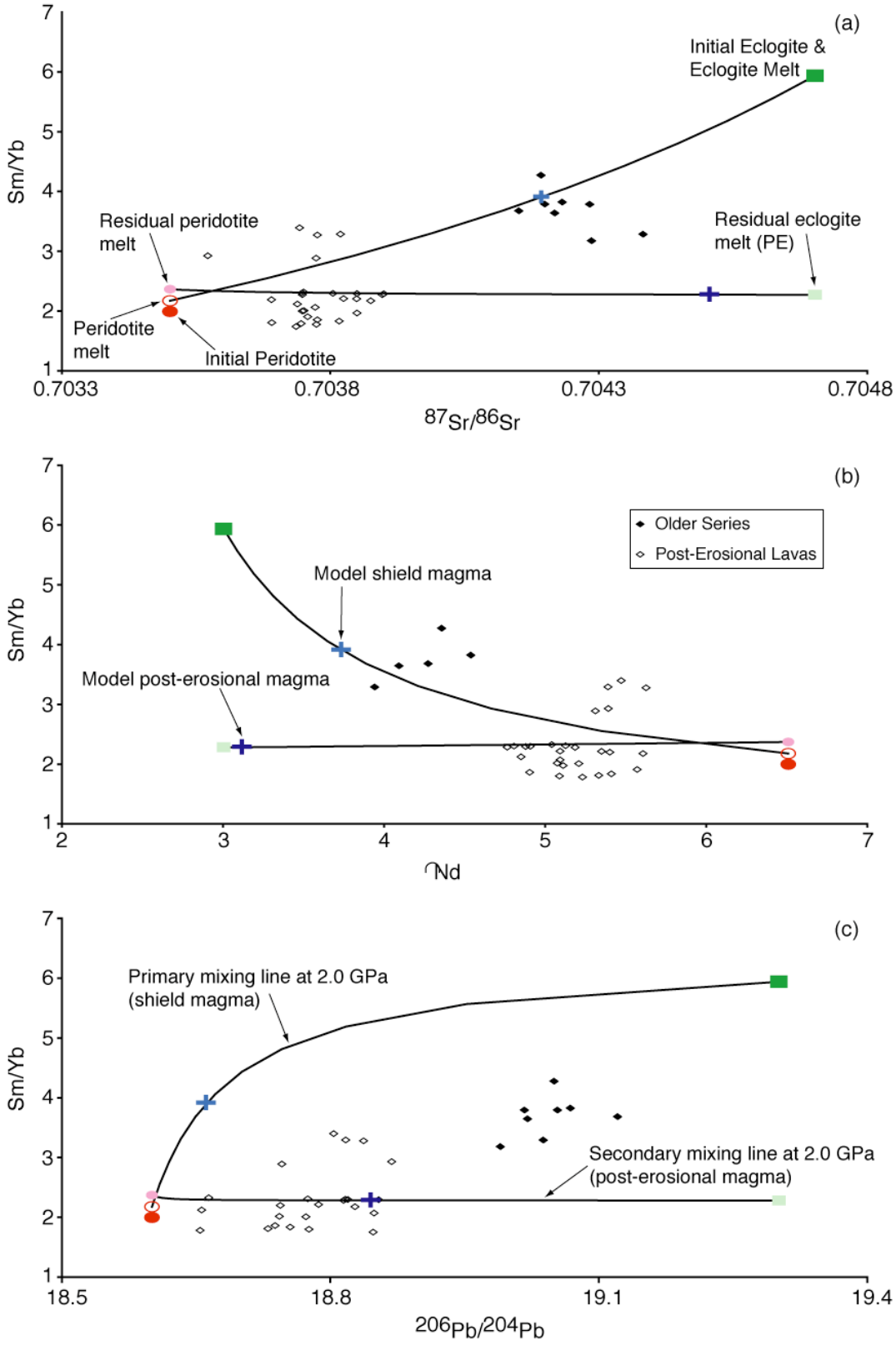
(a)
Initial Eclogite &
Eclogite Melt
Residual peridotite
melt
Residual eclogite
melt (PE)
Peridotite
melt
Initial Peridotite
Sm/Yb
$^{87}Sr/^{86}Sr$
0.7033
0.7038
0.7043
0.7048
(b)
Older Series
Post-Erosional Lavas
Model shield magma
Model post-erosional magma
Sm/Yb
Nd
(c)
Primary mixing line at 2.0 GPa
(shield magma)
Secondary mixing line at 2.0 GPa
(post-erosional magma)
Sm/Yb
$^{206}Pb/^{204}Pb$
18.5
18.8
19.1
19.4

Using the geochemical outputs from the thermodynamic modeling of the binary melt-mixing model from Adiabat_1ph (*i.e.,* major elements, trace elements, isotopic ratios) it is possible to discern the validity of each model variation (*i.e.*, potential temperature and maximum vertical ascent). While each geochemical parameter is worth considering, the isotopic ratios calculated for each model are perhaps the most effective tool for testing model efficacy. Although certain major and trace abundances and ratios for the shield and post-erosional lavas are distinct from one another, each of these can be greatly affected by fractional crystallization and degree of melting, whereas isotope ratios are not.

As worldwide occurrences of post-erosional lavas have isotopic ratios that are systematically depleted relative to those of the shield lavas (Figure 19), the isotopic and trace element budget of the post-erosional parental magma derived from a heterogeneous mantle plume should be largely sourced by the isotopically depleted component. Applying this logic to the convention for relative enrichment of the initial plume components described above, the peridotitic component (*i.e.*, the plume matrix) would be the principle source component of the post-erosional parental magma. Relative to the Older Series shield lavas, the observed post-erosional Intermediate and Younger Series lavas have lower $^{87}Sr/^{86}Sr$ (0.70357 – 0.70390) and Pb-isotopic ratios (*e.g.*, $^{206}Pb/^{204}Pb$ = 18.65 – 18.87) and larger ε_{Nd} values (+4.8 to +5.6).

Looking at the four post-erosional scenarios for the binary melt-mixing model (Table 19), it is clear that three of the four models do not fit the parameters described above and fail to reproduce the isotopic signature of the post-erosional lavas. The post-erosional melts in these three models (T_P = 1525 °C and $P_{max,PE}$ = 3.0, and both models with T_P = 1450 °C) are overwhelmingly sourced by melts of the eclogitic component ($X_{F,ecl}$ = 0.97 – 1.00) and have highly enriched isotopic signatures characteristic of the eclogitic component (*e.g.*, $^{87}Sr/^{86}Sr$ = 0.70450 – 0.70470; Figures

29, 38, and 41). Similarly, trace elements concentrations and ratios are characteristic of melts derived from the eclogitic component (Table 18). These three models thus represent unsatisfactory solution to the binary model.

The sole model that represents an acceptable solution to the binary melt-mixing model is one in which the model post-erosional magmas are sourced entirely from by the peridotitic component. This model (T_P = 1525 °C, $P_{max,PE}$ = 2.5 GPa) experiences no melting of the eclogitic component in the plume tail ($F_{ecl,2522}$ = 0) because the component is melted entirely during the adiabatic ascent to 2.5 GPa within the plume stem ($F_{ecl,425}$ = 1) and is thus unable to melt during the period of secondary melting. Just as observed in the results of the other binary melting models, the isotopic compositions of this parental post-erosional magma are reflective of a single-source origin, although in this model the resulting magma retains the depleted isotopic composition of the peridotitic component (Figure 35). However, to accurately fit the Intermediate and Younger Series lavas, the isotopic compositions of the depleted component would need to be slightly more enriched than chosen (*e.g.*, $^{87}Sr/^{86}Sr \approx 0.70375$, $\varepsilon_{Nd} \approx +5.25$, and $^{206}Pb/^{204}Pb \approx 18.80$). Trace element systematics for this models scenario are reproduced well, the best of any of the models presented in this work (Figure 33). Relative to the post-erosional lavas (Figure 31), the majority of the model post-erosional magma trace element concentrations are low by approximately a factor of two (except for Ba, depleted by a factor of 6). Despite the difference in absolute abundance, the model magma follows the general pattern of the observed lava well. Taken together, this scenario represents a reasonably successful solution of the binary model. However, to thoroughly assess this scenario it is important to consider the lack of consistency in the major elements for the LLOD between the modeled and observed lavas (Figure 34).

Hybrid Pyroxenite Model

The second melting model evaluated here is somewhat more complex and requires the reaction of eclogitic melt and peridotite to form the hybridized pyroxenite. Melts of the hybridized pyroxenite are then mixed with further melts of eclogite and peridotite residues at shallower depths, producing the parental magmas for the shield and post-erosional lavas. The construction of composite P-T profiles, boundary conditions, and component compositions are as described above. Pressure and temperature conditions, and trace element compositions for each model scenario will be discussed individually.

While the fundamental petrologic and geochemical understanding behind the hybrid melting model is sound (*e.g.*, Yaxley and Green, 1998), many of the physical mechanisms involved are not (*e.g.*, Kogiso et al., 2004). Here I present the procedures and assumptions present in this evaluation of the hybrid melting, and attempt to address the viability of a number of pressure and temperature restrictions on the generation of shield and post-erosional lavas from a heterogeneous mantle plume.

Shield Lavas

The hybrid melting model begins at 4.0 GPa and commences as the lithologically heterogeneous peridotitic and eclogitic components are moved adiabatically along a composite P-T path to a chosen depth of 3.0 GPa. At this point, melts derived from the eclogitic component are allowed to segregate and mix thoroughly with the peridotite. The eclogite-derived melts are relatively SiO_2-rich and will react with the olivine-rich peridotite, reducing or eliminating modal olivine in the peridotite, and forming the pyroxene-rich hybrid. The physical mechanisms of melt extraction, transport, and reaction are not well understood (*e.g.*, Kogiso et al., 2004), though the eclogite-derived melts are assumed to segregate efficiently. To assure the

eclogite-derived melts interact with a bulk peridotite composition everywhere, any partial melts of the peridotitic component are assumed to be distributed homogenously the remaining solid. Following Sobolev et al. (2005), the eclogite-derived melts then infiltrate the peridotite matrix and are assumed to react completely with an equal volume of peridotite, in a 1:1 ratio, forming the hybrid pyroxenite. At this point, the plume is composed of three lithologies: (1) unreacted peridotite, (2) residue of an eclogitic source, and (3) hybrid pyroxenite. Each of these components are then run along the remainder of the composite P-T path to 2.0 GPa, where melting ceases at the base of the lithosphere. Any melts generated by the three components at pressures less than 3.0 GPa are assumed to efficiently segregate and mix in their respective proportions to form the model shield parental magma. The parental magma is then assumed to migrate to shallower depths to undergo fractional crystallization. Partition coefficients for the hybrid pyroxenite are assumed to be equivalent to peridotite (after Sobolev et al., 2005).

In this model, the silica-rich eclogite-derived melts are assumed to mix with the surrounding peridotite matrix at 3.0 GPa,. The silica content of the eclogitic-derived melts varies from 55.2 (basaltic andesite) to 48.7 wt. % (basalt; Le Bas et al., 1986), and is a function of both melt fraction and initial eclogite content (Table 20). The extent of melting for the eclogitic component at 3.0 GPa increases from 0.36 for the model with 15% initial eclogite and T_P = 1450 °C to nearly 1.0 for models with a potential temperature of 1600 °C. Directly linked to melt fraction, the silica content of the eclogite-derived melts increases with initial eclogite proportion (cooler P-T path) and decreases with increasing temperature. Silica contents for these melts are lower than those predicted by results from low-degree melt experimental charges (*e.g.*, Takahashi and Nakajima, 2002), but are consistent with experiments extended to

Table 20. Major element concentrations of the modeled shield magmas from the hybrid melting model between 4.0 and 3.0 GPa. Results are shown for 5, 10, and 15% initial eclogite in the plume for (a) T_P = 1450 °C, (b) T_P = 1525 °C, and (c) T_P = 1600 °C. The peridotite composition is shown only once, for reference, at the top of the table, because this component is not assumed to melt before 3.0 GPa. The amount of eclogite derived melt in the model shield magma, $X_{F,ecl}$, is given for each computational run and increases with increasing initial eclogite content and decreasing potential temperature. The eclogite melt is assumed to mix with the bulk peridotite composition in a 1:1 mixture to form the hybrid. The composition of the hybrid is shown in grey.

	SiO_2	TiO_2	Al_2O_3	Cr_2O_3	MgO	CaO	Na_2O	K_2O	P_2O_5	FeO_T	$F_{ecl,43}$
Peridotite	45.57	0.17	2.70	0.44	40.80	2.41	0.24	0.02	0.01	7.24	--
(a) 1450°C Potential Temperature											
5% Eclogite											
	SiO_2	TiO_2	Al_2O_3	Cr_2O_3	MgO	CaO	Na_2O	K_2O	P_2O_5	FeO_T	$F_{ecl,43}$
Eclogite	54.86	1.72	16.57	0.06	4.16	10.07	4.51	0.08	0.21	7.03	0.38
$X_{F,Ecl,43}$	SiO_2	TiO_2	Al_2O_3	Cr_2O_3	MgO	CaO	Na_2O	K_2O	P_2O_5	FeO_T	Mg#
0.50	50.21	0.94	9.64	0.25	22.48	6.24	2.38	0.05	0.11	7.14	85
10% Eclogite											
	SiO_2	TiO_2	Al_2O_3	Cr_2O_3	MgO	CaO	Na_2O	K_2O	P_2O_5	FeO_T	$F_{ecl,43}$
Eclogite	55.05	1.73	16.57	0.06	4.08	9.96	4.54	0.08	0.22	6.98	0.37
$X_{F,Ecl,43}$	SiO_2	TiO_2	Al_2O_3	Cr_2O_3	MgO	CaO	Na_2O	K_2O	P_2O_5	FeO_T	Mg#
0.50	50.31	0.95	9.64	0.25	22.44	6.19	2.39	0.05	0.11	7.11	85
15% Eclogite											
	SiO_2	TiO_2	Al_2O_3	Cr_2O_3	MgO	CaO	Na_2O	K_2O	P_2O_5	FeO_T	$F_{ecl,43}$
Eclogite	55.24	1.75	16.57	0.06	4.01	9.86	4.57	0.08	0.22	6.93	0.36
$X_{F,Ecl,43}$	SiO_2	TiO_2	Al_2O_3	Cr_2O_3	MgO	CaO	Na_2O	K_2O	P_2O_5	FeO_T	Mg#
0.50	50.40	0.96	9.64	0.25	22.40	6.13	2.40	0.05	0.12	7.08	85
(b) 1525°C Potential Temperature											
5% Eclogite											
	SiO_2	TiO_2	Al_2O_3	Cr_2O_3	MgO	CaO	Na_2O	K_2O	P_2O_5	FeO_T	$F_{ecl,43}$
Eclogite	50.51	1.29	16.47	0.04	6.86	12.95	3.40	0.04	0.11	7.59	0.74
$X_{F,Ecl,43}$	SiO_2	TiO_2	Al_2O_3	Cr_2O_3	MgO	CaO	Na_2O	K_2O	P_2O_5	FeO_T	Mg#
0.50	48.04	0.73	9.59	0.24	23.83	7.68	1.82	0.03	0.06	7.41	85
10% Eclogite											
	SiO_2	TiO_2	Al_2O_3	Cr_2O_3	MgO	CaO	Na_2O	K_2O	P_2O_5	FeO_T	$F_{ecl,43}$
Eclogite	50.69	1.32	16.49	0.04	6.69	12.81	3.47	0.04	0.11	7.60	0.71
$X_{F,Ecl,43}$	SiO_2	TiO_2	Al_2O_3	Cr_2O_3	MgO	CaO	Na_2O	K_2O	P_2O_5	FeO_T	Mg#
0.50	48.13	0.74	9.60	0.24	23.74	7.61	1.86	0.03	0.06	7.42	85
15% Eclogite											
	SiO_2	TiO_2	Al_2O_3	Cr_2O_3	MgO	CaO	Na_2O	K_2O	P_2O_5	FeO_T	$F_{ecl,43}$
Eclogite	50.87	1.34	16.51	0.06	6.52	12.67	3.54	0.04	0.12	7.62	0.68
$X_{F,Ecl,43}$	SiO_2	TiO_2	Al_2O_3	Cr_2O_3	MgO	CaO	Na_2O	K_2O	P_2O_5	FeO_T	Mg#
0.50	48.22	0.75	9.60	0.25	23.66	7.54	1.89	0.03	0.07	7.43	85
(c) 1600°C Potential Temperature											
5% Eclogite											
	SiO_2	TiO_2	Al_2O_3	Cr_2O_3	MgO	CaO	Na_2O	K_2O	P_2O_5	FeO_T	$F_{ecl,43}$
Eclogite	48.68	1.01	17.55	0.02	9.07	12.45	2.65	0.03	0.08	7.70	1.00
$X_{F,Ecl,43}$	SiO_2	TiO_2	Al_2O_3	Cr_2O_3	MgO	CaO	Na_2O	K_2O	P_2O_5	FeO_T	Mg#
0.50	47.13	0.59	10.13	0.23	24.93	7.43	1.45	0.03	0.05	7.47	86
10% Eclogite											
	SiO_2	TiO_2	Al_2O_3	Cr_2O_3	MgO	CaO	Na_2O	K_2O	P_2O_5	FeO_T	$F_{ecl,43}$
Eclogite	48.69	1.01	17.55	0.02	9.07	12.45	2.65	0.03	0.08	7.70	1.00
$X_{F,Ecl,43}$	SiO_2	TiO_2	Al_2O_3	Cr_2O_3	MgO	CaO	Na_2O	K_2O	P_2O_5	FeO_T	Mg#
0.50	47.13	0.59	10.12	0.23	24.93	7.43	1.45	0.03	0.05	7.47	86
15% Eclogite											
	SiO_2	TiO_2	Al_2O_3	Cr_2O_3	MgO	CaO	Na_2O	K_2O	P_2O_5	FeO_T	$F_{ecl,43}$
Eclogite	48.69	1.01	17.54	0.02	9.07	12.45	2.65	0.03	0.08	7.70	1.00
$X_{F,Ecl,43}$	SiO_2	TiO_2	Al_2O_3	Cr_2O_3	MgO	CaO	Na_2O	K_2O	P_2O_5	FeO_T	Mg#
0.50	47.13	0.59	10.12	0.23	24.93	7.43	1.45	0.03	0.05	7.47	86

higher-degree melt fractions (*e.g.*, experiment 9014 of Yaxley and Green (1998) with SiO_2 = 51.6 wt. % from a charge with F = 0.714).

Likewise, peridotite melt fraction at 3.0 GPa increases from 0.02 to 0.25 as potential temperatures increase from 1450 to 1600 °C, respectively. By assuming these partial melts of peridotite are distributed homogenously throughout the peridotite component, the silica-rich eclogite-derived melts can be considered to interact with a bulk peridotite composition everywhere. This assumption is likely reasonable for those conditions with relatively low-degree melt fractions (cooler T_P), but is somewhat unlikely for the warmer scenarios as the larger degree peridotite melts will undoubtedly exceed the effective porosity of the peridotite.

Eclogite-derived melts are assumed to segregate efficiently, infiltrate the surrounding peridotite, and interact with an equal volume of the bulk peridotite composition to create the hybrid pyroxenite. The total proportion of newly formed hybrid, X_{hyb}, can be expressed as:

$$X_{hyb} = 2F_{ecl,43} \cdot X_{ecl} \qquad 5.4$$

where $F_{ecl,43}$ is the melt fraction of eclogite from 4.0 to 3.0 GPa, and X_{ecl} is the initial proportion of eclogite, as above. Upon reaction, the silica-rich eclogite-derived melt completely converts the equilibrium peridotite assemblage (olivine + orthopyroxene ± clinopyroxene + spinel; 43 – 59 wt. % olivine) into an olivine-free assemblage (garnet + orthopyroxene + clinopyroxene + spinel; Appendix E). This reaction is consistent with and follows the metasomatic theory (Korzhinskii, 1970) argument of Sobolev et al. (2005). While silica-content decreases with increasing temperature (SiO_2 = 47.13 – 50.40) and MgO contents increase with increasing temperature (MgO = 22.40 – 24.93), the absolute range of each of these oxides is rather restricted. This limited range is largely a product of the relatively high degree melt of the eclogitic component ($F_{ecl,43}$ = 0.36 – 1.0).

The creation of the Older Series parental magma is resumed as the three components (eclogite residue, peridotite, and hybrid pyroxenite) are forced along the remainder of the composite P-T path to 2.0 GPa. The extent of melting for each component increases with increasing temperature, but decreases with increasing eclogite proportion due to the cooler P-T path (Table 21). The hybrid component melts to large degrees at all three temperatures ($F_{hyb,32}$ = 0.55 – 1.00), melting completely along the 1600 °C potential temperature P-T path. Similarly, the eclogitic residue also melts to large degrees ($F_{ecl,32}$ = 0.77 – 0.95), though there is no additional melting along the T_P = 1600 °C path the component melted completely from 4.0 to 3.0 GPa. The peridotitic component melts to the lowest extent of the three, and shows the smallest range of melt fractions ($F_{per,32}$ = 0.04 – 0.31).

Apart from the proportion of hybrid, the proportion of remaining eclogitic residue and unreacted peridotite at 3.0 GPa are required to calculate the mixing proportions for the parental magmas. The proportion of eclogite residue at 3.0 GPa is:

$$X_{ecl,res3} = X_{ecl}\left(1 - F_{ecl,43}\right) \qquad 5.5$$

and the proportion of peridotite that did not react with eclogitic melts to form the hybrid pyroxenite is:

$$X_{per,un3} = X_{per} - F_{ecl,43} \cdot X_{ecl} \qquad 5.6$$

As the creation of these parental magmas is modeled as a two stage melting process, the proportion of the parental magma formed by each component is not simply the amount of melting from 3.0 to 2.0 GPa, but requires knowledge of the history of the components. For example, to calculate the contribution of the peridotite component to the parental magma, it is necessary to know (1) the initial amount of eclogite, (2) the extent of melting of both eclogite and peridotite from 4.0 to 3.0 GPa, (3) the assumed mixing ratio to form the hybrid pyroxenite, and (4) the extent of melting of the unreacted peridotite from 3.0 to 2.0 GPa. Thus, the total melt fraction of the peridotite

Table 21. Major element contents for the hybrid melting model shield magmas with 10% initial eclogite from 3.0 to 2.0 GPa. Results are shown for 5, 10, and 15% initial eclogite in the plume for (a) T_P = 1450 °C, (b) T_P = 1525 °C, and (c) T_P = 1600 °C. The proportion of melt from each component, $X_{F,comp}$, composing the magma is given as well as the melt fraction for each melting stage. The composition of the shield magma is shown in grey.

(a) 1450°C Potential Temperature

5% Eclogite

	SiO_2	TiO_2	Al_2O_3	Cr_2O_3	MgO	CaO	Na_2O	K_2O	P_2O_5	FeO_T	F_{32}	$X_{F,comp}$
Peridotite	43.23	1.31	11.78	0.20	19.17	9.44	3.24	0.43	0.25	9.89	0.06	0.507
Eclogite	45.57	0.60	17.66	0.00	11.55	13.80	1.62	0.00	0.00	8.39	0.91	0.273
Hybrid	47.02	1.40	13.11	0.21	15.86	8.95	3.89	0.09	0.19	8.40	0.60	0.220

SiO_2	TiO_2	Al_2O_3	Cr_2O_3	MgO	CaO	Na_2O	K_2O	P_2O_5	FeO_T	Mg#
44.70	1.13	13.68	0.15	16.36	10.52	2.94	0.23	0.17	9.15	76

10% Eclogite

	SiO_2	TiO_2	Al_2O_3	Cr_2O_3	MgO	CaO	Na_2O	K_2O	P_2O_5	FeO_T	F_{32}	$X_{F,comp}$
Peridotite	43.31	1.35	11.97	0.21	18.84	9.21	3.55	0.49	0.28	9.75	0.05	0.308
Eclogite	45.70	0.63	17.77	0.00	11.11	13.51	1.73	0.00	0.00	8.69	0.83	0.381
Hybrid	47.03	1.43	13.30	0.20	15.45	8.98	4.02	0.09	0.20	8.39	0.58	0.312

SiO_2	TiO_2	Al_2O_3	Cr_2O_3	MgO	CaO	Na_2O	K_2O	P_2O_5	FeO_T	Mg#
45.38	1.10	14.59	0.13	14.84	10.77	3.01	0.18	0.15	8.92	75

15% Eclogite

	SiO_2	TiO_2	Al_2O_3	Cr_2O_3	MgO	CaO	Na_2O	K_2O	P_2O_5	FeO_T	F_{32}	$X_{F,comp}$
Peridotite	43.42	1.38	12.16	0.21	18.49	8.97	3.87	0.55	0.32	9.58	0.04	0.205
Eclogite	45.86	0.66	17.88	0.00	10.68	13.22	1.85	0.00	0.00	8.98	0.77	0.438
Hybrid	47.03	1.48	13.54	0.20	15.12	8.75	4.22	0.10	0.21	8.44	0.55	0.357

SiO_2	TiO_2	Al_2O_3	Cr_2O_3	MgO	CaO	Na_2O	K_2O	P_2O_5	FeO_T	Mg#
45.78	1.10	15.16	0.11	13.87	10.75	3.11	0.15	0.14	8.91	74

Table 21. *(continued)*

(b) 1525°C Potential Temperature

5% Eclogite

	SiO_2	TiO_2	Al_2O_3	Cr_2O_3	MgO	CaO	Na_2O	K_2O	P_2O_5	FeO_T	F_{32}	$X_{F,comp}$
Peridotite	43.41	0.91	10.04	0.23	21.89	10.14	1.61	0.17	0.10	10.37	0.14	0.653
Eclogite	46.51	0.23	17.30	0.00	14.72	11.79	0.57	0.00	0.00	8.05	0.93	0.063
Hybrid	45.49	0.92	11.47	0.20	20.61	9.48	2.40	0.04	0.08	8.43	0.75	0.284

SiO_2	TiO_2	Al_2O_3	Cr_2O_3	MgO	CaO	Na_2O	K_2O	P_2O_5	FeO_T	Mg#
44.20	0.87	10.91	0.21	21.07	10.06	1.77	0.12	0.09	9.67	80

10% Eclogite

	SiO_2	TiO_2	Al_2O_3	Cr_2O_3	MgO	CaO	Na_2O	K_2O	P_2O_5	FeO_T	F_{32}	$X_{F,comp}$
Peridotite	43.33	0.95	10.27	0.22	21.35	10.47	1.71	0.18	0.11	11.37	0.13	0.452
Eclogite	46.27	0.27	17.39	0.00	14.44	12.21	0.66	0.00	0.00	8.69	0.94	0.115
Hybrid	45.33	0.96	11.69	0.19	20.14	9.61	2.52	0.05	0.09	9.36	0.73	0.433

SiO_2	TiO_2	Al_2O_3	Cr_2O_3	MgO	CaO	Na_2O	K_2O	P_2O_5	FeO_T	Mg#
44.54	0.87	11.70	0.18	20.03	10.30	1.94	0.10	0.09	10.19	78

15% Eclogite

	SiO_2	TiO_2	Al_2O_3	Cr_2O_3	MgO	CaO	Na_2O	K_2O	P_2O_5	FeO_T	F_{32}	$X_{F,comp}$
Peridotite	43.25	0.99	10.51	0.21	20.86	10.68	1.84	0.20	0.12	10.23	0.12	0.321
Eclogite	46.21	0.30	17.29	0.00	14.17	12.60	0.75	0.00	0.00	7.89	0.95	0.160
Hybrid	45.20	1.00	11.90	0.19	19.66	9.73	2.65	0.05	0.09	8.64	0.70	0.518

SiO_2	TiO_2	Al_2O_3	Cr_2O_3	MgO	CaO	Na_2O	K_2O	P_2O_5	FeO_T	Mg#
44.73	0.88	12.32	0.16	19.17	10.50	2.08	0.09	0.09	9.03	79

Table 21. *(continued)*

(c) 1600°C Potential Temperature

5% Eclogite

	SiO_2	TiO_2	Al_2O_3	Cr_2O_3	MgO	CaO	Na_2O	K_2O	P_2O_5	FeO_T	F_{32}	$X_{F,comp}$
Peridotite	44.95	0.51	6.89	0.41	28.73	6.22	0.77	0.08	0.05	10.28	0.31	0.734
Eclogite	--	--	--	--	--	--	--	--	--	--	0.00	0.000
Hybrid	47.04	0.59	10.12	0.23	24.85	7.43	1.44	0.03	0.05	7.45	1.00	0.266

SiO_2	TiO_2	Al_2O_3	Cr_2O_3	MgO	CaO	Na_2O	K_2O	P_2O_5	FeO_T	Mg#
45.50	0.53	7.75	0.36	27.70	6.54	0.95	0.06	0.05	9.52	84

10% Eclogite

	SiO_2	TiO_2	Al_2O_3	Cr_2O_3	MgO	CaO	Na_2O	K_2O	P_2O_5	FeO_T	F_{32}	$X_{F,comp}$
Peridotite	44.70	0.55	7.31	0.38	27.87	6.66	0.85	0.09	0.05	10.41	0.28	0.526
Eclogite	--	--	--	--	--	--	--	--	--	--	0.00	0.000
Hybrid	47.04	0.59	10.12	0.23	24.85	7.43	1.44	0.03	0.05	7.45	1.00	0.474

SiO_2	TiO_2	Al_2O_3	Cr_2O_3	MgO	CaO	Na_2O	K_2O	P_2O_5	FeO_T	Mg#
45.81	0.57	8.64	0.31	26.44	7.03	1.13	0.06	0.05	9.01	84

15% Eclogite

	SiO_2	TiO_2	Al_2O_3	Cr_2O_3	MgO	CaO	Na_2O	K_2O	P_2O_5	FeO_T	F_{32}	$X_{F,comp}$
Peridotite	44.48	0.59	7.70	0.36	27.04	7.11	0.93	0.09	0.06	10.50	0.25	0.371
Eclogite	--	--	--	--	--	--	--	--	--	--	0.00	0.000
Hybrid	47.04	0.59	10.12	0.23	24.85	7.43	1.44	0.03	0.05	7.45	1.00	0.629

SiO_2	TiO_2	Al_2O_3	Cr_2O_3	MgO	CaO	Na_2O	K_2O	P_2O_5	FeO_T	Mg#
46.09	0.59	9.22	0.28	25.66	7.31	1.25	0.05	0.05	8.58	84

component is simply the product of the proportion of unreacted peridotite and the extent of melting of the peridotite from 3.0 to 2.0 GPa:

$$F_{per,2} = \left(X_{per} - F_{ecl,43} \cdot X_{ecl}\right) \cdot F_{per,32} = X_{per,un3} \cdot F_{per,32} \qquad 5.7$$

where $F_{per,32}$ is the melt fraction of peridotite from 3.0 to 2.0 GPa and X_{per}, $F_{ecl,43}$, X_{ecl}, and $F_{per,un3}$ are as defined above. The first term represents the amount of unreacted peridotite from the formation of the hybrid component. Likewise, the total melt fraction of the eclogite component is the product of the proportion of eclogite residue and the extent of melting of the eclogite residue from 3.0 to 2.0 GPa:

$$F_{ecl,2} = X_{ecl}\left(1 - F_{ecl,43}\right) \cdot F_{ecl,32} = X_{ecl,res3} \cdot F_{ecl,32} \qquad 5.8$$

where X_{ecl}, $F_{ecl,43}$, $F_{ecl,32}$, and $X_{ecl,res3}$ are as defined above, and where the first term representing the residual eclogite remaining after melt extraction at 3.0 GPa. Finally, the total melt fraction of the eclogite component at 2.0 GPa is the product of the proportion of hybrid created at 3.0 GPa and the extent of melting of the hybrid from 3.0 to 2.0 GPa:

$$F_{hyb,2} = \left(2F_{ecl,43}X_{ecl}\right) \cdot F_{hyb,32} = X_{hyb} \cdot F_{hyb,32} \qquad 5.9$$

where $F_{ecl,43}$, X_{ec}, $F_{hyb,32}$, and X_{hyb} are as defined above, and where the first term represents the amount of hybrid created at 3.0 GPa. The proportion of each in the parental magma can then be calculated as from the sum of the three components. The role of the more fertile eclogite and hybrid components in the formation of the parental magmas increase with both increasing temperature and initial eclogite content (Table 21).

Using the melt proportions calculated in Adiabat_1ph, the major element compositions of these constructed lavas can be compared to the parental estimates (Table 14). Just as in the binary melt-mixing model, the melts generated from the hottest runs, T_P = 1600 °C, are much too magnesian (MgO = 25.7 – 27.7 wt. %; Mg# = 84) for Mauritius. Magmas from the intermediate temperature runs, T_P = 1525 °C,

are also quite magnesian (MgO = 19.2 – 21.1 wt. %; Mg# ≈ 80), relative to the parental estimates (MgO = 14.5 – 16.4 wt. %). Silica contents for these lavas are low (44.2 – 44.7 wt. %), but FeO_T, CaO, Na_2O, and Al_2O_3 all fit within the range of parental estimates. Liquid lines of descent for this model (Figure 42) pass through or very near the Older Series data for the shield lavas. Melts produced by the coolest of the three runs, T_P = 1450 °C, have MgO contents much more consistent with the parental estimates (13.9 – 16.4 wt. %), though silica contents are still slightly lower than estimated (44.7 – 45.8 wt. %).

To this point, the development and presentation of the hybrid melting model has been rather complex. Here I present a detailed analysis of the procedure for major and trace elements for the model shield magmas to aide in understanding the scenario. For the hybrid melting model with T_P = 1525 °C and 10% initial eclogite, the modeling of the major elements are shown in Figure 42. The compositions of the initial peridotite and eclogite are depicted in the figures and Table 14. Looking at panel (a), the initial peridotite has higher MgO (40.80 wt. %) and lower SiO_2 (45.57 wt. %) than the initial eclogite composition (MgO = 9.10 and SiO_2 = 48.68 wt. %). The system rises adiabatically to 3.0 GPa where the large degree melts of the eclogitic component ($F_{ecl,43}$ = 0.71; SiO_2 = 50.69 and MgO = 6.69 wt. %) are efficiently extracted and react with the bulk peridotite composition in a 1:1 ratio to produce the model hybrid pyroxenite (SiO_2 = 48.13 and MgO = 23.74 wt. %; Table 20b). The eclogitic-derived residue has a picritic composition (SiO_2 = 43.57 and MgO = 14.95 wt. %). At this point, three components are present in the system: (1) unreacted peridotite, (2) eclogite-derived residue, and (3) hybrid pyroxenite. Adiabatic decompression and melting continues until 2.0 GPa, when the plume intersects the base of the oceanic lithosphere. At this point, the unreacted portion of the peridotitic component has melted 13% to a picritic composition (SiO_2 = 43.33 and MgO = 21.35

Figure 42. Representative major element compositions for the geochemical evolution of the hybrid melting model with T_P = 1525 °C and a maximum vertical ascent of the post-erosional source in the plume stem to 3.0 GPa, for a plume with 10% initial eclogite. Black diamond – Older Series lavas. Open black diamond – Post-erosional lavas. Green square – Initial eclogite. Open green square – Residual melt at 2.0 GPa. Small light green square – Residual eclogite melt at 2.7 GPa. Red circle – Initial peridotite (not visible, MgO = 40.8 wt. %). Open red circle – Peridotite melt at 2.0 GPa. Small pink circle – Residual peridotite melt at 2.7 GPa. Light blue cross – Model shield magma. Dark blue cross – Model post-erosional magma. Light blue line – LLOD of model shield magma at 0.8 GPa (after Albarède et al., 1997). Dark blue line – LLOD of model post-erosional magma at 0.8 GPa. Blue field – Mixing between melts of peridotite, residual eclogite, and hybrid pyroxenite at 2.0 GPa. Purple field – Mixing between melts of residual peridotite, residual eclogite, and residual hybrid at 2.7 GPa. In the hybrid model, the peridotitic and eclogitic component are each allowed to rise along the 10% initial eclogite composite P-T path from 4.0 to 3.0 GPa. At 3.0 GPa, melts from the eclogitic component react with the peridotite to form a hybrid pyroxenite. The unreacted peridotite, eclogitic residue, and hybrid rise to 2.0 GPa. At 2.0 GPa, the melts of each component generated by this decompression are mixed, producing the model shield magma. The model post-erosional lavas are generated in a very similar manner. After formation of the hybrid pyroxenite at 3.0 GPa, the three components continue decompression through the plume tail from 3.0 to 2.7 GPa. Any melts generated in this region are mixed to form the model post-erosional magma. See text for full description. (a) SiO_2, (b) FeO_T, and (c) CaO plotted against wt. % MgO. The model shield magma composition reproduces SiO_2 and FeO_T well, though CaO is low for a given MgO content. The model post-erosional lava reasonably reproduces the major element characteristics seen in the observed lavas.

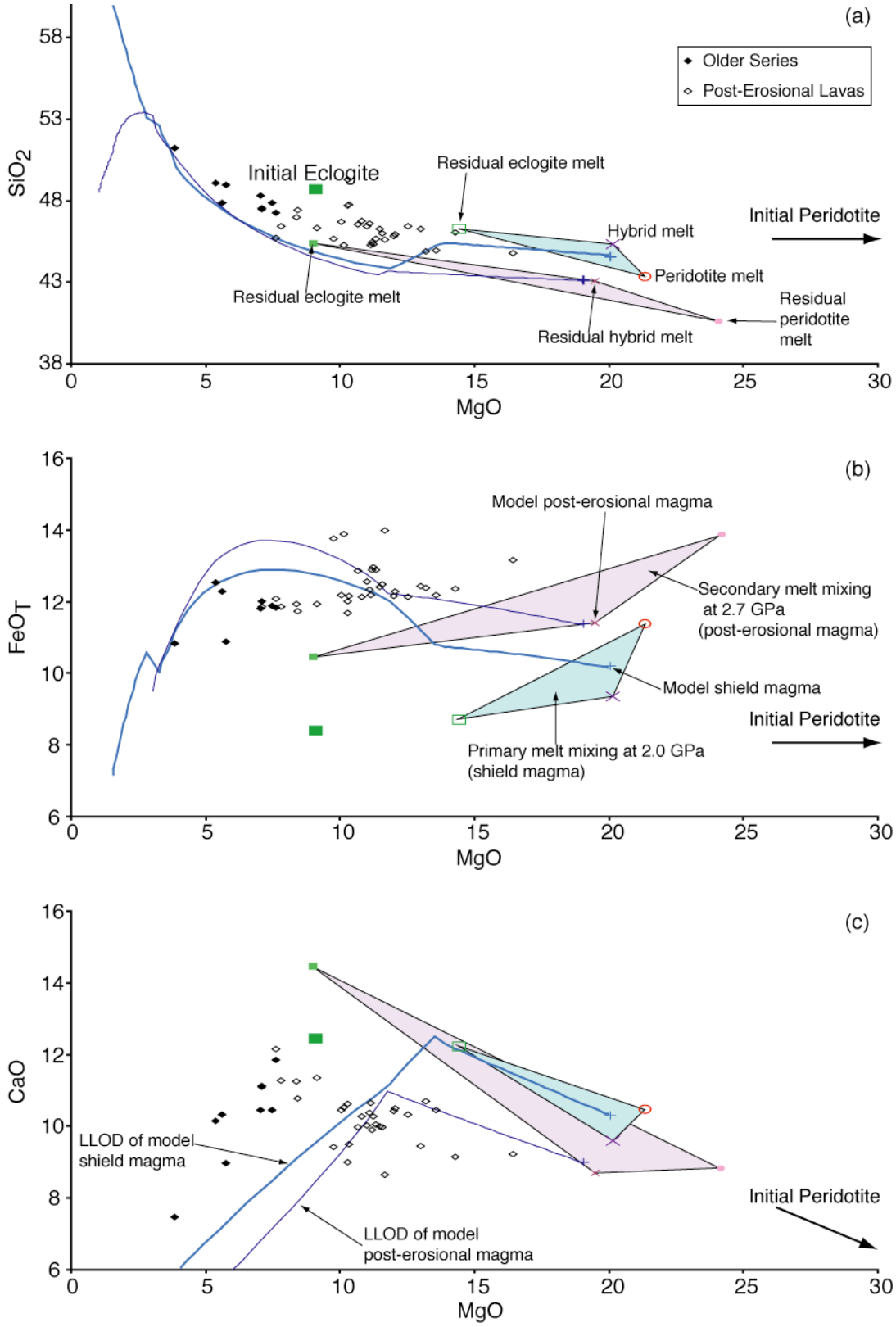
(a)
Older Series
Post-Erosional Lavas
Initial Eclogite
Residual eclogite melt
Hybrid melt
Initial Peridotite
Peridotite melt
Residual eclogite melt
Residual peridotite melt
Residual hybrid melt
SiO2
MgO
(b)
Model post-erosional magma
Secondary melt mixing at 2.7 GPa (post-erosional magma)
Model shield magma
Initial Peridotite
Primary melt mixing at 2.0 GPa (shield magma)
FeOT
MgO
(c)
LLOD of model shield magma
Initial Peridotite
LLOD of model post-erosional magma
CaO
MgO

wt. %). The eclogite-derived residue has melted almost entirely ($F_{ecl,32}$ = 0.94) to a basaltic composition (SiO_2 = 46.27 and MgO = 14.44 wt. %). The hybrid component also melts extensively ($F_{hyb,32}$ = 0.73) to a basaltic composition (SiO_2 = 45.33 and MgO = 20.14 wt. %). The melts of the unreacted peridotite and hybrid components mix in near equal proportions, with lesser amounts of melt from the eclogite-derived residue, to form the basaltic model shield parental magma (SiO_2 = 44.54 and MgO = 20.03 wt. %; Table 21b). This model shield magma can then be used to calculate the LLOD and compare the modeled magma to the observed Older Series data (Figure 42). An identical procedure can be applied to the 5 and 15% initial eclogite models (Table 21).

The procedure for the hybrid melting model with T_P = 1525 °C and 10% initial eclogite can also be described in terms of trace elements for the model shield magmas (Figure 43). The initial peridotite has lower La/Sm (3.33) and Sm/Yb (2.61) than the initial eclogite (La/Sm = 4.61 and Sm/Yb = 4.47; Table 22). These compositions have been fit to the two components such that the model shield magma reproduces the observed Older Series values. When melting commences at 4.0 GPa, the first melts of the eclogite-derived melts (La/Sm = 6.55 and Sm/Yb = 28.88) are greater than the initial components, but decrease as the degree of melting increases (not shown). The system rises adiabatically to 3.0 GPa where the large degree melts of the eclogitic component ($F_{ecl,43}$ = 0.71; La/Sm = 4.93 and Sm/Yb = 10.84) are efficiently extracted and react with the bulk peridotite composition in a 1:1 ratio to produce the model hybrid pyroxenite (La/Sm = 4.84 and Sm/Yb = 9.19). The eclogite-derived residue has low trace element ratio (La/Sm = 0.44 and Sm/Yb = 0.52), complementary to the eclogite-derived melt. At this point, three components are present in the system: (1) unreacted peridotite, (2) eclogite-derived residue, and (3) hybrid pyroxenite. Adiabatic decompression and melting continues until 2.0 GPa, when the plume

Figure 43. Representative incompatible trace element composition for the geochemical evolution of the hybrid melting model with T_P = 1525 °C and a maximum vertical ascent of the post-erosional source in the plume stem to 3.0 GPa, for a plume with 10% initial eclogite. Symbols after Figure 42. See text for full discussion of model systematics. Vertical and horizontal dashed lines represent the trace element ratio of Primitive Mantle (McDonough and Sun, 1995). La/Sm plotted against Sm/Yb. Incompatible trace element compositions of the initial eclogite and initial peridotite are chosen such that the model shield magma fits the observed Older Series trace element data. Trace element compositions of the initial compositions are kept constant for the post-erosional lavas. In this model, the post-erosional lavas are dominated by melts of the hybrid component ($X_{F,hyb}$ = 0.93) and do not resemble the observed post-erosional data.

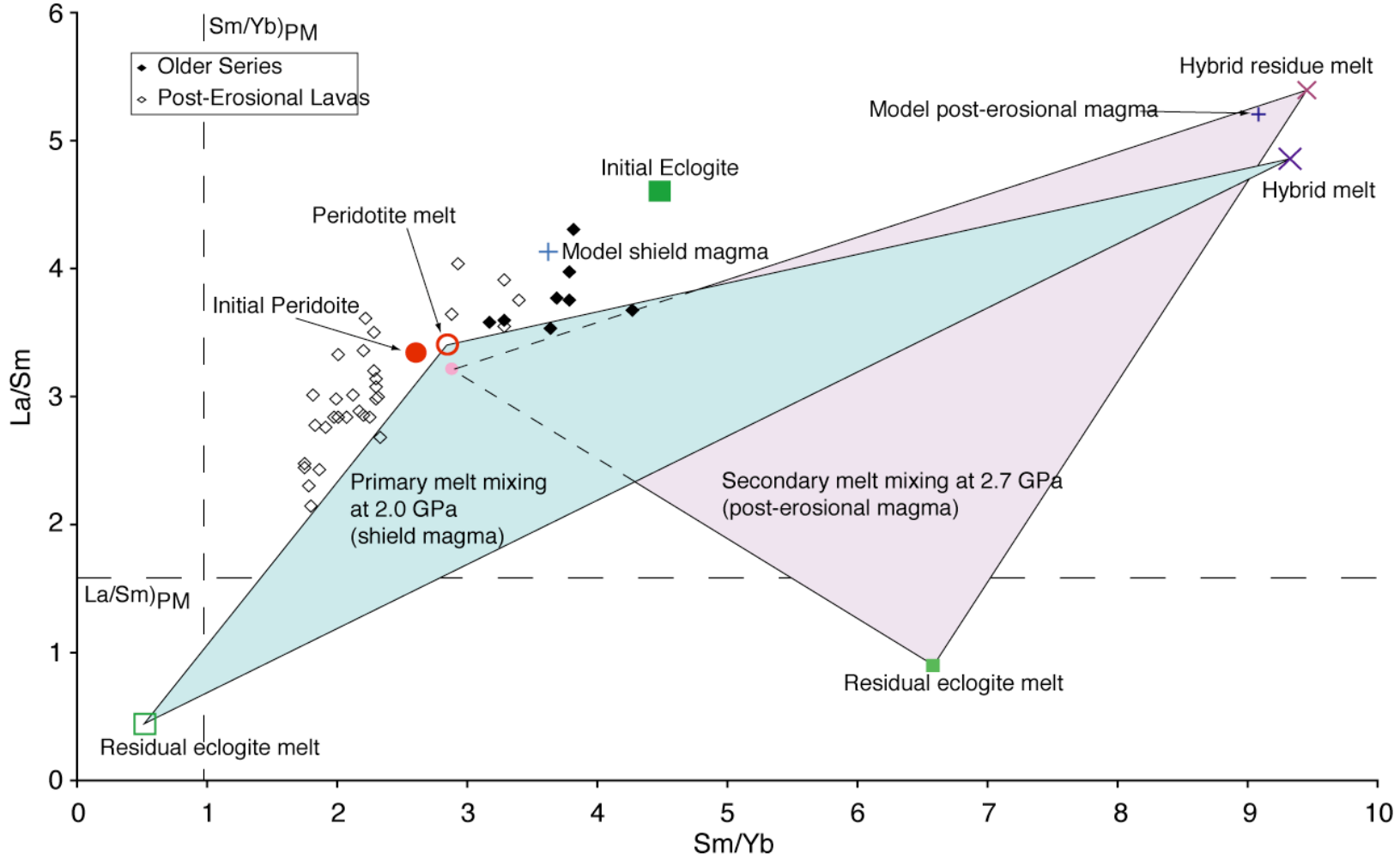
Sm/Yb)PM
Older Series
Post-Erosional Lavas
Hybrid residue melt
Model post-erosional magma
Initial Eclogite
Hybrid melt
Peridotite melt
Model shield magma
Initial Peridoite
Primary melt mixing
at 2.0 GPa
(shield magma)
Secondary melt mixing at 2.7 GPa
(post-erosional magma)
La/Sm)PM
Residual eclogite melt
Residual eclogite melt
La/Sm
Sm/Yb
0
1
2
3
4
5
6
7
8
9
10

Table 22. Hybrid model shield lava trace elements at 2.0 GPa

1525°C Potential Temperature

Init. Conc.	La	Sm	Yb	Hf	Zr	Nb	Sr	Nd	Pb	Ba	La/Sm	Sm/Yb	Hf/Zr	Sr/Nd	La/Nb	Pb/Yb	Zr/Nb	Ba/La
Peridotite	1.00	0.30	0.12	0.32	16.00	2.00	14.70	0.80	0.06	12.00	3.33	2.61	0.020	18.38	0.50	0.52	8.00	12.00
Eclogite	17.50	3.80	0.85	2.20	96.00	12.00	113.20	11.20	2.20	100.00	4.61	4.47	0.023	10.11	1.46	2.59	8.00	5.71

10% Eclogite

	La	Sm	Yb	Hf	Zr	Nb	Sr	Nd	Pb	Ba	La/Sm	Sm/Yb	Hf/Zr	Sr/Nd	La/Nb	Pb/Yb	Zr/Nb	Ba/La	F_{32}	$X_{F,comp}$
Peridotite	7.63	2.24	0.79	2.40	110.50	14.87	111.03	6.02	0.46	92.04	3.41	2.84	0.022	18.45	0.51	0.58	7.43	12.07	0.13	0.45
Eclogite	0.45	1.00	1.92	0.66	21.47	0.09	4.95	1.29	0.17	0.80	0.44	0.52	0.031	3.84	4.97	0.09	239.53	1.79	0.94	0.11
Hybrid	17.50	3.61	0.39	2.17	97.16	12.94	118.07	11.02	2.13	104.83	4.85	9.32	0.022	10.71	1.35	5.50	7.51	5.99	0.73	0.43
	La	Sm	Yb	Hf	Zr	Nb	Sr	Nd	Pb	Ba	La/Sm	Sm/Yb	Hf/Zr	Sr/Nd	La/Nb	Pb/Yb	Zr/Nb	Ba/La		
	11.08	2.69	0.74	2.10	94.51	12.34	101.91	7.64	1.15	87.11	4.12	3.61	0.022	13.33	0.90	1.54	7.66	7.87		

Trace element concentrations for the hybrid melting model shield magmas with 10% initial eclogite from 3.0 to 2.0 GPa. Results are shown for 5, 10, and 15% initial eclogite in the plume for T_P = 1525 °C and 2.5 GPa. The proportion of melt from each component, $X_{F,comp}$, composing the magma is given as well as the melt fraction for each melting stage. The composition of the shield magma is shown in grey.

intersects the base of the oceanic lithosphere. At this point, the unreacted portion of the peridotitic component has melted 13% (La/Sm = 3.41 and Sm/Yb = 2.84). Both the eclogite-derived residue ($F_{ecl,32}$ = 0.94; La/Sm = 0.44 and Sm/Yb = 0.52) and the hybrid component have undergone extensive melting ($F_{hyb,32}$ = 0.73; La/Sm = 4.85 and Sm/Yb = 9.32). The melts of the unreacted peridotite and hybrid components mix in near equal proportions, with lesser amounts of melt from the eclogite-derived residue, to form the model shield parental magma (La/Sm = 4.12 and Sm/Yb = 3.62; Table 22). A similar procedural analysis can be completed for the Sr-, Nd-, and Pb-isotopic ratios (Figure 44).

Though not as extensive as in the binary model, the large degrees of melting of the plume components are again one of the most compelling features of the hybrid melting model. This trait is best illustrated by the eclogitic component, which melts 71% between 4.0 and 3.0 GPa (Table 20b), and an additional 94% from 3.0 GPa and 2.0 GPa (Table 21b). In comparison, the peridotitic component melts 13% from 3.0 to 2.0 GPa (to maintain a bulk peridotite composition for hybrid formation, this component is assumed to effectively forgo melting at pressures greater than 3.0 GPa) and the hybrid component melts 73% from 3.0 to 2.0 GPa. As discussed above, this model also violates the refractory eclogite assumption of Sobolev et al. (2005) (*i.e.*, the eclogite will become refractory and stop melting at F = 0.5), though this is again likely to be a function of the assumption of batch melting rather than (near-) fractional melting for the model.

The hybrid model does not suffer from the same compositional restrictions that result from the complete melting of the eclogitic component. In contrast, the formation of the hybrid component at 3.0 GPa from the reaction of the eclogite-derived melts and the bulk peridotite creates a three-component mixing space (Figure 42), though only two of the components are truly independent. Theoretically, the

Figure 44. Isotope ratios systematics for the geochemical evolution of the hybrid melting model with T_P = 1525 °C and a maximum vertical ascent of the post-erosional source in the plume stem to 3.0 GPa, for a plume with 10% initial eclogite. Symbols after Figure 42. See text for full discussion of model systematics. End-member isotope compositions are chosen to reflect the observed range of Mauritius lavas. Plot of Sm/Yb against $^{87}Sr/^{86}Sr$, (b) ε_{Nd}, and (c) $^{206}Pb/^{204}Pb$. Trace element concentrations for mixing are taken from compositions of the model shield and post-erosional magmas. Model shield magmas reproduce Nd-isotopes well, though small deviations to the selected component compositions would improve fits for Sr- and Pb-isotopes. Model post-erosional magmas are dominated by the enriched melts of the eclogitic and hybrid residues ($X_{F,ecl} + X_{F,hyb} > 0.95$) and are not representative of the observed data.

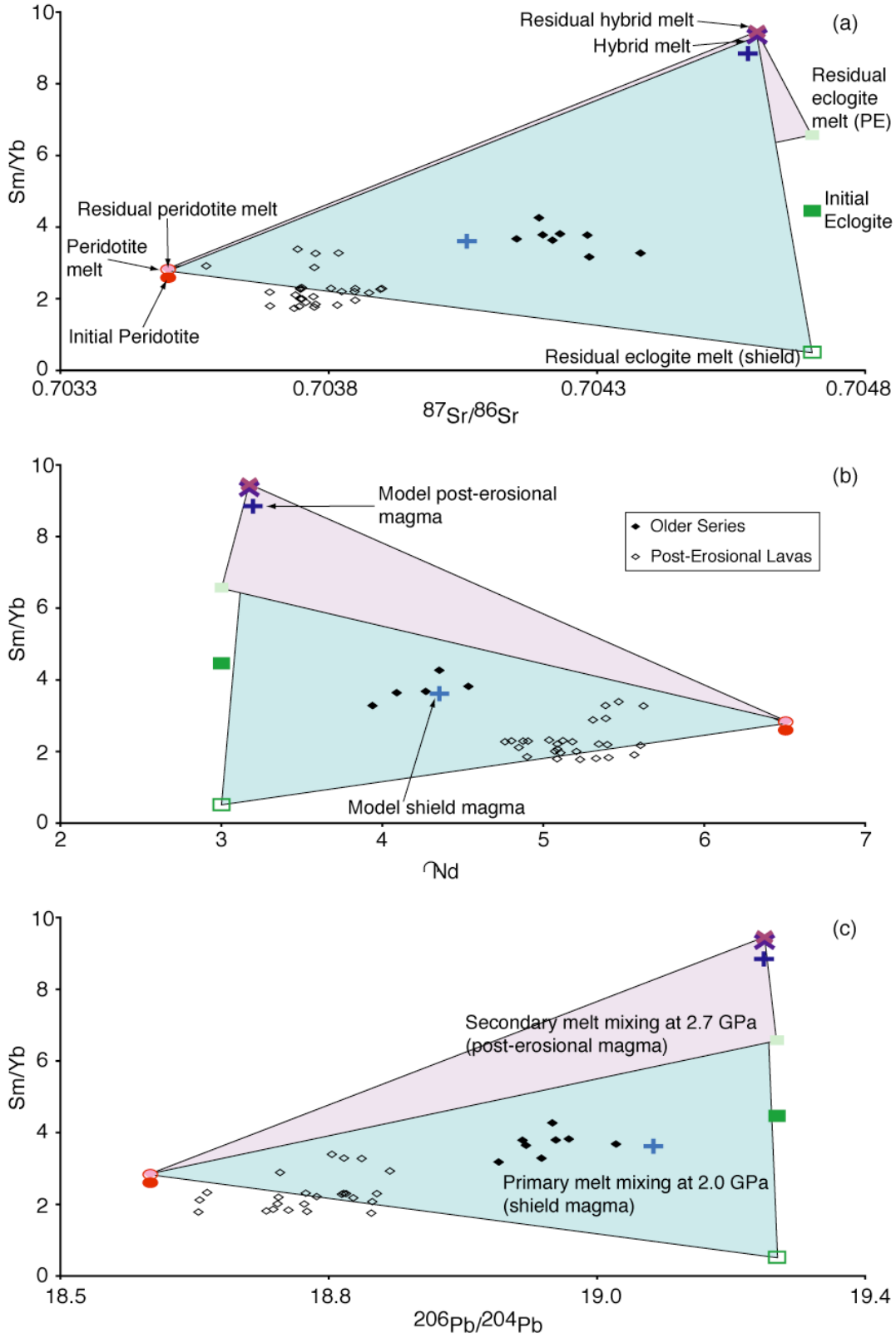
(a)
Residual hybrid melt
Hybrid melt
Residual eclogite melt (PE)
Initial Eclogite
Residual peridotite melt
Peridotite melt
Initial Peridotite
Residual eclogite melt (shield)
Sm/Yb
87Sr/86Sr
0.7033
0.7038
0.7043
0.7048
(b)
Model post-erosional magma
Older Series
Post-Erosional Lavas
Model shield magma
Sm/Yb
εNd
(c)
Secondary melt mixing at 2.7 GPa (post-erosional magma)
Primary melt mixing at 2.0 GPa (shield magma)
Sm/Yb
206Pb/204Pb
18.5
18.8
19.0
19.4

Older Series data being fit by the iterative modeling does not need to be bracketed by the initial compositions, a requirement of the binary model, as the hybrid component has highly enriched trace element ratios (Figure 43). Regardless, the modeled initial trace element compositions for the peridotitic and eclogitic components do bracket the Older Series data, though this solution is decidedly non-unique and would benefit from a more rigorous mathematical treatment (Table 22).

Despite, or rather because of their large differences in degrees of melting, the hybrid and peridotite components contribute near equal amounts of melt to the hybrid shield magma ($X_{F,hyb}$ = 0.45 and $X_{F,per}$ = 0.43). In comparison, the eclogitic component contributes relatively little ($X_{F,ecl}$ = 0.12), a function of the eclogite-derived residue being strongly depleted to create the hybrid component (Table 22). Moreover, the eclogitic component contributes little to the trace element budget, directly, as the concentrations in the eclogite-derived are much lower than from the hybrid and peridotite components.

Several key observations about the modeled initial trace element concentrations are evident from Figure 30b. First, the model peridotitic component is enriched in the most incompatible elements relative to DM, though concentrations are broadly consistent throughout the moderately incompatible elements. The component has higher Zr and lower Yb than DM. A small negative Pb anomaly is observed. Second, the eclogitic component is also enriched in the most incompatible elements relative to N-MORB, and is broadly consistent throughout the moderately incompatible elements. The component has lower Hf and Yb than observed in N-MORB. Finally, each of he model results have steep PM normalized REE patterns ($(La/Sm)_N$, $Sm/Yb)_N$, and $La/Yb)_N > 1$), which differ from the reference values for each source ($(La/Sm)_N$ and $La/Yb)_N < 1$ and $Sm/Yb)_N \approx 1$). The spider diagram of the hybrid shield magma (Figure 31) is very similar to the Older Series lavas, although the

absolute concentration of the model magma trace elements is lower than the observed lavas.

Under the isotopic compositions chosen for the enriched and depleted components, the isotopic results of the hybrid model shield magmas are calculated for the modeled initial trace element compositions (Table 23). These model compositions successfully reproduce the Older Series ε_{Nd} values, though the $^{87}Sr/^{86}Sr$ and $^{206}Pb/^{204}Pb$ are somewhat less and more enriched than the Older Series, respectively (Figure 44). However, the model $^{87}Sr/^{86}Sr$ does maintain the some of the enriched measure of the Older Series lavas (*i.e.*, $^{87}Sr/^{86}Sr > 0.70400$). A small increase in the Sr-isotope ratio of the depleted component ($^{87}Sr/^{86}Sr \approx 0.70375$) and a small decrease in the Pb-isotope ratio of the enriched component ($^{206}Pb/^{204}Pb \approx 19.20$) would better fit the model magmas to the observed lavas. Thus, the hybrid model can reproduce the Older Series lavas with reasonable isotopic compositions.

Post-erosional

Just as in the hybrid model of the shield lavas, the modeled post-erosional lavas undergo hybrid creation at 3.0 GPa, leaving a three-component system of (1) peridotite, (2) eclogite-derived residue, and (3) hybrid pyroxenite. The same pressure and temperature conditions discussed above for the binary melt-mixing model will be applied to the hybrid model. The implications of altering the thickness of the effective upper boundary layer will be assessed, as well as the effects of a uniform plume temperature (T_P = 1525 °C) versus a cooler particle path (T_P = 1450 °C). This modeling outputs geochemical data for the evolution of the major (Figure 42) and trace elements (Figure 43), and isotopic ratios (Figure 44). Here, the procedure implemented for generation of the model post-erosional magma will be review for the trace element ratios.

Table 23. Hybrid model shield lava isotope ratios

1525°C Potential Temperature, 10% Eclogite

	Sr	Nd	Pb	$^{87}Sr/^{86}Sr$	εNd	$^{206}Pb/^{204}Pb$	X_F
Peridotite	111.03	6.02	0.46	0.70350	6.50	18.60	0.452
Eclogite	4.95	1.29	0.17	0.70470	3.00	19.30	0.115
Hybrid	118.07	11.02	2.13	0.70460	3.17	19.29	0.433
	Sr	Nd	Pb	$^{87}Sr/^{86}Sr$	εNd	$^{206}Pb/^{204}Pb$	
	101.91	7.64	1.15	0.70406	4.36	19.16	

Isotope compositions for the hybrid melting model shield magmas with 10% initial eclogite from 3.0 to 2.0 GPa. Results are shown for 5, 10, and 15% initial eclogite in the plume for T_P = 1525 °C and 2.5 GPa. The proportion of melt from each component, XF,comp, composing the magma is given as well as the melt fraction for each melting stage. The composition of the shield magma is shown in grey.

For the hybrid pyroxenite model with a uniform plume temperature (T_P = 1525 °C), 10% initial eclogite, and an effective upper boundary at 3.0 GPa, the initial peridotite has lower La/Sm (3.33) and Sm/Yb (2.61) than the initial eclogite (La/Sm = 4.61 and Sm/Yb = 4.47; Table 24a). In order to main internal consistency between the shield and post-erosional models, the trace element ratios determined for each component for the shield lavas have been applied to the models of the post-erosional lavas. When melting commences at 4.0 GPa, the first melts of the eclogitic component (La/Sm = 6.55 and Sm/Yb = 28.88) are greater than the initial component, but decrease as the degree of melting increases (not shown). The system decompresses adiabatically to 3.0 GPa where the large degree melts of the eclogitic component ($F_{ecl,43}$ = 0.71; La/Sm = 4.93 and Sm/Yb = 10.84; Figure 43) are efficiently extracted and react with the bulk peridotite composition in a 1:1 ratio to produce the model hybrid pyroxenite (La/Sm = 4.84 and Sm/Yb = 9.19). The resulting eclogite-derived residue has low trace element ratios (La/Sm = 0.44 and Sm/Yb = 0.52), complementary to the eclogite-derived melt. At this point, three components are present in the system: (1) unreacted peridotite, (2) eclogite-derived residue, and (3) hybrid pyroxenite. Adiabatic decompression and melting continues through the plume tail along the post-erosional particle path (*e.g.*, Phipps Morgan and others) for 0.3 GPa, finally stopping at an upper limit of 2.7 GPa. At this point, the unreacted portion of the peridotitic component has melted 0.2% in the plume tail (La/Sm = 3.21 and Sm/Yb = 2.88), the eclogite-derived residue has melted 13% in the plume tail (La/Sm = 0.90 and Sm/Yb = 6.58), and the hybrid component has melted to much higher degrees, $F_{hyb,327}$ = 0.47 (La/Sm = 5.38 and Sm/Yb = 9.45). When these melts are mixed, the melts of the hybrid pyroxenite provide the bulk of the post-erosional magma ($X_{F,hyb}$ = 0.95) and impart an enriched flavor to the magma (La/Sm = 5.20 and Sm/Yb = 9.08; Table 24a).

Table 24. Major element contents for the binary melt-mixing model post-erosional magmas with 10% initial eclogite. Results are shown for both the (a) T_P = 1525 °C and $P_{max,PE}$ = 3.0, (b) T_P = 1525 °C and $P_{max,PE}$ = 2.5, (a) T_P = 1450 °C and $P_{max,PE}$ = 3.0, and (a) T_P = 1450 °C and $P_{max,PE}$ = 2.5 models. The proportion of eclogite melt, $X_{F,ecl}$, composing the magma is given as well as the melt fraction for each melting stage. The composition of the post-erosional magma is shown in grey.

(a) 1525 °C Potential Temperature, $P_{max,PE}$ = 3.0 GPa

Init. Conc.	La	Sm	Yb	Hf	Zr	Nb	Sr	Nd	Pb	Ba	La/Sm	Sm/Yb	Hf/Zr	Sr/Nd	La/Nb	Pb/Yb	Zr/Nb	Ba/La
Peridotite	1.00	0.30	0.12	0.32	16.00	2.00	14.70	0.80	0.06	12.00	3.33	2.61	0.020	18.38	0.50	0.52	8.00	12.00
Eclogite	17.50	3.80	0.85	2.20	96.00	12.00	113.20	11.20	2.20	100.00	4.61	4.47	0.023	10.11	1.46	2.59	8.00	5.71

	La	Sm	Yb	Hf	Zr	Nb	Sr	Nd	Pb	Ba	La/Sm	Sm/Yb	Hf/Zr	Sr/Nd	La/Nb	Pb/Yb	Zr/Nb	Ba/La	F_{43}	F_{327}	X_F
Peridotite	9.47	2.95	1.02	3.22	157.29	19.80	151.37	8.08	0.34	21.88	3.21	2.88	0.020	18.73	0.48	0.33	7.94	2.31	0.07	0.00	0.02
Eclogite	2.88	3.19	0.48	1.94	74.14	0.62	30.04	6.12	0.88	5.53	0.90	6.58	0.026	4.91	4.63	1.82	119.25	1.92	0.71	0.13	0.05
Hybrid	26.35	4.90	0.52	3.00	142.26	19.84	171.07	15.34	3.28	162.52	5.38	9.45	0.021	11.15	1.33	6.33	7.17	6.17	--	0.47	0.93
	La	Sm	Yb	Hf	Zr	Nb	Sr	Nd	Pb	Ba	La/Sm	Sm/Yb	Hf/Zr	Sr/Nd	La/Nb	Pb/Yb	Zr/Nb	Ba/La			
	24.80	4.77	0.53	2.95	138.90	18.81	163.20	14.72	3.10	151.63	5.20	9.08	0.021	11.09	1.32	5.90	7.38	6.11			

(b) 1525 °C Potential Temperature, $P_{max,PE}$ = 2.5 GPa

Init. Conc.	La	Sm	Yb	Hf	Zr	Nb	Sr	Nd	Pb	Ba	La/Sm	Sm/Yb	Hf/Zr	Sr/Nd	La/Nb	Pb/Yb	Zr/Nb	Ba/La
Peridotite	1.00	0.30	0.12	0.32	16.00	2.00	14.70	0.80	0.06	12.00	3.33	2.61	0.020	18.38	0.50	0.52	8.00	12.00
Eclogite	17.50	3.80	0.85	2.20	96.00	12.00	113.20	11.20	2.20	100.00	4.61	4.47	0.023	10.11	1.46	2.59	8.00	5.71

	La	Sm	Yb	Hf	Zr	Nb	Sr	Nd	Pb	Ba	La/Sm	Sm/Yb	Hf/Zr	Sr/Nd	La/Nb	Pb/Yb	Zr/Nb	Ba/La	F_{43}	F_{325}	F_{2522}	X_F
Peridotite	4.40	2.27	0.86	2.35	117.89	10.82	95.43	5.83	0.10	5.75	1.94	2.65	0.020	16.37	0.41	0.12	10.90	1.31	0.07	0.09	0.01	0.62
Eclogite	0.03	0.63	0.84	0.45	12.39	0.00	0.56	0.40	0.04	0.02	0.05	0.75	0.037	1.40	15.12	0.05	5419.51	0.62	0.71	0.37	0.49	0.14
Hybrid	8.27	3.44	0.39	1.99	76.45	3.68	90.17	9.92	0.29	0.88	2.40	8.85	0.026	9.09	2.25	0.75	20.79	0.11	--	0.55	0.04	0.24
	La	Sm	Yb	Hf	Zr	Nb	Sr	Nd	Pb	Ba	La/Sm	Sm/Yb	Hf/Zr	Sr/Nd	La/Nb	Pb/Yb	Zr/Nb	Ba/La				
	4.73	2.33	0.74	2.01	93.53	7.63	81.20	6.07	0.14	3.80	1.92	3.13	0.021	13.38	0.62	0.19	12.26	0.80				

Table 24. *(continued)*

(c) 1450 °C Potential Temperature, $P_{max,PE}$ = 3.0 GPa

Init. Conc.	La	Sm	Yb	Hf	Zr	Nb	Sr	Nd	Pb	Ba	La/Sm	Sm/Yb	Hf/Zr	Sr/Nd	La/Nb	Pb/Yb	Zr/Nb	Ba/La				
Peridotite	1.00	0.30	0.12	0.32	16.00	2.00	14.70	0.80	0.06	12.00	3.33	2.61	0.020	18.38	0.50	0.52	8.00	12.00				
Eclogite	17.50	3.80	0.85	2.20	96.00	12.00	113.20	11.20	2.20	100.00	4.61	4.47	0.023	10.11	1.46	2.59	8.00	5.71				
	La	Sm	Yb	Hf	Zr	Nb	Sr	Nd	Pb	Ba	La/Sm	Sm/Yb	Hf/Zr	Sr/Nd	La/Nb	Pb/Yb	Zr/Nb	Ba/La	F_{43}	F_{327}		X_F
Peridotite	--	--	--	--	--	--	--	--	--	--	--	--	--	--	--	--	--	--	0.02	0.00		--
Eclogite	10.97	6.02	0.47	3.49	148.43	2.22	114.68	15.76	2.33	20.5	1.82	12.92	0.023	7.28	4.95	5.01	66.96	1.87	0.37	0.07		0.17
Hybrid	76.52	10.08	0.45	5.89	328.31	57.94	237.87	35.97	9.71	422	7.59	22.45	0.018	6.61	1.32	21.62	5.67	5.52	--	0.28		0.83
	La	Sm	Yb	Hf	Zr	Nb	Sr	Nd	Pb	Ba	La/Sm	Sm/Yb	Hf/Zr	Sr/Nd	La/Nb	Pb/Yb	Zr/Nb	Ba/La				
	65.41	9.39	0.45	5.48	297.81	48.49	216.98	32.54	8.46	354.25	6.96	20.78	0.018	6.67	1.35	18.72	6.14	5.42				

(d) 1450 °C Potential Temperature, $P_{max,PE}$ = 2.5 GPa

Init. Conc.	La	Sm	Yb	Hf	Zr	Nb	Sr	Nd	Pb	Ba	La/Sm	Sm/Yb	Hf/Zr	Sr/Nd	La/Nb	Pb/Yb	Zr/Nb	Ba/La				
Peridotite	1.00	0.30	0.12	0.32	16.00	2.00	14.70	0.80	0.06	12.0	3.33	2.61	0.020	18.38	0.50	0.52	8.00	12.00				
Eclogite	17.50	3.80	0.85	2.20	96.00	12.00	113.20	11.20	2.20	100	4.61	4.47	0.023	10.11	1.46	2.59	8.00	5.71				
	La	Sm	Yb	Hf	Zr	Nb	Sr	Nd	Pb	Ba	La/Sm	Sm/Yb	Hf/Zr	Sr/Nd	La/Nb	Pb/Yb	Zr/Nb	Ba/La	F_{43}	F_{325}	F_{2522}	X_F
Peridotite	20.83	4.71	1.52	5.42	277.70	41.73	290.47	13.79	0.74	39.2	4.42	3.09	0.020	21.06	0.50	0.49	6.66	1.88	0.02	0.03	0.00	0.09
Eclogite	0.22	1.56	1.08	1.06	26.32	0.01	5.61	1.89	0.12	0.1	0.14	1.45	0.040	2.98	23.82	0.11	2788.54	0.44	0.37	0.22	0.38	0.81
Hybrid	22.52	7.09	0.48	3.99	164.89	9.20	223.04	22.81	0.76	2.3	3.18	14.81	0.024	9.78	2.45	1.59	17.93	0.10	--	0.36	0.05	0.10
	La	Sm	Yb	Hf	Zr	Nb	Sr	Nd	Pb	Ba	La/Sm	Sm/Yb	Hf/Zr	Sr/Nd	La/Nb	Pb/Yb	Zr/Nb	Ba/La				
	4.41	2.41	1.06	1.77	63.90	4.85	54.29	5.11	0.24	4.0	1.83	2.28	0.028	10.62	0.91	0.23	13.17	0.90				

This scenario is computationally identical to the generation of the shield lavas (Equations 5.5 – 5.9), though with an upper pressure limit of 2.7 GPa, rather than 2.0 GPa. The melt fraction of peridotite in the hybrid model at 2.7 GPa is:

$$F_{per,27} = \left(X_{per} - F_{ecl,43} \cdot X_{ecl}\right) \cdot F_{per,327} = X_{per,un3} \cdot F_{per,327} \qquad 5.10$$

where X_{per} is the initial proportion of peridotite in the plume, $F_{ecl,43}$ is the melt fraction of eclogite from 4.0 to 3.0 GPa, X_{ecl} is the initial proportion of eclogite in the plume, $F_{per,327}$ melt fraction of peridotite from 3.0 to 2.7 GPa, and $X_{per,un3}$ is the proportion of unreacted peridotite in the plume at 3.0 GPa, all as above. The melt fraction of eclogite at 2.7 GPa is:

$$F_{ecl,27} = X_{ecl}\left(1 - F_{ecl,43}\right) \cdot F_{ecl,327} = X_{ecl,res3} \cdot F_{ecl,327} \qquad 5.11$$

where $F_{ecl,327}$ if the melt fraction of eclogite from 3.0 to 2.7 GPa and $X_{ecl,res3}$ is the proportion of eclogite residue in the plume at 3.0 GPa, as above. The melt fraction of hybrid pyroxenite at 2.7 GPa is:

$$F_{hyb,27} = \left(2F_{ecl,43}X_{ecl}\right) \cdot F_{hyb,327} = X_{hyb} \cdot F_{hyb,327} \qquad 5.12$$

where $F_{hyb,327}$ is the melt fraction of hybrid from 3.0 to 2.7 GPa and X_{hyb} is the proportion of hybrid pyroxenite in the plume at 3.0 GPa, as above. This scenario can be considered to model a plume that produces a relatively thick plume tail or a particle path closer to the periphery of the plume.

To investigate the effect of decreasing the thickness of the effective upper boundary layer on the post-erosional particle paths, $P_{max,PE}$ is changed to 2.5 GPa. This scenario requires a slightly different treatment than the model described above. The initial peridotite has La/Sm = 3.33 and Sm/Yb = 2.61, and the initial eclogite has La/Sm = 4.61 and Sm/Yb = 4.47 (Table 24b). When melting commences at 4.0 GPa, the first melts of the eclogitic component (La/Sm = 6.55 and Sm/Yb = 28.88) are greater than the initial component, but decrease as the degree of melting increases (not shown). The system decompresses adiabatically to 3.0 GPa where the large degree

melts of the eclogitic component ($F_{ecl,43}$ = 0.71; La/Sm = 4.93 and Sm/Yb = 10.84; Figure 45) are efficiently extracted and react with the bulk peridotite composition in a 1:1 ratio to produce the model hybrid pyroxenite (La/Sm = 4.84 and Sm/Yb = 9.19). The resulting eclogite-derived residue has low trace element ratios (La/Sm = 0.44 and Sm/Yb = 0.52), complementary to the eclogite-derived melt. At this point, three components are present in the system: (1) unreacted peridotite, (2) eclogite-derived residue, and (3) hybrid pyroxenite. Adiabatic decompression and melting within the plume stem continues for an additional 0.5 GPa, to an upper limit of 2.5 GPa. At this point, melts generated by each component ($F_{per,325}$ = 0.09, $F_{ecl,325}$ = 0.37, and $F_{hyb,325}$ = 0.55) during this small ascent are efficiently extracted and removed. The peridotite-derived residue (La/Sm = 0.82 and Sm/Yb = 1.57), eclogite residue-derived residue (La/Sm = 0.05 and Sm/Yb = 0.14), and hybrid-derived residue (La/Sm = 1.07 and Sm/Yb = 7.09) are each depleted relative to their analogues at 3.0 GPa. Further melting continues as the three melt-free components undergo adiabatic decompression through the plume tail along the post-erosional particle path (*e.g.*, Phipps Morgan and others) for 0.3 GPa, finally stopping at an upper limit of 2.2 GPa. At this point, the residue of the unreacted peridotitic component has melted 0.01% in the plume tail (La/Sm = 1.94 and Sm/Yb = 2.65), the eclogitic residue-derived residue has melted 49% in the plume tail (La/Sm = 0.05 and Sm/Yb = 0.75), and the hybrid-derived reside has melted 4% in the plume tail (La/Sm = 2.40 and Sm/Yb = 8.85). When these plume tail melts are mixed, the peridotitic component sources the largest fraction of the model post-erosional magma ($X_{F,per}$ = 0.62), with lesser amounts of hybrid and eclogitic components, respectively (Table 24b). As a result, the model magma from this scenario has a much more depleted signature.

Figure 45. Representative trace element ratios for the geochemical evolution of the hybrid melting model with T_P = 1525 °C and a maximum vertical ascent of the post-erosional source in the plume stem to 2.5 GPa, for a plume with 10% initial eclogite. Black diamond – Older Series lavas. Open black diamond – Post-erosional lavas. Green square – Initial eclogite. Open green square – Residual melt at 2.0 GPa. Small light green square – Residual eclogite melt at 2.2 GPa. Red circle – Initial peridotite. Open red circle – Peridotite melt at 2.0 GPa. Small pink circle – Residual peridotite melt at 2.2 GPa. Light blue cross – Model shield magma. Dark blue cross – Model post-erosional magma. Light blue line – LLOD of model shield magma at 0.8 GPa (after Albarède et al., 1997). Dark blue line – LLOD of model post-erosional magma at 0.8 GPa. Blue field – Mixing between melts of peridotite, residual eclogite, and hybrid pyroxenite at 2.0 GPa. Purple field – Mixing between melts of residual peridotite, residual eclogite, and residual hybrid at 2.2 GPa. In this version of the hybrid model the shield lavas are generated in the same manner, but for the post-erosional lavas the initial peridotite and eclogite and allowed to rise to 2.5 GPa before ceasing vertical ascent in the plume stem. Upon formation of the hybrid pyroxenite at 3.0 GPa, the unreacted peridotite, eclogitic residue, and hybrid rise to 2.5 GPa where any melts are removed. The remaining residues then continue decompression through the plume tail from 2.5 to 2.2 GPa. Any melts generated in this region are mixed to form the model post-erosional magma. See text for full description. (a) La/Sm, (b) La/Nb, and (c) Zr/Nb plotted against Sm/Yb. Model shield and post-erosional magmas are reproduced well in this model. The post-erosional lavas differ slightly from the Intermediate and Younger Series, and are largely a two-component mixture between the melts of the hybrid and peridotitic components. Arrows point to the highly fractionated residual eclogite melt in (b) and (c).

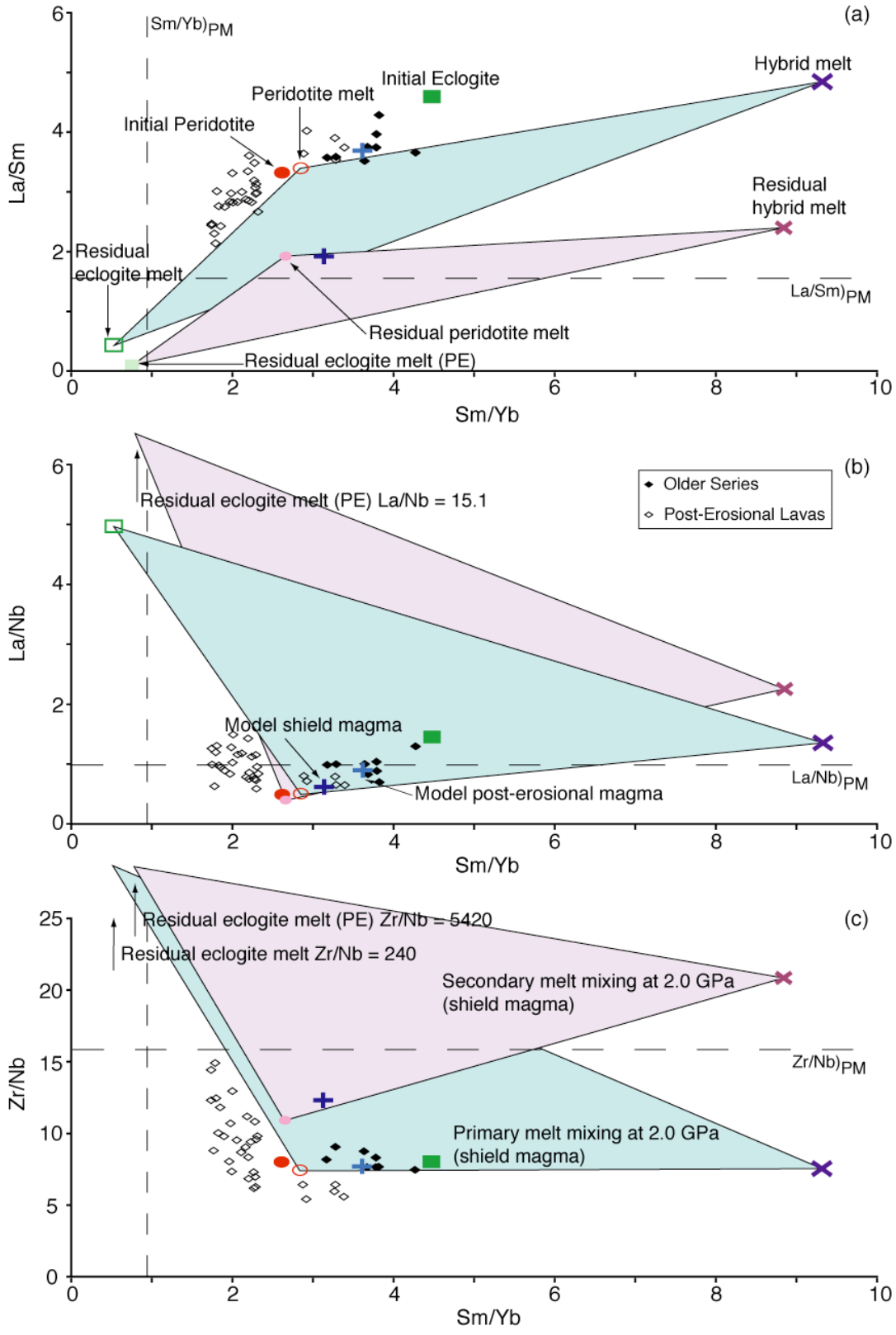
(a)
(Sm/Yb)PM
Initial Eclogite
Peridotite melt
Initial Peridotite
Hybrid melt
Residual hybrid melt
Residual eclogite melt
(La/Sm)PM
Residual peridotite melt
Residual eclogite melt (PE)
La/Sm
Sm/Yb
(b)
Older Series
Post-Erosional Lavas
Residual eclogite melt (PE) La/Nb = 15.1
Model shield magma
Model post-erosional magma
(La/Nb)PM
La/Nb
Sm/Yb
(c)
Residual eclogite melt (PE) Zr/Nb = 5420
Residual eclogite melt Zr/Nb = 240
Secondary melt mixing at 2.0 GPa (shield magma)
Primary melt mixing at 2.0 GPa (shield magma)
(Zr/Nb)PM
Zr/Nb
Sm/Yb

In comparison to the previous, simpler, melting scenario, the melting increment from 3.0 to 2.5 GPa introduces an additional computational wrinkle. The melt fraction of peridotite at 2.2 GPa can be calculated as:

$$F_{per,22} = \left[\left(X_{per} - F_{ecl,43} \cdot X_{ecl}\right) - \left(X_{per} - F_{ecl,43} \cdot X_{ecl}\right) \cdot F_{per,325}\right] \cdot F_{per,2522}$$
$$= \left(X_{per,un3} - X_{per,un3} \cdot F_{per,325}\right) \cdot F_{per,2522} \qquad 5.13$$

where $F_{per,325}$ is the melt fraction of peridotite from 3.0 to 2.5 GPa and $F_{per,2522}$ is the melt fraction of peridotite from 2.5 to 2.2 GPa. This formulation, and those that follow, can be read as the proportion of a component at 3.0 GPa minus the proportion removed by melting from 3.0 to 2.5 GPa, multiplied by the extent of melting in the plume tail. Similarly, the melt fraction of eclogite at 2.2 GPa is:

$$F_{ecl,22} = \left[X_{ecl}\left(1 - F_{ecl,43}\right) - X_{ecl}\left(1 - F_{ecl,43}\right) \cdot F_{ecl,325}\right] \cdot F_{ecl,2522}$$
$$= \left(X_{ecl,res3} - X_{ecl,res3} \cdot F_{ecl,325}\right) \cdot F_{ecl,2522} \qquad 5.14$$

where $F_{ecl,325}$ is the melt fraction of eclogite from 3.0 to 2.5 GPa, $F_{ecl,2522}$ is the melt fraction of eclogite from 2.5 to 2.2 GPa, and $X_{ecl,res3}$ is the proportion of eclogite residue in the plume at 3.0 GPa, as above. Finally, the melt fraction of hybrid pyroxenite at 2.2 GPa is:

$$F_{hyb,22} = \left(2F_{ecl,43}X_{ecl} - 2F_{ecl,43}X_{ecl} \cdot F_{hyb,325}\right) \cdot F_{hyb,2522}$$
$$= \left(X_{hyb} - X_{hyb} \cdot F_{hyb,325}\right) \cdot F_{hyb,2522} \qquad 5.15$$

where $F_{hyb,325}$ is the melt fraction of hybrid from 3.0 to 2.5 GPa and $F_{hyb,2522}$ is the melt fraction of hybrid from 2.5 to 2.2 GPa. This scenario can be considered to model a plume that produces a relatively thinner tail or a particle path closer to the plume stem.

To account for the radially decreasing temperature structure of a mantle plume, the post-erosional particle paths are also modeled as having a potential temperature 75 °C cooler than the axially formed shield magmas (T_P = 1450 °C) for both maximal pressure levels, $P_{max,PE}$ = 2.5 and 3.0 GPa. Deviations in the thermal profile for the

post-erosional particle paths do not alter the procedure from that described above, but will change the degree of melting and extent of fractionation.

With the assumptions of uniform plume temperature (T_P = 1525 °C) and an effective upper boundary layer at 3.0 GPa, the post-erosional lavas are almost completely sourced from the hybrid pyroxenite component, $X_{hyb,27}$ = 0.93 (Tables 24a, 25a, and 26a). This model is identical to the first hybrid post-erosional scenario described above. The modeled post-erosional melts from the eclogitic component are the product of moderate degree melts, $F_{ecl,327}$ = 0.13, of a highly depleted eclogite-derived residue, $F_{ecl,43}$ = 0.71. Melts from the peridotitic component are very low degree melts, $F_{per,327}$ = 0.002, of a slightly depleted peridotite-derived residue, $F_{per,43}$ = 0.07. The hybrid melts to a large degree as it passes through the plume tail, $F_{hyb,327}$ = 0.47. The model post-erosional parental magma is relatively mafic (SiO_2 = 43.13 wt. %; MgO = 19.02 wt. %) with an Mg# (75) nearly in equilibrium with the mantle (Figure 42). FeO_T and CaO are modeled well by LLOD calculations. The dominance of the hybrid derived melts in the model post-erosional parental magma skews the trace element and isotopic ratios away from the observed post-erosional lavas. Trace element ratios of the model melt are relatively fractionated (La/Sm = 5.20 and Sm/Yb = 9.08) with essentially hybrid compositions (Figures 43). Likewise, the isotopic ratios of the model melt are highly enriched ($^{87}Sr/^{86}Sr$ = 0.7440, ε_{Nd} = +3.20, and $^{206}Pb/^{204}Pb$ = 19.29), even more so than many of the Older Series lavas (Figure 44). From trace element and isotopic considerations, this model provides an unacceptable fit to the post-erosional lavas.

Keeping with a uniform plume temperature of T_P = 1525 °C, but decreasing the effective upper boundary layer to 2.5 GPa, a more balanced model parental magma is produced (Tables 24b, 25b, and 26b). Under this scenario, the peridotite component sources the bulk of the melt ($X_{per,22}$ = 0.62), though the eclogitic ($X_{ecl,22}$ = 0.14) and

Table 25. Hybrid melting model for post-erosional major elements, 10% eclogite

(a) 1525 °C Potential Temperature, $P_{max,PE}$ = 3.0 GPa

	SiO_2	TiO_2	Al_2O_3	Cr_2O_3	MgO	CaO	Na_2O	K_2O	P_2O_5	FeO_T	F_{43}	F_{327}	X_F
Peridotite	40.60	1.07	8.88	0.19	24.12	8.84	2.46	0.00	0.00	13.82	0.07	0.00	0.02
Eclogite	45.35	0.87	17.30	0.01	9.02	14.46	2.39	0.00	0.00	10.45	0.71	0.13	0.05
Hybrid	43.05	1.17	12.37	0.09	19.50	8.69	3.48	0.07	0.13	11.39	--	0.47	0.93
	SiO_2	TiO_2	Al_2O_3	Cr_2O_3	MgO	CaO	Na_2O	K_2O	P_2O_5	FeO_T	Mg#		
	43.13	1.15	12.57	0.09	19.02	9.00	3.40	0.07	0.13	11.38	75		

(b) 1525 °C Potential Temperature, $P_{max,PE}$ = 2.5 GPa

	SiO_2	TiO_2	Al_2O_3	Cr_2O_3	MgO	CaO	Na_2O	K_2O	P_2O_5	FeO_T	F_{43}	F_{325}	F_{2522}	X_F
Peridotite	42.10	1.05	10.17	0.20	22.07	10.27	1.86	0.00	0.00	12.24	0.07	0.13	0.01	0.62
Eclogite	45.72	0.16	17.07	0.00	13.31	14.68	0.31	0.00	0.00	8.69	0.71	0.94	0.49	0.14
Hybrid	47.57	1.06	13.75	0.10	16.54	10.52	2.38	0.00	0.00	8.03	--	0.73	0.04	0.24
	SiO_2	TiO_2	Al_2O_3	Cr_2O_3	MgO	CaO	Na_2O	K_2O	P_2O_5	FeO_T	Mg#			
	43.91	0.93	11.97	0.15	19.55	10.93	1.77	0.00	0.00	10.75	76			

(c) 1450 °C Potential Temperature, $P_{max,PE}$ = 3.0 GPa

	SiO_2	TiO_2	Al_2O_3	Cr_2O_3	MgO	CaO	Na_2O	K_2O	P_2O_5	FeO_T	F_{43}	F_{327}	X_F
Peridotite	--	--	--	--	--	--	--	--	--	--	0.02	0.00	--
Eclogite	47.28	1.44	17.49	0.03	6.22	11.14	4.57	0.00	0.00	11.76	0.37	0.07	0.17
Hybrid	45.87	1.95	13.02	0.22	14.50	6.19	6.52	0.19	0.41	11.13	--	0.28	0.83
	SiO_2	TiO_2	Al_2O_3	Cr_2O_3	MgO	CaO	Na_2O	K_2O	P_2O_5	FeO_T	Mg#		
	46.11	1.86	13.78	0.19	13.09	7.03	6.19	0.15	0.34	11.23	68		

(d) 1450 °C Potential Temperature, $P_{max,PE}$ = 2.5 GPa

	SiO_2	TiO_2	Al_2O_3	Cr_2O_3	MgO	CaO	Na_2O	K_2O	P_2O_5	FeO_T	F_{43}	F_{325}	F_{2522}	X_F
Peridotite	42.35	1.40	11.39	0.25	20.03	8.36	4.35	0.00	0.00	11.85	0.02	0.03	0.00	0.09
Eclogite	46.59	0.64	18.16	0.00	9.45	12.97	1.70	0.00	0.00	10.38	0.37	0.22	0.38	0.81
Hybrid	49.15	1.58	14.87	0.13	13.34	8.18	4.10	0.00	0.00	8.64	--	0.36	0.05	0.10
	SiO_2	TiO_2	Al_2O_3	Cr_2O_3	MgO	CaO	Na_2O	K_2O	P_2O_5	FeO_T	Mg#			
	46.45	0.80	17.20	0.04	10.84	12.06	2.19	0.00	0.00	10.34	65			

Trace element concentrations for the binary melt-mixing model post-erosional magmas with 10% initial eclogite. Results are shown for both the (a) T_P = 1525 °C and $P_{max,PE}$ = 3.0, (b) T_P = 1525 °C and $P_{max,PE}$ = 2.5, (a) T_P = 1450 °C and $P_{max,PE}$ = 3.0, and (a) T_P = 1450 °C and $P_{max,PE}$ = 2.5 GPa models. The proportion of eclogite melt, XF,ecl, composing the magma is given as well as the melt fraction for each melting stage. The composition of the post-erosional magma is shown in grey.

Table 26. Hybrid melting model for post-erosional isotope ratios, 10% eclogite

(a) 1525 °C Potential Temperature, $P_{max,PE}$ = 3.0 GPa

	Sr	Nd	Pb	$^{87}Sr/^{86}Sr$	εNd	$^{206}Pb/^{204}Pb$	F_{43}	F_{327}		X_F
Peridotite	151.37	8.08	0.34	0.70350	6.50	18.60	0.07	0.00		0.02
Eclogite	30.04	6.12	0.88	0.70470	3.00	19.30	0.71	0.13		0.05
Hybrid	171.07	15.34	3.28	0.70460	3.17	19.29	--	0.47		0.93
	Sr	Nd	Pb	$^{87}Sr/^{86}Sr$	εNd	$^{206}Pb/^{204}Pb$				
	150.78	13.91	2.89	0.70458	3.20	19.29				

(b) 1525 °C Potential Temperature, $P_{max,PE}$ = 2.5 GPa

	Sr	Nd	Pb	$^{87}Sr/^{86}Sr$	εNd	$^{206}Pb/^{204}Pb$	F_{43}	F_{325}	F_{2522}	X_F
Peridotite	95.43	5.83	0.10	0.70350	6.50	18.60	0.07	0.09	0.01	0.62
Eclogite	0.56	0.40	0.04	0.70470	3.00	19.30	0.71	0.37	0.49	0.14
Hybrid	90.17	9.92	0.29	0.70460	3.17	19.29	--	0.55	0.04	0.24
	Sr	Nd	Pb	$^{87}Sr/^{86}Sr$	εNd	$^{206}Pb/^{204}Pb$				
	81.20	6.07	0.14	0.70379	5.17	18.97				

(c) 1450 °C Potential Temperature, $P_{max,PE}$ = 3.0 GPa

	Sr	Nd	Pb	$^{87}Sr/^{86}Sr$	εNd	$^{206}Pb/^{204}Pb$	F_{43}	F_{327}		X_F
Peridotite	--	--	--	0.70350	6.50	18.60	0.02	0.00		--
Eclogite	114.68	15.76	2.33	0.70470	3.00	19.30	0.37	0.07		0.17
Hybrid	237.87	35.97	9.71	0.70464	3.10	19.29	--	0.28		0.83
	Sr	Nd	Pb	$^{87}Sr/^{86}Sr$	εNd	$^{206}Pb/^{204}Pb$				
	232.08	35.02	9.36	0.70465	3.10	19.29				

(d) 1450 °C Potential Temperature, $P_{max,PE}$ = 2.5 GPa

	Sr	Nd	Pb	$^{87}Sr/^{86}Sr$	εNd	$^{206}Pb/^{204}Pb$	F_{43}	F_{325}	F_{2522}	X_F
Peridotite	290.47	13.79	0.74	0.70350	6.50	18.60	0.02	0.03	0.00	0.09
Eclogite	5.61	1.89	0.12	0.70470	3.00	19.30	0.37	0.22	0.38	0.81
Hybrid	223.04	22.81	0.76	0.70464	3.10	19.29	--	0.36	0.05	0.10
	Sr	Nd	Pb	$^{87}Sr/^{86}Sr$	εNd	$^{206}Pb/^{204}Pb$				
	54.29	5.11	0.24	0.70407	3.93	19.10				

Isotopic compositions for the binary melt-mixing model post-erosional magmas with 10% initial eclogite. Results are shown for both the (a) T_P = 1525 °C and $P_{max,PE}$ = 3.0, (b) T_P = 1525 °C and $P_{max,PE}$ = 2.5, (a) T_P = 1450 °C and $P_{max,PE}$ = 3.0, and (a) T_P = 1450 °C and $P_{max,PE}$ = 2.5 GPa models. The proportion of eclogite melt, $X_{F,ecl}$, composing the magma is given as well as the melt fraction for each melting stage. The composition of the post-erosional magma is shown in grey.

hybrid components ($X_{hyb,22}$ = 0.24) both contribute significantly. The modeled post-erosional melts from the eclogitic component are the product of large degree melts, $F_{ecl,2522}$ = 0.49, of an extensively depleted residue, $F_{ecl,325}$ = 0.94, formed from high degrees of melting of the eclogitic component, $F_{ecl,43}$ = 0.71. Melts from the peridotitic component are very low degree melts, $F_{per,2522}$ = 0.01, of a moderately depleted residue, $F_{per,325}$ = 0.13, formed from moderate degrees of melting of the peridotitic component, $F_{per,43}$ = 0.07. The melts from the hybrid component are the small degree melts, $F_{hyb,2522}$ = 0.04, of a strongly depleted hybrid-residue, $F_{hyb,325}$ = 0.73. The model magma is again relatively mafic (MgO = 19.55 wt. %; Mg# = 76), and reasonably reproduces the Older Series lavas, though the (Figure 46). Though slightly higher than the observed Intermediate and Younger Series samples, the model Sm/Yb (3.14) approximates these values. However, extensive fractionation of the ordinate variable (*e.g.*, La/Sm, La/Nb, and Zr/Nb) within the eclogitic component draws the magmas away from the observed data, though the eclogitic component contributes little to the overall trace element and isotopic budget as it is severely depleted of incompatible elements (Figure 45). Isotopically, the model post-erosional magma reproduces quite well the observed data ($^{87}Sr/^{86}Sr$ = 0.70379, ε_{Nd} = +5.17, and $^{206}Pb/^{204}Pb$ = 18.97), though small deviations to the selected end-members for the Pb-system could improve the fit (Figure 47). This model provides a satisfactory solution.

Returning to an effective upper boundary layer of 3.0 GPa for the post-erosional source components, but running the components along the cooler T_P = 1450 °C particle path, the post-erosional magma is largely composed of hybrid derived melts ($X_{hyb,27}$ = 0.83; Tables 24c, 25c, and 26c). The modeled post-erosional melts from the eclogitic component are the product of small degree melts, $F_{ecl,327}$ = 0.07, of a moderately depleted eclogite-derived residue, $F_{ecl,43}$ = 0.37. The hybrid melts to a moderate degree during as it passes through the plume tail, $F_{hyb,327}$ = 0.28. The

Figure 46. Representative major element compositions for the geochemical evolution of the hybrid melting model with T_P = 1525 °C and a maximum vertical ascent of the post-erosional source in the plume stem to 2.5 GPa, for a plume with 10% initial eclogite. Symbols after Figure 45. Initial peridotite is not visible (MgO = 40.8 wt. %). (a) SiO_2, (b) FeO_T, and (c) CaO plotted against wt. % MgO. LLOD reproduce the major element systematics well, with the exception of CaO in the shield lavas.

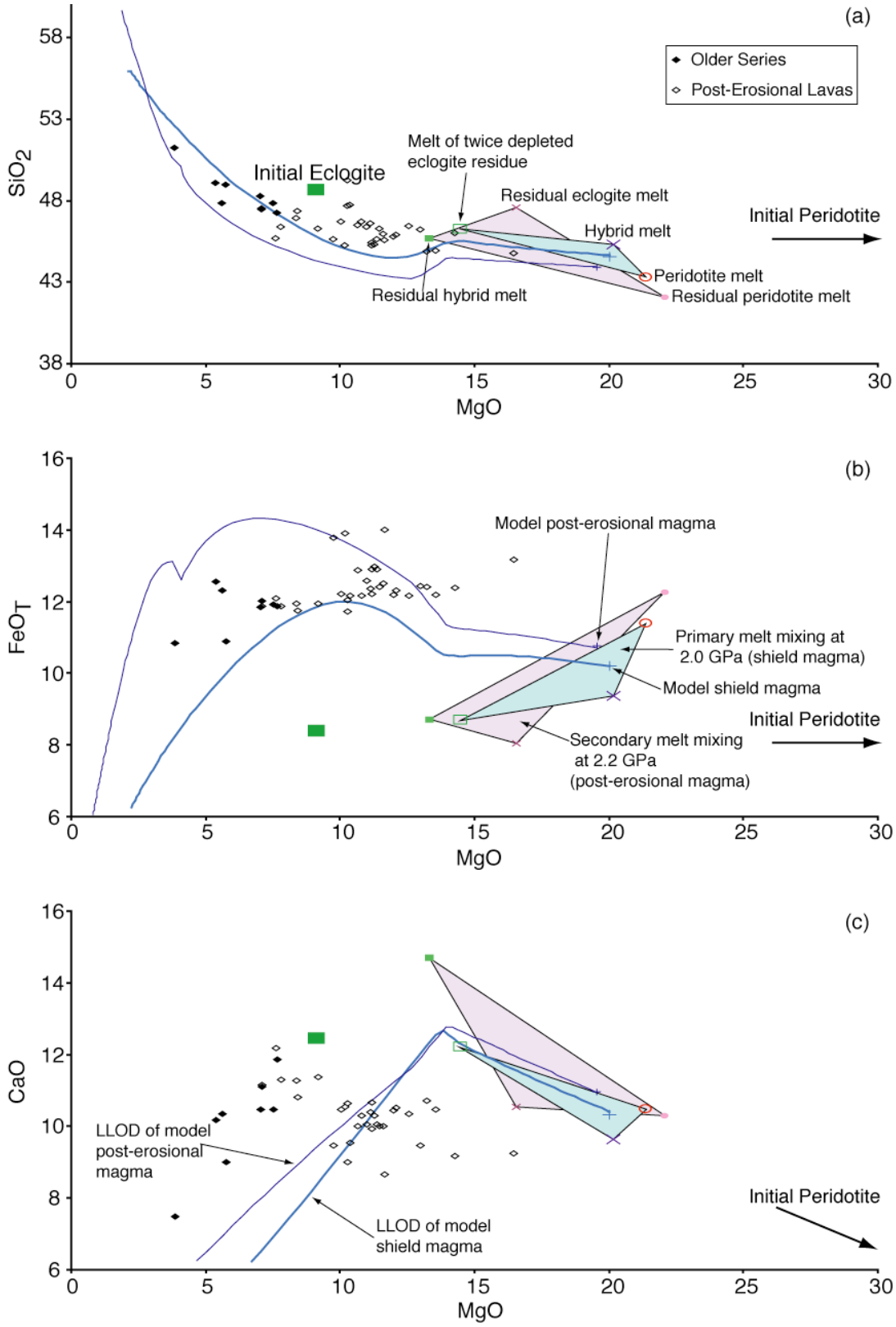
(a)
Older Series
Post-Erosional Lavas
Melt of twice depleted eclogite residue
Initial Eclogite
Residual eclogite melt
Hybrid melt
Initial Peridotite
Peridotite melt
Residual peridotite melt
Residual hybrid melt
SiO2
MgO
(b)
Model post-erosional magma
Primary melt mixing at 2.0 GPa (shield magma)
Model shield magma
Initial Peridotite
Secondary melt mixing at 2.2 GPa (post-erosional magma)
FeOT
MgO
(c)
LLOD of model post-erosional magma
LLOD of model shield magma
Initial Peridotite
CaO
MgO

Figure 47. Isotope ratios systematics for the geochemical evolution of the hybrid melting model with T_P = 1525 °C and a maximum vertical ascent of the post-erosional source in the plume stem to 2.5 GPa, for a plume with 10% initial eclogite. Symbols after Figure 45. See text for full discussion of model systematics. End-member isotope compositions are chosen to reflect the observed range of Mauritius lavas. Plot of Sm/Yb against $^{87}Sr/^{86}Sr$, (b) ε_{Nd}, and (c) $^{206}Pb/^{204}Pb$. Trace element concentrations for mixing are taken from compositions of the model shield and post-erosional magmas. Model Sr- and Nd-isotopes well, though Pb-isotopes are too large for both the shield and post-erosional magmas.

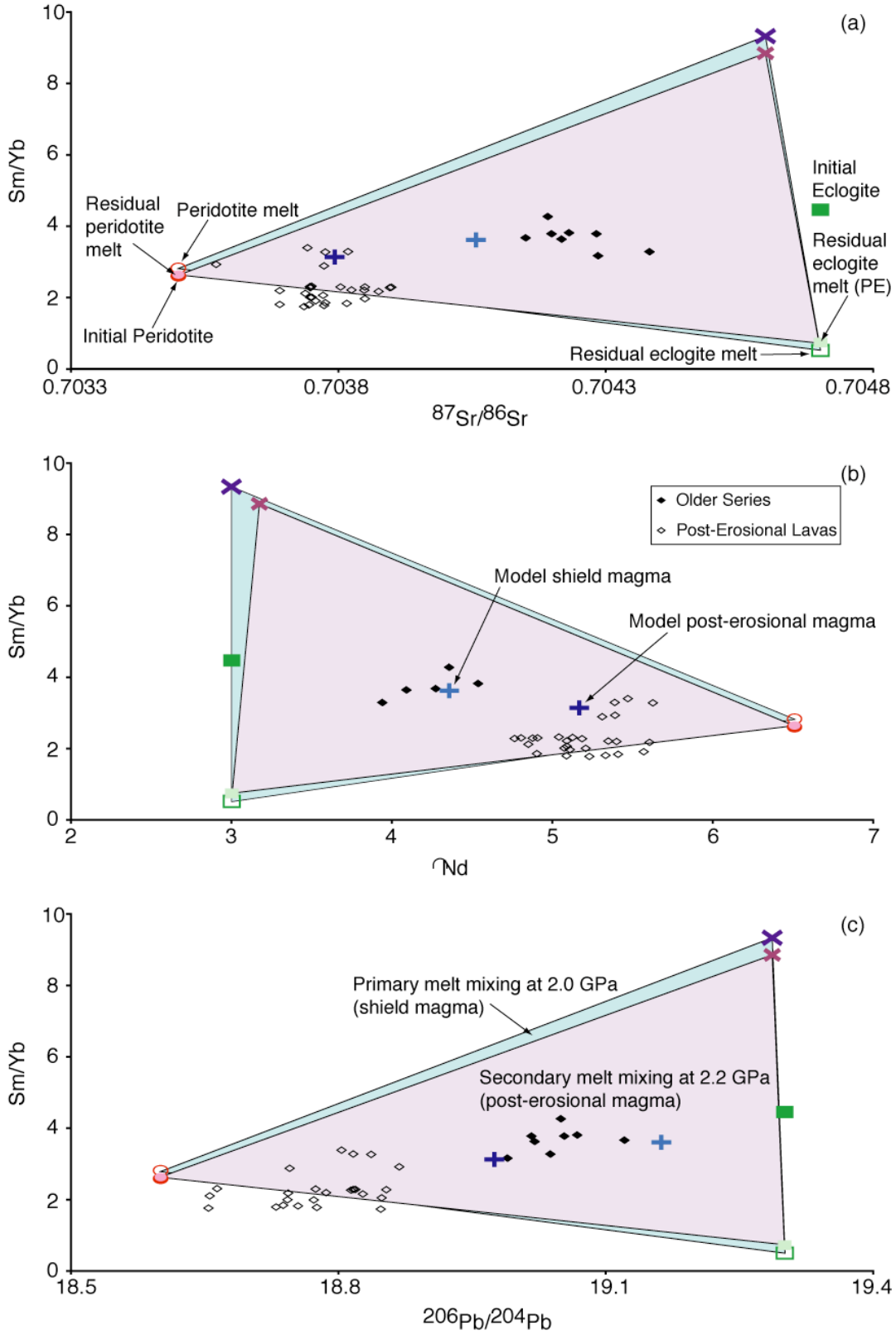
(a)
Sm/Yb
10
8
6
4
2
0
0.7033
0.7038
0.7043
0.7048
87Sr/86Sr
Residual peridotite melt
Peridotite melt
Initial Peridotite
Initial Eclogite
Residual eclogite melt (PE)
Residual eclogite melt
(b)
Older Series
Post-Erosional Lavas
Model shield magma
Model post-erosional magma
Sm/Yb
2
3
4
5
6
7
Nd
(c)
Primary melt mixing at 2.0 GPa (shield magma)
Secondary melt mixing at 2.2 GPa (post-erosional magma)
Sm/Yb
18.5
18.8
19.1
19.4
206Pb/204Pb

peridotite-derived residue does not melt in the plume tail, and thus does not contribute to generating the post-erosional magma. The model magma has a relatively intermediate MgO content (13.09 wt. %; Mg# = 68), relative to the other models, that is more mafic than all but the most magnesian samples (Figure 48). Both CaO and FeO_T are lower than the Intermediate and Younger Series samples, at a given MgO. Trace element ratios for the model magma are very similar to those of the hybrid-derived melts (La/Sm = 6.96 and Sm/Yb = 20.78) and very dissimilar to the observed samples (Figure 49). Similarly, the isotopic ratios for the model post-erosional magma are that of the enriched eclogitic source ($^{87}Sr/^{86}Sr$ = 0.70465, ε_{Nd} = +3.09, and $^{206}Pb/^{204}Pb$ = 19.29; Figure 50), not of the depleted Intermediate and Younger Series lavas. Consequently, this model provides an unsatisfactory solution.

The final iteration of temperature and pressure for the post-erosional lavas in the hybrid model decreases the effective upper boundary layer to 2.5 GPa and uses the cooler temperature of T_P = 1450 °C (Tables, 24d, 25d, and 26d). The modeled post-erosional melts from the eclogitic component are the product of large degree melts, $F_{ecl,2522}$ = 0.38, of a depleted residue, $F_{ecl,325}$ = 0.22, formed by the large degree melting of the eclogitic component, $F_{ecl,43}$ = 0.37. Melts from the peridotitic component are very low degree melts, $F_{per,2522}$ = 0.003, of a lightly depleted residue, $F_{per,325}$ = 0.03, formed from small degrees of melting of the peridotitic component, $F_{per,43}$ = 0.02. The melts from the hybrid component are the small degree melts, $F_{hyb,2522}$ = 0.05, of a strongly depleted hybrid-residue, $F_{hyb,325}$ = 0.36. The model magmas consists principally of the eclogite-derived melts, $X_{F,ecl}$ = 0.81, with the hybrid-, $X_{F,hyb}$ = 0.10, and peridotite-derived melts, $X_{F,per}$ = 0.09, in near-equal proportions. The magma has the lowest MgO content of the hybrid models (10.84 wt. %), and is not magnesian enough to be a parental magma for the majority of the post-erosional lavas (*Mg#* = 65; Figure 51). When considering trace element ratios, the

Figure 48. Representative major element compositions for the geochemical evolution of the hybrid melting model with T_P = 1525 °C for the shield magmas, T_P = 1450 °C for the post-erosional lavas, and a maximum vertical ascent of the post-erosional source in the plume stem to 3.0 GPa, for a plume with 10% initial eclogite. Black diamond – Older Series lavas. Open black diamond – Post-erosional lavas. Green square – Initial eclogite. Open green square – Residual melt at 2.0 GPa. Small light green square – Residual eclogite melt at 2.7 GPa. Red circle – Initial peridotite (not visible, MgO = 40.8 wt. %). Open red circle – Peridotite melt at 2.0 GPa. Small pink circle – Residual peridotite melt at 2.7 GPa. Light blue cross – Model shield magma. Dark blue cross – Model post-erosional magma. Light blue line – LLOD of model shield magma at 0.8 GPa (after Albarède et al., 1997). Dark blue line – LLOD of model post-erosional magma at 0.8 GPa. Blue field – Mixing between melts of peridotite, residual eclogite, and hybrid pyroxenite at 2.0 GPa. Black dashed line – Mixing curve between the residual eclogite and residual hybrid melts at 2.7 GPa. In the hybrid model, the peridotitic and eclogitic component are each allowed to rise along the 10% initial eclogite composite P-T path from 4.0 to 3.0 GPa. At 3.0 GPa, melts from the eclogitic component react with the peridotite to form a hybrid pyroxenite. The unreacted peridotite, eclogitic residue, and hybrid rise to 2.0 GPa. At 2.0 GPa, the melts of each component generated by this decompression are mixed, producing the model shield magma. The model post-erosional lavas are generated in a very similar manner, though nearer the periphery of the plume with a lower T_P = 1450 °C. After formation of the hybrid pyroxenite at 3.0 GPa, the three components continue decompression through the plume tail from 3.0 to 2.7 GPa. Any melts generated in this region are mixed to form the model post-erosional magma. See text for full description. (a) SiO_2, (b) FeO_T, and (c) CaO plotted against wt. % MgO. The model shield magma composition reproduces SiO_2 and FeO_T well, though CaO is low for a given MgO content. As the peridotitic component does not undergo melting within the plume tail, the model post-erosional lava reasonably has a less magnesian composition. Consequently, the LLOD of this model magma does not reproduce the major element characteristics seen in the observed lavas.

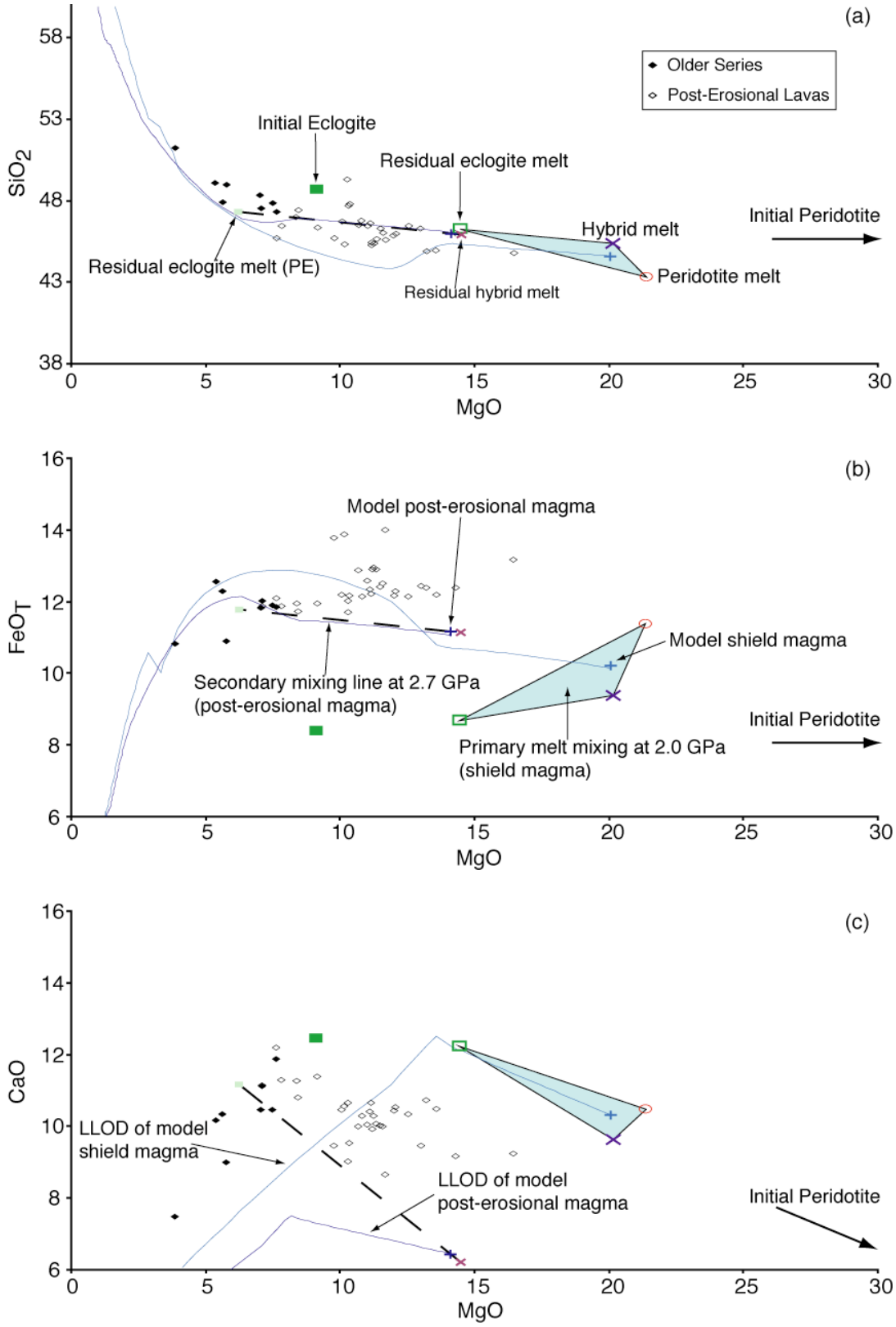
(a)
Older Series
Post-Erosional Lavas
Initial Eclogite
Residual eclogite melt
Hybrid melt
Initial Peridotite
Residual eclogite melt (PE)
Residual hybrid melt
Peridotite melt
SiO2
MgO
(b)
Model post-erosional magma
Model shield magma
Secondary mixing line at 2.7 GPa
(post-erosional magma)
Initial Peridotite
Primary melt mixing at 2.0 GPa
(shield magma)
FeOT
MgO
(c)
LLOD of model
shield magma
LLOD of model
post-erosional magma
Initial Peridotite
CaO
MgO

Figure 49. Representative incompatible trace element composition for the geochemical evolution of the hybrid melting model with T_P = 1525 °C for the shield magmas, T_P = 1450 °C for the post-erosional lavas, and a maximum vertical ascent of the post-erosional source in the plume stem to 3.0 GPa, for a plume with 10% initial eclogite. Symbols after Figure 49. Vertical and horizontal dashed lines represent the trace element ratio of Primitive Mantle (McDonough and Sun, 1995). La/Sm plotted against Sm/Yb. Incompatible trace element compositions of the initial eclogite and initial peridotite are chosen such that the model shield magma fits the observed Older Series trace element data. Trace element compositions of the initial compositions are kept constant for the post-erosional lavas. In this model, no melting of the peridotitic component occurs in the plume tail, and the model post-erosional magmas do not resemble the observed post-erosional data.

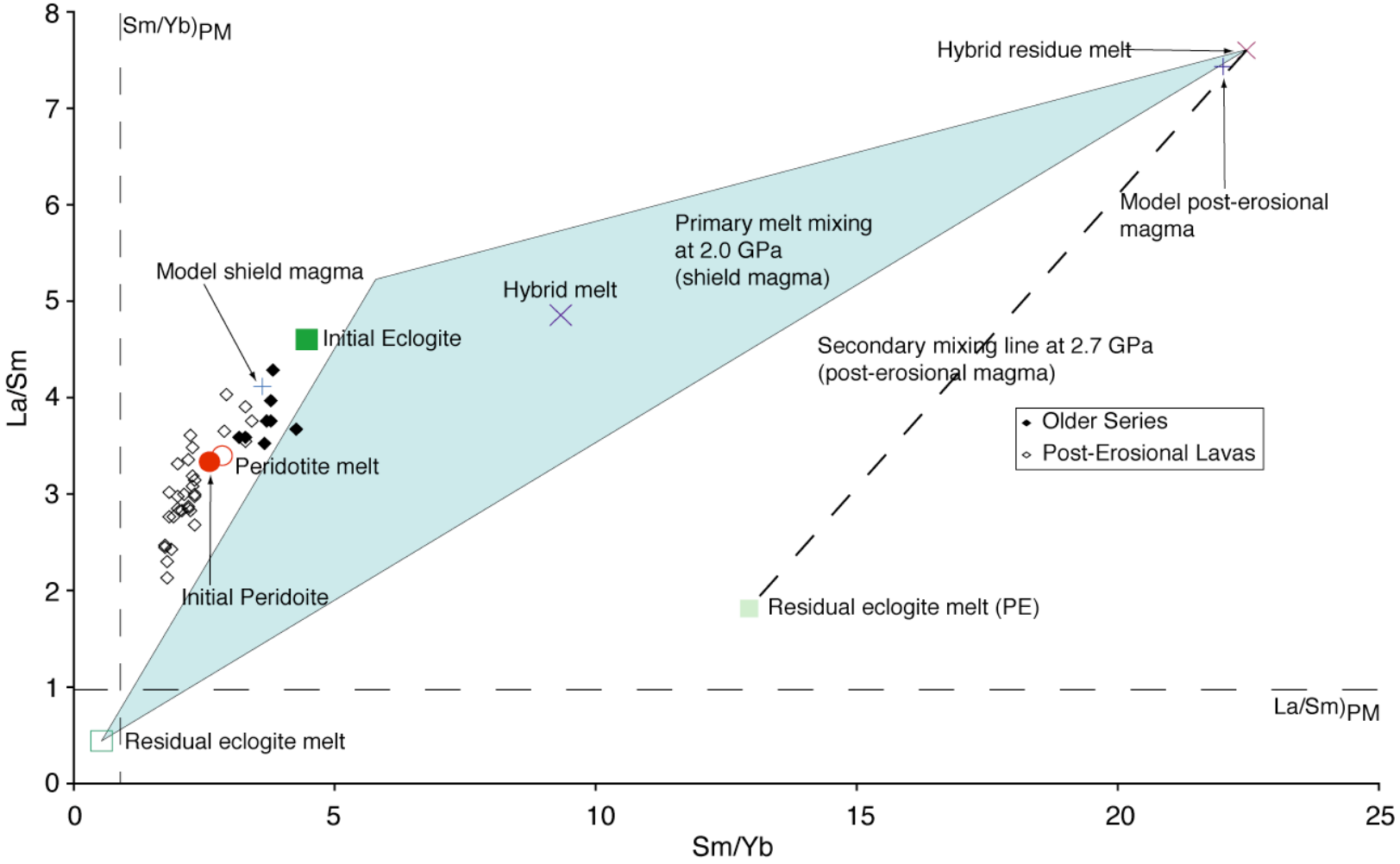
(Sm/Yb)PM
Hybrid residue melt
Model post-erosional magma
Primary melt mixing at 2.0 GPa (shield magma)
Model shield magma
Hybrid melt
Initial Eclogite
Secondary mixing line at 2.7 GPa (post-erosional magma)
Older Series
Post-Erosional Lavas
Peridotite melt
Initial Peridoite
Residual eclogite melt (PE)
Residual eclogite melt
(La/Sm)PM
La/Sm
Sm/Yb
0
1
2
3
4
5
6
7
8
0
5
10
15
20
25

Figure 50. Isotope ratios systematics for the geochemical evolution of the hybrid melting model with T_P = 1525 °C for the shield magmas, T_P = 1450 °C for the post-erosional lavas, and a maximum vertical ascent of the post-erosional source in the plume stem to 3.0 GPa, for a plume with 10% initial eclogite. Symbols after Figure 48. Curved black line represents mixing curve between residual eclogite and residual hybrid melts. See text for full discussion of model systematics. End-member isotope compositions are chosen to reflect the observed range of Mauritius lavas. Plot of Sm/Yb against $^{87}Sr/^{86}Sr$, (b) ε_{Nd}, and (c) $^{206}Pb/^{204}Pb$. Trace element concentrations for mixing are taken from compositions of the model shield and post-erosional magmas. Model shield magmas reproduce Nd-isotopes well, though small deviations to the selected component compositions would improve fits for Sr- and Pb-isotopes. Model post-erosional magmas are sourced completely from the enriched component and are not representative of the observed data.

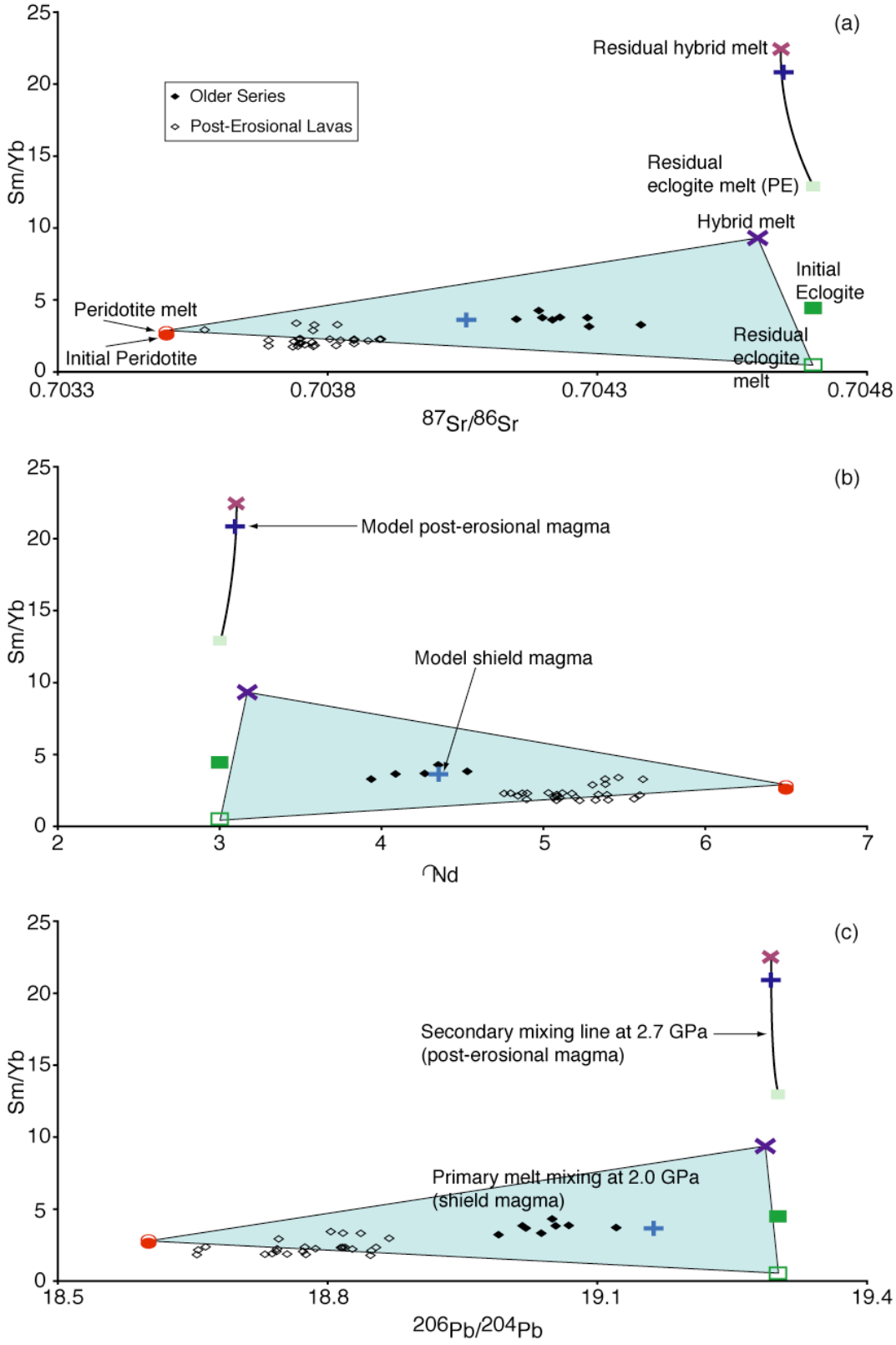
(a)
Residual hybrid melt
Older Series
Post-Erosional Lavas
Residual
eclogite melt (PE)
Hybrid melt
Initial
Eclogite
Peridotite melt
Initial Peridotite
Residual
eclogite
melt
Sm/Yb
25
20
15
10
5
0
0.7033
0.7038
0.7043
0.7048
87Sr/86Sr
(b)
Model post-erosional magma
Model shield magma
Sm/Yb
2
3
4
5
6
7
εNd
(c)
Secondary mixing line at 2.7 GPa
(post-erosional magma)
Primary melt mixing at 2.0 GPa
(shield magma)
Sm/Yb
18.5
18.8
19.1
19.4
206Pb/204Pb

Figure 51. Representative trace element ratios for the geochemical evolution of the hybrid melting model with T_P = 1525 °C for the shield magmas, T_P = 1450 °C for the post-erosional lavas, and a maximum vertical ascent of the post-erosional source in the plume stem to 2.5 GPa, for a plume with 10% initial eclogite. Black diamond – Older Series lavas. Open black diamond – Post-erosional lavas. Green square – Initial eclogite. Open green square – Residual melt at 2.0 GPa. Small light green square – Residual eclogite melt at 2.2 GPa. Red circle – Initial peridotite. Open red circle – Peridotite melt at 2.0 GPa. Small pink circle – Residual peridotite melt at 2.2 GPa. Light blue cross – Model shield magma. Dark blue cross – Model post-erosional magma. Light blue line – LLOD of model shield magma at 0.8 GPa (after Albarède et al., 1997). Dark blue line – LLOD of model post-erosional magma at 0.8 GPa. Blue field – Mixing between melts of peridotite, residual eclogite, and hybrid pyroxenite at 2.0 GPa. Purple field – Mixing between melts of residual peridotite, residual eclogite, and residual hybrid at 2.2 GPa. In this version of the hybrid model the shield lavas are generated in the same manner, but for the post-erosional lavas the initial peridotite and eclogite and allowed to rise to 2.5 GPa along a lower T_P = 1450 °C adiabat nearer the periphery of the plume before ceasing vertical ascent in the plume stem. Upon formation of the hybrid pyroxenite at 3.0 GPa, the unreacted peridotite, eclogitic residue, and hybrid rise to 2.5 GPa where any melts are removed. The remaining residues then continue decompression through the plume tail from 2.5 to 2.2 GPa. Any melts generated in this region are mixed to form the model post-erosional magma. See text for full description. (a) SiO_2, (b) FeO_T, and (c) CaO plotted against wt. % MgO. Fractional crystallization reproduces SiO_2 reasonably well, but FeO_T and CaO are not reproduced well.

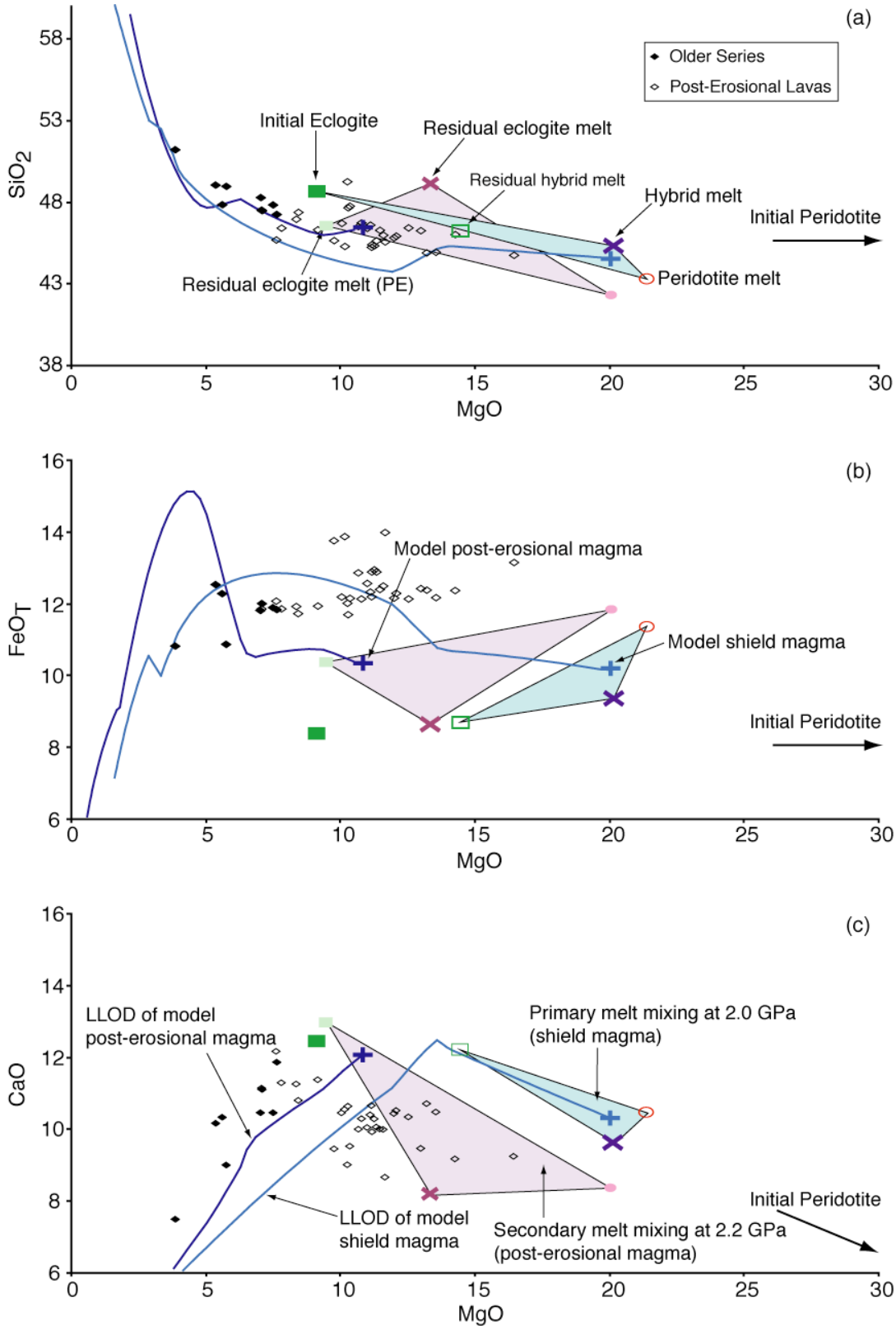
(a)
Older Series
Post-Erosional Lavas
Initial Eclogite
Residual eclogite melt
Residual hybrid melt
Hybrid melt
Initial Peridotite
Peridotite melt
Residual eclogite melt (PE)
SiO2
MgO
(b)
Model post-erosional magma
Model shield magma
Initial Peridotite
FeOT
MgO
(c)
LLOD of model post-erosional magma
Primary melt mixing at 2.0 GPa (shield magma)
LLOD of model shield magma
Secondary melt mixing at 2.2 GPa (post-erosional magma)
Initial Peridotite
CaO
MgO

model magma reproduces the observed samples (La/Sm = 1.83, Sm/Yb = 2.28, La/Nb = 0.91, and Zr/Nb = 13.17) closely (Figure 52). This model reproduces some of the median characteristics of the observed lavas ($^{87}Sr/^{86}Sr$ = 0.70407, ε_{Nd} = +3.93, and $^{206}Pb/^{204}Pb$ = 19.10), though quite erratically (Figure 53). Together with the low MgO content, this model is not a satisfactory solution.

In comparison to the binary mixing model, in which model melts are effectively end-member compositions (*i.e.*, entirely peridotite- or eclogite-derived melts), the parental hybrid melting post-erosional magmas are generated from a broader spectrum of component mixtures. Isotope ratios calculated for each model again provide the most effective tool for testing the efficacy of each parameter set within the hybrid model. Of the four post-erosional scenarios, it is clear that three of the four models do not fit the parameters described above and fail to reproduce the isotopic signature of the Intermediate and Younger Series lavas. The post-erosional magmas in these three models (T_P = 1525 °C and $P_{max,PE}$ = 3.0, and both models with T_P = 1450 °C) are overwhelmingly sourced by melts of the isotopically enriched components (*i.e.*, $X_{F,ecl} + X_{F,hyb} > 0.91$). Consequently, the models have enriched isotopic compositions (*e.g.*, $^{87}Sr/^{86}Sr$ = 0.70450 – 0.70465; Figures 44, 50, and 53). Similarly, trace elements concentrations and ratios are characteristic of melts derived from the enriched component (Table 24). These three models thus represent unsatisfactory solution to the hybrid model.

The one hybrid model that presents an acceptable solution is the sole model in which the melts of the peridotitic component dominate the trace element budget of the post-erosional magma ($X_{F,per}$ = 0.62). This model (T_P = 1525 °C, $P_{max,PE}$ = 2.5 GPa) reproduces the $^{87}Sr/^{86}Sr$ and ε_{Nd} of the Intermediate and Younger Series well, but is somewhat enriched in $^{206}Pb/^{204}Pb$ (Figure 47), similar to the model shield lavas. From Figure 45 it is evident that the model post-erosional magmas do not fully reproduce

Figure 52. Representative incompatible trace element composition for the geochemical evolution of the hybrid melting model with T_P = 1525 °C for the shield magmas, T_P = 1450 °C for the post-erosional lavas, and a maximum vertical ascent of the post-erosional source in the plume stem to 2.5 GPa, for a plume with 10% initial eclogite. Symbols after Figure 51. Vertical and horizontal dashed lines represent the trace element ratio of Primitive Mantle (McDonough and Sun, 1995). Incompatible trace element compositions of the initial eclogite and initial peridotite are chosen such that the model shield magma fits the observed Older Series trace element data. Trace element compositions of the initial compositions are kept constant for the post-erosional lavas. (a) La/Sm, (b) La/Nb, and (c) Zr/Nb plotted against Sm/Yb.

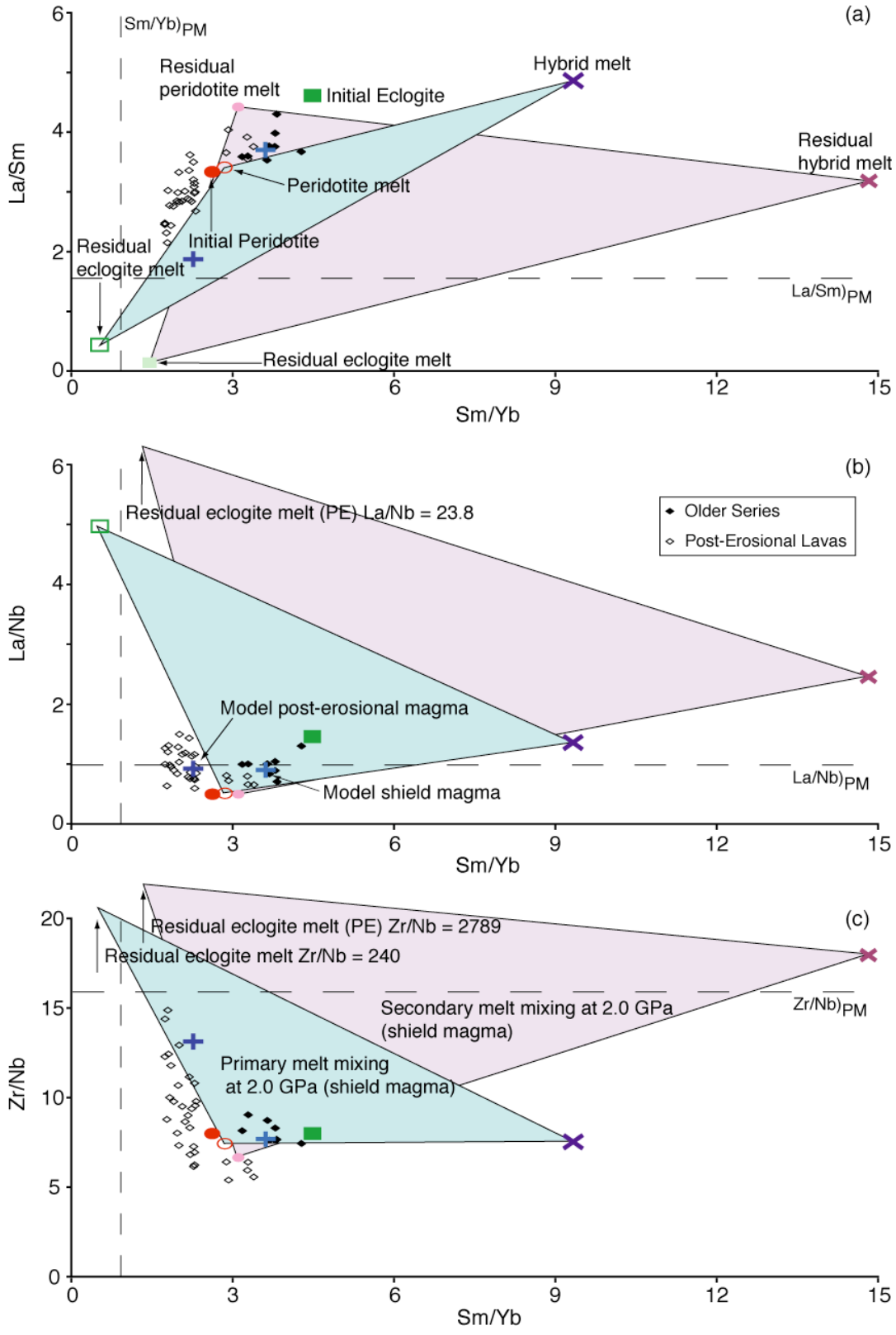
(a)
(Sm/Yb)PM
Residual peridotite melt
Initial Eclogite
Hybrid melt
Residual hybrid melt
Peridotite melt
Initial Peridotite
Residual eclogite melt
(La/Sm)PM
Residual eclogite melt
La/Sm
Sm/Yb
(b)
Residual eclogite melt (PE) La/Nb = 23.8
Older Series
Post-Erosional Lavas
Model post-erosional magma
Model shield magma
(La/Nb)PM
La/Nb
Sm/Yb
(c)
Residual eclogite melt (PE) Zr/Nb = 2789
Residual eclogite melt Zr/Nb = 240
Secondary melt mixing at 2.0 GPa (shield magma)
Primary melt mixing at 2.0 GPa (shield magma)
(Zr/Nb)PM
Zr/Nb
Sm/Yb

Figure 53. Isotope ratios systematics for the geochemical evolution of the hybrid melting model with T_P = 1525 °C for the shield magmas, T_P = 1450 °C for the post-erosional lavas, and a maximum vertical ascent of the post-erosional source in the plume stem to 2.5 GPa, for a plume with 10% initial eclogite. Symbols after Figure 51. See text for full discussion of model systematics. End-member isotope compositions are chosen to reflect the observed range of Mauritius lavas. Plot of Sm/Yb against $^{87}Sr/^{86}Sr$, (b) ε_{Nd}, and (c) $^{206}Pb/^{204}Pb$. Trace element concentrations for mixing are taken from compositions of the model shield and post-erosional magmas. Model shield magmas are low in Sr, and high in Pb, though Nd is reproduced quite well. Model post-erosional magmas are high in Sr- and Pb-isotopes, and quite low in Pb. Small deviations to the selected component compositions would improve isotopic fits.

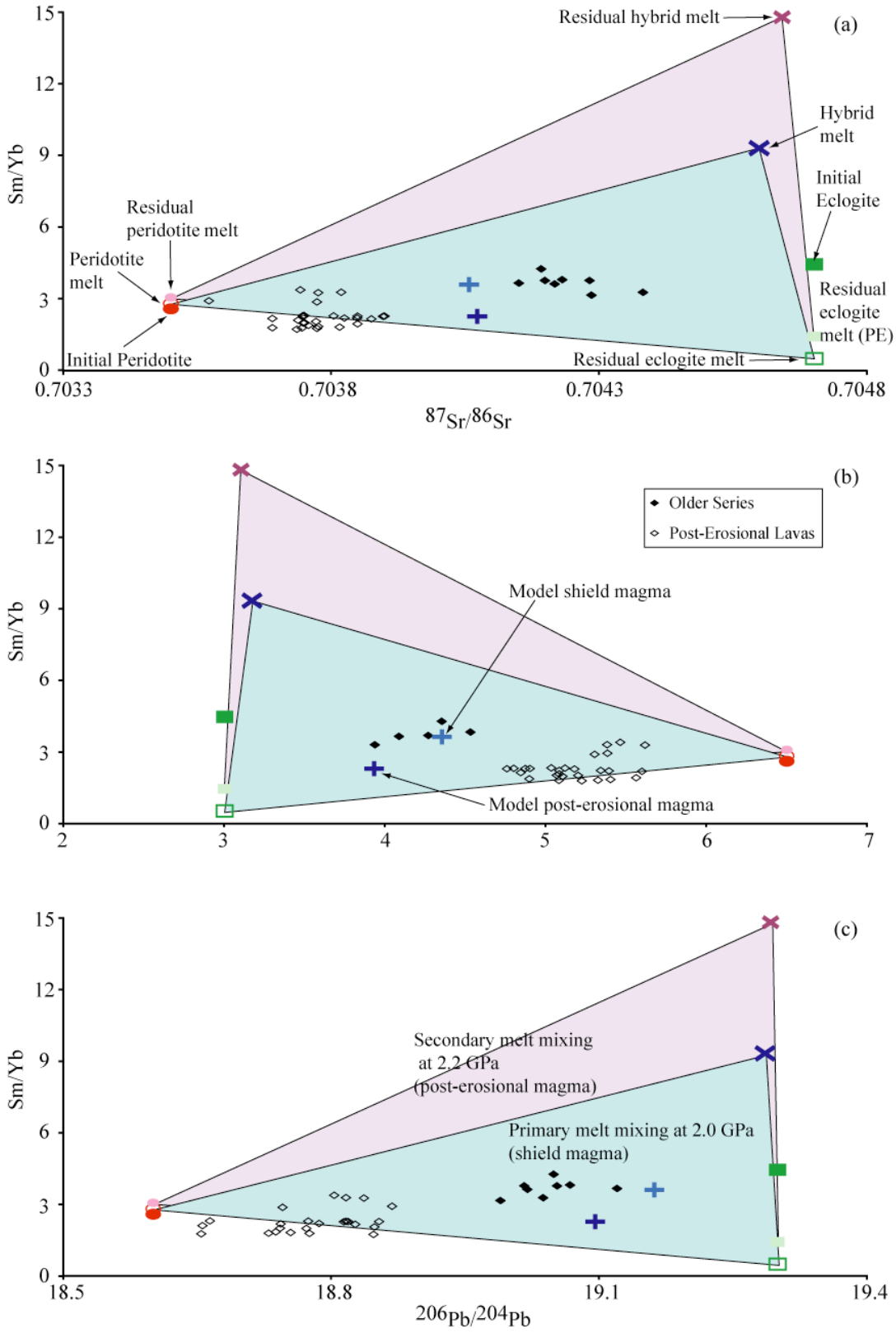
(a)
Residual hybrid melt
Hybrid melt
Initial Eclogite
Residual eclogite melt (PE)
Residual eclogite melt
Residual peridotite melt
Peridotite melt
Initial Peridotite
Sm/Yb
87Sr/86Sr
0.7033
0.7038
0.7043
0.7048
(b)
Older Series
Post-Erosional Lavas
Model shield magma
Model post-erosional magma
(c)
Secondary melt mixing at 2.2 GPa (post-erosional magma)
Primary melt mixing at 2.0 GPa (shield magma)
206Pb/204Pb
18.5
18.8
19.1
19.4

the trace element ratios of the Mauritian post-erosional lavas, however they do replicate several key characteristics. Most notably, the model post-erosional magmas have lower Sm/Yb, just as in the observed lavas. However, the systematics of the ordinate variables in Figure 45 (*e.g.*, La/Sm, La/Nb, and Zr/Nb) are not entirely consistent. For example, La/Sm and Zr/Nb follow the systematics observed in the Mauritian lavas (lower and higher than the Older Series, respectively), but La/Nb (and other ratios not shown) does not. This inconsistency is also observed in the spider diagram of the model post-erosional magma (Figure 31). While relative slopes are similar for many element-pairs, and most element concentrations are depleted by a factor of approximately 2, certain modeled concentrations (Ba, Pb, and Sr) were strikingly difficult to reproduce under the conditions necessary to satisfy the shield magmas. The strong negative Pb anomaly associated with this magma is a product of the majority of the model post-erosional magma being sourced from the peridotitic component ($X_{F,per}$ = 0.62), which has a negative Pb anomaly.

Discussion and Implications of Modeling

The ultimate goal of the thermodynamic modeling presented above was to determine whether a lithologically heterogeneous mantle plume could plausibly be the source of both the Mauritius shield and post-erosional lavas. In this approach, I tested the efficacy of two proposed melting models for a heterogeneous plume (*i.e.*, binary and hybrid) and established that both classes of models are indeed plausible. Modeled results show a surprising degree of inter-model similarity.

Perhaps the most notable similarity between the two models is in the physical conditions necessary to produce a successful solution. Each of the two models produced their sole successful solution with a potential temperature of 1525 °C, for generating both the model shield and post-erosional magmas, and an effective upper

boundary layer thickness for the post-erosional modeling of 2.5 GPa. Each of these physical conditions provides insight into the temperature and pressure conditions of the plume, though the meaning is not always clear. The use of the same T_P for both magma series indicates that even though each series was modeled independently, the thermal structure of the plume is radially uniform. The post-erosional magmas are assumed to form from particle paths peripheral to the plume center, though the distance was not specified. The use of the same T_P for both magma series indicates that even though each series was modeled independently, the thermal structure of the plume is radially uniform to the distance of the post-erosional particle paths. However, the common T_P may also indicate that the distance between the center of the plume and the post-erosional particle paths, while still peripheral, may be minimized somewhat. Ribe and Christensen found the post-erosional particle path to be ~40 km from the axis of the plume (their Figure 5), relatively central given that the radii of plumes is on the order of several hundred km (*e.g.*, Montelli et al., 2004). Furthermore, the common thickness of the effective upper boundary layer also caries implications about the physical characteristics of the plume. For each model, the effective upper boundary layer thickness was found to be a common parameter at 2.5 GPa. In comparison to the other parameter modeled, 3.0 GPa, the common boundary thickness can be easily interpreted as a thinner plume tail. For all models, the base of the oceanic lithosphere was held at 2.0 GPa, giving the favored model a plume tail thickness of 0.5 GPa (versus 1.0 GPa). The significance of a thinner plume tail can be thought of in one of several ways. In one, the thinner tail could indicate a narrower plume. A narrower plume would transport less material to the upper mantle, necessitating a thinner tail. Alternatively, the thinner tail could indicate that the lateral spreading of upwelling plume material is more efficient than in the thicker (3.0 GPa) plume tail. The author has been unable to discover any underlying biases that would

systematically impart a specific set of pressure and temperature conditions on a successful solution.

When comparing source compositions between the binary and hybrid melting models, it is clearly evident that many similarities exist between the two classes of models (Figure 30). For the eclogite component, both models are enriched in highly incompatible trace element concentrations relative to N-MORB. Both models also display similar concentrations of moderately incompatible trace elements, and lower Yb compared to N-MORB. However, whereas the binary model eclogite has a negative Pb anomaly, the hybrid model eclogite has no Pb anomaly. For the peridotitic component, both models are also enriched in highly incompatible trace element concentrations relative to DM. Both models also display similar concentrations of moderately incompatible trace elements, and lower Yb compared to DM. In contrast to the eclogitic component, the hybrid component has a negative Pb anomaly while the binary component has a small Pb anomaly. Despite these differences, both models have are strongly light rare earth enriched for both the peridotitic and eclogitic components $(La/Sm)_N$, $Sm/Yb)_N$, and $La/Yb)_N > 1$) for each component.

The strong LREE enrichment in the modeled source components is perhaps the most worrisome result from the heterogeneous plume models when the Mauritian data set is considered in its entirety. The lavas of Mauritius are well established as having positive ε_{Nd} values (*e.g.*, Sheth et al., 2003), and the initial components were modeled as such (*e.g.*, Table 16). Because of the relative incompatibilities of Nd and Sm in the mantle, a $+\varepsilon_{Nd}$ value implies a long-term LREE depletion in the magma source. However, the modeled trace element compositions of each source (peridotitic and eclogitic) are light REE enriched. Thus, a disconnect exists between the modeled trace element ratios in the component sources and the ε_{Nd} values of the model shield

magmas. Geochemically, this inconsistency can be rationalized if the source has undergone an enrichment process recently enough as to not disrupt the long-term LREE depletion signature. As ^{87}Rb and ^{147}Sm were not measured in this work, neither the Rb-Sr nor Sm-Nd decay systems are capable of providing direct evidence into the relative age of enrichment. A $^{207}Pb/^{204}Pb$-$^{206}Pb/^{204}Pb$ isochron can be calculated from the high-precision Pb isotope data collected for this work. Since the incompatible trace elements were fit to the Older Series data, the Pb data for these samples will be used for the isochron. This isochron produces an Archean age of 2830 Ma for the Older Series (though only a Proterozoic age of 1695 Ma when the high $^{207}Pb/^{204}Pb$ sample M30 is excluded; Figure 12c). Regardless, a LREE enriched source with either age would certainly produce a corresponding negative ε_{Nd} value.

Two problems exist with this approach. First, Pb is not a light rare earth element, and does not properly record changing rare earth conditions. Second, the linear $^{207}Pb/^{204}Pb$-$^{206}Pb/^{204}Pb$ trend can also be interpreted as a mixing line. Indeed, the two-source modeling presented in this work would seem to dictate that the trend be viewed as a mixture between components rather than a simple isochron (small variations in the initial isotope ratios and the amount of initial eclogite in the plume would accommodate the range of isotopic compositions).

Ultimately, the model requires strong LREE enrichment in each source because the eclogite melts completely. The eclogitic component is fundamentally more fertile than the peridotitic component and expected to produce larger degree melts, but the degree to which it melts are perhaps unrealistic for several reasons. First, is the assumption of batch melting. Though discussed elsewhere, partial melting in the mantle is known to occur (near-) fractionally (*e.g.,* Shaw, 1970; Albarède, 1995) and batch melting systematically overestimates the degree of melting (Kushiro, 2001). This is a known and significant problem with the current form of the model. The

second reason involves the use of the pMELTS algorithm to calculate the phase equilibria on the basaltic compositions of the eclogitic component. pMELTS is calibrated exclusively for peridotitic systems (Ghiorso et al., 2002), so applying it to an eclogitic composition requires the program to extrapolate beyond its calibrated range, decreasing precision. Together, these issues likely exaggerate the degree to which the eclogitic component melts. However, it is very difficult, if not impossible, to untangle the contribution of each factor. The large degrees of melting calculated for the eclogitic composition have a direct effect on the source composition of the binary model, and an indirect effect on the hybrid model. Were the eclogitic component to melt to a lesser degree, fractionation between trace elements in the model melts would be less extreme (*e.g.*, lower La/Sm and Sm/Yb), with larger concentrations, allowing the use of a less enriched initial ratio to produce the same ratios in the final modeled melt.

A comparison of modeled magmas shows both great consistency (shield magmas) and inconsistency (post-erosional magmas) between the binary and hybrid models. The modeled shield magmas all follow the pattern of the Older Series lavas very well, as expected, but concentrations are lower by approximately by a factor of three (Figure 31). The hybrid model shield magma has the lowest incompatible trace element concentrations of the three models (two binary, one hybrid), but does not differ significantly from the binary magmas. In comparison, the binary and hybrid model post-erosional magmas show great differences (Figure 31). Both models have lower absolute concentrations than the post-erosional lavas by approximately a factor of two. Perhaps the most notable difference between the two magmas is the strong negative Pb anomaly in the hybrid magma (0.92 ppm). This anomaly is directly related to the negative anomaly present in the peridotitic source of the hybrid model, which contributes 62% of the melt to the magma. The hybrid magma also has

significantly lower Ba (0.58 ppm) relative to the binary magma (Ba = 1.82 ppm), though the element is not modeled well in either model. The binary magma does a better job of reproducing the element-to-element slope exhibited by the post-erosional lavas. Furthermore, the binary model more closely reproduces the trace element ratios of the post-erosional magmas than does the hybrid model (Figure 47).

When considering the two thermodynamic melting models on the whole, it is relatively clear that neither of the proposed melting models of a lithologically heterogeneous mantle plume fully reproduce all of the chemical characteristics and signatures observed in the Mauritian lavas. Despite these flaws, each model is capable of plausibly reproducing certain key characteristics of each of the lava suites. A likely source of error within the models resides in the choice of individual components. There is no reason to believe that the composition selected for the peridotitic component (Depleted Mantle of McKenzie and O'Nions, 1991; 1995) is the true composition of the plume matrix. This composition is merely chosen to represent a component with relatively depleted isotopic signatures trace element compositions. Likewise, the composition of the eclogitic component need not be N-MORB (Hofmann, 1988; Allan et al., 1989), but is likely to be a product of recycling (*e.g.*, upper or lower oceanic lithosphere, delaminated subcontinental lithospheric mantle). Furthermore, there is no *a priori* reason to believe that the plume is composed of only two components. Though a few components may be volumetrically dominant, it is quite likely that many components contribute melt on small scales. Of course, attempting to model a system with many components in untenable, though a third primary component would be advantageous in many regards. Ito and Mahoney (2005a, b) modeled such a system, consisting of a depleted component and two components with different degrees of enrichment. Their model, in many ways, is quite similar to the hybrid model after fertilization of the peridotite to form the

reaction hybrid. Of course, it is reasonable to believe that much of the misfit error in the lavas, and subsequently in the source abundances are operator error, and further refinement would produce more consistent results. Regardless, additional improvements on the model are important.

Having established that a lithologically heterogeneous mantle plume is capable of plausibly reproducing the geochemical signatures observed in the lavas of Mauritius, it is important to address the temporal aspect of the erupted lavas. In review, the Older Series (8.4 – 5.5 Ma), Intermediate Series (3.5 – 1.9 Ma), and Younger Series (1.00 Ma – 10's ka) each are temporally distinct, though the two post-erosional suites are essentially chemically identical. To this point, the Intermediate and Younger Series lavas were treated homogenously, as if they were created through exactly the same process. This treatment poses an important question: what is the relationship between the sources of the temporally distinct Intermediate and Younger Series?

This question can be addressed by considering an analysis of relative velocities in the western Indian Ocean. Near Mauritius, the African plate is passing over the Réunion plume to the northeast at roughly 25 km/My, and has been doing so consistently since approximately 10 Ma (DeMets et al., 1994; DeMets et al., 2005). Mantle material within the plume ascends until it intersects the base of the lithosphere and begins to spread laterally. The large-scale shear of the overriding lithospheric plate couples weakly with the buoyant plume material, generating the elongated plume tail (*e.g.*, Ribe and Christensen, 1994). While the buoyancy-driven upwelling velocity of material within the Réunion plume is on the order of several hundred km/My (Albarède et al., 1997), material within the spreading and thinning plume tail is migrating at approximately the same rate as the overriding lithosphere, crust, and volcanic island. Consequently, the same packet of plume material will remain beneath

the island as it moves downstream. This concept is further illustrated in Figure 54, where the grey box illustrates the collective downstream movement of Mauritius Island and the plume material beneath it through time. This analysis implies that both the Intermediate and Younger Series lavas must be sourced from the same packet of plume material.

If the multiple Mauritian post-erosional lava suites are indeed sourced from the same packet of plume material, several magma generation scenarios are possible. In the first scenario, both the Intermediate and Younger Series lavas are generated from exactly the same plume material (Figure 54a). That is, after extraction of the Intermediate Series melts, the same source rocks are re-melted to form the Younger Series lavas. This scenario seems unlikely, and can be excluded each of the melting models described above. The binary model, as modeled, relies on a single melting event within the plume tail to generate the post-erosional magmas and is strictly capable of producing the Intermediate Series or the Younger Series, but not both. The hybrid model is not capable of producing both post-erosional magmas suites either. Although the hybrid model for $P_{max,PE}$ = 2.5 GPa consists of two melting stages after the formation of the hybrid component, during adiabatic decompression from 3.0 to 2.5 GPa and from 2.5 to 2.2 GPa, the magma produced in the first melting stage is not a suitable post-erosional parent. The first stage magma is consists of over 95% melt from the two enriched components and has a strongly enriched trace element and isotopic signature, not the depleted signature observed in the post-erosional lavas. Furthermore, it is difficult to believe that two distinct melting events on a single source (melting and re-melting) would produce two temporally distinct lava suites that are essentially chemically identical (*e.g.*, Tables 9 and 10). This scenario, as discussed, presents an unlikely solution.

A second scenario involves generating the Intermediate and Younger Series

Figure 54. Cartoon illustrating three hypothesized models for generating post-erosional lavas from a lithologically heterogeneous plume tail. (a) Re-melting of plume material beneath the island. When the relative velocities of material within the plume tail and the overriding plate are considered, the two are found to travel downstream at approximately the same rate. Therefore, this model depicts the generation of the two post-erosional lava suites from Mauritius as the re-melting of a single packet of plume material. The Intermediate Series would be generated from a first batch of melting, and is analogous to the post-erosional modeling described in the text. The Younger Series has no analogue in this modeling. The re-melting of a once-depleted source to produce two lavas with statistically equivalent trace element concentrations would require suspect circumstances. Furthermore, this model cannot account for the Pb-isotopic differences between the lavas. (b) Melting of spatially stratified heterogeneous filaments within the plume tail. Farnetani and Samuel (2005) found that bodies within an adiabatically upwelling plume were sheared into long, vertical filaments. Once these filaments enter the plume tail they are bent over and stacked, providing vertical heterogeneity from horizontal bodies. By melting the peripheral and central filament at different times, similar lavas could be produced given a limited chemical range between the different groups of filaments. (c) Differential velocities between the plume tail and the lithosphere introduce fresh plume material for melting. Given a greater velocity within the plume tail, new plume material would be emplaced beneath Mauritius, providing a fresh source for melting. However, velocities in the plume would need to approach the equivalent of the upwelling rate of the plume to source new material in the given time intervals.

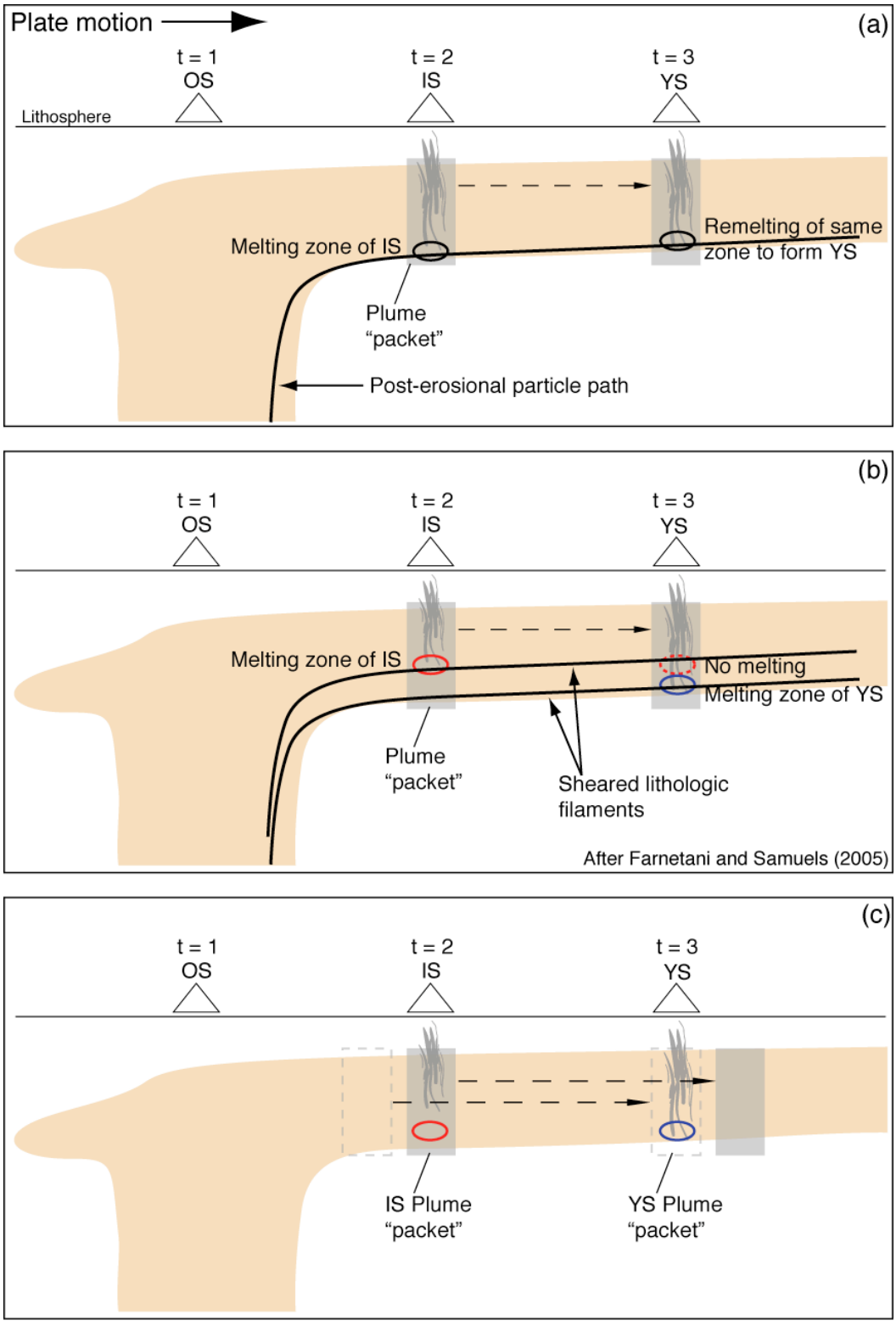
Plate motion
(a)
t = 1
OS
t = 2
IS
t = 3
YS
Lithosphere
Melting zone of IS
Remelting of same
zone to form YS
Plume
"packet"
Post-erosional particle path
(b)
t = 1
OS
t = 2
IS
t = 3
YS
Melting zone of IS
No melting
Melting zone of YS
Plume
"packet"
Sheared lithologic
filaments
After Farnetani and Samuels (2005)
(c)
t = 1
OS
t = 2
IS
t = 3
YS
IS Plume
"packet"
YS Plume
"packet"

from distinct zones within the plume packet (Figure 54b). Farnetani and Samuel (2005) found that bodies within an adiabatically upwelling plume were sheared into long, vertical filaments (their Figure 1j). Once these filaments enter the plume tail they are bent over and stacked, providing vertical heterogeneity from horizontal bodies. Fundamentally, the warmer and less peripheral filaments (stratigraphically higher) would melt sooner than the cooler, more peripheral filaments (stratigraphically lower) and could theoretically produce very similar magmas given similar abundances and compositions in each filament bunch. However, modeling in this work has demonstrated the sensitivity of varying pressure and temperature on trace element concentrations and ratios, and isotopic composition. This scenario, as discussed, presents a plausible solution. Finally, to explain the long-term homogeneity of the Réunion plume (*e.g.*, Fisk et al., 1988), and the similarity of the Intermediate and Younger Series, the compositional range of the heterogeneous filaments is severely limited.

The third and final scenario discussed here assesses the plausibility of the overriding lithosphere and plume tail moving downstream at different rates (Figure 54c). This scenario diverges from the assumptions held in the above two scenarios. If the material within the plume tail moves downstream more rapidly than overriding lithosphere, and the plume packet is taken to represent the area sampled by a post-erosional eruption, then it is possible that the Intermediate and Younger Series lavas each come from similarly composed yet distinct packets. To allow the Younger Series to be sourced by a distinct packet from the Intermediate Series, the Intermediate packet must be completely cleared from the melting zone and replaced by new material within the timeframe established by radiometric dating (*i.e.*, the duration of the volcanic hiatus, ~1 Ma). For example, given a plume packet with r = 25 km (sample area 50 km wide), the downstream rate of material within the plume tail

would be a minimum of 75 km/My. For r = 50 km, the downstream rate in the plume tail would be a minimum of 150 km/My. These sampling areas are consistent with other estimates for post-erosional eruptions (Bianco et al., 2005) and produce rates three to six times the downstream rate of the overriding lithosphere, respectively. Furthermore, these results approach estimates of the upwelling rates within the Réunion plume (~200 km/My; Albarède et al., 1997) that would be applicable to the plume tail only in a pipe-flow type setting. Given these unrealistic results, replacing the plume packet entirely presents an unsatisfactory solution.

Despite the successes and flaws of a lithologically heterogeneous plume as an internally consistent source for the entire suite of Mauritian lavas, one of the requirements set forth for a geologically consistent model was the prediction of a mechanism to explain the eruptive hiatus associated with post-erosional volcanism. Neither of the thermodynamic melting models are explicitly capable of explaining the eruptive hiatus or multiplicity of post-erosional volcanism. The correct combination of initial parameters and component compositions could conceivably lead to the multiple stages of melting in the hybrid model generating both post-erosional suites, though the details of the results are not known. Due to a lack of internal solutions, an external factor must be included. Flexure is therefore assumed to play an important role in this physical model for the post-erosional lavas. ten Brink and Brocher (1987) discussed how changes in stress conditions can effectively open or seal off conduits for melt migration as a volcano travels downstream atop the oceanic lithosphere. I call on these changing stress environments in conjunction with the filament scenario described above. Thus, post-erosional lavas are only produced on an island when the stress conditions are favorable for melt extraction from a bundle of filaments.

CHAPTER 6 – CONCLUSIONS

Conclusions

New sampling of deep Mauritius lavas was conducted from previously unavailable drill cores. These cores were expected to yield an unseen stratigraphic history of the Older Series lavas, but were dominated instead by post-erosional Intermediate and Younger Series lavas. Significant details about the eruptive history of the post-erosional lavas was obtained from these cores. Previously though to only mantle the Older Series deposits, Intermediate Series lavas were found as deep as 220 m and Younger Series lavas as deep as 153 m. Using stratigraphic information obtained from the analysis of the deep drill cores in conjunction with published geologic maps and cross sections for Mauritius, an estimated volume of the combined Intermediate and Younger Series post-erosional volcanics was calculated as a minimum of 35 km^3. This volume is much greater than expected and forms a linear relationship with similar data from Kauai and Oahu (Figure 23). Together this data suggests common processes govern the generation of post-erosional lavas worldwide.

The basal breccia of the Older Series identified by Perroud (1982) were sampled and analyzed, with the first geochemical data on the unit presented here. These samples are essentially identical to the known Older Series lavas, though at 8.00 Ma, are older than most sampled exposures. This age is consistent with its stratigraphic position at the base of the eroded massif. The Sr-isotopic ratios for these samples display strong Older Series signatures and show no evidence for seawater interaction. The suggestion of Perroud (1982) of a phreatomagmatic origin for this unit is still plausible, but would require interaction with meteoric water.

Isotopic composition data on samples from Paul et al. (2007) was jointly collected between Cornell and MPI Mainz and presented here. Together with the new

observations and results presented here, this isotopic data suggests that the deep samples identified as Older Series have been mistakenly identified as post-erosional samples. Subsequently, the compositional diversity known to exist between the shield and post-erosional lavas was interpreted as compositional diversity associated with the Réunion source.

Trace element and isotope compositions reported here are entirely consistent with those reported in previous studies. The Older Series lavas have higher concentrations of incompatible trace elements than do the post-erosional lavas. The Intermediate and Younger Series have statistically equivalent incompatible element concentrations. Isotopically, the Older Series is enriched relative to the post-erosional lavas, most notably in $^{87}Sr/^{86}Sr$ where there is no overlap between the shield and the post-erosional lavas. Similar differences are observed for Pb-isotopes as well. Within the post-erosional lavas, the $^{206}Pb/^{204}Pb$ and $^{208}Pb/^{204}Pb$ ratios of the Intermediate Series were found to be statistically distinct from those of the Younger Series. All other measured ratios were equivalent between the two series. Furthermore, a small subset of Intermediate Series lavas appears to be more enriched in the incompatible elements than the remainder of the group, though their isotopic compositions are no more enriched.

When compared to other well-studied worldwide occurrences of post-erosional volcanism, the trace element systematics of Mauritius are quite unique (Figure 19). The shield lavas of Mauritius are enriched in incompatible trace elements relative to the post-erosional lavas. In contrast, other islands with occurrences of post-erosional volcanism including Oahu and East Maui (Hawaii), Tahaa (Societies), Samoa, and Madeira display enrichments in trace element concentrations in the post-erosional lavas relative to the shield lavas. Despite these differences in trace element

concentrations, isotope systematics amongst the islands remains consistent with relatively enriched shield lavas and relatively depleted post-erosional lavas.

Evidence for significant clinopyroxene fractionation is seen in the Older Series, but not in the post-erosional lavas. Calculated liquid lines of descent mimic the strong decrease in CaO with MgO observed for the shield lavas (Figure 6). Strong trends are also observed in the Older Series data in Sc/Yb vs. CaO/Al_2O_3 (Figure 13) and FeO/MgO vs. CaO/Al_2O_3, both indicative of clinopyroxene fractionation. These results are consistent with Albarède et al. (1997) for Réunion, where significant clinopyroxene fractionation was identified as magmas passed through the lithosphere. Herzberg and Asimow (2008) identified the magmas of Réunion as having fractionated signification clinopyroxene, and were unable to calculate a primary magmas composition for all but a handful of samples.

Driven primarily by the isotopic distinction between the Older Series and the post-erosional lavas, it is evident that the lavas of Mauritius are derived from distinct sources. Here we propos that this diversity is solely the product of a lithologically heterogeneous mantle plume, extending the work of Paul et al. (2005). Under this hypothesis, the Réunion plume is composed of a modally minor enriched component (eclogite) within a matrix of a depleted component (peridotite). This model simulates the melting of a heterogeneous plume in thermal equilibrium under two conditions: (1) simple binary mixing of melts from the two components to for the primary magmas for the shield lavas, and (2) reaction of the melts at depth to form a hybrid pyroxenite, with subsequent melting and mixing to form the primary magmas.

Modeling of the heterogeneous plume under mantle conditions produced primary lavas with major element compositions similar to independent estimates. Fractional crystallization of these magmas produces liquid line of descent paths similar to the observed Older Series lavas. Varying the amount of eclogite initially

imposed on the system does little to affect the P-T profile or the major element composition of the individual components, but is important when mixing is considered. The proportion of melts derived from the eclogitic component increases with increasing eclogite content, and decreases with increasing temperature. The latter decrease is associated with the complete to near-complete melting of the eclogitic component under all conditions of shield magma generation. The extensive melting of the eclogitic component is the most important result from the shield modeling, and dictates the major element, trace element, and isotopic characteristics of the entire system. A potential temperature of 1525 °C best fits the observed data under most conditions for both melting models, and is near the lower range of estimates for the potential temperature of the Réunion plume.

Trace element ratios for each model component were iteratively fit to the Older Series lavas. The extensive melting of the eclogitic component imposed restrictions on trace element ratios, resulting in significant LREE enrichment and HREE depletion in both source components. In general, both the peridotitic and eclogitic sources for each model are strongly enriched in most incompatible element with little to no enrichment in the moderately incompatible elements, and strong depletion in the HREE. The binary eclogite source shows Pb depletion, while in the hybrid model the Pb depletion exists in the peridotite component. The incompatible trace element concentrations in the source patterns for both models do not look like hypothesized mantle sources and may be an artifact of computational concessions necessary for model stability (*i.e.*, melting parameterization and algorithm).

The post-erosional lavas are also modeled in this work via independent P-T profiles nearer the periphery of the plume. These outer particle-paths control the pressure, and thus the degree of depletion the components experience before entering the plume tail. A single successful solution was attained for each model, reaching its

effective upper boundary layer at 2.5 GPa before the components enter the plume tail. To maintain geochemical consistency within the models, the trace element concentrations fit to the shield lavas were utilized for the post-erosional models as well. The trace element ratios of the Intermediate and Younger Series lavas are reproduced excellently in the binary model, and with varying degrees of success. Incompatible trace element patterns reproduce the general slope and pattern of the Intermediate and Younger Series lavas, but at lower concentrations (ratios were explicitly modeled, not concentrations). Both models succeed in reproducing the geochemical characteristics of the post-erosional lavas because they are each sourced principally by peridotite-derived melts. In the binary model, the peridotitic component supplies all of the melt, while the hybrid model if formed by a three-component mixture dominated by the trace element budget of the peridotite-derived melts ($X_{F,ecl}$ = 0.62). Overall, the binary melt-mixing model is more successful at reproducing the geochemical signatures of the post-erosional lavas, but both models remain completely plausible.

Drawing upon the success of modeling to reproduce the major elements and isotopic compositions, a physical model is presented for the generation of the post-erosional lavas. Buoyant mantle material within the plume tail, spreading laterally as it upwells adiabatically, is weakly coupled to the overriding oceanic lithosphere and travels downstream at approximately the same rate (~25 km/My). Consequently, the same packet of plume material remains beneath the oceanic island during the period of post-erosional activity (several My) and would necessarily be the source of both the Intermediate Series and Younger Series lavas. Rather than both post-erosional series being sourced by exactly the same plume material, lithologic heterogeneities are stretched during ascent through the plume stem into laterally heterogeneous filaments that become vertical heterogeneity within the plume tail (Farnetani and Samuel, 2005).

The Mauritian post-erosional lava suites each sample a distinct bunch of heterogeneous filaments, though the compositional difference between bunches must be narrow.

APPENDIX A

DRILL CORE SAMPLING AND STRATIGRAPHIC DETAILS

Included in Appendix A are detailed notes from the sampling of the hydrologic drill cores provided by the Mauritius Water Resources Unit. These samples were collected during the 2007 field campaign in Mauritius (J. Moore, W. White, and D. Paul). Distinguishing between the Intermediate and Younger Series by hand sample was very difficult, and any descriptions that specify an origin from a particular suite should be crosschecked against samples of known age (*i.e.*, dated). Sample B18-1 is the only known Older Series sample from these drill cores. Depth is given in meters below surface level.

Table A.1. Detailed stratigraphic information from Mauritius Water Resources Unit drill cores. Sampling notes on stratigraphic information and core composition is given for each drill core from the 2007 field campaign (JCM, WMW, and DP). Longitude and latitude for each core can be found in Table 1.

Core No.	Location	Depth (m)	Stratigraphic Information
B1	Pierrefonds	157.3	
B1-1		1.2	Flow unit continuous to 14.3 m.
B1-2		14.3	
B1-3		29.6	Flow unit continuous from 25.9 to 36.6 m.
B1-4		88.4	
B1-5		152.7	
B2	Trianon	223.4	
B2-1		219.8	Flow unit continuous to 227.1 m. Portion of core missing.
B2-2		218.5	Change in appearance of core between B2-1 and B2-2.
B2-3		150.6	
B2-4		116.4	
B2-5		98.5	
B2-6		82.0	
B2-7		37.2	Vesicular basalt, tuff continuous to 19.8 m.
B2-8		18.9	
B5	Poudre d'Or	60.7	No stratigraphic information recorded for B5-1.
B6	Fond du Sac	164.6	
B6-1		144.8	
B6-2		89.9	
B6-3		16.8	
B6-4		3.4	First occurrence of lava at 3.4 m, remainder of core composed of soil.
B12	Notre Dame	71.9	
B12-1		70.1	
B12-2		50.3	
B12-3		43.3	Lava is light colored, minerals are visible.
B12-4		16.8	Core above B12-4 mostly composed of loose soil of red color (Fe-rich?).

Table A.1. *(continued)*

Core No.	Location	Depth (m)	Stratigraphic Information
B18	Beau Bois	221.0	
B18-1		219.8	Core consists of fine mud from 203.3 to 204.2 m. Lavas between 190.5 and 192.0 m are highly altered.
B18-2		177.7	Lavas in core are highly altered or brecciated between 160.0 and 164.6 m. Soil formation from 156.4 to 158.5 m.
B18-3		154.5	
B18-4		139.0	Soil formation in core between 100.6 and 111.9 m. Lavas are massive and dark, with olivine phenocrysts.
B18-5		99.1	Soil formation between 95.4 and 97.5 m. Lavas beneath soil are altered. Lavas between 74.7 and 91.4 are brecciated and deeply weathered. Lavas are massive and dark with fresh olivine. Slightly vesicular.
B18-6		71.0	Lavas are dark grey and massive. Slight alteration has resulted in minor formation of secondary minerals.
B18-7		64.3	Lavas of medium vesicularity are dark grey. Olivine and plagioclase are small and fresh. Plagioclase is quite abundant.
B18-8		41.8	Soil formation in core with alteration and weathering of lavas from 21.3 to 38.1 m. Medium grey with abundant plagioclase. Olivine are present and appear mostly fresh, but are small.
B18-9		20.7	Core above B18-9 is highly altered and has soil formation. Sample is light grey with abundant pyroxene but little olivine.
B19	Eau Bleu	99.1	
B19-1		89.9	Dark and massive flow with minor vesiculation. Alteration of olivine and formation of secondary minerals in vesicles.
B19-2		71.6	Dark flow with olivine. Abundant formation of secondary minerals, but no apparent alteration of olivine.
B19-3		35.1	Soil formation between 24.1 and 26.2, and 19.2 and 20.4 m. Lava is dark and massive with scattered formation of secondary minerals.
B19-4		18.9	Core is strongly weathered from 13.1 to 16.2 m. Lava is vesiculated and medium grey in color.
B19-5		8.5	Soil formation in the core between 4.3 and 5.5 m.

APPENDIX B

MAJOR ELEMENT ANALYTICAL UNCERTAINTY

Included in Appendix B are major element oxide XRF results for duplicate analyses of Mauritian samples (B1-2 and M12) and analytical results on geostandards (BHVO-1, BCR-2, and B-EN).

Table B.1. Duplicate XRF analyses of major elements for Mauritius samples

oxide (Wt.%)	B1-2	B1-2R	M12	M12R
SiO2	46.95	46.93	45.34	45.49
TiO2	1.72	1.71	2.78	2.79
Al2O3	16.18	16.15	13.54	13.57
FeO(T)	11.61	11.46	11.35	11.50
MnO	0.18	0.18	0.17	0.17
MgO	8.36	8.36	7.33	7.34
CaO	10.69	10.63	11.37	11.40
Na2O	2.88	2.86	2.78	2.79
K2O	0.38	0.37	0.93	0.93
P2O5	0.15	0.15	0.35	0.35
Sum	99.08	98.79	95.94	96.33
LOI (%)	0.09	0.09	1.15	1.15

Major element contents are unnormalized. Total Fe reported as Fe^{2+}.

Table B.2. XRF major element analysis on geostandards

	BHVO-1	Ref. Value	2σ	**BCR-2**	Ref. Value	2σ	**BE-N**	Ref. Value	2σ
SiO2	50.17	49.8	0.3	54.90	54.1	0.8	39.78	38.2	0.62
TiO2	2.801	2.75	0.04	2.342	2.26	0.05	2.812	2.61	0.14
Al2O3	13.74	13.74	0.2	13.77	13.5	0.2	10.50	10.07	0.41
FeO(T)	11.13	11.16	0.18	12.36	12.42	0.18	*12.24*	11.55	0.31
MnO	0.174	0.17	0.006	0.206	0.2	0.01	0.212	0.2	0.02
MgO	*7.37*	7.22	0.07	3.69	3.59	0.05	13.92	13.15	0.44
CaO	11.57	11.4	0.2	7.33	7.12	0.11	14.62	13.87	0.87
Na2O	2.25	2.3	0.1	3.23	3.16	0.11	3.34	3.18	0.23
K2O	0.52	0.53	0.01	1.82	1.79	0.05	1.47	1.39	0.11
P2O5	0.270	0.274	0.007	0.361	0.35	0.02	1.101	1.05	0.13
Total	100.00			100.00			100.00		

XRF values are normalized. BHVO-1 and BCR-2 are GeoReM preferred values.

BE-N values from Govindaraju (1995). Total Fe reported as Fe^{2+}. Italisized values are outside published 2σ of reference values.

APPENDIX C

TRACE ELEMENT ANALYTICAL UNCERTAINTY

Included in Appendix C are analytical uncertainties (2σ) for ICP-MS trace element analyses of Mauritius lava samples and trace element results and analytical uncertainty of geostandards (BHVO-1, BCR-2, and B-EN).

Table C.1. Trace element standard deviations for Mauritius samples. Errors are standard deviations between multiple runs over multiple days.

element	**Older Series**								**Intermediate Series**	
(ppm)	B18-1	M6	M12	M30	M35	M36	M37	M39	B2-1	B5-1
Li	0.11	0.02	0.09	0.09	0.06	0.11	0.09	0.11	0.11	0.11
Be	0.1	0.0	0.0	0.0	0.1	0.0	0.1	0.1	0.0	0.0
B	0.2	0.2	0.1	0.1	0.1	0.6	0.0	0.0	0.1	0.1
Sc	1.20	0.55	0.17	0.85	0.33	0.60	1.06	0.81	1.18	0.34
Ti	1844	1078	50	886	68	2826	2324	492	1194	773
V	29.5	18.6	0.8	7.1	2.8	52.2	35.9	9.0	20.9	4.0
Cr	6.3	1.6	0.6	1.4	0.6	0.9	0.4	1.2	4.1	1.6
Co	1.46	0.79	0.78	0.34	0.65	1.19	0.20	0.90	0.74	2.03
Ni	3.13	1.39	0.98	1.32	0.62	0.71	0.72	0.23	6.46	6.95
Cu	4.63	0.69	0.38	0.69	1.41	1.16	2.21	1.99	3.60	1.90
Zn	5.65	2.28	0.42	0.81	1.67	0.92	3.88	2.07	3.59	0.18
Ga	0.78	1.06	0.93	1.28	0.36	0.07	1.49	1.31	1.20	0.39
Rb	0.5	1.4	0.2	1.8	0.3	0.3	0.1	0.2	0.3	0.1
Sr	1.7	24.3	3.6	15.1	4.3	2.5	2.7	1.0	6.2	1.8
Y	0.63	0.96	0.55	0.32	0.16	0.00	0.48	1.20	0.71	0.09
Zr	10.4	30.8	2.0	3.9	42.1	40.9	13.5	0.3	9.5	8.6
Nb	3.95	4.68	0.52	3.37	1.23	7.41	5.76	2.57	2.41	2.46
Cs	0.003	0.002	0.000	0.003	0.012	0.004	0.002	0.002	0.003	0.001
Ba	3.0	10.0	3.9	9.9	0.2	1.9	0.9	2.5	3.5	1.8
La	0.29	1.17	0.30	0.53	0.91	0.35	0.39	0.68	0.22	0.05
Ce	2.20	1.26	0.92	0.08	0.97	0.43	1.04	1.79	0.70	0.18
Pr	0.16	0.31	0.01	0.09	0.17	0.02	0.18	0.41	0.05	0.02
Nd	0.55	1.81	0.15	0.72	0.98	0.18	0.20	0.17	0.15	0.13
Sm	0.09	0.33	0.04	0.17	0.04	0.02	0.03	0.06	0.05	0.00
Eu	0.02	0.13	0.01	0.03	0.01	0.02	0.02	0.01	0.01	0.00
Gd	0.04	0.43	0.01	0.31	0.25	0.13	0.24	0.17	0.04	0.05
Tb	0.01	0.05	0.01	0.03	0.01	0.01	0.02	0.01	0.01	0.01
Dy	0.10	0.28	0.08	0.25	0.17	0.06	0.07	0.14	0.10	0.04
Ho	0.01	0.04	0.00	0.03	0.00	0.00	0.03	0.01	0.00	0.00
Er	0.05	0.08	0.01	0.01	0.04	0.01	0.08	0.02	0.04	0.03
Yb	0.03	0.08	0.01	0.04	0.06	0.04	0.10	0.08	0.03	0.02
Lu	0.01	0.01	0.00	0.00	0.01	0.01	0.01	0.01	0.00	0.01
Hf	0.22	0.30	0.03	0.13	0.13	0.57	0.05	0.14	0.12	0.11
Ta	0.23	0.15	0.03	0.18	0.04	0.38	0.32	0.11	0.11	0.11
Pb	0.05	0.07	0.12	0.06	0.10	0.13	0.03	0.01	0.33	0.03
Th	0.09	0.05	0.00	0.07	0.03	0.04	0.09	0.00	0.01	0.00
U	0.031	0.007	0.003	0.019	0.010	0.004	0.021	0.001	0.002	0.001

Table C.1. *(continued)*

element	**Intermediate Series**									
(ppm)	B6-1	B6-2	B12-1	B18-2	B18-3	B18-4	B18-5	B18-6	B18-7	B18-8
Li	0.15	0.11	0.15	0.03	0.02	0.21	0.17	0.23	0.12	0.20
Be	0.0	0.0	0.0	0.0	0.0	0.0	0.0	0.0	0.0	0.0
B	0.1	5.4	0.0	0.1	0.2	0.1	0.3	9.2	0.2	0.4
Sc	1.10	0.17	0.29	0.79	0.17	1.13	1.12	1.11	0.42	1.04
Ti	673	901	242	1121	416	363	259	168	641	230
V	16.3	15.5	3.7	23.7	7.6	11.9	2.6	5.4	13.0	5.6
Cr	13.6	4.4	1.7	1.2	8.9	11.9	1.5	3.6	10.1	4.3
Co	3.03	1.04	0.17	0.12	1.84	3.50	1.24	0.57	1.19	3.33
Ni	10.28	4.05	0.38	5.35	8.39	18.86	0.61	2.42	10.87	2.50
Cu	2.75	1.26	0.73	2.74	1.00	3.59	2.77	3.58	1.54	1.55
Zn	3.15	1.11	0.05	3.09	2.60	3.98	5.36	5.54	2.28	0.44
Ga	0.57	0.35	0.18	0.11	0.44	0.59	1.04	0.48	0.98	0.84
Rb	0.1	0.1	0.1	0.3	0.2	0.1	0.1	0.1	0.3	0.4
Sr	5.7	4.4	3.3	0.3	6.3	7.2	0.2	5.9	13.4	16.6
Y	0.90	0.12	0.35	0.05	0.52	0.26	0.15	0.91	0.88	0.71
Zr	10.1	9.4	2.3	3.2	6.3	3.2	17.9	9.8	5.5	18.2
Nb	2.05	1.05	0.60	2.91	1.03	0.05	2.24	0.29	0.48	0.16
Cs	0.005	0.000	0.000	0.009	0.001	0.001	0.015	0.001	0.002	0.005
Ba	6.6	0.2	2.5	1.7	2.5	4.0	0.2	4.0	4.3	4.2
La	0.09	0.09	0.01	0.24	0.04	0.26	0.07	0.20	0.31	0.53
Ce	0.65	0.21	0.45	0.38	0.29	0.86	1.10	0.81	0.61	0.72
Pr	0.05	0.05	0.04	0.04	0.02	0.11	0.12	0.12	0.09	0.08
Nd	0.11	0.05	0.41	0.13	0.12	0.51	0.47	0.18	0.53	0.91
Sm	0.04	0.01	0.07	0.04	0.02	0.12	0.12	0.01	0.14	0.17
Eu	0.02	0.02	0.01	0.00	0.00	0.05	0.01	0.00	0.04	0.08
Gd	0.03	0.07	0.01	0.12	0.03	0.10	0.14	0.00	0.16	0.23
Tb	0.01	0.00	0.00	0.01	0.01	0.02	0.00	0.01	0.02	0.04
Dy	0.10	0.02	0.11	0.06	0.02	0.06	0.07	0.01	0.20	0.16
Ho	0.01	0.01	0.02	0.01	0.00	0.02	0.01	0.01	0.04	0.03
Er	0.06	0.01	0.01	0.05	0.00	0.09	0.04	0.00	0.08	0.07
Yb	0.02	0.02	0.03	0.05	0.01	0.08	0.02	0.01	0.08	0.09
Lu	0.01	0.01	0.00	0.00	0.00	0.01	0.00	0.00	0.01	0.01
Hf	0.10	0.06	0.05	0.02	0.11	0.13	0.23	0.13	0.06	0.24
Ta	0.15	0.01	0.04	0.12	0.05	0.00	0.02	0.02	0.03	0.17
Pb	0.41	0.42	0.03	0.06	0.01	0.11	0.21	0.83	0.05	0.50
Th	0.07	0.02	0.01	0.04	0.01	0.07	0.02	0.05	0.04	0.04
U	0.015	0.002	0.001	0.003	0.002	0.025	0.005	0.015	0.010	0.009

Table C.1. *(continued)*

element	**Intermediate Series**					**Younger Series**				
(ppm)	B19-1	B19-2	B19-3	M15	M20	B1-1	B1-2	B1-3	B1-4	B1-5
Li	0.08	0.03	0.13	0.07	0.23	0.12	0.05	0.16	0.05	0.00
Be	0.0	0.0	0.0	0.1	0.0	0.0	0.0	0.0	0.0	0.0
B	0.1	0.2	0.2	0.0	0.2	0.1	0.1	0.0	0.0	0.0
Sc	0.33	0.41	0.67	0.01	1.60	0.32	0.08	0.88	0.37	0.62
Ti	1744	1697	261	117	1512	749	724	923	1294	661
V	32.7	31.5	11.4	2.2	35.9	9.5	14.1	22.8	22.1	9.4
Cr	9.9	16.5	12.9	0.2	10.3	5.3	2.8	8.2	8.3	2.7
Co	2.43	2.93	0.36	0.35	3.90	0.81	0.79	1.02	2.01	0.14
Ni	9.42	19.80	4.90	0.31	5.80	2.99	1.47	2.94	2.51	1.96
Cu	0.51	1.03	3.21	0.09	3.64	0.96	0.87	1.66	0.97	1.73
Zn	0.40	0.57	5.76	0.26	4.59	3.64	1.57	2.30	3.24	3.62
Ga	0.19	0.12	0.64	0.92	1.08	1.36	0.28	1.04	2.29	0.80
Rb	0.2	0.1	0.0	0.2	0.2	0.3	0.2	0.1	0.5	0.2
Sr	6.4	8.6	6.3	0.7	12.5	18.8	3.2	2.3	18.2	4.8
Y	0.15	0.43	0.90	0.38	1.45	1.03	0.19	0.36	1.25	0.98
Zr	22.2	8.1	11.9	0.7	14.8	7.8	10.0	4.1	5.8	0.1
Nb	6.40	4.18	0.48	0.33	2.14	1.18	1.88	2.10	3.61	2.54
Cs	0.002	0.001	0.007	0.001	0.001	0.000	0.002	0.003	0.003	0.003
Ba	0.4	1.6	1.1	1.2	2.6	2.4	3.4	1.8	2.5	1.0
La	0.12	0.03	0.09	0.13	0.37	0.26	0.06	0.03	0.25	0.20
Ce	0.34	0.09	0.64	0.26	0.46	0.29	0.11	1.12	0.12	0.06
Pr	0.03	0.06	0.05	0.00	0.09	0.09	0.02	0.03	0.03	0.04
Nd	0.26	0.15	0.01	0.08	0.44	0.25	0.26	0.02	0.07	0.15
Sm	0.01	0.02	0.07	0.04	0.11	0.13	0.04	0.02	0.02	0.01
Eu	0.02	0.01	0.01	0.02	0.04	0.02	0.01	0.00	0.01	0.01
Gd	0.10	0.03	0.05	0.06	0.18	0.18	0.16	0.12	0.19	0.13
Tb	0.00	0.01	0.00	0.00	0.03	0.01	0.01	0.01	0.02	0.01
Dy	0.05	0.02	0.05	0.12	0.24	0.05	0.03	0.07	0.03	0.02
Ho	0.01	0.00	0.01	0.01	0.05	0.02	0.03	0.01	0.02	0.02
Er	0.02	0.01	0.05	0.00	0.10	0.04	0.09	0.03	0.08	0.06
Yb	0.05	0.01	0.02	0.00	0.09	0.05	0.07	0.05	0.08	0.06
Lu	0.00	0.00	0.01	0.00	0.01	0.01	0.01	0.01	0.01	0.01
Hf	0.28	0.09	0.00	0.02	0.24	0.07	0.11	0.02	0.01	0.08
Ta	0.26	0.17	0.11	0.02	0.10	0.03	0.08	0.06	0.19	0.23
Pb	0.05	0.02	0.10	0.04	2.04	0.02	0.62	0.05	0.01	0.03
Th	0.06	0.02	0.14	0.00	0.05	0.02	0.02	0.01	0.00	0.02
U	0.009	0.005	0.035	0.004	0.010	0.002	0.008	0.007	0.005	0.005

Table C.1. *(continued)*

element	**Younger Series**								
(ppm)	B6-3	B6-4	B18-9	B19-4	B19-5	M17	M22	M29	M33
Li	0.12	0.08	0.01	0.11	0.03	0.30	0.11	0.08	0.20
Be	0.0	0.0	0.0	0.0	0.0	0.0	0.0	0.0	0.0
B	0.0	0.3	0.1	0.1	0.0	0.0	0.2	0.2	0.1
Sc	0.73	0.11	0.04	0.77	0.02	0.93	0.95	0.16	1.01
Ti	1147	340	217	977	5	2434	1214	1379	1436
V	25.0	3.2	1.9	17.0	0.2	55.9	24.3	25.1	22.7
Cr	9.0	8.0	1.7	5.1	1.0	4.1	0.3	7.1	6.5
Co	1.57	0.18	0.12	1.93	0.48	0.46	0.08	0.39	2.40
Ni	6.29	0.24	4.72	4.13	0.48	0.66	0.74	0.68	13.64
Cu	1.20	1.18	0.66	2.40	0.53	3.07	1.68	1.57	3.34
Zn	1.49	2.16	0.88	3.34	0.44	5.06	2.85	1.70	3.08
Ga	0.81	0.39	0.77	1.30	0.60	0.94	1.17	0.82	0.87
Rb	0.1	0.0	0.1	0.2	0.0	0.1	0.2	0.1	0.1
Sr	3.3	4.7	4.9	4.3	0.4	4.9	1.8	4.0	3.8
Y	0.29	0.48	0.62	0.72	0.27	0.75	0.49	1.34	0.35
Zr	8.6	7.3	1.5	11.3	1.7	14.9	3.9	7.7	10.7
Nb	1.59	0.82	0.72	2.66	0.08	3.74	3.78	2.69	2.32
Cs	0.004	0.002	0.002	0.003	0.001	0.000	0.002	0.001	0.001
Ba	0.7	1.2	0.6	1.7	0.2	1.9	2.9	0.8	1.5
La	0.05	0.01	0.01	0.28	0.02	0.08	0.25	0.18	0.23
Ce	0.30	0.54	0.33	0.57	0.18	0.48	0.58	0.20	0.41
Pr	0.03	0.00	0.03	0.08	0.01	0.01	0.06	0.03	0.06
Nd	0.09	0.39	0.23	0.12	0.03	0.03	0.12	0.07	0.29
Sm	0.05	0.00	0.02	0.09	0.02	0.02	0.02	0.00	0.07
Eu	0.04	0.01	0.01	0.01	0.02	0.01	0.01	0.00	0.04
Gd	0.12	0.02	0.01	0.05	0.03	0.04	0.11	0.14	0.05
Tb	0.01	0.01	0.00	0.00	0.00	0.01	0.01	0.01	0.02
Dy	0.08	0.06	0.07	0.12	0.07	0.08	0.07	0.07	0.13
Ho	0.02	0.02	0.01	0.01	0.00	0.00	0.02	0.01	0.02
Er	0.04	0.08	0.02	0.03	0.05	0.01	0.07	0.05	0.04
Yb	0.03	0.04	0.00	0.03	0.01	0.05	0.08	0.06	0.02
Lu	0.00	0.01	0.00	0.00	0.00	0.00	0.01	0.00	0.00
Hf	0.10	0.05	0.01	0.11	0.01	0.26	0.02	0.08	0.15
Ta	0.08	0.03	0.04	0.14	0.01	0.18	0.20	0.12	0.12
Pb	0.11	0.10	0.03	0.01	0.01	0.02	0.04	0.02	0.04
Th	0.01	0.04	0.01	0.01	0.00	0.01	0.04	0.01	0.02
U	0.005	0.012	0.002	0.003	0.002	0.002	0.000	0.000	0.004

Table C.2. ICP-MS geostandard analysis values

element	**BCR-2**	*n = 28*		**BIR-1**	*n = 4*		**B-EN**	*n = 4*		**PAL-889**	*n = 4*		
(ppm)	Mean	σ	Ref. Value	Mean	σ	Ref. Value	Mean	σ	Ref. Value	Mean	σ	Ref. Kay	Ref. White
Li	7.33	0.14	9	2.85	0.06	3.2	13.00	0.38	13	22.95	0.28		
Be	1.9	0.1		0.1	0.0	0.12	1.6	0.1	1.9	0.6	0.0		
B	0.3	0.1		0.6	0.0	0.33	75.3	2.2		0.8	0.1		
Sc	33.43	0.80	33	44.29	1.29	43	23.16	0.95	22	40.34	0.91	37.5	
Ti	15474	434	13500	5554	356	5600	13545	921	16000	8374	270		
V	521.9	16.1	416	371.6	16.8	319	285.3	5.6	235	368.9	12.4		
Cr	30.1	1.2	18	403.0	13.7	391	363.9	3.7	360	325.9	4.7	314	
Co	38.49	0.73	37	55.10	1.43	52	58.57	0.46	60	57.17	0.72	53	
Ni	13.06	0.38	18	172.81	4.03	166	257.49	0.69	267	95.18	1.17	89	
Cu	21.64	1.08	21	114.02	3.13	119	70.14	2.36	72	113.30	1.38		
Zn	134.85	2.61	127	75.91	1.91	72	177.64	3.39	120	88.23	1.86		
Ga	23.49	0.70	23	16.60	0.28	15.3	19.21	1.03	17	19.28	0.59		
Rb	47.3	1.1	46.9	0.3	0.0	0.2	48.6	0.9	47	33.0	0.9		33.8
Sr	336.5	6.6	340	111.0	5.1	109	1394.1	17.1	1370	190.7	2.4	183	177
Y	35.23	0.70	37	15.64	0.45	15.6	28.93	0.65	30	23.53	0.57	22	
Zr	218.1	13.9	184	17.9	0.9	14	156.7	21.8	260	116.9	7.8	88.8	
Nb	15.16	0.44	12.6	0.58	0.06	0.55	58.19	11.61	105	9.00	0.49	6.6	
Cs	1.097	0.030	1.1	0.005	0.001	0.007	0.685	0.023	0.8	2.036	0.078	2.19	2.25
Ba	664.4	13.4	677	6.8	0.3	7.14	990.1	8.1	1025	193.4	2.5	188	197
La	24.48	0.56	24.9	0.63	0.02	0.615	79.69	0.56	82	11.38	0.16	10.52	11.41
Ce	53.12	1.06	52.9	2.00	0.10	1.92	152.51	2.45	152	25.03	0.49	23.6	25.5
Pr	6.88	0.13	6.7	0.39	0.01	0.37	16.92	0.08	17.5	3.33	0.07		3.41
Nd	28.77	0.67	28.7	2.43	0.09	2.38	65.22	0.14	67	14.28	0.08	13.0	14.5
Sm	6.60	0.14	6.58	1.12	0.05	1.12	12.19	0.10	12.2	3.68	0.08	3.42	3.67
Eu	1.98	0.04	1.96	0.53	0.02	0.53	3.68	0.04	3.6	1.21	0.01	1.070	1.190
Gd	6.64	0.18	6.75	1.87	0.08	1.87	9.87	0.39	9.7	4.12	0.10		4.22
Tb	1.02	0.03	1.07	0.36	0.01	0.36	1.26	0.03	1.3	0.67	0.01	0.67	0.770
Dy	5.29	0.18	6.41	2.78	0.06	2.51	5.56	0.13	6.4	3.90	0.09		4.37
Ho	1.27	0.03	1.28	0.58	0.01	0.56	1.06	0.03	1.1	0.87	0.01		0.909
Er	3.56	0.07	3.66	1.72	0.04	1.66	2.49	0.06	2.5	2.43	0.04		2.44
Yb	2.99	0.07	3.38	1.59	0.06	1.65	1.75	0.05	1.8	2.07	0.06	2.18	2.32
Lu	0.49	0.01	0.503	0.26	0.01	0.25	0.24	0.00	0.24	0.33	0.01	0.33	0.362
Hf	5.16	0.13	4.9	0.61	0.01	0.582	2.80	0.40	5.6	2.79	0.05	2.56	
Ta	0.85	0.01	0.74	0.03	0.01	0.0357	2.72	0.55	5.7	0.65	0.03	0.65	
Pb	12.01	0.32	11	3.56	0.10	3.1	5.10	0.06	4	6.18	0.10	4.58	
Th	5.71	0.09	5.7	0.03	0.00	0.032	10.02	0.15	10.4	2.14	0.03	2.07	
U	1.637	0.027	1.69	0.010	0.001	0.01	2.451	0.036	2.4	0.515	0.009	0.50	

B-EN values from Govindaraju (1995). BCR-2 and BIR-1 are GeoRem prefered values from GeoRem database. PAL reference values from Kay are INAA working values and from White are isotope dilution values.

APPENDIX D

INTRODUCTION TO TRACE ELEMENTS

Introduction to Trace Elements

In most igneous systems, ten or fewer elements compose 99 % (wt. % or mol %) or more of a system. For most silicate systems the "major" elements are typically Si, Mg, Fe, Ca, Al, Na, and O. The elements Ti, Cr, Mn, K, P, S, C, and H occasionally form stoichometric components or phases in igneous systems, and are often referred to as "minor elements". This leaves approximately 75 naturally occurring elements, which collectively compose the "trace elements". A relatively simplistic, though useful, definition identifies a trace element as any element that composes less than 0.1 % of a system (i.e., approaching the dilute limit) in oxide form (e.g., La_2O_3). Trace elements are not *a priori* restricted from forming stoichometric components or phases (e.g., $LiAlSi_2O_6$, Spodumene), though these types of phases are typically restricted to modally insignificant accessory phases or metamorphic-type assemblages, requiring special circumstances for formation.

Certain groups of trace elements tend to behave similarly to each other, and differently from other groups, and are thus of great interest to geochemists. Due in large part to their relative electronegativities, the alkali and alkaline earth elements are form strongly ionic bonds, and can be considered to behave approximately as hard spheres. These bonds tend to be disrupted by the polar nature of aqueous fluids (i.e., water) and are thus soluble, which allows them to be highly mobile during metamorphism and weathering. Potassium, Rb, Cs, Sr, and Ba have large ionic radii, ranging from 1.18 angstroms (Å, 1 Å = 10^{-10} m) for Sr to 1.67 Å for Cs (VI-coordination; Shannon, 1976) and are collectively referred to as the large-ion-

lithophile (LIL)[13] elements. These elements are larger than even the largest cation lattice sites (octahedral) in most silicate minerals, and are therefore preferentially concentrated into the melt phases during melting or crystallization. These elements are thus highly incompatible with silicate mineral assemblages. The lanthanides and Y are collectively referred to as the rare earth elements (REE)[14]. These elements are highly electropositive and tend to form ionic bonds, also behaving approximately as hard spheres. The REE have a valence state of 3+ over the common range of oxygen fugacities found on Earth, though Eu can be partially in the 2+ state under the low fugacity conditions of the mantle. The REE all exhibit similar chemical behavior as the 4*f* electrons are being filled first, so the valence electrons are all similar. The decrease in ionic radii from La^{3+} (1.16 Å) to Lu^{3+} (0.977 Å; VIII-coordination) governs the behavior of the elements, with relative incompatibility decreasing with decreasing ionic radius. The actinides U and Th behave similarly to the REE, and can be modeled as hard spheres. Thorium always has a valence state of +4 and U commonly has a valence state of 4+, though U can be 6+ under oxidizing conditions, where it is also soluble. Because of their high valence, U and Th are highly incompatible. The combination of high valence and relatively small ionic radii give U and Th certain similarities to the high field strength elements (HFSE), Zr, Hf, Nb, and Ta. Zirconium and Hf have valence states of 4+, and Nb and Ta have +5 valence states. The high charge leads to relatively small cations, with ionic radii of 0.64 Å for Nb and Ta, 0.71 Å for Zr, and 0.72 Å for Hf (VI-coordination). Hafnium and Zr are moderately incompatible, while Nb and Ta are highly incompatible elements. These

[13] Lithophile elements show an affinity for silicate minerals and are thus concentrated in the silicate portion (mantle + crust) of the Earth. Lithophile derives from the Greek *lithos* meaning rock and *phile* meaning loving.

[14] In geochemistry only the lanthanides are truly considered rare earth elements. Uranium and Th are the only actinides stable over the history of the Earth, and are thus treated independently.

elements are also highly insoluble. The transition metals are more complicated than the elements described above. These elements tend to have multiple valence states, are highly electronegative and tend to form covalent bonds, and have a variety of *d*-orbital geometries that lead to complicating crystal field effects. The compatibility of these elements in magmas is highly dependent on the composition and structure of both the solid and melt phases.

The wide variety of properties within the trace elements, both similar and different, provides geologists with an extensive array of tools for investigation. As the trace elements are not primary structural building blocks in the construction of most minerals, they are able to provide geochemists and petrologists with a wealth of information about the history of the rock: from insight into melting and crystallization histories, to assimilation and mixing within magma chambers, from ages of formation to extraction rates and compaction length scales. Trace elements tell a story well beyond their proportion and, including the noble metals, are worth their weight in gold.

Using the notation of Beattie et al. (1993), the relative affinity for a trace element between two phases is defined as the partition, or distribution, coefficient *D*:

$$D_i^{\alpha/\beta} = C_i^{\alpha} / C_i^{\beta} \qquad \text{D.1}$$

where *C* is concentration, *i* refers to the element of interest, and α and β are the phases of interest. For igneous geochemistry, our system of interest most commonly consists of a mineral and a melt phase, and by convention the partition coefficient is written as:

$$D_i^{s/l} = C_i^{s} / C_i^{l} \qquad \text{D.2}$$

where *s* is a solid phase and *l* is the liquid phase. A *D* greater than 1 indicates an affinity for the solid phase, and such elements are considered compatible. An element with a *D* less than 1 indicates an affinity for the melt phase, and such elements are considered incompatible. The partition coefficient for different phases (minerals) can

vary widely for an individual element. A mantle rock will typically be composed of several minerals in varying proportions, each with (potentially) different partition coefficients for each element. A bulk partition coefficient for an element can be calculated for a given rock by a summation of the individual mineral-melt partition coefficients weighted by abundance:

$$\overline{D_i} = \sum_{\phi} m_{\phi} D_i^{\phi/l} \qquad \text{D.3}$$

where m is the molar mass fraction of phase ϕ.

Partition coefficients are measured on both natural and experimental samples. Naturally derived samples are, as the name suggests, geologic rock samples collected from outcrops that contain solid (i.e., mineral) and melt (i.e., glass) phases thought to be in equilibrium. The concentration of trace element i is measured analytically in each phase, typically by secondary ion mass spectrometry (SIMS), and ratioed to produce the final partition coefficient. In contrast, experimentally derived samples are produced in a laboratory by equilibrating a composition of interest at a pressure and temperature (and oxygen fugacity, f_{O_2}) of interest. Analytical methods and partition element calculation techniques for experimental charges are essentially identical to natural samples. With data derived from laboratory experiments, it is possible to more tightly control the system, and thus determine the degree to which each factor is responsible for certain partitioning behaviors within the system. Regardless, the natural system provides the range and breadth of complexity to address experimentally. Despite the abundance of analytical data on natural mineral-melt pairs, controlled laboratory experiments have taken root as the de facto method of choice for geochemical and petrologic modeling, particularly with the construct of readily accessible online databases (i.e., PetDB, Lehnert et al., 2000; LEPR, Hirschmann et al., 2008). The construction of a similar database for partition

coefficients measured from published igneous phase equilibrium is currently underway (M. M. Hirschmann personal communication, 2007).

Geochemical and petrologic modeling makes extensive use of trace elements as controls on physical and chemical processes unobservable at the surface. As such, the understanding of how partitioning functions is of great interest. Despite the great quantity of published partition coefficients from natural and experimental mineral-melt pairs, certain limitations are implicitly built in to these results. Most notable of these limitations is the fact that a mineral-melt pair provides information on partitioning only at the single pressure (P), temperature (T), and composition (X) of the sample, which cannot always be tightly constrained. Therefore, to understand partitioning across the complete Earth system, it would be necessary to conduct experiments at every pressure, temperature, and composition.

Alternatively, the parameterization of known information about partitioning from experiments and natural samples can provide further insight into the mechanisms responsible for partitioning. If P, T, and X are the dominant factors controlling partitioning between solid and melt phases, a thermodynamic basis must underlie these parameters. Indeed, it can be readily shown that for an ideal solution at equilibrium:

$$D_i = \exp\left(\frac{-\Delta G_i^o}{RT}\right) \qquad \text{D.4}$$

where ΔG^o is the Gibbs free energy, R is the gas constant, and T is temperature in Kelvins. This relationship is quite similar to the equilibrium constant. Goldschmidt (1937) proposed several qualitative rules regarding the substitution of ions in a crystal lattice based on empirical observation, focusing on charge and ionic radii. These rules can be condensed into the concept of lattice strain energy, or the energy penalty required for a lattice to accommodate a substituted ion of different size and/or charge.

This energy is related to the Gibbs free energy of reaction. As an example, we can consider the formation of diopside (Appendix E) containing a metal ion M^{2+} in the dodecahedral $^{VIII}M2$ site normally occupied by Ca^{2+} by formulating the crystallization of diopside:

$$CaO^{l} + MgO^{l} + 2SiO_2 \rightleftarrows CaMgSi_2O_6 \qquad \text{D.5}$$

and the exchange of M^{2+} for Ca^{2+}

$$M^{l} + CaMgSi_2O_6 \rightleftarrows Ca^{l} + MMgSi_2O_6 \qquad \text{D.6}$$

The combined Gibbs free energy change of the system is thus

$$\Delta G_r = \Delta G_{ex}^{M-Ca} - \Delta G_{melt}^{Di} \qquad \text{D.7}$$

The first term is the energy associated with transferring M^{2+} from the melt into the crystal lattice site and transferring Ca^{2+} from the lattice site to the melt. The second term involves the melting of the diopside and governs the partitioning of Ca between diopside and the melt. The partition coefficient for element M thus depends on this Gibbs free energy difference:

$$D_M^{Di/l} = \exp\left(\frac{\Delta G_{melt}^{Di} - \Delta G_{ex}^{M-Ca}}{RT}\right) \qquad \text{D.8}$$

As the first term governs the distribution of Ca between the diopside crystal and the melt, and substituting Ca for itself imparts no strain on the lattice, the term is of the same form as equation x.4 and can be removed outside the exponential. The exchange term is dominated by the substitution of M^{2+} for Ca^{2+}, with the incompressible and non-rigid melt contributing negligible strain to the energy balance (Beattie, 1994; Blundy and Wood, 1994), thus allowing the approximation of the Gibbs free energy of the exchange term as the Gibbs free energy of the strain. Brice (1975) empirically determined that the strain energy, ΔG_{strain}, could be calculated from:

$$\Delta G_{strain} = 4\pi E N_A \left[\frac{r_0}{2}\left(r_M - r_0\right)^2 + \frac{1}{3}\left(r_M - r_0\right)^3\right] \qquad \text{D.9}$$

where E is the effective Young's Modulus for the lattice site of interest, a measure of the elasticity of a material, N_A is Avogadro's Number, r_0 is the optimal radius of the lattice site, and r_M is the ionic radius of element M. All together:

$$D_M^{Di/l} = D_{Ca}^{Di/l} \exp\left(\frac{\Delta G_{strain}^{M-Ca}}{RT}\right) = D_{Ca}^{Di/l} \exp\left(\frac{-4\pi E N_A \left[\frac{r_0}{2}\left(r_M - r_0\right)^2 + \frac{1}{3}\left(r_M - r_0\right)^3\right]}{RT}\right) \quad \text{D.10}$$

or, more generally, the equation can be written as:

$$D_i^{s/l} = D^0 \exp\left(\frac{-4\pi E N_A \left[\frac{r_0}{2}\left(r_M - r_0\right)^2 + \frac{1}{3}\left(r_M - r_0\right)^3\right]}{RT}\right) \quad \text{D.11}$$

where D^0 is the partition coefficient of an ion of radius r_0 that has the same charge as i and enters the lattice site without strain (Blundy and Wood, 1994). Nasagawa (1966) derived a similar empirical formulation for strain energy. Like that of Brice (1975), this derivation involved r_0, r_M, the bulk modulus, and Poisson's ratio (where the latter two are together proportional to Young's Modulus, E). The two derivations produce similar results, though the Nasagawa formulation is mathematically less elegant. Figure D.1 illustrates both the strong non-linearity of the relationship between the ionic radius and the partition coefficient (Onuma et al., 1968), and the interrelationships between the three principal variables: D^0, r_0, and E. D^0 is the apex of the parabaloid and corresponds to the optimal value of r_0 (most compatible), with D-values decreasing (more incompatible) as r_M increases away from r_0. The effective Young's Modulus controls the width of the parabola, with larger values of E (stiffer lattice) creating a narrower parabola, and thus smaller values of D^0 (more incompatible) at a given r_0. More advanced formulations of Equation D.11 have since been developed for clinopyroxene (Wood and Blundy, 1997) and garnet (van

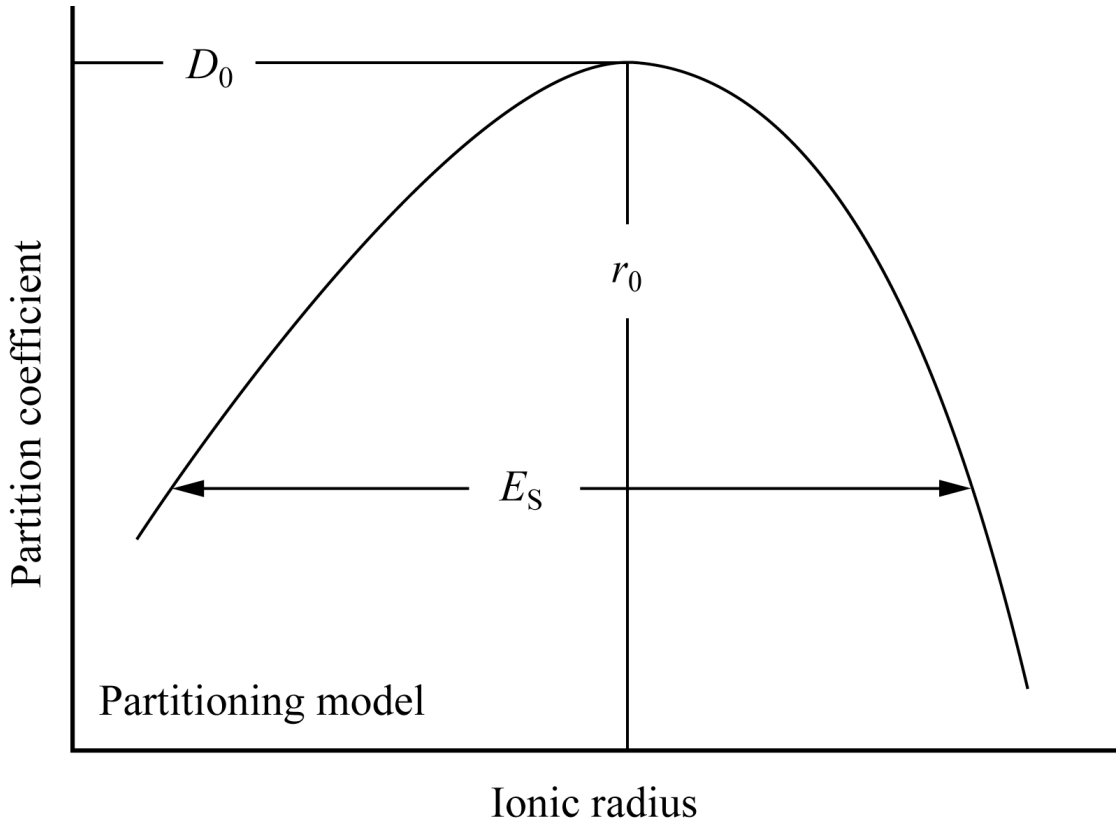

Figure D.1 Cartoon illustrating the non-linearity relationship between ionic radius and partition coefficient. This relationship can be summarized by three variables: r_0, the optimal radius of a fictive element that fits in a given mineral lattice site. D_0, the most compatible element that fits in the fictive r_0 lattice site. And E_S, the Young's Modulus, measure of elasticity, for the fictive element. Incompatibility increases as the radius of an element is both increased and decreased from this radius.

Westrenen et al., 1999; Draper and van Westrenen, 2007; van Westrenen and Draper, 2007) that use parameterized experimental results to predict E, D^0, and r_0 for common trace element valencies from major element compositions of minerals and melts.

Other formulations for partitioning have been developed, and one will be briefly considered here. Gallahan and Nielsen (1992) parameterized partition coefficients for mafic to intermediate lavas (47.7 – 54.5 wt. % SiO_2) using the two-lattice model of Bottinga and Weill (1972) originally modified by Nielsen and Dungan (1983) to model partitioning as a function of silicate melt component activities. This method incorporates the major element composition of the silicate melt as a whole into the activities of the individual components in the form of network formers (SiO_2, Na_2O, and K_2O) and network modifiers (Al_2O_3, CaO, MgO, FeO, P_2O_5, TiO_2, MnO, and Cr_2O_3). From partitioning experiments on Sc, Y, and REE between clinopyroxene and melt over a range of initial compositions but nearly constant temperature, Gallahan and Nielsen (1992) observed an inverse relation between the activities of SiO_2 and Al_2O_3 in the melt and the equilibrium constant which related to the degree of polymerization and depolymerization by the network formers and modifiers, respectively. The equilibrium constant was in turn parameterized against temperature as ln$K$ versus 1/T, producing a linear relationship between composition and temperature.

Until recently, trace element modeling was conducted almost exclusively using single partition coefficients for each element. These partition coefficients are carefully chosen from high-quality natural or experimental samples at similar pressure, temperature, and composition to the model system. This single partition coefficient is then used throughout the modeled parameters, be it crystallization or melting, and can be considered as "static" as the coefficient does not change. However, it is well known that mineral and melt compositions evolve as a system undergoes

crystallization, melting, or experiences changes in pressure and/or temperature (e.g., Bowen, 1913). Partition coefficients for minerals formed in equilibrium with melt of different compositions can vary from a factor of 2 to more than an order of magnitude. For example, Pertermann et al. (2004) found D_{La} = 0.027 for a clinopyroxene in equilibrium with a basaltic andesite liquid (SiO_2 = 55.65 wt. %; Mg# = 49.3; sample A343), whereas Adam and Green (1994) found D_{La} = 0.28 for a high Ti-Al clinopyroxene in equilibrium with a basanitic liquid (SiO_2 = 44.48 wt. %; Mg# = 51.1; sample 1450)[15]. Modeling the evolution of partition coefficients may contribute toward resolution in areas of longstanding debate, such as the melting effects on relative U and Th incompatibility in mantle minerals on U-series disequilibria (e.g., Salters and Longhi, 1999), and further demonstrates the need for accurate partitioning models that accommodate the dynamic nature of evolving systems and reflect the underlying properties. However, the requirement for mineral and melt major element composition data has somewhat complicated the usage of these formulations and principally limited their application to experimental studies.

The development of advanced thermodynamic algorithms during the past decades (e.g., MELTS, THERMOCALC, and Perple_X; Ghiorso and Sack, 1995; Powell and Holland, 1988; Connolly and Petrini, 2002) has facilitated sophisticated geochemical and petrologic modeling of mantle processes. The synthesis of thermodynamic algorithms with predictive trace element partitioning is a seemingly natural association. Smith and Asimow (2005) successfully integrated the dynamic partitioning of trace elements in garnet, clinopyroxene, and feldspar (see references therein) with the MELTS and pMELTS algorithms, presented as the Adiabat_1ph interface. This application allows the direct calculation of partition coefficients

[15] Lanthanum partition coefficient data taken from GERM database: http://earthref.org/GERM/

directly from the mineral chemistry of the equilibrium assemblages. Moreover, this allows the partition coefficients to evolve as the mineral chemistry evolves, reflecting changes in the system relating to common petrogenetic processes such as melting, crystallization, and assimilation. Potentially limiting the applicability of the predictive models at present, these types of partitioning models have not been formulated for all of the common mantle minerals (e.g., orthopyroxene, olivine) and elements (e.g., high field strength elements). Furthermore, the predictive ability of the equations are highly dependent upon the accuracy of the solid phase compositions, and both MELTS and pMELTS are known to have temperature offsets (Hirschmann et al., 1998; Ghiorso et al., 2002), providing additional uncertainty. Due largely to the absence of a fully quantitative model for the HFSE (van Westrenen et al., 2001), modeling in this work for Mauritius will not utilize these formulations for trace element modeling. The lack of an implemented parameterization for the HFSE (and other static partition coefficients) may produce potentially spurious ratios between ratios of elements dynamic and static elements. However, the integration of trace element partitioning into these types of major elements models can provide insight into many potential problems and has many advantages, and should not be abandoned.

APPENDIX E

CRYSTALLOGRAPHIC DATA OF EARTH MINERALS

Crystallographic Data of Earth Minerals

Here, crystallographic data is presented for earth materials discussed in the body of this thesis. In the geosciences, a mineral can be defined as a naturally occurring crystalline solid with a definite, but not necessarily fixed, chemical composition. The minerals of the solid earth[16] are predominantly silicate based, and are built from the silica tetrahedron (SiO_4^{4-}). The basic structural silicate groups include the orthosilicates (nesosilicates) in which no oxygen anions are shared; the disilicates (sorosilicates) share a single O^{2-} between two silicate tetrahedra; the ring silicates (cyclosilicates) share two O^{2-} each and form rings, usually with six tetrahedral; the chain silicates (inosilicates) can share two O^{2-} per tetrahedra and form a single chain, or two single chains can be joined together by some tetrahedral sharing three O^{2-} and some sharing two; the sheet silicates (phyllosilicates) share three O^{2-} per tetrahedra in a plane to form continuous sheets; and the framework silicates (tectosilicates) which share all four O^{2-} with adjacent tetrahedra to form a three-dimensional framework. Other common classes of Earth minerals include oxides (*e.g.*, rutile, TiO_2), sulfates (*e.g.*, anhydrite, $CaSO_4$), carbonates (*e.g.*, calcite, $CaCO_3$), and phosphates (*e.g.*, apatite, $Ca_5(PO_4)_3(OH, F, Cl)$).

Minerals are presented below by common name with solid-solution end-members (where appropriate). Crystallographic data is taken from the American Mineralogist Crystal Structure Database[17], webmineral.com, and mindat.org, and unit cell diagrams are from webmineral.com.

[16] The solid earth is a combined term for the crust and mantle (both upper and lower), and excludes the solid inner core, a Fe-Ni alloy.
[17] http://rruff.geo.arizona.edu/AMS/amcsd.php

Garnet

The garnet group forms orthosilicate minerals and has the general formula $X_3^{VIII}Y_2^{VI}Z_3^{IV}O_{12}$. The Z cations in the tetrahedra are most commonly Si^{4+}, although Al^{3+} can substitute. X cations occupy the large dodecahedral M2-site, which is commonly filled by Ca^{2+}, Mg^{2+}, and Fe^{2+}. The trivalent rare earth elements are believed to substitute in the X-site. Trivalent Al usually fills the smaller octahedral Y-site, and this site it believed to be the site of quadrivalent HFSE (e.g., Zr and Hf) substitution. Garnets with Al in the Y-site are referred to as "pyralspite" and include *pyr*ope, *al*mandine, and *sp*essartine.

Almandine (Figure E.1)

- Chemical formula: $Fe^{2+}{}_3Al_2Si_3O_{12}$
- Space group: Ia3d
- Unit cell: a = 11.526 Å, Z = 8

Grossular (Figure E.2)

- Chemical formula: $Ca_3Al_2Si_3O_{12}$
- Space group: Ia3d
- Unit cell: a = 11.851 Å, Z = 8

Pyrope (Figure E.3)

- Chemical formula: $Mg_3Al_2Si_3O_{12}$
- Space group: Ia3d
- Unit cell: a = 11.459 Å, Z = 8

Spessartine (Figure E.4)

- Chemical formula: $Mn_3Al_2Si_3O_{12}$
- Space group: Ia3d
- Unit cell: a = 11.621 Å, Z = 8

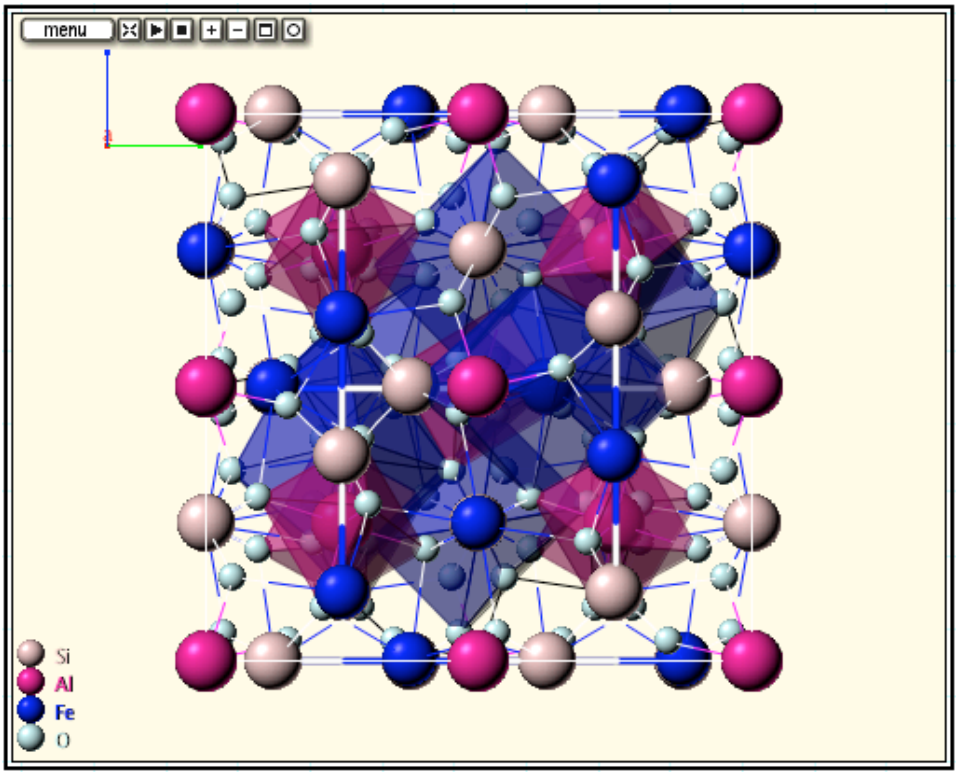

Figure E.1. Unit cell structure of Almandine (data for sample A1 of Novak and Gibbs, 1973).

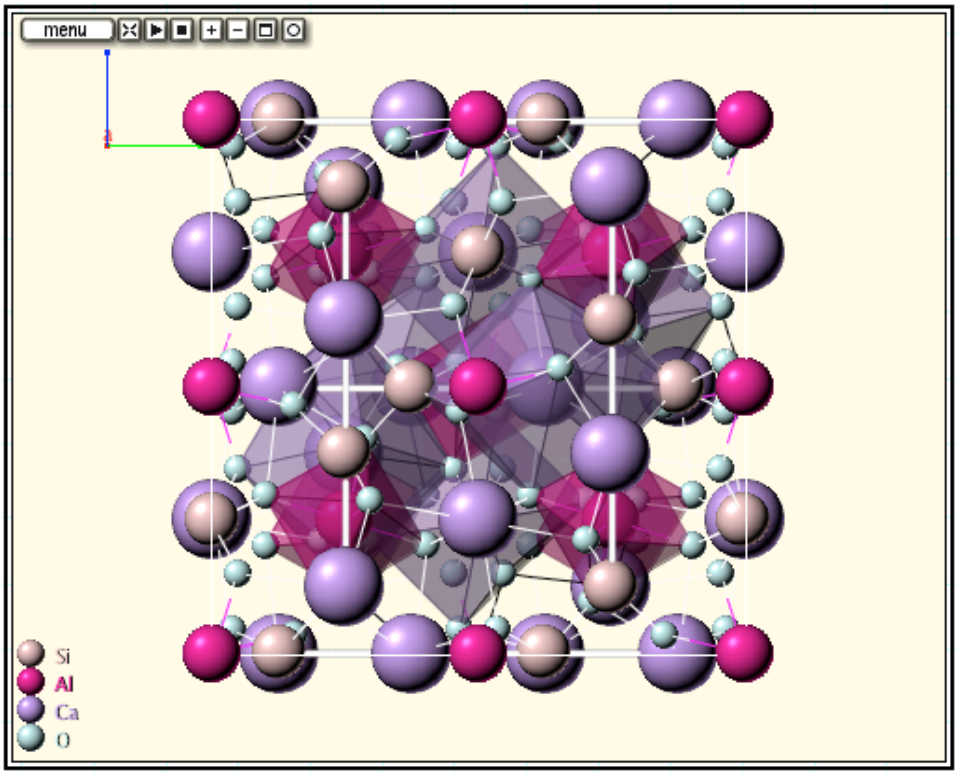

Figure E.2. Unit cell structure of Grossular (data for sample Mn-Gr of Novak and Gibbs, 1973).

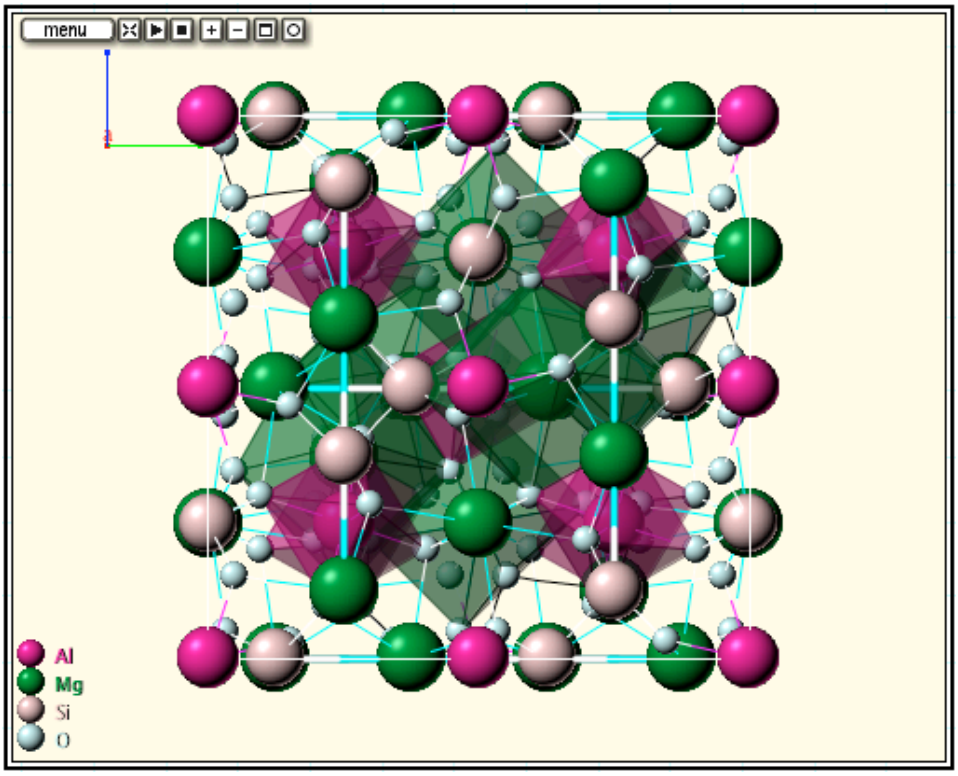

Figure E.3. Unit cell structure of Pyrope (data for refinement D of Gibbs and Smith, 1965).

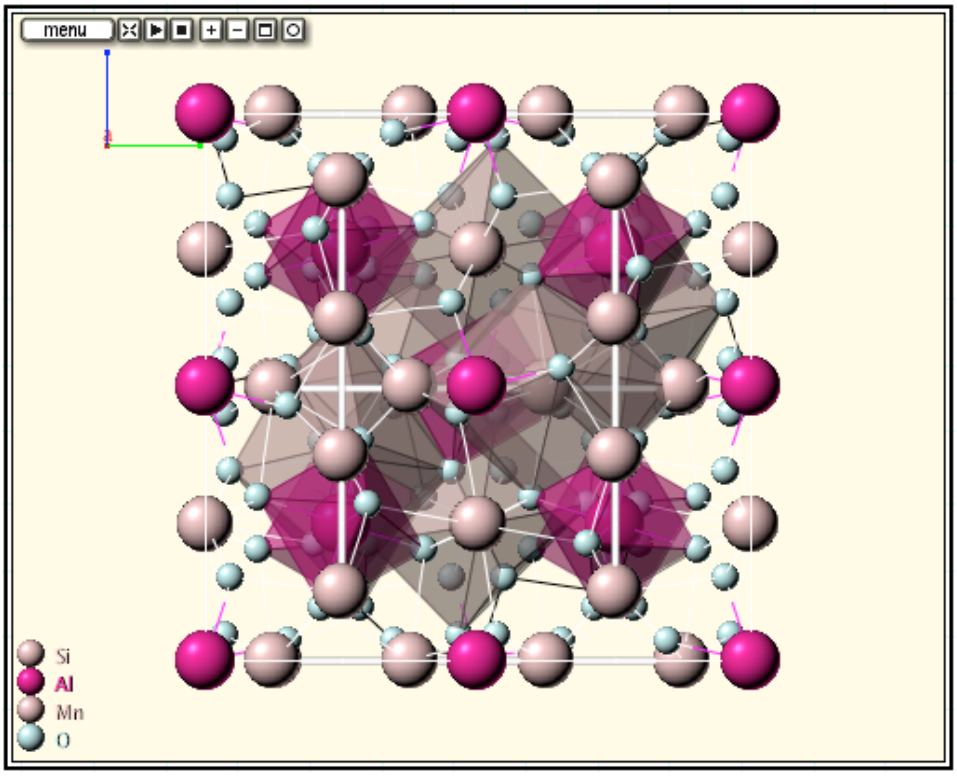

Figure E.4. Unit cell structure of Spessartine (data for sample Mn-Gr of Novak and Gibbs, 1973).

Olivine

The olivine group forms orthosilicates minerals and has the general formula X_2SiO_4. The Si-tetrahedra share oxygen with adjacent octahedral, but not with other tetrahedra. The X-sites are composed of distorted edge sharing M1-sites that form chains parallel to the *c*-axis, and less distorted M2-sites attached to these chains. Divalent Mg and Fe fill the X-site, with such little substitution that the system may be treated as a simple Mg-Fe solid solution.

Fayalite (Figure E.5)

- Chemical formula: $Fe^{2+}{}_2SiO_4$
- Space group: Pbnm
- Unit cell: a = 4.76 Å, b = 10.2 Å, c = 5.98 Å, Z = 4

Forsterite (Figure E.6)

- Chemical formula: Mg_2SiO_4
- Space group: Pbnm
- Unit cell: a = 4.756 Å, b = 10.195 Å, c = 5.981 Å, Z = 4

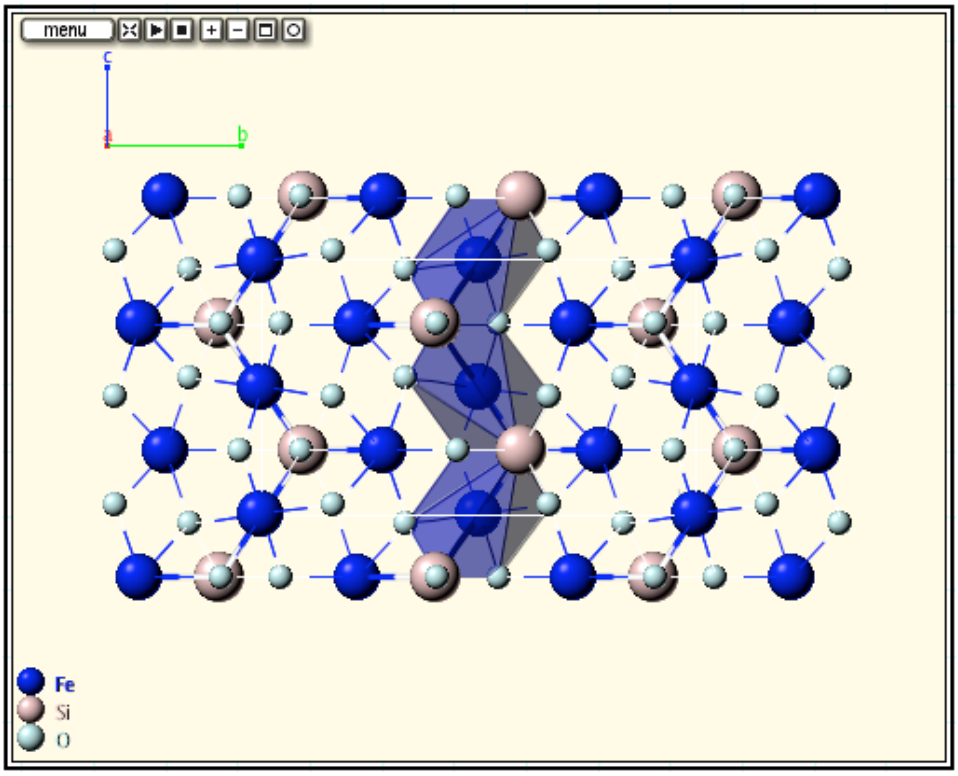

Figure E.5. Unit cell structure of Fayalite (data of Birle et al., 1968).

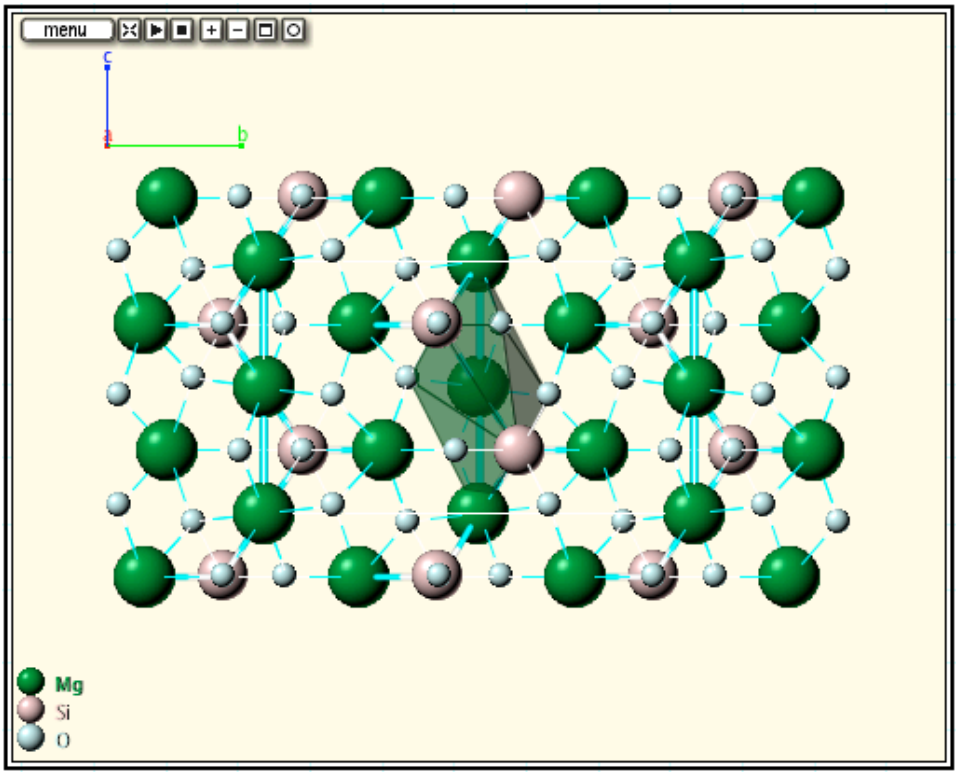

Figure E.6. Unit cell structure of Forsterite (data of Birle et al., 1968).

Epidote

Epidote is a disilicate mineral and has the general formula $A_2M_3(O(OH)(SiO_4)(Si_2O_7)$. The M1 and M2 sites contain dominantly $Al^{3=}$, while the M3 site can absorb up to about 35% Fe^{3+}. The epidote group of minerals has two different chains of octahedral. One is a simple edge-sharing chain of M1 octahedra with additional M3 octahedra attached on alternate sides along its length. The M2 sites in the simple chain usually contain only Al. In the M1-M3 chain the M1 sites are usually occupied by Al, and the M3 sites by non-AL cations. The two chains are arranged in an alternating fashion and extend parallel to the *b* axis. These chains are linked laterally through both single (SiO4) and double (Si2O7) tetrahedra that both share oxygen anions with the octahedral. This arrangement produces cavities (A-sites) with distorted 7- to 11-fold coordination for larger cations, usually Ca.

Epidote (Figure E.7)

- Chemical formula: $Ca_2Al_2(Al, Fe^{3+})O(OH)(SiO_4)(SiO_7)$
- Space group: $P2_1/m$ (monoclinic)
- Unit cell: $a = 8.98$ Å, $b = 5.64$ Å, $c = 10.22$ Å, $\beta = 115.4$, $Z = 2$

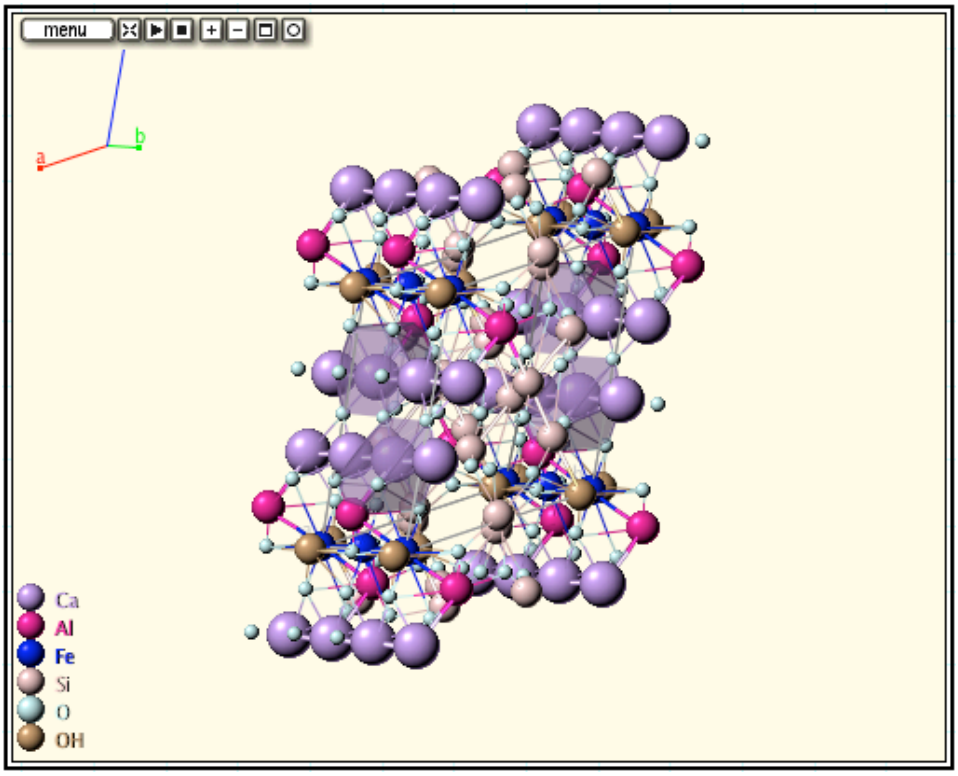

Figure E.7. Unit cell structure of Epidote (data of Ito, 1947).

Beryl

Beryl is a ring silicate whose structure is based on 6-fold rings of silicon and aluminum tetrahedra that are stacked atop each other for form columns parallel to the *c* axis. Adjacent columns of 6-fold rings are cross-linked through other cations. Beryllium occupies distorted 4-fold sites formed by oxygen anions from adjacent columns of rings and links the rings laterally and vertically. Aluminum occupies distorted 6-fold sites formed by oxygen anions from three adjacent columns of rings.

Beryl (Figure E.8)

- Chemical formula: $Al_2Be_3Si_6O_{18}$
- Space group: P6/mmc (hexagonal)
- Unit cell: $a = 9.215$ Å, $c = 9.192$ Å, $Z = 2$

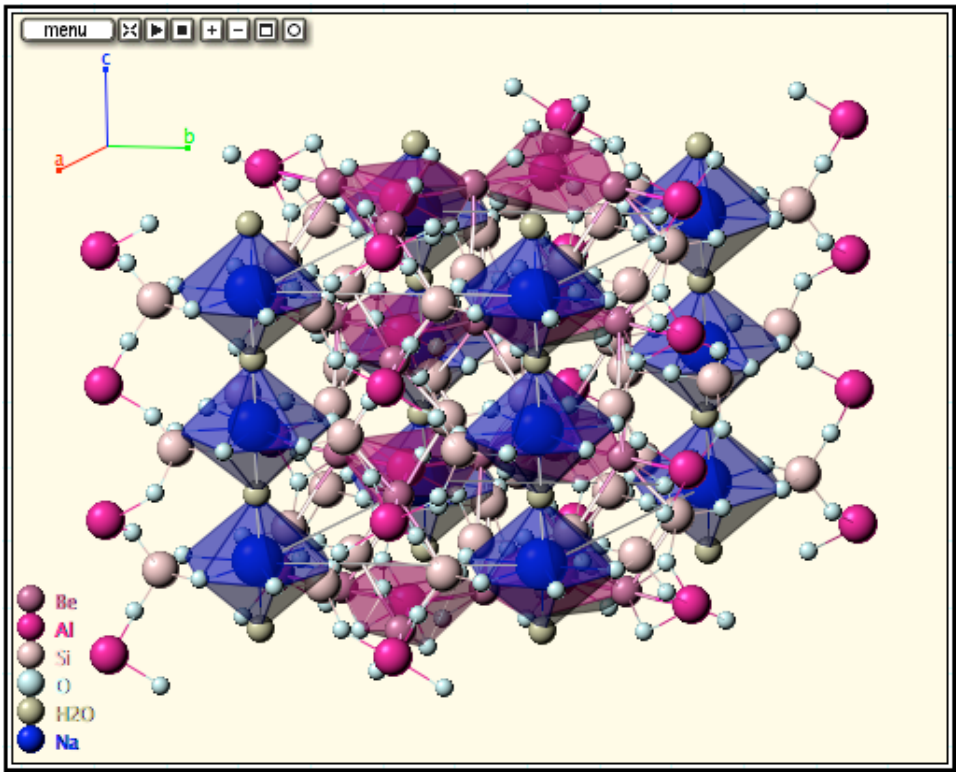

Figure E.8. Unit cell structure of Beryl (data for sample T = 24 °C before heating of Brown and Mills, 1986).

Clinopyroxene

The clinopyroxene group forms inosilicates (single chain) minerals and has the general formula $X^{VIII}Y^{VI}Z_2^{IV}O_6$. The Z cations in the tetrahedra are most commonly Si^{4+}, although Al^{3+} can substitute. X cations occupy the dodecahedral M2-site, which is commonly filled by Ca^{2+} in many mantle clinopyroxene compositions, though Na+ can substitute. The trivalent rare earth elements are believed to substitute in the M2-site. The octahedral M1-site (Y) is usually filled by Mg^{2+} and Fe^{2+}, though trivalent Fe^{3+} and Al^{3+} can also fill this site. Clinopyroxene has monoclinic symmetry.

Augite (Figure E.9)

- Chemical formula: (Ca, Na)(Mg, Fe, Al, Ti)(Si, Al)$_2$O$_6$
- Space group: C 2/c
- Unit cell: a = 9.750 Å, b = 8.902 Å, c = 5.274, β = 106.02°, Z = 4

Diopside (Figure E.10)

- Chemical formula: $CaMgSi_2O_6$
- Space group: C 2/c
- Unit cell: a = 9.761 Å, b = 8.926 Å, c = 5.258, β = 105.8°, Z = 4

Omphacite (Figure E.11)

- Chemical formula: (Ca, Na)(Mg, Fe^{2+}, Al)Si_2O_6
- Space group: P 2/n
- Unit cell: a = 9.585 Å, b = 8.776 Å, c = 5.26, β = 106.85°, Z = 4

Spodumene (Figure E.12)

- Chemical formula: $LiAlSi_2O_6$
- Space group: C 2/c
- Unit cell: a = 9.52 Å, b = 8.32 Å, c = 5.25, β = 110.3°, Z = 4

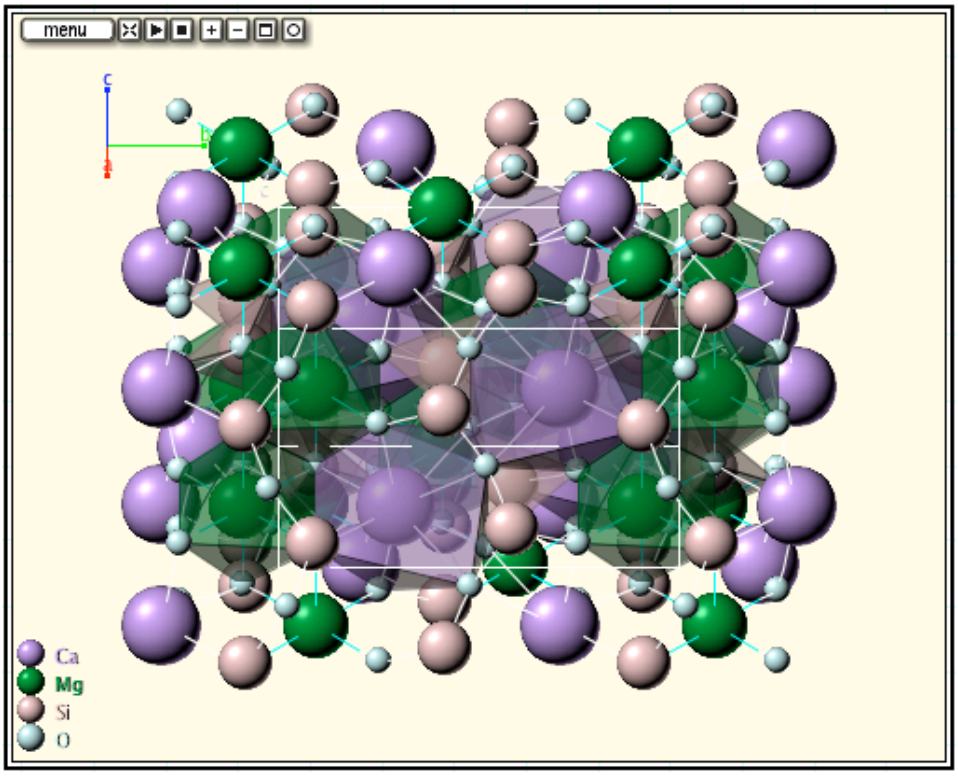

Figure E.9. Unit cell structure of Augite (Gualtieri, 2000).

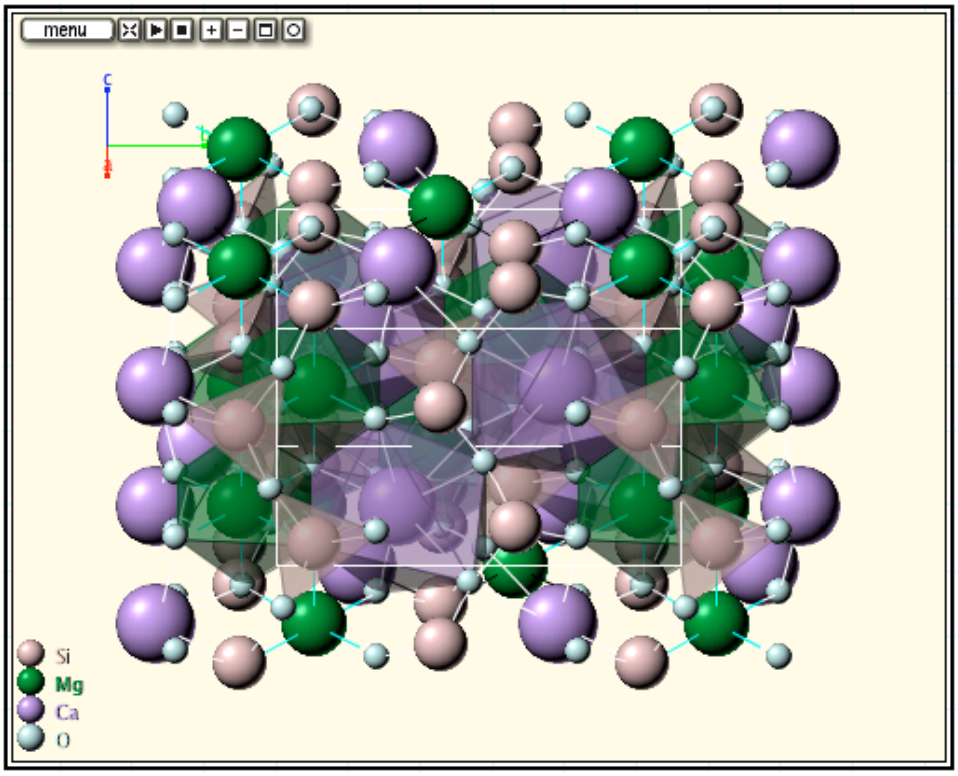

Figure E.10. Unit cell structure of Diopside (data for T = 24 °C pyroxene of Cameron et al., 1973).

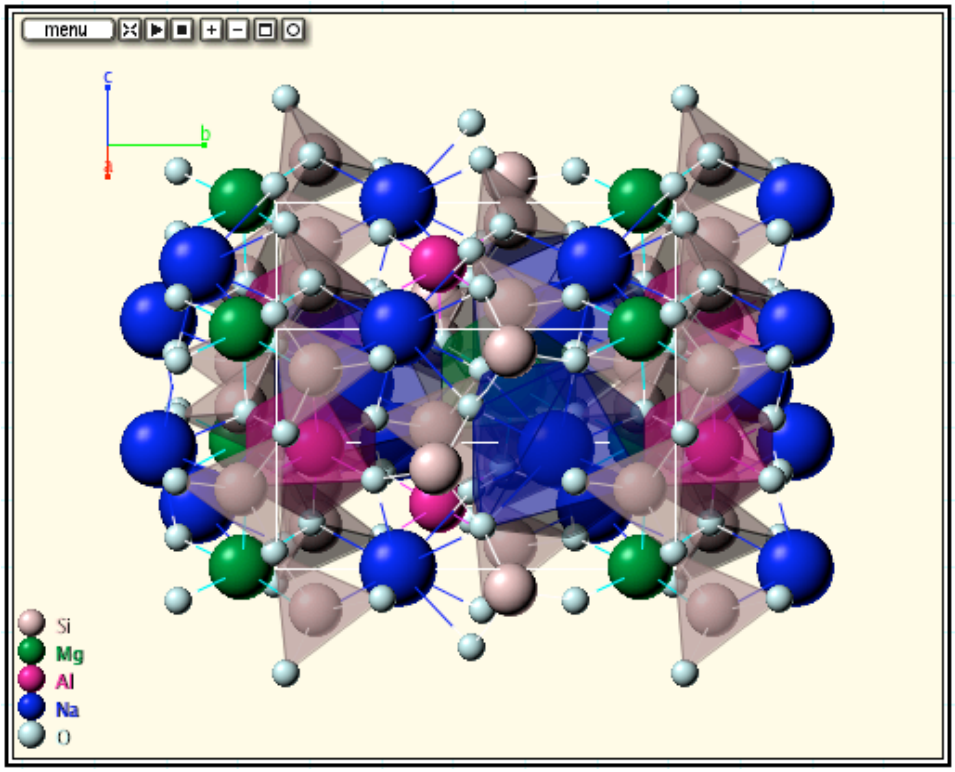

Figure E.11. Unit cell structure of Omphacite (data of Clarke and Papike, 1968).

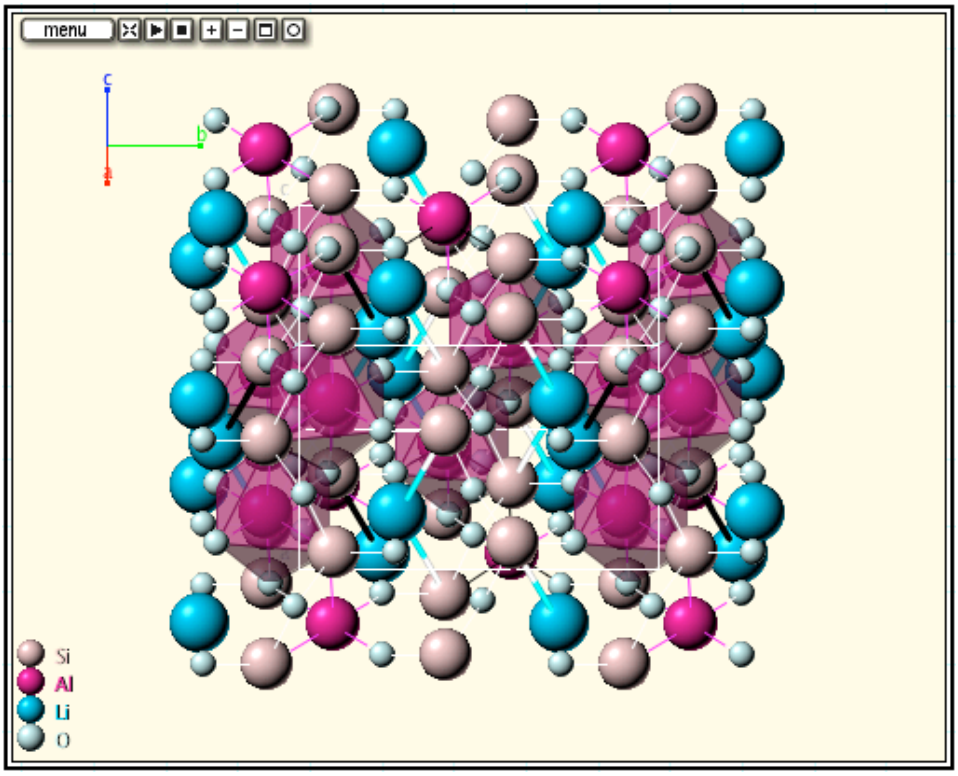

Figure E.12. Unit cell structure of Spodumene (data for T = 24 °C pyroxene of Cameron et al., 1973).

Orthopyroxene

Minerals in the orthopyroxene group form inosilicates (single chain) minerals and have the general formula $X^{VIII}Y^{VI}Z_2{}^{IV}O_6$. The principal chemical variation is substation of Mg and Fe in the M1 (X) and M2 (Y) sites. As opposed to clinopyroxene, orthopyroxene has orthorhombic symmetry.

Enstatite (Figure E.13)

- Chemical formula: $Mg_2Si_2O_6$
- Space group: Pbca
- Unit cell: a = 18.228 Å, b = 8.805 Å, c = 5.185 Å, Z = 8

Ferrosilite (Figure E.14)

- Chemical formula: $(Fe^{2+}, Mg)_2Si_2O_6$
- Space group: Pbca

  Unit cell: a = 18.418 Å, b = 9.078 Å, c = 5.237 Å, Z = 8

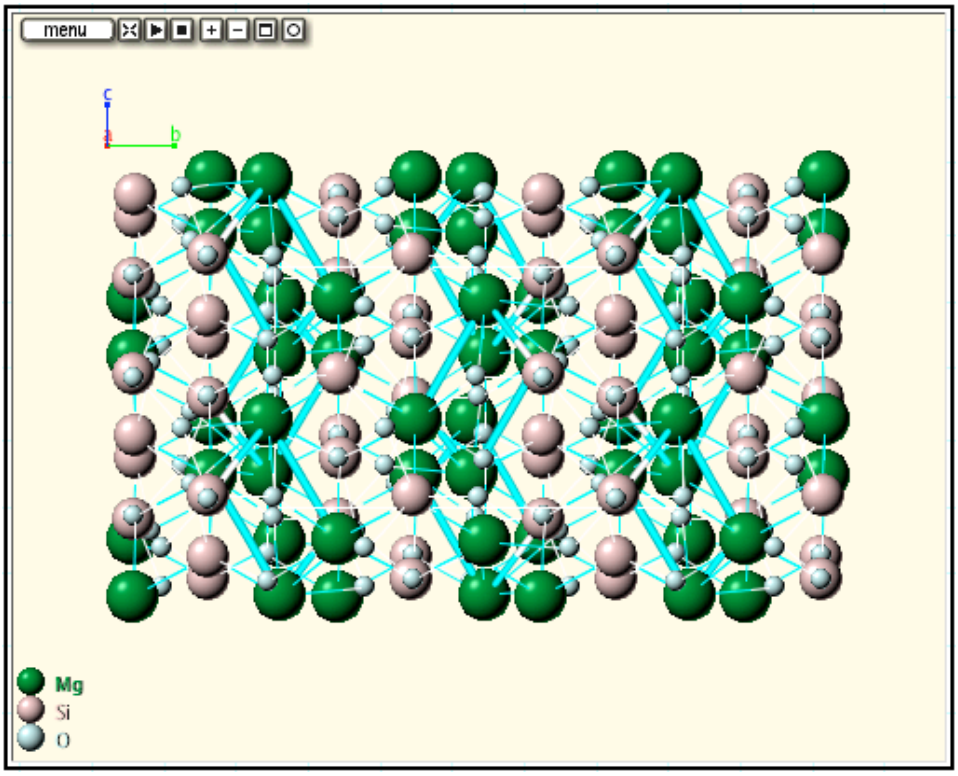

Figure E.13. Unit cell structure of Enstatite (data of Carlson et al., 1988).

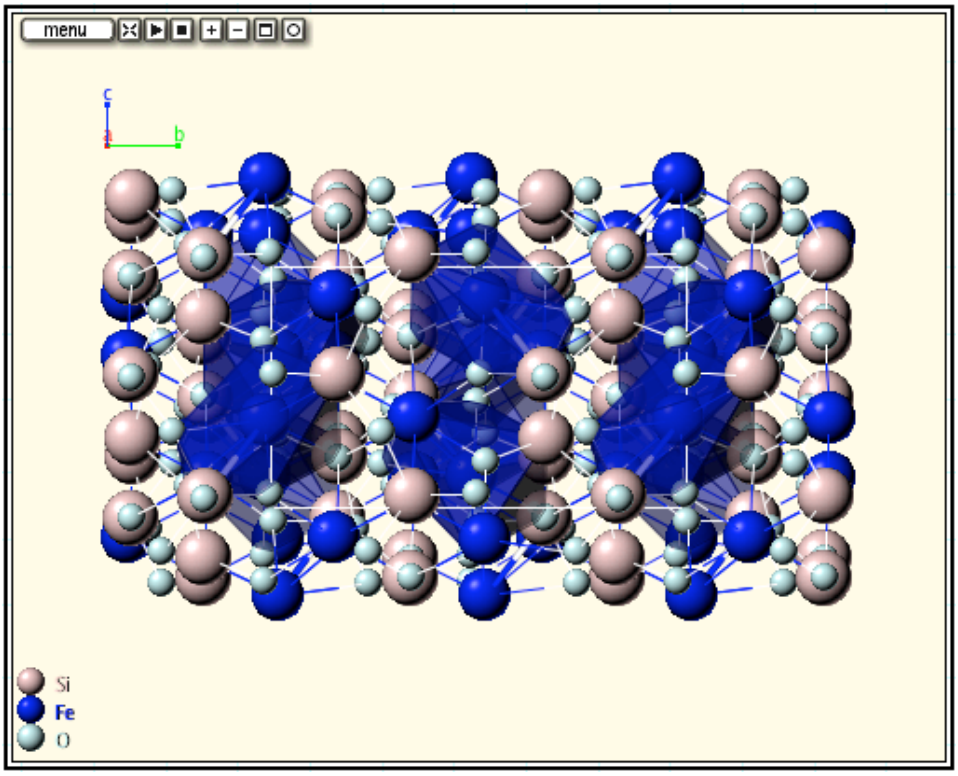

Figure E.14. Unit cell structure of Ferrosilite (data of Burnham et al., 1971).

Biotite

Biotite is a sheet silicate with a *TOT* + *c* structure. That is, biotite is composed of stacks of two *T*etrahedral sheets and one *O*ctahedral sheet. These three layer stacks are separated and bonded to other stacks by interlayer *c*ations. The tetrahedral sheets consist of tetrahedrally coordinated Si^{4+}, Al^{3+}, and sometimes Fe^{3+}. These tetrahedra are arranged in a mesh of 6-fold rings so that three O^{2-} on each tetrahedra are shared with adjacent tetrahedra. The octahedral sheets consist of two planes of OH^- anionic groups with Fe^{2+} and Mg^{2+} commonly filling the octahedral sites created between the hydroxyls. The interlayer cations are situated in the center of the tetrahedra rings in the tetrahedral sheets.

Biotite (Figure E.15)

- Chemical formula: $K(Fe, Mg)_3AlSi_3O_{10}(OH)_2$
- Space group: C2/m
- Unit cell: $a = 5.34$ Å, $b = 9.26$ Å, $c = 10.23$ Å, $\beta = 100.26°$, $Z = 4$

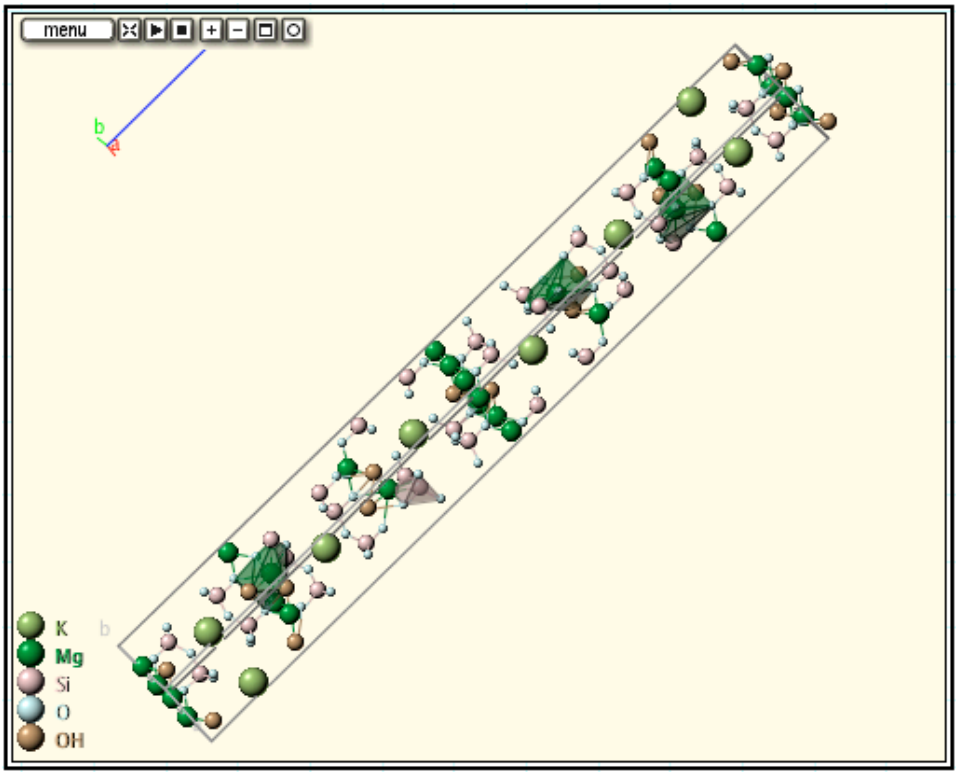

Figure E.15. Unit cell structure of Biotite (data of Hendricks and Jefferson, 1939).

Feldspar

The feldspar group is a part of the framework silicate class of minerals and is comprised of three compositional end members: anorthite, albite, and alkali feldspar. Solid solutions exist between anorthite and albite, and albite and alkali feldspar. The feldspars consist of a framework of corner sharing Si and Al tetrahedra. The tetrahedra are arranged to form four member rings with the apex of two tetrahedra pointing "up" and two "down", relative to the *a* axis. The rings are joined to other rings by sharing oxygens to form crankshaft-like chains that extend parallel to *a*. These crankshafts are joined to others by sharing the remaining oxygen anions. Large sites thus exist between the chains for Ca^{2+}, Na^{+}, and K^{+}, which are coordinated with 9 oxygens. Both solid-solutions can experience exsolution.

Anorthite (Figure E.16)

- Chemical formula: $CaAl_2Si_2O_8$
- Space group: P1barI1bar (triclinic)
- Unit cell: a = 8.177 Å, b = 12.877 Å, c = 141.16 Å, α = 93.166°, β = 115.85°, γ = 91.216° Z = 8

Albite (Figure E.17)

- Chemical formula: $NaAlSi_3O_8$
- Space group: C1bar (triclinic)
- Unit cell: a = 5.34 Å, b = 9.26 Å, c = 10.23 Å, β = 100.26°, Z = 4

Alkali feldspar (Figure E.18)

- Chemical formula: $KAlSi_3O_8$
- Space group: C2/m (monoclinic)
- Unit cell: a = 8.625 Å, b = 12.996 Å, c = 7.19 Å, β = 116.0°, Z = 4

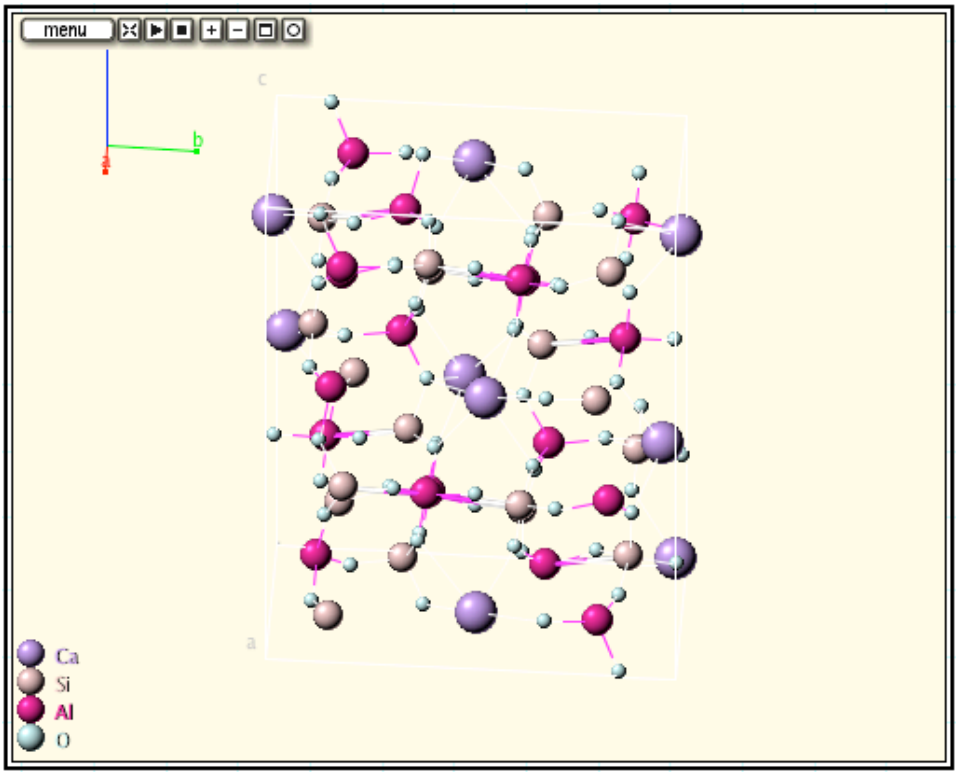

Figure E.16. Unit cell structure of Anorthite (data for T = 410 °C of Foit and Peacor, 1973).

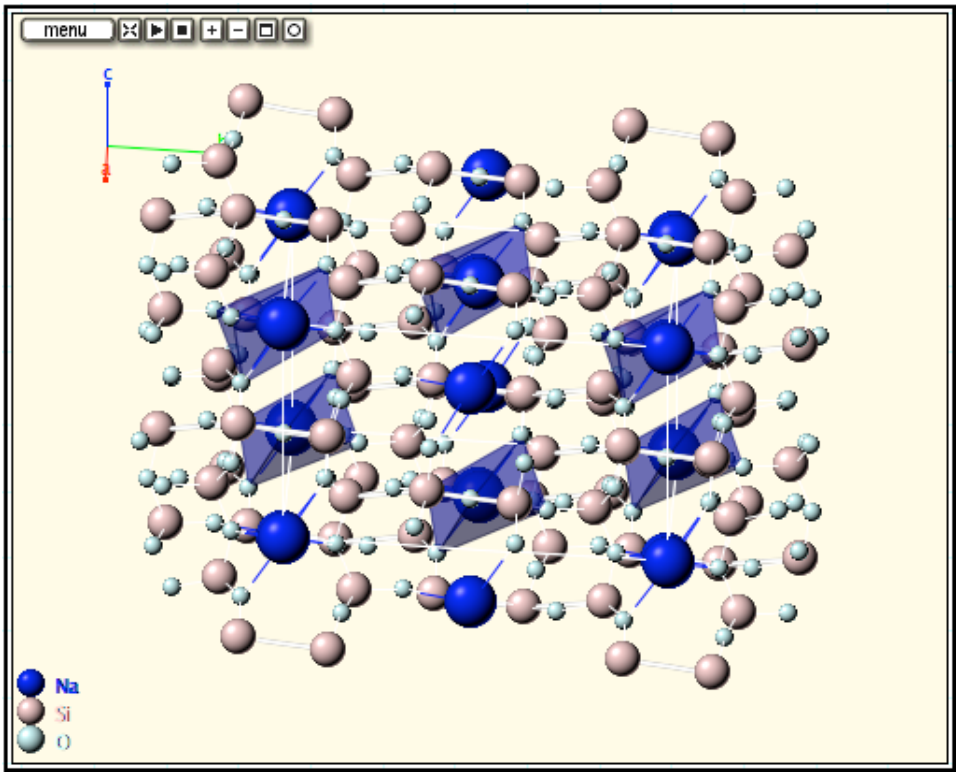

Figure E.17. Unit cell structure of Albite (data for T = 24 °C feldspar of Prewitt et al., 1976).

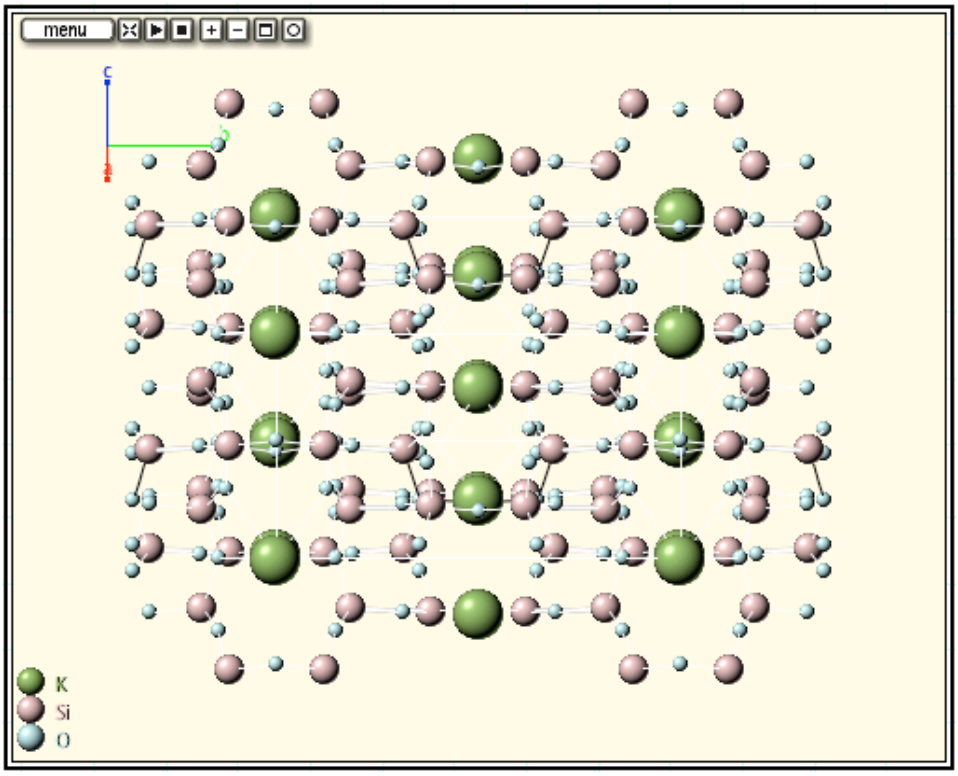

Figure E.18. Unit cell structure of Alkali feldspar (Colville and Ribbe, 1968).

Spinel

The spinel group of ferromagnesian oxide minerals is composed of a solid-solution of aluminous oxide (spinel) and chrome-rich oxide (chromite). The system has a general formula of $X^{IV}Y_2{}^{VI}O_4$. The structure is based on cubic close-packed oxygen.

Spinel (Figure E.19)

- Chemical formula: $(Fe,Mg)Al_2O_4$
- Space group: Fd3m
- Unit cell: a = 8.08 Å, Z = 8

Chromite (Figure E.20)

- Chemical formula: $(Fe,Mg)Cr_2O_4$
- Space group: Fd3m
- Unit cell: a = 8.36 Å, Z = 8

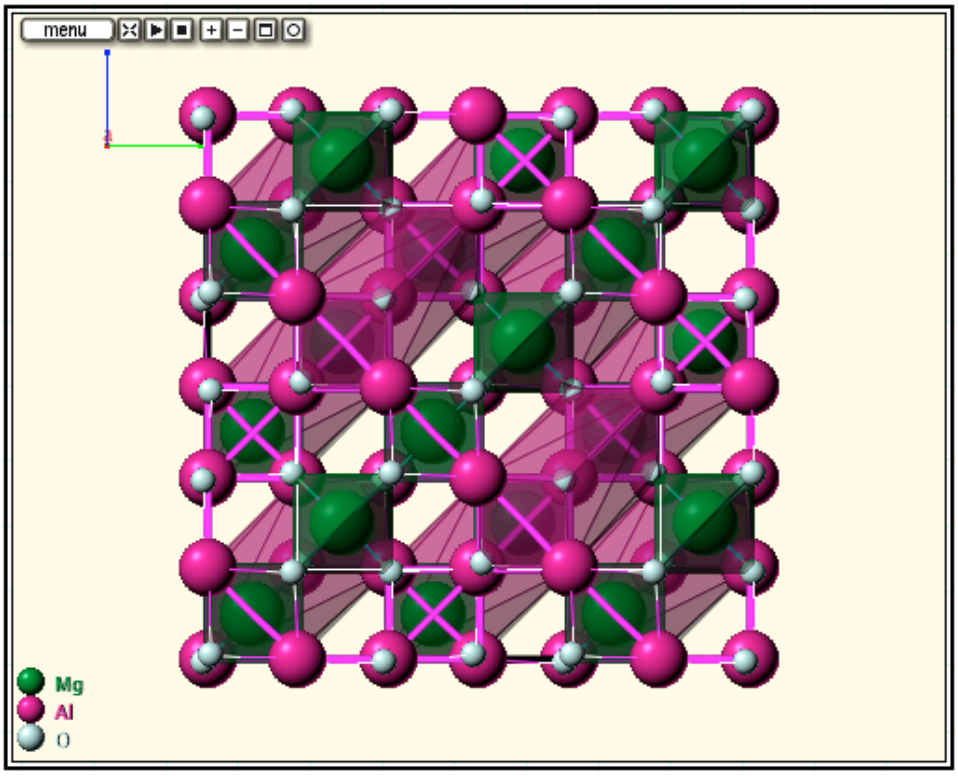

Figure E.19. Unit cell structure of Spinel (data for sample W (T = 293 K) of Peterson et al., 1991).

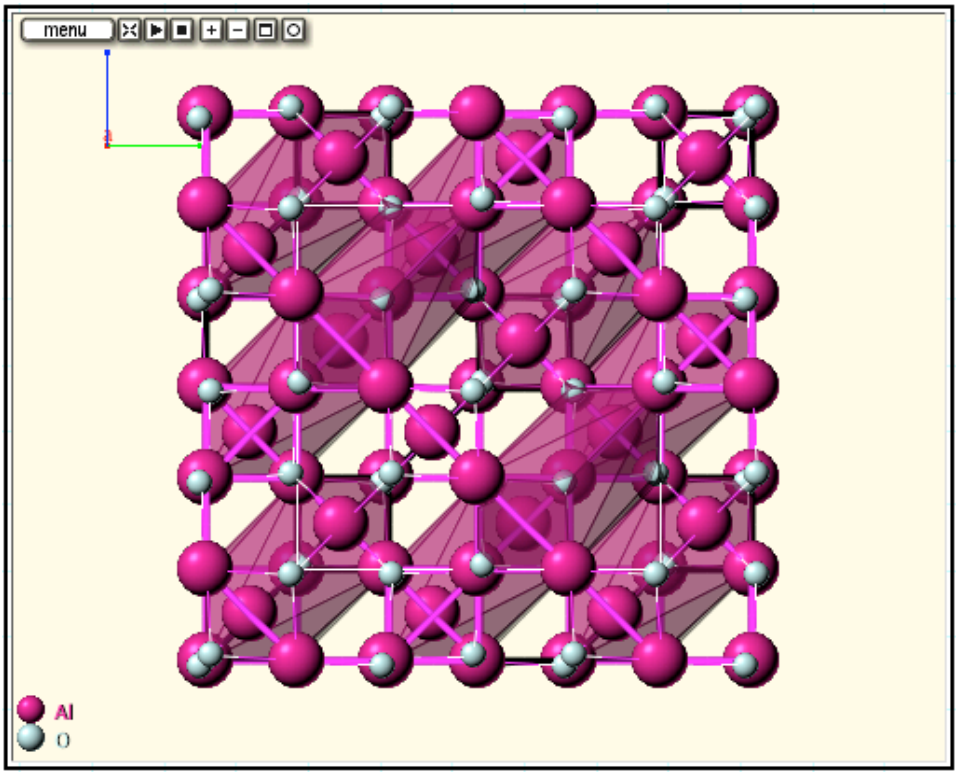

Figure E.20. Unit cell structure of Chromite (data for sample CL 1 of Lenaz and Princivalle, 2005).

Whitlockite

Whitlockite is a calcium phosphate mineral commonly found as a secondary mineral in complex zoned granite pegmatites. pMELTS utilizes whitlockite as a high-pressure phase to accommodate phosphorus.

Whitlockite (Figure E.21)

- Chemical formula: $Ca_9(Mg, Fe^{2+})(PO_4)(PO_3OH)$
- Space group: R3c
- Unit cell: a = 10.33 Å, c = 37.103 Å

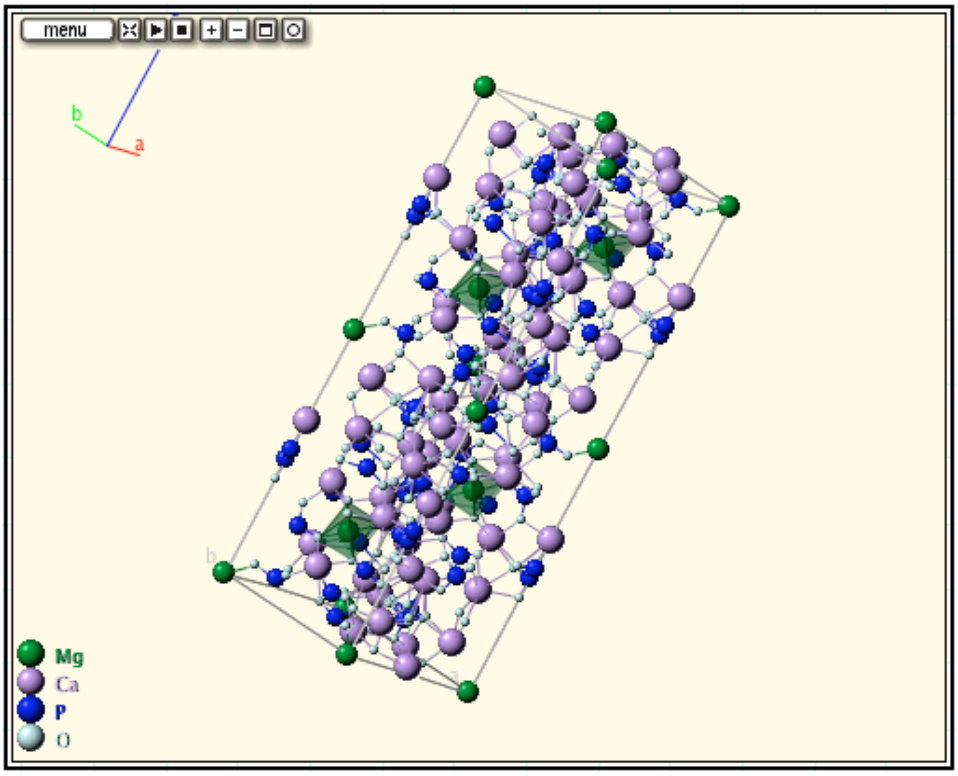

Figure E.21. Unit cell structure of Whitlockite (data of Calvo and Gopal, 1975).

REFERENCES

Abouchami, W., Galer, S.J.G. and Koschinsky, A., 1999. Pb and Nd isotopes in NE Atlantic Fe-Mn crusts: Proxies for trace metal paleosources and paleocean circulation. Geochimica et Cosmochimica Acta 63, 1489-1505.

Abouchami, W., Galer, S.J.G. and Hofmann, A.W., 2000. High precision lead isotope systematics of lavas from the Hawaiian Scientific Drilling Project. Chemical Geology 169, 187-209.

Adam, J. and Green, T.H., 1994. The effects of pressure and temperature on the partitioning of Ti, Sr and REE between amphibole, clinopyroxene and basanitic melts. Chemical Geology 117, 219-233. doi: 10.1016/0009-2541(94)90129-5.

Albarède, F., 1995. Introduction to Geochemical Modeling. Cambridge University Press. 543 pp.

Albarède, F., Luais, B., Fitton, G., Semet, M., Kaminski, E., Upton, B. G. J., Bachelery, P., and Cheminee, J. L., 1997. The geochemical regimes of Piton de la Fournaise Volcano (Réunion) during the last 530 000 years. Journal of Petrology 38, 171-201.

Allan, J.F., Batiza, R., Perfit, M.R., Fornari, D.J., and Sack, R.O., 1989. Petrology of lavas from the Lamont seamount chain and adjacent East Pacific Rise, 10° N. Journal of Petrology 30, 1245-1298.

Allègre, C.J. and Turcotte, D.L., 1986. Implications of a two-component marble-cake mantle. Nature 323, 123-127.

Asimow, P.D. and Ghiorso, M.S., 1998. Algorithmic modifications extending MELTS to calculate subsolidus phase relations. American Mineralogist 83(9-10), 1127-1132.

Bailey, D.K., 1964. Crustal warping a possible tectonic control of alkaline magmatism. Journal of Geophysical Research B 69, 1103-1111.

Bargar, K.E. and Jackson, E.D., 1974. Calculated volumes of individual shield volcanoes along the Hawaiian-Emperor Chain. Journal of Research of the U.S. Geological Survey 2, 545-550.

Baxter, A. N., 1975a. Petrology of the Older Series lavas from Mauritius, Indian Ocean. Geological Society of America Bulletin 86, 1449-1458.

Baxter, A. N., 1975b. K/Rb ratios in some volcanic rocks from Mauritius, Indian Ocean. Geochimica et Cosmochimica Acta 39, 1573-1576.

Baxter, A. N., 1976. Geochemistry and petrogenesis of primitive alkali basalt from Mauritius, Indian Ocean. Geological Society of America Bulletin 87, 1028-1034.

Baxter, A. N., 1978. Ultramafic and mafic nodule suites in shield-forming lavas from Mauritius. Journal of the Geological Society of London 135, 565-581.

Beattie, P., Drake, M., Jones, J., Leeman, W., Longhi, J., McKay, G., Nielsen, R., Palme, H., Shaw, D., Takahashi, E., and Watson, B., 1993. Terminology for trace-element partitioning. Geochimica et Cosmochimica Acta 57, 1605-1606.

Beattie, P., 1994. Systematics and energetics of trace-element partitioning between olivine and silicate melts: Implications for the nature of mineral/melt partitioning. Chemical Geology 117, 57-71.

Berggren, W. A., Kent, D. V., Flynn, J. J., and van Couvering, J. A., 1985. Cenozoic geochronology. Geological Society of America Bulletin 96, 1407-1418.

Bianco, T.A., Ito, G., Becker, J.M., and Garcia, M.O., 2005. Secondary Hawaiian volcanism formed by flexural arch decompression. Geochemistry, Geophysics, Geosystems 6, Q08009, doi: 10.1029/2005GC000945.

Birle, J.D., Gibbs, G.V., Moore, P.B., and Smith, J.V., 1968. Crystal structures of natural olivines. American Mineralogist 53, 807-824.

Blundy, J. and Wood, B., 1994. Prediction of crystal-melt partition coefficients from elastic moduli. Nature 372, 452-454.

Bonneville, A., Barriot, J. P., and Bayer, R., 1988. Evidence from geoid data of a hotspot origin for the southern Mascarene Plateau and Mascarene Islands (Indian Ocean). Journal of Geophysical Research 93, 4199-4212.

Bosch, D., Blichert-Toft, J., Myonier, F., Nelson, B. K., Telouk, P., Gillot, P.-Y., and Albarède, F., 2008. Pb, Hf and Nd isotope compositions of the two Réunion volcanoes (Indian Ocean): A tale of two small-scale mantle "blobs"? Earth and Planetary Science Letters, 265, 748-768.

Bottinga, Y. and Weill, D.F., 1972. Viscosity of magmatic silicate liquids: A model calculation. American Journal of Science 272, 438-475.

Bowen, N.L., 1913. Melting phenomena in the plagioclase feldspars. American Journal of Science 39, 175-191.

Brice, J.C., 1975. Some thermodynamic aspects of the growth of strained crystals. Journal of Crystal Growth 28, 249-253.

Brousse, R., Gisbert, T., and Léotot, C., 1986. L'ile de Tahaa: un volcan à deux caldeiras successives, C. R. Acad. Sc. Paris. II, 303, 247-250.

Brown, G.E. and Mills, B.A., 1986. High-temperature structure and crystal chemistry of hydrous alkali-rich beryl, from the Harding pegmatite, Taos County, New Mexico. American Mineralogist 71, 547-556.

Burnham, C.W., Ohashi, Y., Hafner, S.S., and Virgo, D., 1971. Cation distribution and atomic thermal vibrations in an iron-rich orthopyroxene. American Mineralogist 56, 850-876.

Calvo, C. and Gopal, R., 1975. The crystal structure of whitlockite from the Palermo quarry. American Mineralogist 60, 120-133.

Cameron, M., Sueno, S., Prewitt, C.T., and Papike, J.J., 1973. High-temperature crystal chemistry of acmite, diopside, hedenbergite, jadeite, spodumene, and ureyite. American Mineralogist 58, 594-618.

Carlson, W.D., Swinnea, J.S., and Miser, D.E., 1988. Stability of orthoenstatite at high temperature and low pressure. American Mineralogist 73, 1255-1263.

Chase, C.G., 1981. Oceanic island Pb: Two-stage histories and mantle evolution. Earth and Planetary Science Letters 52, 277-284.

Charvis, P., Laesanpura, A., Gallart, J., Hirn, A., Lépine, J.-C., de Voogd, B., Minshull, T., Hello, Y., and Pontoise, B., 1999. Spatial distribution of hotspot material added to the lithosphere under La Réunion, from wide-angle seismic data. Journal of Geophysical Research 104(B2), 2875-2893.

Chauvel., C., McDonough, W., Guille, G., Maury, R., and Duncan, R., 1997. Contrasting old and young volcanism in Rurutu Island, Austral chain. Chemical Geology 139, 125-143.

Cheatham, M.M., Sangrey, W.F., and White, W.M., 1993. Sources of error in external calibration ICP-MS analysis of geological samples and an improved non-linear drift correction. Spectrochimica Acta, 48B, E487-E506.

Chen, C.-Y. and Frey, F.A., 1985. Trace element and isotopic geochemistry of lavas from Haleakala Volcano, East Maui, Hawaii: Implications for the origin of Hawaiian basalts. Journal of Geophysical Research 90(B10), 8743-8768.

Cheng, Q., Park, K.-H., Macdougall, J.D., Zindler, A., Lugamair, G.W., Staudigel, H., Hawkins, J.W., and Lonsdale, P.F., 1987. Isotopic evidence for a hotspot origin of the Louisville seamount chain. In: Keating, B.H., Fryer, P., Batiza,

R., and Boehlert, G.W. eds., Seamounts, Islands, and Atolls. AGU, Washington, D.C. pp. 235-254.

Clague, D. A., 1987. Hawaiian alkaline volcanism. In: Fitton, J. G. and Upton, B. G. J. Eds.), Alkaline Igneous Rocks. Geological Society, London.

Clague, D.A. and Dalyrmple, G.B., 1987. The Hawaiian-Emperor Volcanic Chain. USGS Professional Paper 1350, 5-54.

Clague, D.A., Holcomb, R.T., Sinton, J.M., Detrick, R.S., and Torresan. M.E., 1990. Pliocene and Pleistocene alkalic flood basalts on the seafloor north of the Hawaiian Islands. Earth and Planetary Science Letters 98, 175-191.

Clague, D.A., Uto, K., Satake, K., and Davis, A.S., 2002. Eruption style and flow emplacement in the submarine North Arch Volcanic Field, Hawaii. In: Takahashi, E., ed., Hawaiian Volcanoes: Deep Underwater Perspective, Geophysical Monograph Series 128. AGU, Washington, D.C. pp. 65-84.

Clague, D.A. and Dalyrmple, G.B., 1988. Age and petrology of alkalic postshield and rejuvenated-stage lavas from Kauai, Hawaii. Contributions to Mineralogy and Petrology 99, 202-218.

Clague, D.A. and Frey, F.A., 1982. Petrology and trace element geochemistry of the Honolulu Volcanic Series, Oahu: Implications of the oceanic mantle beneath Hawaii. Journal of Petrology 23, 447-504.

Clague, D.A., Paduan, J.B., Mcintosh, W.C., Cousens, B.L., Davis, A.S., and Reynolds, J.R., 2006. A submarine perspective of the Honolulu Volcanics, Oahu. Journal of Volcanology and Geothermal Research 151, 279-307.

Clarke, J.R. and Papike, J.J., 1968. Crystal-chemical characterization of omphacites. American Mineralogist 53, 840-868.

Cochran, J.R., 1990. Himalayan uplift, sea level, and the record of Bengal Fan sedimentation at the ODP leg 116 sites. Proc. Ocean Drill. Prog. Sci. Res. 116, 397-414.

Colville, A.A. and Ribbe, P.H., 1968. The crystal structure of an adularia and a refinement of the structure of orthoclase. American Mineralogist 53, 25-37.

Connolly, J.A.D. and Petrini, K., 2002. An automated strategy for calculation of phase diagram sections and retrieval of rock properties as a function of physical conditions. Journal of Metamorphic Geology 20, 697-708.

Courtillot, V., Davaille, A., Besse, J., and Stock, J., 2003. Three distinct types of hotspots in the Earth's mantle. Earth and Planetary Science Letters 205, 295-308.

Darwin, C. R., 1844. Geological observation on the volcanic islands visited during the voyage of H.M.S. Beagle, together with some brief notices on the geology of Australia and the Cape of Good Hope. Being the second part of the geology of the voyage of the Beagle, under the command of Capt. Fitzroy, R.N. during the years 1832 to 1836. Smith Elder and Co., London.

Davies, G.F. and Richards, M.A., 1992. Mantle convection. Journal of Geology 100(2), 151-206.

de Voogd, B., Palomé, S.P., Hirn, A., Charvis, P., Gallart, J., Rousset, D., Dañobeitia, J., and Perroud, H.., 1999. Vertical movements and material transport during hotspot activity: Seismic reflection profiling offshore La Réunion. Journal of Geophysical Research 104(B2), 2855-2874.

DeMets, C., Gordon, R. G., Argus, D. F., and Stein, S., 1994. Effect of recent revisions to the geomagnetic reversal time scale on estimates on current plate motions. Geophysical Research Letters 21, 2191-2194.

DeMets, C., Gordon, R.G., and Royer, J.-Y., 2005. Motion between the India, Capricorn and Somalian plates since 20 Ma: Implications for the timing and magnitude of distributed lithospheric deformation in the equatorial Indian ocean. Geophysical Journal International 161, 445-468.

Deniel, C., Kieffer, G., and Lecointre, J., 1992. New 230Th-238U and 14C age determinations from Piton des Neiges Volcano, Reunion--a revised chronology for the Differentiated Series. Journal of Volcanology and Geothermal Research 51, 253-267.

DePaolo, D.J. and Stolper, E.M., 1996. Models of Hawaiian volcano growth and plume structure: implications of results from the Hawaiian Scientific Drilling Project. Journal of Geophysical Research 101(B5), 11643-11654.

DePaolo, D.J., Bryce, J.G., Dodson, A., Shuster, D.L., and Kennedy, B.M., 2001. Isotopic evolution of Mauna Loa and the chemical structure of the Hawaiian plume. Geochemistry, Geophysics, Geosystems 2.

Deplus, C., de Voogd, B., Dyment, J., Depuiset, F., Sisavath, E., and N/O L'Atlante Scientific Party, 2007. Does the Réunion hotspot volcano emplace on a fossil ridge or a fracture zone? EOS Trans. AGU, 88(52), Fall Meet. Suppl., Abstract V31F-05.

Detrick, R.S. and Crough, S.T., 1978. Island subsidence, hot spots, and lithospheric thinning. Journal of Geophysical Research 83, 1236-1244.

Dickey, J.S., Jr., 1970. Partial fusion products in alpine-type peridotites: Serrania de la Rhonda and other examples. In Mineralogical Society of America Special Paper 3, 33-49.

Draper, D.S. and van Westrenen, W., 2007. Quantifying garnet-melt trace element partitioning using lattice-strain theory: Assessment of statistically significant

controls and a new predictive model. Contributions in Mineralogy and Petrology 154, 731-746.

Duncan, R. A., 1990. The volcanic record of the Réunion hotspot. In: Duncan, R. A., Backman, J., and Peterson, L. C. Eds.), Proceedings of the Ocean Drilling Program, Scientific Results. Ocean Drilling Program, College Station, TX. pp. 3-10.

Duncan, R.A., Fisk, M.R., White, W.M., and Nielsen, R.L., 1994. Tahiti: Geochemical evolution of a French Polynesian volcano. Journal of Geophysical Research 99, 24,341-24,357.

Duncan, R.A. and Keller, R.A., 2004. Radiometric ages for basement rocks from the Emperor Seamounts, ODP Leg 197. Geochemistry, Geophysics, Geosystems Q08L03, doi:10.1029/2004GC000704.

Dyment, J., Gallet, Y., and the Magofond 2 scientific party, 1999. The Magofond 2 cruise: A surface and deep tow survey on the past and present Central Indian Ridge, InterRidge News 8, 25-31.

Dyment, J., Hemond, C., Guillou, H., Maia, M., Briais, A., and Gente, P., 2001. Central Indian Ridge and Réunion Hotspot in Rodrigues area: Another type of ridge-hotspot interaction? Eos Trans. AGU 82, Fall Meet. Suppl., Abstract T31D-05.

Farnetani, C.G. and Richards, M.A., 1995. Thermal entrainment and melting in mantle plumes. Earth and Planetary Science Letters 136, 251-267.

Farnetani, C.G., Legras, B., and Tackley, P.J., 2002. Mixing and deformation in mantle plumes. Earth and Planetary Science Letters 196, 1-15.

Farnetani C.G. and Samuel, H., 2005. Beyond the thermal plume paradigm. Geophysical Research Letters 32, L07311, doi:10.1029/2005/GL022360.

Fekiacova, Z., Abouchami, W., Galer, S. J. G., Garcia, M. O., and Hofmann, A. W., 2007. Origin and temporal evolution of Ko'olau Volcano, Hawai'i: Inferences from isotope data on the Ko'olau Scientific Drilling Project (KSDP), the Honolulu Volcanics and ODP Site 843. Earth and Planetary Science Letters 261, 65-83.

Fisk, M.R., Upton, B.G.J., Ford, C.E., and White, W.M., 1988. Geochemical and experimental study of the genesis of Réunion Island, Indian Ocean. Journal of Geophysical Research B 93, 4933-4950.

Foit, F.F. and Peacor, D.R., 1973. The anorthite crystal structure at 410 and 830 °C. American Mineralogist 58, 665-675.

Fretzdorff, S., Stoffers, P., Devey, C. W., and Munschy, M., 1998. Structure and morphology of submarine volcanism in the hotspot region around Réunion Island, western Indian Ocean. Marine Geology 148, 39-53.

Frey, F.A., Garcia, M.O., and Roden, M.F, 1994. Geochemical characteristics of Koolau Volcano: Implications of intershield geochemical differences among Hawaiian volcanoes. Geochimica et Cosmochimica Acta 58, 1441-1462.

Galer, S.J.G., 1986. Chemical and isotopic studies of crust-mantle differentiation and the generation of mantle heterogeneity. Ph.D. thesis, University of Cambridge. 249 p.

Galer, S.J.G., 1997. Optimal triple spiking for high precision lead isotope ratio determination. Terra Nova 9, 441.

Galer, S.J.G., 1999. Optimal double and triple spiking for high precision lead isotopic measurement. Chemical Geology 157, 255-274.

Galer, S.J.G. and Abouchami, W., 1998. Practical application of lead triple spiking for correction of instrumental mass discrimination, Mineral. Mag. 62A, 491-492

Gallahan, W.E. and Nielsen, R.L., 1992. The partitioning of Sc, Y, and the rare-earth elements between high-Ca pyroxene and natural mafic to intermediate lavas at 1-atmosphere. Geochimica et Cosmochimica Acta 56, 2387-2404.

Gallart, J., Driad, L., Charvis, P., Sapin, M., Hirn, A., Diaz, J., de Voogd, B., and Sachpazi, M., 1999. Perturbation to the lithosphere along the hotspot track of La Reunion from an offshore-onshote seismic transect. Journal of Geophysical Research 104(B2), 2895-2908.

Gandy, C.E., Garcia, M.O., and Blay, C., 2005. Volume and petrologic characteristics of the Kola Volcanics, Kauai, Hawaii. Eos Trans. AGU 86, Fall Meet. Suppl., Abstract V51A-1474.

Gandy, C.E., Garcia, M.O., and others, submitted 2008. Implications of the volume of Kauai's Koloa volcanics for the origin of Hawaiian rejuvenated volcanism. Geology.

Gao, Y., Huang, J., Casey, J.F., submitted 2008. Data report: Trace element geochemistry of oceanic crust formed at a super-fast spreading ridge, Hole 1256D. Geochemistry, Geophysics, Geosystems, 19p.

Geldmacher, J. and Hoernle, K., 2000. The 72 Ma geochemical evolution of the Madeira hotspot (eastern North Atlantic): Recycling of Paleozoic (≤ 500 Ma) oceanic lithosphere. Earth and Planetary Science Letters 183, 73-92.

Gerstenberger, H. and Haase, G., 1997. A highly effective emitter substance for mass spectrometric Pb isotope ratio determinations. Chemical Geology 136. 309-312.

Ghiorso, M.S., 1997. Thermodynamic models of igneous processes. Ann. Rev. Earth. Planet. Sci. 25, 221-241.

Ghiorso, M.S. and Sack, R.O., 1995. Chemical mass transfer in magmatic processes IV. A revised and internally consistent thermodynamic model for the

interpolation and extrapolation of liquid-solid equilibria in magmatic systems at elevated temperatures and pressures. Contributions in Mineralogy and Petrology, 119, 197-212.

Ghiorso, M.S., Hirschmann, M.M., Reiners, P.W., and Kress, V.C., III, 2002. The pMELTS: A revision of MELTS for improved calculation of phase relations and major element partitioning related to partial melting of the mantle to 3 GPa. Geochemistry, Geophysics, Geosystems 3(5), doi:10.1029/ 2001GC000217.

Ghiorso, M.S., Hirschmann, M.M., and Grove, T.L., 2007. xMELTS: A thermodynamic model for the estimation of magmatic phase relations over the pressure range 0-30 GPa and temperatures up to 2500 °C. Eos Trans. AGU 88(52), Fall Meet. Suppl., Abstract V31C-0608.

Gibbs, G.V. and Smith, J.V., 1965. Refinement of the crystal structure of synthetic pyrope. American Mineralogist 50, 2023-2039.

Gillot, P.-Y., Lefevre, J.-C., and Nativel, P.-E., 1994. Model for the structural evolution of the volcanoes of Réunion Island. Earth and Planetary Science Letters 122, 291-302.

Gillot, P. Y. and Nativel, P., 1989. Eruptive history of the Piton de la Fournaise Volcano, Réunion Island, Indian Ocean. Journal of Volcanology and Geothermal Research 36, 53-65.

Giorgi, L., Borchiellini, S., and Delucchi, L., 1999. Carte Géologique de l'Ile Maurice, 1:50.000: Schéma Hydrogéologique. GEOLAB/BURGEAP (France).

Goldschmidt, V.M., 1937. The principles of distribution of chemical elements in minerals and rocks. Journal of the Chemical Society, 655-673.

Govindaraju, K., 1994. 1994 compilation of working values and sample description for 383 geostandards. Geostandards Newsletter 18 (Special Issue), 158 pp.

Govindaraju, K., 1995. 1995 working values with confidence limits for twenty-six CRPT, ANRT and IWG-GIT geostandards. Geostandards Newsletter 19, 1-32.

Graham, D., Lupton, J., Albarède, F., Condomines, M., 1990. A 360,000 year helium isotope record from Piton de la Fournaise, Réunion Island. Nature 347, 545-548.

Green, D.H. and Ringwodd, A.E., 1967. The genesis of basaltic magmas. Contributions in Mineralogy and Petrology 18, 105-162.

Gualtieri, A.F., 2000. Accuracy of XRPD QPA using the combined Rietveld-RIR method, Locality: Napoli, Italy. Journal of Applied Crystallography 33, 267-278.

Gurriet, P., 1987. A thermal model for the origin of post-erosional alkalic lavas, Hawaii. Earth and Planetary Science Letters 82, 153-158.

Harrison, T.M., Copeland, P., Kidd, W.S.F., and Yin, A., 1992. Raising Tibet. Science 255, 1663-1670.

Hauri, E.H., 1996. Major element variability in the Hawaiian mantle plume. Nature 382, 415-419.

Hess, H.H., 1962. History of Ocean Basins. In: Engel, A.E.J., James, H.L., and Leonard, B.F., eds., Petrologic Studies: A Volume in Honor of A. F Buddington. GSA, pp. 599-620.

Hendricks, S.B. and Jefferson, M.E., 1939. Polymorphism of the micas with optical measurements. American Mineralogist 24, 729-771.

Herzberg, C., 2006. Petrology and thermal structure of the Hawaiian plume from Mauna Kea volcano. Nature 444, 605-609. doi: 10.1038/nature05254.

Herzberg, C., Asimow, P.D., Arndt, N., Niu, Y., Lesher, C.M., Fitton, J.G., Cheadle, M.J., and Saunders, A.D., 2007. Temperatures in ambient mantle and plumes:

Constraints from basalts, picrites, and komatiites. Geochemistry, Geophysics, Geosystems 8, Q02006, doi:10.1029/2006GC001390.

Herzberg, C. and Asimow, P.D., 2008. Petrology of oceanic island basalts: PRIMELT2.XLS software for primary magma calculation. Geochemistry, Geophysics, Geosystems 9(9), Q09001, doi:10.1029/2008GC002057.

Hirano, N., Takahashi, E., Yamamoto, J., Abe, N., Ingle, S.P., Kaneoka, I.,Hirata, T., Kimura, J.-I., Ishii, T., Ogawa, Y., Machida, S., and Suyehiro, K., 2006. Volcanism in response to plate flexure. Science 313, 1426-1428.

Hirschmann, M.M., Ghiorso, M.S., Wasylenki, L.E., Asimow, P.D., and Stolper, E.M., 1998. Calculation of peridotite partial melting from thermodynamic models of minerals and melts. I. Review of methods and comparison with experiments. Journal of Petrology 39(6), 1091-1115.

Hirschmann, M.M., Ghiorso, M.S., Davis, F.A., Gordon, S.M., Mukherjee, S., Grove, T.L., Krawczynski, M., Medard, E., and Till, C.B., 2008. Library of Experimental Phase Relations (LEPR): A database and Web portal for experimental magmatic phase equilibria data. Geochemistry, Geophysics, Geosystems 9, Q03011, doi:10.1029/2007GC001894.

Hoernle, K. and Schminke, H.-U., 1993. The petrology of the tholeiities through melilite nephelinites on Gran Canaria, Canary Islands: Crystal fractionation, accumulation, and depths of melting. Journal of Petrology 34, 573-597.

Hodell, D.A., Mueller, P.A., and Garrido, J.R., 1991. Variations in the strontium isotopic composition of seawater during the Neogene. Geology 19, 24-27.

Hofmann, A.W. and White, W.M., 1982a. Ba, Rb, and Cs in the Earth's mantle. Z. Naturforsch., 38, 256-266.

Hofmann, A.W. and White, W.M., 1982b. Mantle plumes from ancient oceanic crust. Earth and Planetary Science Letters 57, 421-436.

Hofmann, A.W., 1997. Mantle geochemistry: the message from oceanic volcanism. Nature 385, 219-229.

Hollocher, K., 2008. Oxide and hydroxide interferences for Ba, lanthanides, Hf, and Ta. http://www.union.edu/PUBLIC/GEODEPT/hollocher/icp-ms/ree_corrections.htm

Horn, I., Foley, S.F., Jackson, S.E., and Jenner, G.A., 1994. Experimentally determined partitioning of high-field strength and selected transition elements between spinel and basaltic melts. Chemical Geology 117, 193-218.

Ito, G. and Mahoney, J.J., 2005a. Flow and melting of a heterogeneous mantle: 1. Method and importance to the geochemistry of ocean island and mid-ocean ridge basalts. Earth and Planetary Science Letters 230, 29-46.

Ito, G. and Mahoney, J.J., 2005b. Flow and melting of a heterogeneous mantle: 1. Implications for a chemically nonlayered mantle. Earth and Planetary Science Letters 230, 47-63.

Ito, T., 1947. The structure of epidote ($HCa_2(Al, Fe)al_2Si_3O_{13}$). American Mineralogist 32, 309-321.

Johnson, D.M., Hooper, P.R. and Conrey, R.M., 1999. XRF analysis of rocks and minerals for major and trace elements on a single low dilution Li-tetraborate fused bead. Advances in X-ray Analysis 41, 843-867.

Jull, M. and Ribe, N.M., 2002. The geochemistry of Hawaiian plume dynamics. Geochemistry et Cosmochimica Acta 66, A375.

Keating, B.H., Mattey, D.P., Naughton, J., and Helsley, C.E., 1984. Age and origin of Truk Atoll, eastern Caroline Islands: Geochemical, radiometric-age, and paleomagnetic evidence. GSA Bulletin 95. 350-356.

Klein, E.M. and Langmuir, C.H., 1987. Global correlations of ocean ridge basalt chemistry with axial depth and crustal thickness. Journal of Geophysical Research 92(B8), 8089-8115.

Kogiso, T., Tatsumi, Y., and Nakano, S., 1997. Trace element transport during dehydration processes in the subducted oceanic crust: 1. Experiments and implications for the origin of ocean island basalts. Earth and Planetary Science Letters 148, 193-205.

Kogiso, T., Hirschmann, M.M., and Reiners, P.W., 2004. Length scales of mantle heterogeneities and their relationship to ocean island basalt geochemistry. Geochimica et Cosmochimica Acta 68(2), 345-360. doi:10.1016/S0016-7037(03)00419-8

Koppers, A.A.P., Staudigel, H., Wijbrans, J.R., and Pringle, M.S., 1998. The Magellan Seamount trail: Implications for Cretaceous hotspot volcanism and absolute Pacific Plate motion. Earth and Planetary Science Letters 163, 53-68.

Kornprobst, J., 1969. The Beni Bouchera ultrabasic massif, inner Rif zone, Morocco: study of high-temperature, high-pressure peridotites and associated pyroxenites, with or without garnet. Contributions to Mineralogy and Petrology 23(4), 283-322.

Korzhinskii, D.S., 1970. Theory of Metasomatic Zoning. Oxford: Clarendon Press. 162 pp.

Kushiro, I., 2001. Partial melting experiment on peridotite and origin of mid-ocean ridge and backarc basin magmas. Annual Review of Earth and Planetary Sciences 29, 71-107.

Lacroix, A., 1936. Le volcan actif de l'île de la Réunion et ses produits. Paris: Gauthier-Villars, 297 pp.

Langmuir, C.H., Vocke, R.D., Hanson, G.N., and Hart, S.R., 1978. A general mixing equation with applications to Icelandic basalts. Earth and Planetary Science Letters 37(3), 380-392, doi: 10.1016/0012-821X(78)90053-5.

Lassiter, J.C., Hauri, E.H., Reiners, P.W., and Garcia, M.O., 2000. Generation of Hawaiian post-erosional lavas by melting of a mixed lherzolite/pyroxenite source. Earth and Planetary Science Letters 178, 269-284.

Le Bas, M.J., LeMaitre, R.W., Streckeisen, A.L., and Zanettin, B., 1986. A chemical classification of volcanic rocks based on the total alkali-silica diagram. Journal of Petrology 27, 745-750.

Lehnert, K., Su, Y., Langmuir, C.H., Sarbas, B., and Nohl, U., 2000. A global geochemical database structure for rocks. Geochemistry, Geophysics, Geosystems 1, doi:10.1029/1999GC000026.

Leitch, A.M. and Davies, G.F., 2001. Mantle plumes and flood basalts: Enhanced melting from plume ascent and an eclogite component. Journal of Geophysical Research 106(B2), 2047-2059.

Lénat, J. F. and Bachelery, P., 1988. Dynamics of magma transerts at Piton de la Fournaise volcano (Réunion Island, Indian Ocean). In: King, C.-Y. and Scarpa, R. Eds.), Modeling of Volcanic Processes, Wiesbaden.

Lénat, J.F., Gilbert-Malengreau, B., Galdéano, A., 2001. A new model for the evolution of the volcanic island of Réunion (Indian Ocean). Journal of Geophysical Research 106(B5), 8645-8663.

Lenaz, D. and Princivalle, F., 2005. The crystal chemistry of detrital chromian spinel from the southeastern Alps and Outer Dinarides: The discrimination of supplies from areas of similar tectonic setting? The Canadian Mineralogist 43, 1305-1314.

Lipman, P.W., Clague, D.A., Moore, J.G., and Holcomb, R.T., 1989. South Arch volcanic field: Newly identified young lava flows on the sea floor south of the Hawaiian Ridge. Geology 17, 611-614.

Macdonald, G.A. and Katsura, T., 1964. Chemical composition of Hawaiian lavas. Journal of Petrology 5, 82-133.

Mahoney, J.J., Natland, J.H., White, W.M., Poreda, R., Bloomer, S.H., Fisher, R.L., and Baxter, A.N., 1989. Isotopic and geochemical provinces of the western Indian Ocean spreading centers. Journal of Geophysical Research B 94, 4033-4052.

Mahoney, J. J., Duncan, R. A., Khan, W., Gnos, E., and McCormick, G. R., 2002. Cretaceous volcanic rocks of the South Tethyan suture zone, Pakistan: implications for the Réunion hotspot and Deccan Traps. Earth and Planetary Science Letters 203, 295-310.

Malengreau, B., Lénat, J.F., and Froger, J.L., 1999. Structure of Réunion Island (Indian Ocean) inferred from the interpretation of gravity anomalies. Journal of Volcanology and Geothermal Research 88, 131-146.

McDonough, W.F. and Sun, S.-S., 1995. Composition of the Earth. Chemical Geology 120, 223-253, doi:10.1016/0009-2541(94)00140-4.

McDougall, I., Upton, B.G.J., and Wadsworth, W.J., 1965. A geological reconnaissance of Rodriquez Island, Indian Ocean. Nature 206, 26-27.

McDougall, I. and Chamalaun, F. H., 1969. Isotopic dating and geomagnetic polarity studies on volcanic rocks from Mauritius, Indian Ocean. Geological Society of America Bulletin 80, 1419-1442.

McKenzie, D. and Bickle, M.J., 1988. The volume and composition of melts generated by extension of the lithosphere. Journal of Petrology 29, 625-679.

McKenzie, D. and O'Nions, R.K., 1991. Partial melt distributions from inversion of rare earth element concentrations. Journal of Petrology 32(5), 1021-1091.

McKenzie, D. and O'Nions, R.K., 1995. The source regions of ocean island basalts. Journal of Petrology 36(1), 133-159.

Meagher, E.P., 1980. Silicate garnets, in Orthosilicates. ed. Ribbe, P.H. Rev. Mineral. 5, 25-66.

Merkouriev, S. and DeMets, C., 2006. Constraints on Indian plate motion since 20 Ma from dense Russian magnetic data: Implications for Indian plate dynamics. Geochemistry et Cosmochimica Acta 7, Q02002, doi:10.1029/2005GC001079.

Molnar, P., England, P., and Maritond, J., 1993. Mantle dynamics, uplift of the Tibetan plateau, and the Indian monsoon. Rev. Geophys 31, 357-396.

Montelli, R., Nolet, G., Dahlen, F. A., Masters, G., Engdahl, E. R., and Hung, S.-H., 2004. Finite-frequency tomography reveals a variety of plumes in the mantle. Science 303, 338-343.

Moore, D.G., Curray, J.R., Raitt, R.W., and Emmel, F.J., 1974. Stratigraphic-seismic section correlations and implications to Bengal Fan history. Initial Rep. Deep. Sea Drill. Proj. 22, 403-412.

Moore, J.G., 1970. Relationship between subsidence and volcanic load, Hawaii. Bulletin Volcanologique 34, 562-576.

Moore, J. G., Clague, D. A., and Normark, W. R., 1982. Diverse basalt types from Loihi Seamount, Hawaii. Geology 10, 88-92.

Morgan, W.J., 1971. Convection plumes in the lower mantle. Nature 230, 42-43.

Morgan, W.J., 1978. Rodriguez, Darwin, Amsterdam,…, a second type of hotspot island. JGR 83(B11), 5355-5360.

Morgan, J. W., 1987. Relative motions of hotspots in the Pacific, Atlantic and Indian oceans since Late Cretaceous time. Nature 327, 587-591.

Morgan, W. J., 1981. Hotspot tracks and the opening of the Atlantic and Indian Oceans. In: Emiliani, C. (Ed.), The Sea.

Müller, R.D., Royer, Y.-J., and Lawyer, L.A., 1993. Revised plate motions relative to the hotspots from combined Atlantic and Indian Ocean hotspot tracks. Geology 21, 275-278.

Murton, B. J., Tindle, A. G., Milton, J. A., and Sauter, D., 2005. Heterogeneity in southern Central Indian Ridge MORB: implications for ridge-hot spot interaction. Geochemistry, Geophysics, Geosystems 6.

Nasagawa, H., 1966. Trace element partition coefficients in ionic crystals. Science 152, 767-769.

Natland, J.H. and Turner, D.L., 1985. Age progression and petrological development of Samoan shield volcanoes: Evidence from K-Ar ages, lava compositions, and mineral studies. In Brocher, T.M., ed., Investigations of the Northern Melanesian Borderland. Circum-Pacific Council for Energy and Resources, Houston, TX, pp. 139-171.

Nauret, F., Abouchami, W., Galer, S.J.G., Hofmann, A.W., Hémond, C., Chauvel, C., and Dyment, J., 2006. Correlated trace element-Pb isotope enrichments in Indian MORB along 18-20°S, Central Indian Ridge. Earth and Planetary Science Letters 245, 137-152.

Nielsen, R.L. and Dungan, M.A., 1983. Low pressure mineral-melt equilibria in natural anhydrous mafic systems. Contributions to Mineralogy and Petrology 84, 310-326.

Nohda, S., Kaneoka, I., Hanyu, T., Xu, S., and Uto, K., 2005. Systematic variation of Sr-, Nd- and Pb-isotopes with time in lavas of Mauritius, Reunion hotspot. Journal of Petrology 46, 505-522.

Novak, G.A. and Gibbs, G.V., 1971. The crystal chemistry of the silicate garnets. American Mineralogist 56, 791-825.

Onuma, N., Iguchi, H., Wakita, H., and Nagasawa, H., 1968. Trace element partition between two pyroxenes and the host lava. Earth and Planetary Science Letters 5, 47-51

Paul, D.P., White, W.M., and Blichert-Toft, J., 2005. Geochemistry of Mauritius and the origin of rejuvenescent volcanism on oceanic island volcanoes. Geochemistry, Geophysics, Geosystems 6(6), doi:10.1029/2004GC000883.

Paul, D., Kamenetsky, V.S., Hofmann, A.W. and Stracke, A., 2007. Compositional diversity among primitive lavas of Mauritius, Indian Ocean: Implications for mantle sources. Journal of Volcanology and Geothermal Research 164, 76-94.

Perroud, B., 1982. Etude volcano-structurale des îles Maurice et Rodrigues (Océan Indien Occidental). Origine du volcanisme. Ph.D., Université Scientifique et Médicale de Grenoble.

Pertermann, M., Hirschmann, M.M., Hametner, K., Günther, D., and Schmidt, M.W., 2004. Experimental determination of trace element partitioning between garnet and silica-rich liquid during anhydrous partial melting of MORB-like eclogite. Geochemistry, Geophysics, Geosystems 5(5), Q05A01, doi: 10.1029/2003GC000638.

Peterson, R.C., Lager, G.A., and Hitterman, R.L., 1991. A time-of-flight neutron powder diffraction study of $MgAl_2O_4$ at temperatures up to 1273 K. American Mineralogist 76, 1445-1458.

Phipps Morgan, J. and Morgan, W.J., 1999. Is the Hawaiian basalt progression a consequence of progressive melt extraction from the upwelling Hawaiian Plume? In: EUG conference abstracts 10. Cambridge Publications. pp. 354.

Phipps Morgan, J., 2001. Thermodynamics of pressure release melting of a veined plum pudding mantle. Geochemistry, Geophysics, Geosystems 2, doi: 20000GC000049.

Pin, C. and Zalduegui, J. F. S., 1997. Sequential separation of light rare-earth elements, thorium and uranium by miniaturized extraction chromatography: Application to isotopic analyses of silicate rocks. Analytica Chimica Acta 339, 79-89.

Plank, T. and Langmuir, C.H., 1998. The chemical composition of subducting sediment and its consequence for the crust and mantle. Chemical Geology 145, 325-394.

Powell, R. and Holland, T.J.B., 1988. An internally consistent thermodynamic dataset with uncertainties and correlations: 3. Application methods, worked examples and a computer program. Journal of Metamorphic Geology 6, 173-204.

Prewitt, C.T., Sueno, S., and Papike, J.J., 1976. The crystal structures of high albite and monalbite at high temperatures. American Mineralogist 61, 1213-1225.

Rançon, J.P., Lerebour, P., and Auge, T., 1989. The Grane Brûlé exploration drilling: New data on deep framework of the Piton de la Fournaise volcano. Part 1: Lithostratigraphic units and volcanostructural interpretation. Journal of Volcanology and Geothermal Research 36, 113-127.

Renne, P.R., Swisher, C.C., Deino, A.L., Karner, D.B., Owens, T.L., and DePaolo, D.J., 1998. Intercalibration of standards, absolute ages and uncertainties in $^{40}Ar/^{39}Ar$ dating. Chemical Geology 145, 117-152.

Ribe, N.M. and Christensen, U.R., 1994. Three-dimensional modeling of plume-lithosphere interaction. Journal of Geophysical Research 99, 669-682.

Ribe, N.M. and Christensen, U.R., 1999. The dynamical origin of Hawaiian volcanism. Earth and Planetary Science Letters 171, 517-531.

Robinson, J.E. and Eakins, B.W., 2006. Calculated volumes of individual shield volcanoes at the young end of the Hawaiian Ridge. Journal of Volcanology and Geothermal Research 151, 309-307.

Royer, J. Y., Sclater, J. G., Sandwell, D. T., Cande, S. C., Schlich, R., Munschy, M., Dyment, J., Fisher, R. L., Mueller, R. D., Coffin, M. F., Patriat, P., and Bergh, H. W., 1992. Indian Ocean plate reconstructions since the Late Jurassic. Synthesis of results from scientific drilling in the Indian Ocean 70, 471-475.

Royer, J.Y., Gordon, R.G., DeMets, C., and Vogt, P.R., 1997. New limits on the motion between India and Australia since chron 5 (11 Ma) and implications for lithospheric deformation in the equatorial Indian Ocean. Geophysical Journal International 129, 41-53.

Saal, A.E., Hart, S.R., Shimizu, N., Hauri, E.H, and Layne, G.D., 1998. Pb isotopic variability in melt inclusions from oceanic island basalts, Polynesia. Science 282, 1481-1484.

Salters, V.J.M. and Longhi, J., 1999. Trace element partitioning during initial stages of melting beneath mid-ocean ridges. Earth and Planetary Science Letters 166, 15-30.

Shannon, R.D., 1976. Revised effective ionic radii and systematic studies of interatomic distances in halides and chalcogenides. Acta Cryst. A32, 751-767.

Sherrod, D.R. and Nishimitsu, Y.T.T., 2003. New K-Ar ages and the geologic evidence against rejuvenated-stage volcanism at Haleakala, East Maui, a postshield-stage volcano of the Hawaiian Island chain. GSA Bulletin 115, 683-694.

Sheth, H.C., Mahoney, J.J., and Baxter, A.N., 2003. Geochemistry of lavas from Mauritius, Indian Ocean: Mantle sources and petrogenesis. International Geology Review 45, 780-797.

Simpson, E. S. W., 1950. The geology and mineral resources of Mauritius. Colonial Geology and Mineral Resources 1, 217-238.

Sleep, N.H., 1984. Tapping of magmas from ubiquitous mantle heterogeneities: An alternative to mantle plumes? Journal of Geophysical Research B 89, 10029-10041.

Sleep, N. H., 1990. Hotspots and mantle plumes: some phenomenology. Journal of Geophysical Research 95(B5), 6715-6736.

Smith, P.M., and Asimow, P.D., 2005. Adiabat_1ph: A new public front-end to the MELTS, pMELTS, and pHMELTS models. Geochemistry, Geophysics, Geosystems 6, Q02004, doi:10.1029/2004GC000816.

Smith, W.H.F. and Sandwell, D.T., 1997. Global seafloor topography from satellite altimetry and ship depth soundings. Science 277, 1957-1962.

Sobolev, A.V., Hofmann, A.W., Sobolev, S.V., and Nikogosian, I.K., 2005. An olivine-free mantle source of Hawaiian shield basalts. Nature 434, 590-597.

Sobolev, A.V., Hofmann, A.W., Kuzmin, D.V., Yaxley, G.M., Arndt, N.T., Chung, S.-L., Danyushevsky, L.V., Elliott, T., Frey, F.A., Garcia, M.O., Gurenko, A.A., Kamentsky, V.S., Kerr, A.C., Krivolutskaya, N.A., Matvienkov, V.V., Nikogosian, I.K., Rocholl, A., Sigurdsson, I.A., Sushchevskaya, N.M., and Teklay, M., 2007. The amount of recycled crust in sources of mantle-derived melts. Science 316, 412-417.

Sobolev, A.V. and Nikogosian, I.K., 1994. Petrology of long-lived mantle plume magmatism: Hawaii, Pacific and Réunion island, Indian Ocean. Petrology 2, 111-144.

Swinnard, L., Garcia, M.O. and others, submitted 2008. Geochemistry of rejuvenated, post-shield and late shield volcanism on the island of Kauai, Hawaii. Earth and Planetary Science Letters.

Takahashi, E. and Nakahima, K., 2002. Melting processes in the Hawaiian Plume: An experimental study. In: Takahashi, E., Lipman, P.W., Garcia, M.O., Naka, J., and Aramaki, S., Eds. Hawaiian Volcanoes: Deep Underwater Perspectives, 99. 403-418. Geophysical Monograph 128. AGU, Washington, D.C.

ten Brink, U.S. and Brocher, T.M., 1987. Multichannel seismic evidence for a subcrustal intrusive complex under Oahu and a model for Hawaiian volcanism. Journal of Geophysical Research 92, 13,687-13,707.

Turcotte, D.L. and Schubert, G., 2002. Geodynamics. Cambridge University Press: Cambridge. 456 pp.

Upton, B. G. J. and Wadsworth, W. J., 1965. Geology of Réunion Island, Indian Ocean. Nature 207, 151-154.

van Westrenen, W. and Draper, D.S., 2007. Quantifying garnet-melt trace element partitioning using lattice-strain theory: New crystal-chemical and thermodynamic constraints. Contributions to Mineralogy and Petrology 154, 717-730.

van Westrenen, W., Blundy, J.D., and Wood, B.J., 1999. Crystal-chemical controls on trace element partitioning between garnet and anhydrous silicate melt. American Mineralogist 84, 838-847.

van Westrenen, W., Blundy, J.D., and Wood, B.J., 2001. High field strength element/rare earth element fractionation during partial melting in the presence of garnet: Implications for identification of mantle heterogeneities. Geochemistry, Geophysics, Geosystems 2.

Vlastelic, I., Staudacher, T., and Semet, M., 2005. Rapid change of lava composition from 1998 to 2002 at Piton de la Fournaise (Réunion) inferred from Pb isotopes and trace elements: Evidence for variable crustal contamination. Journal of Petrology 46, 79-107.

Walker, F. and Nicolaysen, L. O., 1954. The petrology of Mauritius. Colonial Geology and Mineral Resources 4, 3-43.

Watts, A.B, 2001. Isostasy and flexure of the lithosphere. Cambridge University Press, Cambridge.

Weissel, J.K., Anderson, R.N., and Geller, C.A., 1980. Deformation of the Indo-Australian plate. Nature 287, 284-291.

White, R.S., 1993. Melt production rates in mantle plumes. Philosophical Transactions: Physical Sciences and Engineering 342(1663), 137-153.

White, R.S. and McKenzie, D., 1995. Mantle plumes and flood basalts. Journal of Geophysical Research 100(B17), 17543-17585.

White, W.M., 1985. Sources of oceanic basalts: Radiogenic isotopic evidence. Geology 13, 115-118.

White, W.M., 1989. Geochemical evidence for crust to mantle recycling in subduction zones. In: Hart, S.R. and Gulen, L., eds., Crust/Mantle Recycling at Convergence Zones. Kluwer Academic Publishers, pp. 43-58.

White, W.M., 2007. Geochemistry. http://www.geo.cornell.edu/geology/classes/geo455/Chapters.html.

White, W.M. and Duncan, R.A., 1996. Geochemistry and geochronology of the Society Islands: New evidence for deep mantle recycling. In Basu, A. and Hart, S.R., eds., Earth Processes: Reading the Isotopic Code. AGU, p. 183-206.

White, W.M., Cheatham, M.M., and Duncan, R.A., 1990. Isotope geochemistry of Leg 115 basalts and inferences on the history of the Réunion mantle plume. In: Duncan, R. A., Backman, J., and Peterson, L. C. Eds.), Proceedings of the Ocean Drilling Program, Scientific Results. Ocean Drilling Program, College Station, TX. pp. 53-61.

Wilson, J.T., 1963. A possible origin of the Hawaiian islands. Canadian Journal of Physics 41, 863-870.

Wood, B.J. and Blundy, J.D., 1997. A predictive model for rare earth element partitioning between clinopyroxene and anhydrous silicate melt. Contributions to Mineralogy and Petrology 129, 166-181.

Woodhead, J.D. and McCulloch, M.T., 1989. Ancient seafloor signals in Pitcairn Island lavas and evidence for large amplitude, small length-scale mantle heterogeneities. Earth and Planetary Sciences 94, 257-273, doi: 10.1016/0012-821X(89)90145-3.

Workmann, R.K. and Hart, S.R., 2005. Major and trace element composition of the depleted MORB mantle (DMM). Earth and Planetary Science Letters 231, 53-72. doi:10.1016/j.epsl.2004.12.005.

Yaxley, G.M. and Green, D.H., 1998. Reactions between eclogite and peridotite: Mantle refertilisation by subduction of oceanic crust. Schweiz. Mineral. Petrogr. Mitt 78, 243-255.

Zindler, A. and Hart, S.R., 1986. Chemical geodynamics. Annual Review of Earth and Planetary Sciences 14, 493-571.